The storm time evolution in the night side high altitude field aligned wave Poynting flux and its relation to low altitude downward electron kinetic energy flux at low latitudes

A THESIS

SUBMITTED TO THE FACULTY OF

UNIVERSITY OF MINNESOTA

BY

Scott A Thaller

IN PARTIAL FULFILLMENT OF THE REQUIRMENTS

FOR THE DEGREE OF

DOCTOR OF PHILOSOPHY

John R. Wygant, Adviser

April, 2014

Acknowledgments

Here I would like to acknowledge the people who played an important role in making this thesis possible, in my education and research at the University of Minnesota, as well as those whom made the graduate student experience a good one for me. First, my adviser John Wygant, who provided me with the opportunity to conduct this research and to whom I owe most of my education and training in experimental space plasma physics, in how to conduct research, in how to interact with other investigators, how to present research, and for encouragement. I'm sure I will still be improving the above skills and learning new things from John well into the future. Second, I'd like to acknowledge the other space physics faculty, Cindy Cattell, Bob Lysak, and Paul Kellogg, whom have also been an integral part of my education in the space physics group, both inside and outside of formal course instruction, and important sources of advice and encouragement as well. Third, the research I've had the privilege and opportunity to conduct could not have happened without the hard work of all those involved on the Polar, FAST, DMSP, and Van Allen Probes missions. In particular Forrest Mozer and Peter Harvey for the Polar EFI electric field data; C.T. Russell for the Polar MFE magnetic field data; Jack Scudder for the Polar Hydra data; George Parks for Polar UVI data, L.A. Frank and Mary Rae Dvorsky for Polar VIS images; James McFadden for the FAST electron data; Patrick Newell, Dave Hardy, and Fred Rich for the DMSP electron data. I'd also like to thank John Wygant, John Bonnell, and the rest of the Van Allen probes (RBSP) EFW team as well as the EMFISIS team for support with related inner magnetosphereic research. The

research presented in this thesis was also made possible by the assistance, advice, encouragement, and friendship of the rest of the researchers, staff, and graduate students in the UMN space physics group: John Dombeck, Aaron Breneman, Chris Colpitts, Kris Kersten, Yan Song, Keith Goetz, Steve Monson, Dai Lei, Xiangwei Tang, Adam Hupach, Sheng Tian, and Charles McEachern. With specific regards to editing this thesis I'd like to thank Cindy Cattell and John Wygant for feedback on the science, structure and mechanics of the thesis; as well as Aaron Breneman, Dai Lei, and Charles McEachern for helping to proof read it (at least the first chapter). I'd also like to thank some past members of the UMN space physics group; Jesse Woodroffe and Lynn Wilson, both are good friends and have provided much help both in computing and science issues. Also Alyssa Hamre, with whom I was first working when starting the investigation of the Poynting flux at the Polar spacecraft; Toshi Nishimura, who has likewise provided me with programing help, science advice, and friendship; Lily Hanson who's also helped out with programming and is a good friend; and Justin Willmert for programming assistance. I'd like to thank my thesis committee members for being on said committee and providing feedback on the thesis. I'd like to thank my fiancée Katy Byrd for love, support and encouragement; and to both my parents, Mary and Howard Thaller;,my sister, Julia Thaller,; my grandma Phyllis Thaller; and Katy's dad and step mom, Rick and Pam Byrd, all of who have encouraged me to get this thesis finished. I'd also like to that the School of Physics and Astronomy staff, their efforts being integral to the functioning of the department; in particular I'd like to thank Jody Kaplan, Julie Murphy, Mette Stewart, and Sean Albiston, they've been very helpful. Finally, I'd like to thank my present and

former fellow UMN physics grad student friends not already mentioned: Matt Fritts, Scott Fallows, Chris West, J.J. Nelson, Terry Bretz-Sullivan, Paul Barsic, Taylor Childers, Pearl Sandick, Beth Lusczek, Aaron McGowan, Sean Corum, Abe DeBenedetti, Marie Lopez del Puerto, Charlie Blackwell, and Hannes Hubmayr. Parts of this research were funded with JHU/APL contract 922613 (RBSP-EFW).

Dedication

This thesis is dedicated first and foremost to Katy Byrd, the love of my life.

This thesis is also dedicated to my parents; Mary and Howard Thaller, who have encouraged and supported my interest and involvement with science and scientific study from a young age.

Finally, this thesis is dedicated to the UMN Space Physics group. It is an old saying that "the grass is always greener on the other side of the fence" however being in this group I always felt to be on the greener side.

The storm time evolution in the night side high altitude field aligned wave Poynting flux and its relation to low altitude downward electron kinetic energy flux at low latitudes

By Scott Thaller

Abstract

In this thesis we investigate the evolution of the wave and large scale Poynting flux on earth's night side at altitudes from the auroral acceleration regions to the near earth tail over the course of major geomagnetic storms. Specifically, we are examining the field aligned components of the Poynting flux which carries energy from the tail into the auroral acceleration regions and to the ionosphere, and the down going field aligned electron kinetic energy flux. During major storm Poynting flux, over the range of observed time scales (from 6-180 seconds, and 600 -7200 seconds) intensify significantly (between one and three orders of magnitude), even down to low latitudes ($\leq 65^{o}$ invariant latitude). Concurrently, over the same range of latitudes, but at low altitudes, the downward electron kinetic energy flux enhances by at least an order of magnitude. The wave Poynting flux is thus shown to be a significant energy transport mechanism at low

latitudes during storms, which provides strong evidence that Alfvén waves can be an important mechanism for auroral electron acceleration at low latitudes. This result is important, in part because low latitudes are on field lines mapping to the inner magnetosphere, and the nature of the energy transport processes associated with the near tail and inner magnetosphere are not yet fully understood. Most previous research on the Alfvén wave powered aurora focused on the higher latitude regions of the auroral zone and plasma sheet boundary layer. Prior studies were also conducted with either localized spacecraft conjunctions or with long term statistical compilations. The study presented herein is the first to examine the wave Poynting flux evolution over the course of major storms, from pre-storm, main phase, and recovery phase, from a high altitude standpoint on an orbit by orbit basis and to compare this to the low altitude electron kinetic energy flux. We find that the latitudinal evolution of the intensities of the high altitude wave Poynting flux and low altitude electron kinetic energy flux correspond well with each other. This suggests that there is a generative relation between them that exists over the course of the storm; i.e. either some of the electrons are accelerated by the waves or the electrons and waves are both produced by some third mechanism. A quantitative comparisons of the mapped wave Poynting flux to auroral images and to integrated electron kinetic energy flux, suggests the Poynting flux carries anywhere from ~5% to well over 100% of the energy needed to drive the low altitude electron acceleration processes. This fraction depends on both the level of geomagnetic activity and the assumptions that underlie the integration technique. The similarities between the distribution in time and latitude of the Poynting flux and electron kinetic energy flux

extends to low latitudes ($\leq 65^o$ ILAT) during major storms. At such times the Poynting flux typically intensify about three orders of magnitude, to intensities of 1 to 10 ergs/cm^{2}s, with such enhancements extending down to latitudes of at least 55^o ILAT. The low latitude ($\leq 65^o$ ILAT), low altitude electron kinetic energy flux (peak intensities) are typically on the order of 0.1 ergs/cm^{2}s pre storm, and intensifies to the order of 1 to 10s ergs/cm^{2}s during storms. The existence of intense Poynting flux at low latitudes, similar to those at which intense downward electrons are also observed, suggest that Alfvén waves are important for, or at least closely related to, low latitude auroral acceleration processes. We also find that though the intense wave Poynting flux tends to occur in conjunction with large scale Poynting flux. And that while the wave Poynting flux is typically an order of magnitude greater in peak intensities, the large scale Poynting flux carries more energy to the ionosphere overall.

The arrangement of this thesis is as follows. First, in the introduction, we go over basic space plasma physics with specific focus on energy transfer. We also discuss magnetohydrodynamics (MHD), Alfvén waves, and how Alfvén waves accelerate auroral electrons. In the second chapter we discuss previous work, both observational and theoretical, on the nature of Alfvén wave powered aurora. In the third chapter, we discuss the satellites, the instruments they carry, and other sources of data used in the research presented herein. In chapter four we present the main part of the thesis research, described above in this abstract. In the fifth chapter, we investigate the large scale Poynting flux and its relation to the wave Poynting flux. Finally, in chapter six, the conclusion, we summarize the findings.

Table of Contents

List of Tables

List of Figures

Chapter 1:

1.1 Introduction

Earth's magnetosphere is the region around Earth filled with collisionless plasma and dominated by the Earth's geomagnetic field, forming a cavity in the solar wind. From a perspective moving from low to high altitude, away from Earth, the magnetosphere starts at the top of the upper ionosphere and extends out to the magnetopause, beyond which is the magnetosheath, the flow of shocked solar wind, a few Earth radii in thickness [Kivelson and Russell, 1995], diverted around the magnetosphere. The magnetosheath is separated from the solar wind by the bow shock, a feature which comes about due to the fact that the solar wind flow is supersonic. Figure 1 illustrates these and other major components of the magnetosphere as well as the magnetospheric current systems, which will be discussed in the present chapter.

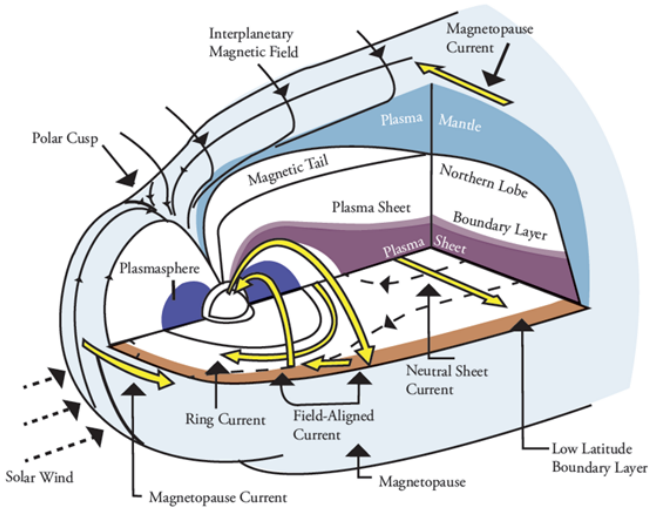

(a) The magnetosphere, large scales structures and current systems. Adapted from Paschmann, Haaland, and Treumann

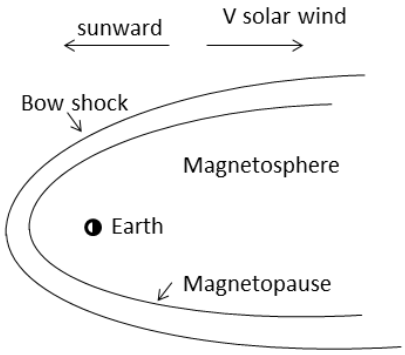

(b) Schematic of the bow shock around the magnetosphere

Figure 1.1: Drawing of earth's magnetosphere (a) showing major large scale structures and current systems. In (b) is a schematic of the relative location of the magnetosphere, magnetopause, bow shock, and solar wind.

On its own Earth's geomagnetic field is approximately a dipole, but the interaction with the solar wind and interplanetary magnetic field (IMF) compresses the geomagnetic field on the dayside and stretches it out on the night side to form the geomagnetic tail (also called the "magnetotail"). The sunward side of the magnetosphere is compressed by the solar wind ram pressure. The balancing point between solar wind ram pressure and the magnetic pressure of the magnetosphere varies with solar wind speed and density, but a typical value is ~ 10 Earth radii (R_E) in the subsolar region. The subsolar region of the compressed dipole field is accompanied by a current running duskward, or eastward, around the nose of the magnetosphere, consistent with Ampères law. This magnetopause

current is effectively a shielding current and is known as the Chapman-Ferraro current. There are shielding currents in other regions of the sheath (discussed more below) as well, associated with the closure of magnetospheric currents, and which play an important role in energy transport.

1.2 The inner magnetosphere

Close to the Earth, roughly inside a radial distance of 3 to 6 R_E geocentric, the magnetic field remains approximately dipolar; though during geomagnetic storms (discussed below) this dipolar region shrinks in size according to the severity of the storm disturbance. This approximately dipolar region is the inner magnetosphere and it is the location of a variety of important plasma populations; in particular, the plasmasphere, ring current, and the radiation belts.

The plasmasphere is a torus shaped region of cold dense plasma (densities $\sim 10 - 10^4$ cm^{-3} and temperatures ~ 1 eV), populated by ionospheric plasma and extending to an equatorial distance typically between 3 and 5 R_E geocentric, terminating in an outer boundary known as the plasmapause. The plasmapause is often a sharp boundary, but can also be a smooth transition to the regions of less dense plasma beyond, or an irregular transition consisting of detached regions of plasmasphere plasma [Carpenter and Anderson 1992]. During prolonged geomagnetically quiet intervals the plasmasphere can extend out to geosynchronous orbit, 6.6 R_E [Goldstein, 2006]. Plasmasphere erosion occurs when the large scale dawn to dusk convection electric field becomes enhanced,

extending its domination over the corotation electric field closer in towards the Earth[1]. When this occurs plasma on closed drift paths corotating by the **E**×**B** drift in the outer part plasmasphere is now on open drift paths and escapes to the magnetopause.

The ring current is a torus of westward current around the Earth, consists of ions and electrons (though ions are the main current carrier) with energies of ~1keV to a few hundred keV which are magnetically trapped and are mirroring[2] back and forth along field lines roughly between 1.5 and 9.5 R_E [Daglis et al, 1999]. In addition to mirroring, the ring current particles undergo both curvature and gradient B drifts[3], the ions drifting azimuthally westward and the electrons eastward, establishing the westward current.

Ring current particles are driven into the inner magnetosphere from the plasma sheet in the geomagnetic tail by the enhanced convection electric field [e.g. see Wygant et al.

---

[1] Charged particles placed in an electric **E** and magnetic **B** field will undergo **E×B** drift motion with a velocity given by $\boldsymbol{v} = \boldsymbol{E} \times \boldsymbol{B}/B^2$. In the inner magnetosphere the large scale electric field to first order is given by the sum of the large scale dawn-dusk convection electric field, **E**c, and the corotation field **E**$cr = -(\boldsymbol{\omega} \times \boldsymbol{r}) \times \boldsymbol{B}$, where $\boldsymbol{\omega}$ is the angular rotation of the Earth and$\boldsymbol{B}$ is the magnetic field at position $\boldsymbol{r}$. So when $Ec \gg Ecr$ the drift velocity **v** of plasma in the outer plasmasphere is primarily sunward and not azimuthal.

[2] A charged particle moving with velocity **v** in a converging magnetic field **B** geometry from a region of weaker to stronger field will experience an opposing force (a component of **F** = q**v**x**B**) decreasing its parallel velocity $v_{||}$. But as the total magnetic field does no work, the decrease in $v_{||}$ is accompanied by an increase in the perpendicular velocity $v_\perp$, conserving its total kinetic energy. If the angle between the particle's velocity and magnetic field, (called the pitch angle), is greater than some minimal angleα_o , where $\sin^2(\alpha_0) = B_0/B_m$ (the 0 and m subscripts refer to the initial (weaker) and mirroring (stronger) field strengths respectively), $v_\parallel$ will decrease to zero and the particle will mirror. But if the pitch angle is smaller thanα_0, the particles will not mirror but escape confinement, the angular region in which particles can escape is the loss cone.

[3] The gradient B and curvature drifts are experienced primarily by hot changed particles in a curved magnetic field. These drifts, given by $\boldsymbol{v}_{grad} = \left(\frac{mv_\perp^2}{2qB}\right)\left(\frac{\boldsymbol{b}\times\nabla B}{B}\right)$ and $\boldsymbol{v}_{cur} = -\frac{mv_\parallel^2}{R_c}\left(\frac{\boldsymbol{R_c}\times\boldsymbol{B}}{qB^2}\right)$ respectively (where m, q, $v_\perp$ $v_\parallel$ are the mass, charge, perpendicular and parallel velocity, Rc is the radius of curvature of the field line), the hotter the particles are the higher their drift velocity will be. Thus these drifts are typically more important than the **E×B** for hot particles, as these drifts have a direct dependence on the particle energy.

1998 and references therein]. In this case, the **E×B** drift moves the ions and electrons from the tail, a region of weaker magnetic field, to the inner magnetosphere, a region of stronger magnetic field, and as a result the particles are energized by the conservation of their first adiabatic invariant[4].

Since the ring current is azimuthally westward, it gives rise to a southward magnetic field inside the current loop that opposes the northward direction of Earth's natural dipole field around the equator. The ring current becomes enhanced during storms, due to the enhancement in the large scale convection electric field, and the observed decrease in the magnetic field on the Earth's surface is an important storm indicator known as the Disturbance storm time (Dst) index. A storm signature in Dst consists of three parts: Typically present is an initial positive perturbation caused by an enhanced compression of the geomagnetic field when it encounters enhanced solar wind flows, this initial phase lasts a few hours to a day. The second part of a storm is the main phase, characterized by a rapid decrease in Dst over a few hours as enhanced convection transports plasma into the ring current. The third part is the recovery phase, which is slower, lasting a few days or longer over which ring current particles are lost due to processes discussed below. As far as classification of storms by Dst goes, one categorization [Gonzalez et al, 1994]

[4] Adiabatic invariants are conserved so long as the particle motion is not perturbed suddenly on the time scale of their corresponding cyclical motion, i.e. by a sharp spatial gradient, a collision, waves, etc. There are three adiabatic invariants. The first is associated with the gyromotion of the particle around a field line: $\mu = mv_{\perp}^2/2B = const1$, i.e. the ratio of the perpendicular particles energy to the magnetic field strength. The second is for bounce motion between two mirror points $\oint v_{\parallel}\, ds = \int_a^b (1 - B(s)/B_m)^{1/2} ds = conts2$, where ds is the differential displacement along the magnetic field B(s) and Bm is the field at the mirror point. The third is for azimuthal drift motions, such as those around the Earth, $\Phi_B = \pi R^2 B = const3$, where the invariant is the magnetic flux enclosed by the particles drift motion of radius R. In the case of motion around the dipole, the third invariant is actually also equal to the total flux outside the enclosed orbit, because of the reversed magnetic flux of the field lines passing through the core of the dipole.

regards a small storm as Dst <∼-30 nT, a modest storm as Dst < ∼-50 nT and an intense storm as Dst < ∼ -100 nT. Generally the most intense storms are Dst ∼ -250- to -500 nT. Major storms, which will be examined in this thesis shall be considered as having Dst < ∼ -150 nT.

The decay of the ring current occurs primarily through a process in which ring current ions capture electrons from cold exosphere neutral atoms. The resulting energetic neutral atoms are not magnetically confined by mirroring and escape from the magnetic bottle. Another ring current loss process takes place when there is an overlap between the warm ring current population and cold dense plasmasphere population. An overlap of such plasma populations creates a favorable environment for the growth of electromagnetic ion-cyclotron (EMIC) waves [Goldstein 2006 and references therein]. EMIC waves scatter ring current ions into the loss cone where they are lost to atmospheric precipitation.

The inner and outer radiation belts are the other population of magnetically trapped energetic particles in the inner magnetosphere. The outer radiation belt is a torus of plasma located roughly between 3-6.5 R_E geocentric equatorial , and consists of trapped mirroring particles of energy ~100keV- few MeV. The outer belt is highly dynamic and the relativistic particle flux may increase, decrease or be left unchanged by storms [Reeves et al., 2003]. The inner radiation belt, also a torus of trapped energetic particles, at about 1.5-2 R_E is created by the decay of neutrons ejected into space from the interaction of cosmic rays with atmospheric atoms. The inner belt is stable even under storm conditions. The processes that energize particles in the outer belt are still not fully

understood, but proposed mechanisms include the conservation of the first adiabatic invariant while particles diffuse to regions of stronger geomagnetic field [e.g. Schulz and Lanzerotti 1974], many interactions with high frequency waves, namely whistler mode chorus[5] [Meredith et al 2001; Horne et al 2005], or via a few interactions with extremely large amplitude whistlers [Cattell et al 2008; Bortnik et al 2008; Cattell et al 2012 and references therein]. Loss mechanisms of radiation belt electrons include loss cone scattering (i.e. being scattered into the loss cone) by waves, and magnetopause shadowing. In the plasmasphere, radiation belt electrons may be pitch angle scattered into the loss cone by broad-band whistler mode waves known as the plasmaspheric hiss. The plasmaspheric hiss is largely responsible for the slot region, the region between the inner and outer belt largely devoid of energetic electrons [Millan and Thorne 2007 and references therein]. Magnetopause shadowing occurs when enhancements in the ring current result in a significant decrease in magnetic field strength inside the closed drift path of the radiation belt particles, such that the particles drift radially outward in order to conserve the third adiabatic invariant. At the same time, strong solar wind pressure may push the magnetopause inwards towards the outwardly expanded particle drift paths. If the magnetopause encounters the closed drift path of the radiation belt particles, they can be lost to the magnetopause [see Millan and Thorne 2007 and references therein].

[5] Whistlers are right-handed polarized electromagnetic waves that tend to propagate along field lines. Whistlers are electron waves, and in the magnetosphere their frequency is typically on the order of a few kHz. Hiss and chorus are two important types of whistler mode emissions in the inner magnetosphere. Hiss mode has a roughly featureless spectrum and is associated with the balance of wave growth due to loss-cone anisotropy and the scattering of electrons into the loss cone (thus reducing anisotropy). Chorus mode emissions have a structured spectrum with many discrete tones, believed to be associated with the trapping of resonant electrons in the rotating wave field [Gurnett and Bhattacharjee, 2005]. They often appear as two distinct bands, one just above and [footnote continued from pervious page] another below one half the electron cyclotron frequency, fce/2, and are generated in the equatorial regions of the magnetosphere.

Temporary dropouts and flux decrease in the energetic particles are possible even if the particles remain but are located in a region of weakened field. In this case the decrease in energy is a temporary flux dropout corresponding to conservation of the first adiabatic invariant. The flux of energetic particles will reappear once the field strength recovers.

1.3 The Geomagnetic Tail

Further away from Earth, outside of the inner magnetosphere, on the night side, is the geomagnetic tail. The geomagnetic tail is a region of field lines stretched anti-sunward of Earth by interaction with the solar wind. The stretched field lines of the tail act as a reservoir of energy that is released during storms and substorms (discussed below). The tail geometry is roughly cylindrical with a diameter of approximately 50 - 60 R_E and a length that extends for 100s of R_E in the anti-sunward direction on the night side. The major structures of the geomagnetic tail are the north and south lobes, and the plasma sheet lying in between the lobes. The plasma sheet is divided into the central plasma sheet, and the plasma sheet boundary layers (PSBL) separating the lobes and the central plasma sheet. The north (south) lobe field lines connect to the ionosphere in the north (south) polar caps, the region poleward of the auroral oval. On the opposite end these field lines are open to and merge with the IMF. Lobe plasma is cool and rarified, with densities ~0.01 cm^{-3} and ion (electron) temperatures of ~300 eV (~50 eV) respectively. The north (south) lobe field points roughly in the sunward (anti-sunward) direction [figure 2] and the field strength varies, decreasing with distance from Earth (~100nT in the near tail at ~6-10 R_E, ~20 nT further back at 20-30RE, and ~10nT in distant tail, at ~60R_E).

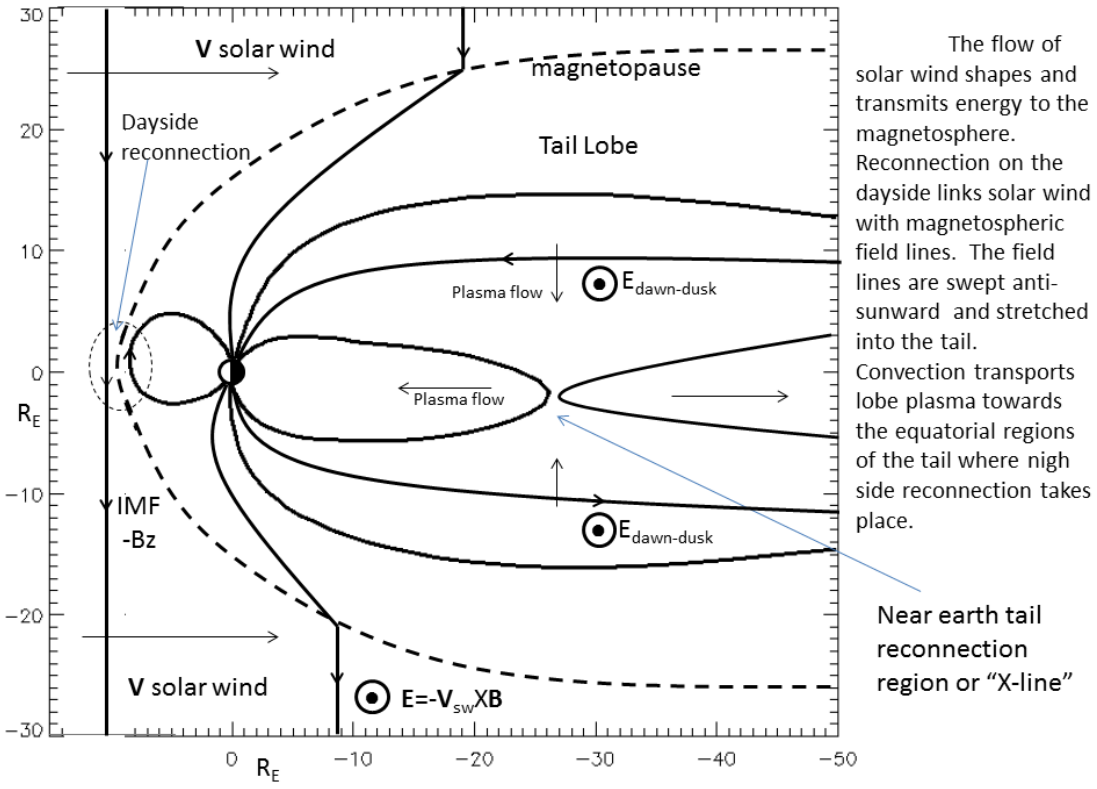

Figure 1.2: Magnetic field lines and magnetospheric convection.

The plasma sheet consists of denser and hotter plasma than is in the lobe, and its plasma pressure balances the magnetic pressure in the lobes to maintain equilibrium. The central plasma sheet has a density of n ~0.1-1 cm^{-3} and ion (electron) temperature of ~2 to 20 keV (0.4-4 keV) . In the PSBL the particle density and ion (electron) temperatures are ~ 0.1cm^{-3} and ~1000 eV (~150 eV) respectively. The plasma sheet in the near Earth region is ~6 R_E thick [Baumjohann and Paschmann 1990]. Between the lobes, embedded in the plasma sheet near the equatorial plane, the field reversal takes place. An area of

locally weak magnetic field occurs around the tail field reversal, as illustrated in Figure 2. Associated with this magnetic field reversal is the cross tail current sheet, the current pointing in the duskward direction, as is consistent with Ampère's law. This current sheet is often thinner than the plasma sheet itself [Sergeev et al, 1993]. At the edge of the tail, the cross tail current meets with the magnetosheath which carries a current in the dawn-ward direction around and over the tail, closing the cross tail current and providing a shielding current around the tail, consistent with the magnetic field shear between the lobes and solar wind. In the Earthward part of the tail, the magnetosheath current also closes the Region 1 large scale field aligned currents (FAC), which are discussed below.

Plasma sheet particles can be heated through acceleration by the large scale dawn-dusk convection electric field. In the lobe, the particles undergo **E**×**B** drift, which does not energize them since the drift motion is perpendicular to **E**, towards the plasma sheet [Figure2]. In the plasma sheet however, the particles may undergo what is called Speiser motion in which they are displaced along the electric field as they do a half gyration in the small northward component of **B** that threads the plasma sheet. The plasma sheet field lines are closed, both ends map to the ionosphere in north and south hemispheres, and the northward **B** is a component of the closed field lines passing through the plasma sheet. On such a field line, electrons and ions can mirror back and forth between the north and south hemisphere magnetic foot points. If the northward B field in the central plasma sheet is sufficiently small, the particle's adiabatic invariant will be broken and it will execute a half gryo-orbit around the northward field component, along the direction of the electric field (for ions, and opposite **E** for electrons) to a new closed field line.

This process tends to energize ions more because they have larger gyro-radii and so experience a larger potential drop with each bounce. Alternatively, if the particles maintain their adiabatic invariants, they can undergo curvature drift in the curved field closing through the plasma sheet, this motion is also along (opposite) **E** for ions (electrons) allowing for energy gain [see Cowley 1991 and references therein].

1.4 Magnetic reconnection, the Dungey cycle, and magnetospheric convection

The source of energy powering magnetosphere dynamic is ultimately supplied by the Sun, mainly through the magnetosphere's interaction with the solar wind. One important way in which the solar wind interacts with the magnetosphere is through magnetic reconnection.

Magnetic reconnection is a process in which magnetic energy is converted into particle energy and large scale topological reconfiguration of the magnetic field takes place. A rough conception of how reconnection leads to topological reconfigurations may be had by considering two magnetic flux tubes with field directions oriented anti parallel to each other at some place where a segment of each comes very close to one another [Figure 3]. At this location, called the "X-line", the fields reconnect after which the two parts of each flux tube on either side of the initial reconnecting segment are connected to the respective pieces of the other flux tube.

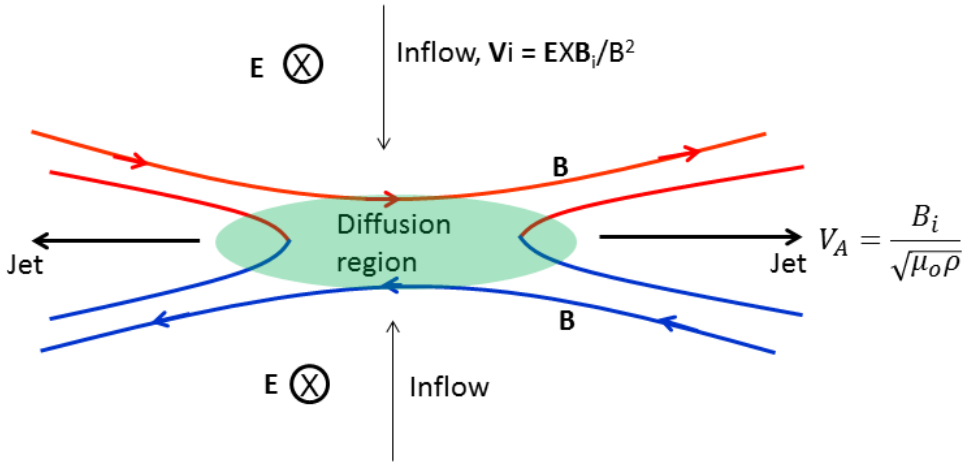

Figure 1.3: Simplified diagram illustrating some basic aspects of magnetic reconnection. From above and below field lines drift in toward the diffusion region where the plasma flow, indicated by the black arrows, becomes separate from the magnetic field lines drifting in from above (red) and below (blue). These field lines are oppositely directed relative to one another and leaving the diffusion region, the magnetic field topology has changed with the top inflowing segments to the right or left of the diffusion region becoming connected with their respective counterpart inflowing from the bottom. The "new" reconnected field lines are a joining of these two and are illustrated by the bicolor red/blue lines in the outflow, they now form one field line. The outflow jets carry away energy that was initially in the magnetic field.

The newly reconnected magnetic field lines move away from the reconnection region driven in part by the magnetic tension associated with their bent geometry. Associated with reconnection are back to back plasma jets ejecting plasma outwards from the reconnection region perpendicular to the inflow. These jets come about from plasma flow accelerated by the release of tension in the bent magnetic field configuration of the newly reconnected field lines. The speed of plasma outflow jets from the reconnection region is on the order of the Alfvén speed, $V_A = B/\sqrt{\rho\mu_o}$, where ρ is the plasma mass density, μ_o is the permeability of free space, and B is the magnetic field strength in the

upstream region of plasma flowing into the reconnection region[6]. In the inflowing and outflowing plasma, the field lines act as if they are frozen into the plasma and move with it (the "frozen-in" condition will be discussed more below). In order for reconnection to take place, the magnetic field and plasma must able to move separately, otherwise the field lines would stagnate at the center of the reconnection region. This uncoupling of the field lines from the plasma flow occurs at the diffusion region.

The early Sweet-Parker model of reconnection [Parker, 1957; Sweet, 1958] assumes that the magnetic field diffused through the plasma and the dissipation of the magnetic energy is due to the finite conductivity of the plasma. The Sweet-Parker model gives a reconnection rate that is much too slow to explain reconnection based phenomena, in particular solar flares. Solar flares are sudden releases of massive amounts of energy on the Sun's surface that come about through reconnection transforming energy stored in twisted magnetic field structures (e.g. prominences, arcs, etc.) into particles energy. According to the Sweet-Parker model, flares should develop over a time of tens of days as opposed to a few minutes as is observed. Petschek [1964] provided an alternative model in which the diffusion region is contracted to a small area and the change in magnetic field occurs at a standing Magnetohydrodynamic (MHD- discussed more below) shock wave that opens out at an angle from the diffusion region. In this model, most of the plasma does not flow through the diffusion region, and the reconnection rate

[6] This can be seen by considering an equilibrium situation in which the plasma pressure in the diffusion region is equal to the magnetic pressure in the upstream flow ($P_{mag} = B^2/2\mu_o$) a fluid element accelerated from the diffusion region to a distant region in the ion jet direction where the local pressure is small will reach a speed on the order of the Alfvén speed in the inflow plasma. Alternatively, by equating the inflowing flux of electromagnetic energy to the kinetic energy flux carried by the plasma jets one also obtains a jet speed on the order of the Alfvén speed.

is much greater. In any case, it is important to keep in mind that the "X-line", reconnection or diffusion region, is in reality a highly dynamic three dimensional region a full explanation of which must invoke waves and particle kinetics [e.g. Song and Lysak 2001, Mozer et al 2003, Wygant et al 2005, Cattell et al 2005, Mozer 2006].

The plasma flows/jets exhausting from the reconnection region play an important role in magnetospheric energy transport; they carry energy away from the initially stretched field lines, and also provide a source of energy for Alfvén waves. The slowing of these flows as they propagate Earthward is an important energy source for Alfvén waves that carry more than sufficient Poynting flux to power aurora [Angelopoulos et al 2002; Dai et al, 2011; Zhang et al 2012]. Reconnection in the tail closes the field lines Earthward of the reconnection region. The PSBL, being the region separating the open field lines of the lobe and closed plasma sheet field lines, is expected to map back to the reconnection region, and earthward to the poleward boundary of the auroral oval. Alfvén waves carrying intense Earthward Poynting flux are frequently observed at the PSBL [Wygant et al 2000; Keiling et al 2002], as will be discussed in more detail in the next chapter.

A very rough sketch of the interaction of the IMF with the geomagnetic field via reconnection can be thought of as the following processes. The solar wind carries the IMF out into interplanetary space, as the IMF magnetic field acts as if it is frozen into the solar wind plasma. The direction of the IMF is variable. When the IMF is directed southward, it is opposite to the orientation of Earth's field in the equatorial plane. The IMF flows earthward and reconnects with Earth's field on the day side and the continued flow of the solar wind passed Earth with the IMF frozen in but also now attached to the

geomagnetic field results in the field lines being pulled back to the Earth's night side [Figure 3]. This night side pileup of stretched magnetic field forms the geomagnetic tail. The oppositely directed lobe field lines (open to the IMF) later reconnect in the plasma sheet and these closed magnetic field lines move Earthward, replenishing the magnetic flux depletion on the dayside. If the IMF is directed northward, reconnection between the IMF and the geomagnetic field takes place in the cusp. Cusp reconnection does not result in a net flux accumulation in the tail, as it removes as much flux from the tail as it puts into it. Magnetospheric reconnection thus takes place on the dayside magnetopause, in the tail and in cusps [dayside and tail reconnection are illustrated in Figure 2]. The basic picture of a southward IMF reconnecting with the dayside geomagnetic field, opening the geomagnetic field to the IMF, and the returning of flux lines to the dayside after closing again through reconnection on the night side was first proposed by Dungey [1961] and is sometimes referred to as they Dungey cycle.

The Dungey cycle of magnetic flux in the magnetosphere plays a central role in magnetosphere-ionosphere coupling. After the IMF reconnects with the geomagnetic field on the day side, the open field lines are swept anti-sunward and associated with this flow is a large scale duskward convection electric field $\mathbf{E} = -\mathbf{v}\times\mathbf{B}$, where $\mathbf{v}$ is the plasma flow velocity in the Earth stationary frame and $\mathbf{B}$ is the magnetic field. The field lines are equipotential contours[7] and the convection electric field maps down to a duskward electric field in the ionosphere across the polar cap (i.e. to the ionospheric region of open

[7] Charge carriers move quickly on the time scales involved here, and thus will short out any electric field along B, effectively the field lines are perfect conductors and no potential drop occurs. Later we will discuss cases where parallel potential drops are important.

field lines). This duskward polar cap electric field then drives a nightward flow of ionospheric plasma [see Figure4]. The open field lines of the lobes are convected towards the plasmasheet and are closed by reconnection in the tail plasma sheet [see Figure 2]. The closed tail field lines then move Earthward and westward (eastward) around the dusk (dawn) side of the Earth to the dayside replacing the flux eroded by dayside reconnection. The closed field lines have footpoints equatorward of the polar cap. From a perspective looking down on the North hemisphere [Figure 4], equatorward of the polar cap, the downward directed magnetic field of the closed returning flux will be associated with a poleward (equatorward) electric field the dusk (dawn) side. The total resulting electric field pattern in the ionosphere thus converges on the dusk flank of the polar cap and diverges on its dawn flank. This electric field is the $-\mathbf{v}\times\mathbf{B}$ field associated with the two-cell "convection" pattern of the ionospheric plasma driven by the Dungey cycle, and is closely related to the ionospheric currents and their relation to the FAC [Cowley, 2000].

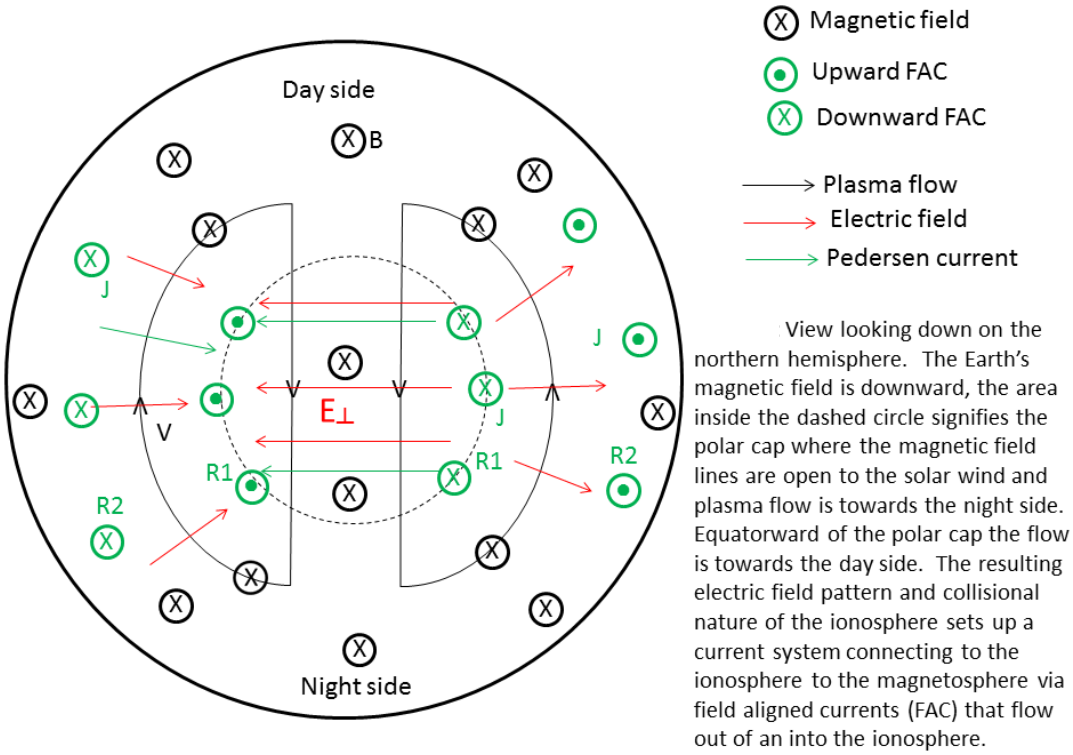

Figure 1.4 : Ionospheric "two-cell" convection driven by magnetic field line convection.

1.5 Conductivity of the Ionosphere

In collisionless plasma the E×B drift does not produce a current since both ions and electrons have the same drift velocity. But in the plasma of the lower ionosphere (~100-200km) both ions and electrons collide with neutral atoms. The ion-neutral collision frequency is comparable to the ion gyro frequency, and the ion fluid motion consists of both the E×B drift and a component along the electric field associated with collisions, and the appropriate force balance expression is $e(\boldsymbol{E} + \mathbf{v}_i \times \boldsymbol{B}) = m_i \nu_{in} \mathbf{v}_i$ (eq1), where the "i" subscript means ion, $\mathbf{v}_i$ is the ion velocity, and ν_{in} is the ion neutral collision frequency. The electron gyro frequency is large relative to the electron-neutral collision frequency and so the electron fluid remains frozen in and its motion is described by just

the E×B drift: $\boldsymbol{E} + \mathbf{v}_e x \boldsymbol{B} = 0$ (eq. 2), where $\mathbf{v_e}$ is the electron velocity. The difference in drift velocities of electrons and ions results in a current, $\boldsymbol{j} = en(\mathbf{v}_i - \mathbf{v}_e)$ (eq. 3) with one component parallel to E carried by ions, called the Pedersen current, and another opposite the E×B drift of the two-cell drift pattern, carried by electrons, called the Hall current. The total current in the ionosphere consists of the perpendicular Hall and Pedersen currents as well as a parallel current. Since electric fields associated with the two-cell convection pattern converge (diverge) on the dusk side (dawn side) flank of the Polar cap, so do the Pedersen currents. Since the current flow is divergent free $\nabla \cdot \boldsymbol{j} = 0$ it flows up (down) along field lines on the dusk (dawn) flanks of the polar cap. These large-scale field aligned currents (FACs) are referred to as the Region 1 currents. In the collisional ionosphere the parallel current is carried by electrons and is proportional to the electric field via Ohms law, $j = \sigma_{\parallel} E$, (eq. 4). The parallel conductivity $\sigma_{\parallel}$ is found by balancing the collisional drag force between electrons and neutral atoms with the electrostatic force on electrons $-e\boldsymbol{E} + \nu_{en} m_e \mathbf{v}_e = 0$, solving for E and substituting it and $j = en\mathrm{v}_e$ into eq. 4. The Hall and Pedersen conductivities may be found by writing an expression for the total perpendicular current by solving eq. 1 and 2 for $\mathbf{v}_e$ and $\mathbf{v}_i$ and substituting into eq 3, and grouping the terms multiplied by the electric field $\boldsymbol{E}$ and the $-\boldsymbol{E} \times \boldsymbol{B}$ term separately, so that $\boldsymbol{j}_{\perp} = \sigma_P \boldsymbol{E} + \sigma_H \widehat{\boldsymbol{B}}_o \times \boldsymbol{E}$ where $\widehat{\boldsymbol{B}}_o$ is the unit vector along **B,** and $\boldsymbol{E}$ is in the corotating frame, and it is assumed that there are no neutral winds. In the general form, the parallel, Pedersen and Hall conductivities ($\sigma_{\parallel}, \sigma_p, \sigma_H$ respectively), for plasma with s species of charge carrier of mass m_s and each of charge e are:

$$\sigma_{\parallel} = \sum_s \frac{n_s e^2}{m_s \nu_s} \quad , \quad \sigma_P = \sum_s \frac{n_s e^2}{m_s} \frac{\nu_s}{\nu_s^2 + \omega_{cs}^2} \quad , \sigma_H = -\sum_s \frac{n_s e^2}{m_s} \frac{\omega_{cs}}{\nu_s^2 + \omega_{cs}^2} \quad \text{(eq 5)}$$

where n_s , ν_s , ω_s are the number density, collision frequency and cyclotron frequency of charge carrier of species s respectively [Paschmann et al. 2002].

During times of enhanced magnetospheric convection, and at lower latitudes, a second region of field aligned downward (upward) currents, called region 2 (R2) currents, occur on the dusk side (dawn side) equator ward of the polar cap and help to feed the higher latitude Region 1 currents. At higher altitudes, the region 2 FAC connect to the night side partial ring current. The partial ring current is associated with storm time enhancements in Earthward convection of hot plasma sheet ions into the inner magnetosphere [e.g. Hashimoto et al 2002]. This creates a region of high pressure between the inner magnetosphere and the inner edge of the geomagnetic tail and establishes a current in the westward (duskward) direction. On the dusk (dawn) side the partial ring current closes through the downward (upward) region 2 FAC. The partial ring current changes into a symmetric ring current in a very short time (< 1 min) after Bz turns northward [Hashimoto et al, 2002]. In the absence of the partial ring current the region 2 currents do not form and closure of the equatorward edge of the Pedersen currents is through the lower latitude (relative to the polar cap) ionosphere [e.g. Goldstein 2006 and references therein].

1.6 Generator Physics

The magnetosphere can be viewed as a system of generators, energy transport processes, and loads. The generator and load regions are distinguishable by considering the sign of

$\boldsymbol{E} \cdot \boldsymbol{j}$, which is the work done per unit volume per unit time $\boldsymbol{E} \cdot \boldsymbol{j} = n(e\boldsymbol{E} \cdot d\boldsymbol{x})/dt$; a load being indicated by $\boldsymbol{E} \cdot \boldsymbol{j} > 0$, a generator by $\boldsymbol{E} \cdot \boldsymbol{j} < 0$. The quantity $\boldsymbol{E} \cdot \boldsymbol{j}$ is related to the flux of electromagnetic energy, given by the Poynting vector, $\boldsymbol{S} = \boldsymbol{E} \times \boldsymbol{B}/\mu_o$ (eq. 6) via Poynting theorem:

$\boldsymbol{j} \cdot \boldsymbol{E} + \partial/\partial t(B^2/2\mu_o + \epsilon_o E^2/2) + \nabla \cdot \boldsymbol{S} = 0$, which related the work done on/by the plasma per unit time per unit volume to the divergence of the electromagnetic energy flow and the change in energy stored in the electric and magnetic fields. Poynting's theorem can be obtained by dotting **E** into the form of Ampère's law that includes the displacement current, $\nabla \times \boldsymbol{B} = \mu_o \boldsymbol{j} + \mu_o \epsilon_o \partial \boldsymbol{E}/\partial t$ (eq. 7) and, after some manipulation, using Faradays law $\nabla \times \boldsymbol{E} = -\partial \boldsymbol{B}/\partial t$ (eq 8). The relation between $\boldsymbol{j} \cdot \boldsymbol{E}$ and the kinetic energy of the bulk plasma motion can be seen by writing $\boldsymbol{j} \cdot \boldsymbol{E}$ with the convection electric field $\boldsymbol{E} = -\boldsymbol{v} \times \boldsymbol{B}$ and using the force relation between the gradient in plasma pressure ∇P, the $\boldsymbol{j} \times \boldsymbol{B}$ term , and the acceleration of the fluid given by, $\rho\, d\boldsymbol{v}/dt = -\nabla P + \boldsymbol{j} \times \boldsymbol{B}$, (eq. 9) we obtain

$\boldsymbol{j} \cdot \boldsymbol{E} = -\boldsymbol{j} \cdot (\boldsymbol{v} \times \boldsymbol{B}) = \boldsymbol{v} \cdot (\boldsymbol{j} \times \boldsymbol{B}) = \rho \boldsymbol{v} \cdot d\boldsymbol{v}/dt + \boldsymbol{v} \cdot \nabla P$. In cases where the pressure is negligible $\nabla P = 0$, then $\boldsymbol{j} \cdot \boldsymbol{E} > 0$ (< 0) corresponds to increase (decrease) in kinetic energy density $1/2\, \rho v^2$.

The ionosphere acts as a load, that $\boldsymbol{E} \cdot \boldsymbol{j} > 0$ can be seen from the fact that the Pedersen currents are in the same direction as the electric field. This implies that there is a generator ($\boldsymbol{E} \cdot \boldsymbol{j} < 0$) in the magnetosphere that supplies the power dissipated in the ionosphere. To explore this further we consider that the field lines in the Polar cap are

open to the IMF and are swept anti-sunward by the flow of solar wind and sheath plasma. In the plasma sheath the field transitions from an IMF field to the magnetosphere field configuration and this transition involves a sunward (anti-sunward) perturbation of the magnetic field in the north (south) hemisphere sheath [see Figures 5 and 2]. This perturbation is associated with the shielding current in the sheath which flows from the dusk side flank of the tail to the dawn side around the tail while the $\boldsymbol{v} \times \boldsymbol{B}$ convection electric field points with a duskward component; since **j** and **E** are opposite $\boldsymbol{j} \cdot \boldsymbol{E} < 0$ indicating that the sheath is a generator region [Figure 5]. The large scale field aligned R1/R2 currents thus transmit stress from the magnetosheath/magnetosphere to the ionosphere. This can be seen in the corresponding Poynting vector found from the sheath electric field (roughly duskward) crossed with the sheath magnetic field perturbation (sunward for the north lobe and anti-sunward for the south lobe). This Poynting vector has a component aligned with the geomagnetic field and is Earthward, consistent with and indicating the flow of electromagnetic energy from the sheath to the ionosphere.

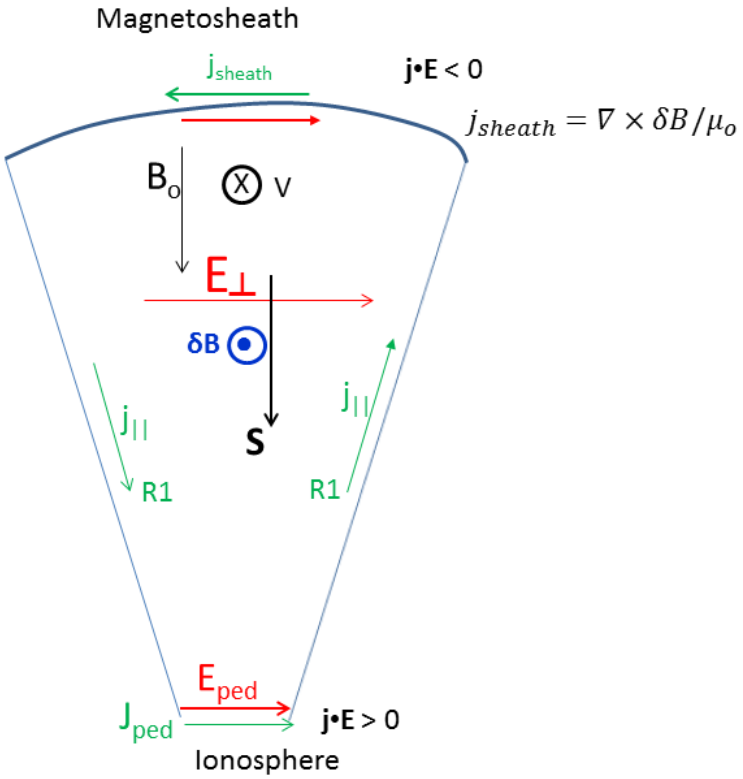

Figure 1.5: Schematic representation of the magnetosheath generator and ionosphere load. Viewed sunward of the Earth, a schematic showing northern hemisphere open polar cap field lines being swept anti-sunward due to solar wind flow, and the relation between the resulting magnetosheath generator, ionosphere load, and large scale Poynting vector associated with $E_\perp = -V \times B_o$, $S = E_\perp \times \delta B/\mu_0$.

Earthward large scale Poynting flux is associated with the return, dayward, flow of magnetic flux as well. The ionospheric electric field that drives the Pedersen current between the region 2 and region 1 FAC corresponds to an electric field that maps along magnetic field lines into the magnetosphere such that the $\boldsymbol{E} \times \boldsymbol{B}_o$,where B_o is the background magnetic field, velocity is consistent with the field line convection around Earth from night side to the dayside [Figure 6].

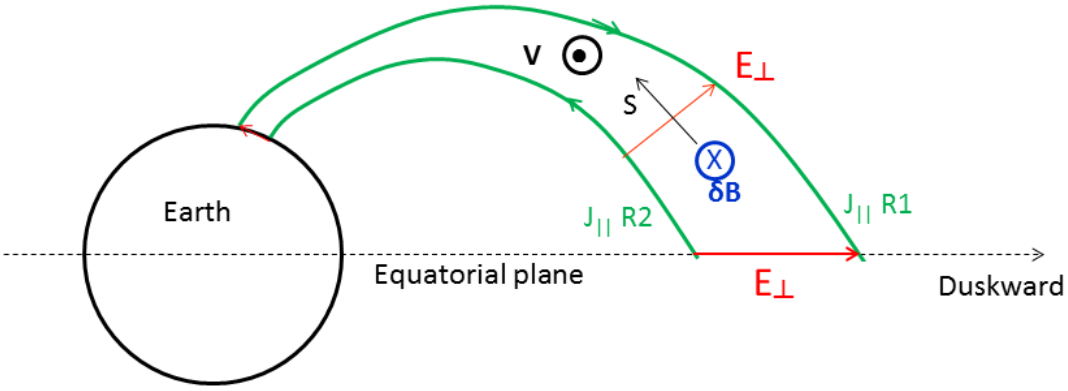

Figure 1.6: Schematic of the sunward return flow, V, of the dusk side, north hemisphere, magnetic field lines, and corresponding convection electric field, $E_\perp$, R1 and R2 FAC, magnetic field perturbation δB , and Poynting flux, S.
$E_\perp = -V \times B_o$, $S = E_\perp \times \delta B/\mu_0$

In the magnetosphere, between the Region 1 and Region 2 currents is an eastward (westward) magnetic field perturbation on the dusk (dawn) side associated with the FAC and consistent with magnetospheric magnetic field lines convecting sunward while the ionosphere resists the motion. The Poynting vector found by crossing this convection electric field $E_\perp$ with the magnetic field perturbation associated with the FAC system yields a field aligned Poynting flux directed Earthward along the field lines to the ionosphere.

1.7 More on Magnetosphere Ionosphere coupling

An important relation between the perpendicular electric and perturbation magnetic field of the large scale FAC system can be found by inserting Ampère's law for parallel current $j_\parallel = 1/\mu_o\,(\nabla \times \delta \boldsymbol{B})_\parallel$ (eq 10) and the height integrated (along B, which will be

referred to as the z direction) Ohm's law $\boldsymbol{J}_\perp = \Sigma_P \boldsymbol{E}_\perp$ (eq. 11) (where Σ_P is the height integrated Pedersen conductivity) into the height integrated divergence free continuity equation $j_\parallel = \nabla_\perp \cdot \boldsymbol{J}_\perp$ (eq. 12). Assuming that the fields vary predominantly in the x direction (i.e. the North-South direction; the y direction is East-West) we can write $1/\mu_o \left(\partial \delta \boldsymbol{B}_y / \partial x\right) = \partial/\partial x \left(\Sigma_P \boldsymbol{E}_x\right)$ from which it follows that $E_x/\delta B_y = 1/\mu_o \Sigma_P$ (eq. 13). This E to B ratio obtains even when observed at higher altitudes in the magnetosphere.

Mapping of the perpendicular electric field between the magnetosphere and a lower altitude reference point, such as the ionosphere, assuming no parallel potential can be accomplished for the steady state case with $E_{\perp m} l_m = E_{\perp i} l_i$ (eq. 14) (where $l_{m,i}$ is the spatial scale length perpendicular to the background field, and the m and i subscripts refer to their respective quantities in the magnetosphere and ionosphere respectively) [8]. The relation between the magnetosphere and ionosphere spatial lengths can be approximated from the non-divergence of magnetic flux, $B_i A_i = B_m A_m$ (eq. 15) where $A_{i,m}$ are the areas with surface normal parallel to the field threaded by the magnetic flux. From equation 15 along with the approximation that $l \approx \sqrt{A}$ we find an approximate relation for mapping perpendicular scale lengths between the ionosphere and magnetosphere: $l_i/l_m \approx \sqrt{A_i/A_m} = \sqrt{B_m/B_i}$ (eq. 16). Combining equations 16 and 14, yields the

[8] Consider a loop formed from the two legs along the perpendicular (to B) electric field in the magnetosphere and ionosphere respectively and another two legs along the converging magnetic field lines connecting these (see fig. 5?). In an approximately steady state situation, $\partial \boldsymbol{B}/\partial t = -\nabla \times \boldsymbol{E} = 0$, the potential drop integrated around the closed loop will be zero. If then there is no parallel electric field the potential drop in the ionosphere is the same as that in the magnetosphere; $\Delta\Phi_{\perp_m} = \Delta\Phi_{\perp_i}$ where $\Delta\Phi_{\perp_{i,m}} = E_{i,m} l_{\perp_{i,m}}$.

approximation for mapping the electric field $E_{\perp m} \approx E_{\perp i}\sqrt{B_m/B_i}$ (eq. 17). Likewise, scaling the magnetic field perturbation associated with the FAC along converging field lines can be accomplished using current continuity, equation 16, and the approximation that $\partial B/\partial x \approx \delta B/l$ to obtain $\delta B_m \approx \delta B_i\sqrt{B_m/B_i}$ so that we find that the E to B ratio in the magnetosphere is the same as that in the ionosphere $E_{\perp m}/\delta B_m \approx E_{\perp i}/\delta B_i$. Thus the E to B ratio in the magnetosphere contains information as to whether these field perturbations are associated with FAC.[9]

1.8 Cases where $\boldsymbol{E_{\parallel} \neq 0}$

The above mapping approximation assumes that there is no parallel electric field. However it often happens that such a parallel field is necessary. The magnetosphere is only able to provide electrons at such a rate to carry the FAC in the absence of any acceleration processes. In the population of magnetospheric electrons, only a small fraction will have pitch angles in the loss cone. Electrons that undergo acceleration along the magnetic field increase their parallel velocity, this not only enables them to carry more current, but also gives them smaller pitch angle, which places more of them in the loss cone, allowing more current flow into and out of the ionosphere. A parallel potential thus not only effectively widens the loss cone and increases **j**, but also partly uncouples the magnetosphere from the ionosphere, by allowing some of the potential drop to occur along B above the top of the ionosphere.

---

[9] This conclusion is consistent with the continuity of the Poynting flux; starting with conservation of energy assuming no dissipation, $S_{\parallel m}A_m = S_{\parallel i}A_i$ rewriting this with eq 6 and eq. 16 we find $E_{\perp m}\delta B_m = E_{\perp i}\delta B_i\ (B_m/B_i)$, using eq. 17 we then obtain $E_{\perp m}/\delta B_m \approx E_{\perp i}/\delta B_i$.

The Knight [1973] relation $j_\parallel = j_o(1 + e\Delta\Phi_\parallel/k_BT)$ relates the parallel current $j_\parallel$ to a parallel potential drop along the field line $\Delta\Phi_\parallel$ in the limit that $e\Delta\Phi_\parallel/k_BT \ll B_i/B_m$ where e ,k_B, T are the electron charge, Boltzmann constant and electron temperature respectively, and $j_o = ne\sqrt{k_BT/2\pi m}$ is the maximum current in the absence of a potential drop, where n is the plasma density in the magnetosphere[10]. In the additional limit that $1 \ll e\Delta\Phi_\parallel/k_BT$ the Knight relation becomes simply $j_\parallel = K\Delta\Phi_\parallel$, where $K = e^2n/\sqrt{2\pi m_e k_BT}$ [e.g. Lyons 1980].

In the absence of a parallel electric field, the potential drop along the perpendicular electric field in the magnetosphere is equal to that along the electric field in the ionosphere. If there is a parallel electric field, then the two perpendicular potentials will not be equal, instead the potential sum around the loop will be $\Delta\Phi_{\perp m} = \Delta\Phi_{\perp i} + \Delta\Phi_\parallel$. The magnetospheric electric field is well coupled to the ionosphere if $\Delta\Phi_{\perp m} \approx \Delta\Phi_{\perp i}$. If the necessary intensity of the FAC require that there be a significant parallel potential drop $\Delta\Phi_\parallel$, then $\Delta\Phi_{\perp m} \gg \Delta\Phi_{\perp i}$ and the magnetospheric electric field is not well coupled to the ionosphere. An expression indicating how well electrically coupled the magnetosphere and ionosphere can be found using the Knight relation $j_\parallel = K\Delta\Phi_\parallel$, $\Delta\Phi_{\perp m} = \Delta\Phi_{\perp \mathrm{i}} + \Delta\Phi_\parallel$, eq.11 and eq. 12 and the approximations $E_{\perp i} \sim \Delta\Phi_{\perp i}/l_i$, and

[10] In the absence of a parallel potential the current at the ionosphere is $j_o = nev_{th}$. This result comes about from the fact that the fraction of electrons in the loss cone is small at the equator, and because the pitch angle depends on the ratio of field strength, $\sin^2\alpha_c = B_m/B_i$ For small angles $\sin(\alpha) \approx \alpha$ such as are obtained when comparing the field strengths at the equator to the ionosphere, $\alpha_c^2 \approx B_{eq}/B_i$, and the solid angle is $\Omega = 2\pi(1 - \cos(\alpha)) \approx \pi\alpha^2$ so that the fraction of particles in the loss cone is proportional to the ratio of field strength. Since the mapping of the current density is also proportional to the field strength ratio, but in the opposite sense: $j_o = j_{\parallel i} = j_{\parallel m}(B_i/B_{eq}) \sim nev_{th}(B_{eq}/B_i)(B_i/B_{eq}) = nev_{th}$.

$\nabla_\perp E_{\perp i} \sim \Delta\Phi_{\perp i}/l_i^2$. After some algebra we find $(1 + \lambda_E^2/l_i^2)\Delta\Phi_{\perp i} = \Delta\Phi_{\perp m}$ where $\lambda_E \equiv \sqrt{\Sigma_p/K}$ is the electrostatic scale length. For typical values of ionospheric conductance of 10 Siemens and K = 10^{-9} Sm^{-2} the electrostatic scale length is $\lambda_E \approx 100km$ [Paschmann et al ch3]. If $l_i \gg \lambda_E$ then $\Delta\Phi_{\perp i} \approx \Delta\Phi_{\perp m}$ but if $l_i \ll \lambda_E$ then $\Delta\Phi_{\perp i} \ll \Delta\Phi_{\perp m}$.

1.9 Parallel electric fields and Aurora

The quasi static parallel electric fields are sometimes part of a structure of U shaped equipotential contours in which the upper parts of the U correspond to a pair of converging (diverging) perpendicular electric fields at higher altitudes and the bottom of the U is the parallel upward (downward) electric field [Mozer et al, 1997][Figure 7].[11] In the case of upward directed quasi-static electric fields, electrons from the magnetosphere are accelerated through the corresponding potential drop and precipitate into the upper atmosphere with typically high enough energy to excite photon emission from neutral atoms resulting in aurorae. The intensity threshold for visible aurora is ~ 1 erg/cm^{2}s. These U shaped potentials are longitudinally extended, and the resulting auroral arcs are typically several 1000km long by 100m-10km thick. This type of auroral electron acceleration takes place at altitudes of 2000-10,000 km and typical energies of these electrons are ~several keV -10 keV [Paschmann et al, 2002]. The electrons accelerated in this way are roughly monoenergetic, in that the potential drop often accelerates them to energies greater than their initial thermal energies resulting in energy spectra in which the

[11] More complex potential electrostatic configuration are possible, such as those involving S-shaped potential (along with a U potential) corresponding to structures where part of the field becomes aligned with the magnetic field while the rest maps to the ionosphere [Mizera et al, 1982].

differential energy flux is narrowly peaked over a small range of energies. The monoenergetic beam rises and falls in characteristic energy (kinetic energy flux/number flux) as seen in time series data as the observing spacecraft or sounding rocket transverses the accelerated beam below the U-shaped potential structure. For this reason, electrons accelerated in this way are often referred to as "inverted-V". Above the parallel electric field accelerated ion beams are observed, and below the accelerating parallel potential, perpendicularly heated (by EMIC waves) ions, called conics, feed ions to the higher altitude region of parallel potential drop after being ejected by the mirror force. The upgoing ion beam energy is often similar to the potential determined by integrating the perpendicular electric field, $E_{\perp}$, along the spacecraft trajectory, this is consistent with the idea that these perpendicular potentials map down to the parallel potential that accelerates the ions upwards. Associated with the upward current inside the U shaped potential is a magnetic field $\delta\boldsymbol{B}$ perturbation such that $\boldsymbol{E}_{\perp}$ crossed into it correspond to a downward Poynting flux. Further, the perpendicular electric field and background magnetic field correspond to a shear flow via $\boldsymbol{E}_{\perp} \times \boldsymbol{B}_{o}$ which may give rise of Kelvin-Helmholtz vortices that could explain some of the wavy features observed in auroral arcs. Also, a twist in the magnetic field which corresponds to the curl in **B** associated with intense $j_{\parallel}$ also may account for such wavy features [Paschmann et al 2002].

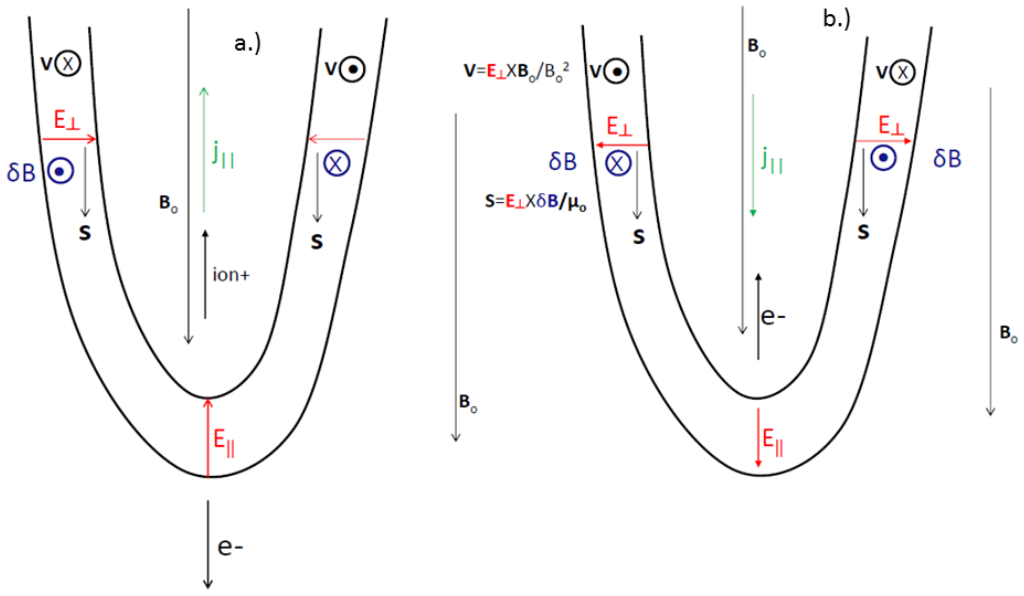

Figure 1.7: The upward (a) and downward (b) current system associated with an upward/downward field aligned electric field. Part of the perpendicular electric field becomes decoupled from the ionosphere through a parallel E field. This enhances the current through parallel acceleration and effectively widens the loss cone for downward electrons. The associated magnetic field perturbation and perpendicular electric field yield a downward Poynting vector in both cases. The shear in the E×B flow associated with $E^{\perp}$ and the background field Bo, may give rise to flow instabilities, which in the upward current region may appear as curls in the auroral arc.

A similar U-shaped potential structure exists for downward current regions with diverging perpendicular electric field at higher altitudes and a downward quasi-static electric potential drop at lower altitudes [Figure 7b]. The electron current shows good quantitative agreement with the magnetic field deflection (perturbation) and electron energies are consistent with $E_{\perp}$ integrated along the spacecraft trajectory [Paschmann et al 2002]. As in the former case, the Poynting flux associated with this structure is downward. The presence of the downward electric field accelerates cool ionospheric

electrons upwards and reflects up going ions that have been heated perpendicular to the background field and ejected by the mirror force. The reflected ions are heated more at lower altitudes and the cycle continues until they gain enough energy to overcome the downward electric field, this process is known as the "pressure cooker". In both cases, upgoing ions are present and in the magnetosphere are indicators of being magnetically conjugate with such a potential structure. In the case of pressure cooker ions, they have a lower energy cut off since ions with energy less that the potential drop cannot escape the pressure cooker.

1.10 Large scale aurora and Substorms

The auroral ovals are the annulus shaped regions characterized by auroral activity and centered on the magnetic north and south poles, roughly being between 62-72 degrees magnetic latitude [Kivelson and Russell, 1995]. The magnetic field lines mapping to the auroral oval are generally those associated with the sunward return flow of the convection cycle. The nightside auroral oval maps out into the plasma sheet and plasma sheet boundary layer Earthward of the reconnection region, where the flow is predominantly sunward.

The field lines of the auroral oval thus maps to dynamic energy release and transport processes in the magnetosphere. On the night side, one such dynamic process (or series of processes) associated with intense, dynamic auroral displays is the auroral substrom. In response to enhanced solar wind conditions, such as increased velocity and southward Bz, the flux transport to the tail from dayside reconnection can increase rapidly. The

energy stored in the tail is released in bursts through reconnection, associated with which is a set of characteristic signatures observed in the magnetosphere, in the aurora, and on the ground. It is still a debated topic, however, whether the substorm starts with near earth reconnection or if it commences with other processes closer to the Earth such as current disruption [Akasofu 2004]. Substorms have three phases; the growth phase, the expansion phase, and recovery phase [Akasofu 1964; McPherron 1970, 1972; Russell and McPherron 1973]. The growth phase commences with a southward Bz and lasts about an hour, during this time magnetic flux accumulates in the tail and the current sheet thins. Quiet auroral arcs drift towards the equator and fade before the second phase, expansion, begins. The expansion phase is a sudden release of some of the stored energy in the tail, and is accordingly the most dynamic phase of the substorm, though the triggering mechanism is not fully understood. The start of the expansion phase is called the "onset" and is characterized by sudden brightening and expansion of the aurora starting at the most equatorward arc. With specific reference to auroral activity, the onset is also called "auroral breakup". Near Earth (~15-20 R_E) reconnection occurs in association with this phase [e.g. Hones 1976]. The closing of the open lobe field lines and their earthward convection corresponds to a reconfiguration of the magnetic field lines from a stretched to dipolar configuration (dipolarization). This reorientation of the near earth tail to dipolar geometry is associated with the tail current being diverted into and through the ionosphere. On the ground, these currents cause a depression in the horizontal component of the magnetic field, a signal sometimes referred to as a magnetic bay [e.g. Hones et al 1984]. During the expansion phase, in association with dipolarizations, ULF

waves (such as Pi1 pulsations 1-40 sec.) are observed both in space and on the ground [Arnoldy et al 1998] and energetic particles ~10s keV are observed at geosyncronous orbit [Arnoldy and Moore 1983; Apatenkov, et al. (2007)] as well as high speed flows observed in the plasma sheet [Baumjohann et al. 1990; Angelopoulos et al. 1992]. The recovery phase lasts about an hour and is when the plasma sheet and tail return to their pre-substorm state, the ionospheric current decreases as the reestablishment of the near earth tail diverts the current into the cross tail current.

1.11 Three kinds of auroral electrons

Above we discussed the origin of monoenergetic or inverted V aurora, this is one type of discrete aurora. The other is wave aurora, in which the electrons are accelerated via the parallel electric field of kinetic Alfvén waves, discussed below. Discrete aurora are so called because they have a structure, resembling curtains of light, often wavy and exhibiting dynamic activity. Another significant type of aurora is the diffuse aurora. Diffuse aurorae are without any internal structure, and they are typically more prominent in the equatorward portion of the auroral oval. Electron scattering by chorus waves are the dominant source of diffuse auroral electron precipitation [Thorne et al, 2010]. Below and in subsequent chapters we will discuss wave acceleration of electrons.

1.12 MHD, the frozen-in condition and Alfvén waves:

In addition to the large scale FAC system, energy is also transported through the magnetosphere and from the magnetosphere to the ionosphere by plasma waves. The magnetized plasma of the magnetosphere supports an important class of waves called

MHD waves. MHD is a useful approximation for discussing the behavior of highly conducting fluid plasmas permeated by a magnetic field. The fluid approximation assumes that we are dealing with spatial and temporal scales larger than those on the order of an ion gyroradius and gyrofrequency respectively, i.e. scales larger than those at which individual particle motion is important. Under these conditions, the magnetic field behaves as if it were frozen into the plasma, such that the magnetic flux through any closed curve moving with the plasma fluid is constant, this is known as the "frozen-in" condition. Under the assumption of very high conductivity, i.e. $\sigma \to \infty$, Ohm's law $\boldsymbol{j} = \sigma(\boldsymbol{E} + \boldsymbol{v} \times \boldsymbol{B})$ can be expressed as $\boldsymbol{E} + \boldsymbol{v} \times \boldsymbol{B} = 0$. The frozen-in condition follows from this and Faraday's law.

The basic MHD physics is expressed in part by Maxwell 's equations under the approximation that the displacement current is small, $\partial \boldsymbol{E}/\partial t = 0$, compared to the physical current in Ampère's law j, and that there is no net charge accumulation, such that the electric field and current density are divergence free (in the highly conducting plasma, charge buildup does not occur since the charge would rapidly disperse along the magnetic field). Under these condition Maxwell equation can be written:

$$\nabla \times \boldsymbol{B} = \mu_o \boldsymbol{j} \text{ (eq 18)}$$

$$\nabla \cdot \boldsymbol{B} = 0 \text{ (eq 19)}$$

$$\nabla \times \boldsymbol{E} = -\partial \boldsymbol{B}/\partial t \text{(eq 8)}$$

$$\nabla \cdot \boldsymbol{E} = 0 \text{ (eq 20)}$$

The generalized Ohm's law[12], relating the current to the force on the charge carries,

$$\boldsymbol{E} + \boldsymbol{v} \times \boldsymbol{B} = \eta \boldsymbol{j} \text{ (eq. 21)}$$

where $= 1/\sigma$.

The mass continuity equation,

$$\partial\rho/\partial t + \nabla \cdot (\rho \boldsymbol{v}) = 0 \text{ (eq. 22)}$$

The momentum equation, which relates the acceleration of the fluid to the pressure gradient ∇P and the $\boldsymbol{j} \times \boldsymbol{B}$ force, which we encountered above (eq. 9) but here it is expressed in eq 23 with the convective derivative,

$$\rho(\partial \boldsymbol{v}/\partial t + \boldsymbol{v} \cdot \nabla \boldsymbol{v}) = -\nabla P + \boldsymbol{j} \times \boldsymbol{B} \text{ (eq. 23)}$$

Finally, the equation of state which relates plasma gas pressure P and density ρ

$$P = c\rho^{\gamma} \text{ (eq. 24)}$$

where c and γ are constants.

1.13 MDH waves:

In cold MHD plasma, i.e. one in which the plasma pressure is small relative to the magnetic pressure, $nk_BT/(B^2/2\mu_o) \equiv \beta \ll 1$, the pressure term ∇P in the momentum equation can be neglected and there are two MHD wave modes. One is the shear or

[12] A fuller version of the generalized Ohm's law is $\boldsymbol{E} + \boldsymbol{v} \times \boldsymbol{B} = \eta \boldsymbol{j} + \frac{1}{en}(\boldsymbol{j} \times \boldsymbol{B} - \nabla P_e)$, typically the last two terms on the right hand side are negligible. When the plasma can be considered highly conductive, $\eta \to 0$ and we can then use $E + v \times B = 0$.

transverse Alfvén wave, also simply called the Alfvén wave, which has a dispersion relation $\omega = \boldsymbol{V_A} \cdot \boldsymbol{k}$, where ω is the wave frequency, $\boldsymbol{k}$ is the wave vector and $\boldsymbol{V_A} = V_A \widehat{\boldsymbol{B}}_o$ where again $V_A = B/\sqrt{\rho\mu_o}$, and $\widehat{\boldsymbol{B}}_o$ is the unit vector along the magnetic field. The Alfvén wave phase velocity is $\boldsymbol{v_P} = (\omega/k)\,\widehat{\boldsymbol{k}} = V_A cos\theta\, \widehat{\boldsymbol{k}}$, where θ is the angle between the magnetic field and the wave vector, and the group velocity is $\boldsymbol{v}_g = \nabla_k \omega = \boldsymbol{V}_A$. Alfvén waves propagate along the magnetic field lines at the Alfvén speed and are somewhat analogous to waves on a taut string; the magnetic tension along with the inertia of the plasma mass density determines the Alfvén speed similar to the way in which tension and linear mass density determine the wave speed in a string. The fluid fluctuations, $\delta\boldsymbol{v}$, of the Alfvén wave are perpendicular to the plane containing the background magnetic field and wave vector, which means that there are no density perturbations $\delta\rho$ as is evident from the linearized continuity equation $\delta\rho = (\rho_o/\omega)\,(\boldsymbol{k} \cdot \delta\boldsymbol{v}) = 0$, thus the Alfvén wave is non-compressional. The magnetic field perturbations are also perpendicular to the background field and so the total field is approximately constant $(\boldsymbol{B_o} + \delta\boldsymbol{B})^2 \approx B_o^2 + 2\boldsymbol{B_o} \cdot \delta\boldsymbol{B} = B_o^2$ meaning that the Alfvén wave bends the magnetic field, changing its direction, without changing its magnitude. The electric and magnetic field perturbations ($\delta\boldsymbol{E}$, $\delta\boldsymbol{B}$ respectively) of the Alfvén wave are in phase with one another and are perpendicular to each other and to the background magnetic field. The Poynting vector $\boldsymbol{S} = \delta\boldsymbol{E}x\delta\boldsymbol{B}/\mu_o$ is thus along the background magnetic field and the wave transports energy along the background field as was also evident above from the group velocity. The ratio of the electric to magnetic field perturbations is equal to the Alfvén speed $\delta E/\delta B = V_A$.

The other MHD wave mode found in cold plasma has a phase and group velocity of $\boldsymbol{v}_P = \boldsymbol{v}_g = V_A\hat{\boldsymbol{k}}$. In general this wave has a higher phase velocity than the Alfvén wave and is therefore referred to as the fast mode wave. The fast mode wave sets the plasma in motion in the plane containing the wave vector and background field. Because of this, the wave is compressional $\delta\rho = (\rho_o/\omega)(\boldsymbol{k}\cdot\delta\boldsymbol{v}) \neq 0$ and the field strength varies, $\boldsymbol{B}\cdot\delta\boldsymbol{B} \neq 0$. Fast mode waves propagate isotropic, their direction not being determined by the magnetic field.

In a warm plasma, one in which β is not small, the pressure is important and is kept in the momentum equation (eq. 23). In this case the MHD wave dispersion relation becomes;

$$(\omega^2 - \cos^2\theta k^2 V_A^2)[\omega^4 - \omega^2 k^2(c_s^2 + V_A^2) + \cos^2\theta k^4 V_A^2 c_S^2] = 0$$

where c_s is the sound speed $c_s = \sqrt{\partial P/\partial\rho}$. This dispersion relation has three solutions: the first being $\omega^2 = V_A^2\,\mathrm{k}^2\cos^2\theta$ which is the same as the Alfvén wave above and has all the same properties since as a non-compressional wave, the density perturbations are zero and thus pressure perturbations do not enter into consideration. The other two solutions are:

$\frac{\omega^2}{k^2} = \frac{1}{2}\left\{c_S^2 + V_A^2 \pm [(c_S^2 + V_A^2)^2 - 4c_S^2 V_A^2\cos^2\theta]^{\frac{1}{2}}\right\}$ These are the fast and slow magnetosonic waves corresponding to the + and – signs respectively. For fast (slow) mode waves, the thermal pressure and magnetic field perturbations are in phase (180 degrees out of phase). Fast mode wave propagation is nearly isotropic (as in the cold

plasma case), propagating at an arbitrary angle to the background field while the slow mode wave propagates along the background field.

The fast and slow mode waves reduce pressure gradients. Slow mode waves keep the total pressure approximately constant along B, pressure gradients of the total pressure along B drive slow mode waves. The Alfvén wave reduces bending of the magnetic field and can be launched by a sheared flow of plasma across the background magnetic field or by reconfiguration of bent magnetic field lines. This happens in the magnetosphere during reconnection as a result of the plasma jets and the resulting sudden reconfiguration of the magnetic field, during the expansion of plasma into the inner magnetosphere during substorms, or by solar wind forcing the magnetopause boundary.

Alfvén waves carry energy along the background field from the magnetosphere to the ionosphere. The field lines that guide the Alfvén waves to the ionosphere are essentially transmission lines in this respect and, as with the other transmission lines, if the impedances are mismatched part of the wave energy will be reflected. The reflection coefficient R for Alfvén waves incident on the ionosphere is

$R \equiv E_{\perp}^{refl}/E_{\perp}^{inc} = (\Sigma_A - \Sigma_P)/(\Sigma_A + \Sigma_P)$ where $\Sigma_A = 1/\mu_o V_A$ is the Alfvén conductivity[13]. The Alfvén conductivity is (0.8 mho)/V_A, where V_A is in units of 1000 km/s, and it is typically smaller than the Perdersen conductivity, which tends to be ~1-10 mhos, varying with auroral activity and solar illumination. When an Alfvén wave reflects off a conducting surface, the sign of the electric field is reversed and the sign of

[13] Since the ionosphere has a finite parallel conductivity the effective Pedersen conductivity is modified to become $\Sigma_{P_{eff}} = \Sigma_P/(1 + k_\perp^2 \lambda_E^2)$ where $k_\perp$ is the perpendicular scale length of the Alfvén wave in the ionosphere [See Paschmaann at al 2002 and references therein].

the magnetic field is preserves. (When reflection off a non-conducting surface occurs, the situation is opposite, the electric field is preserved and the magnetic field is reversed.) When incident and reflected waves are superimposed, the electric to magnetic field perturbations are shifted 90 degrees out of phase relative to each other.

1.14 Kinetic Alfvén Waves and $E_{\parallel}$

Up to this point we have been discussing MHD waves in cases where the fluid approximation of the plasma holds. The scale size of pure MHD wavelengths extends over a wide range but in the small limit is limited to scales larger than those at which the motion of individual particles becomes important. Such particle motion is important at scales sizes of the ion acoustic gyroradius $\rho_{ia} = \sqrt{T_e/m_i}\,/\omega_{ci}$, the ion thermal gyroradius $\rho_i = \sqrt{T_i/m_i}\,/\omega_{ci}$,or to the electron inertial length $\lambda_e = c/\omega_{pe}$,where c is the speed of light ω_{ci} is the ion cyclotron frequency and ω_{pe} is the plasma frequency. In the limit where the perpendicular wavelength become comparable to such scales, the kinetic properties become important and the plasma can no longer be treated as a pure fluid. An important property of these Alfvén waves is that a component of their electric field is aligned with the background magnetic field, allowing them to accelerate electrons along the field line. This cannot occur in the ideal MHD limit where $E_{\parallel} = 0$. Small scale Alfvén wave are often called either "Inertial Alfvén waves" or "Kinetic Alfvén waves" depending on their plasma environment [e.g. Stasiewicz et al 2000], though both of these are just different limits of one dispersion relation [Lysak and Lotko 1996]. In the cold electron limit that $\beta_e < m_e/m_i$ and for low frequencies $\omega < \omega_{ci} = eB/m_i$, the full

dispersion relation reduces to: $\omega = k_{\parallel} V_A \sqrt{(1 + k_{\perp}^2 \rho_i^2 / 1 + k_{\perp}^2 \lambda_e^2)}$ [Stasiewicz et al, 2000 and references therein]. From this dispersion relation it can be seen that when the perpendicular wavelength is large relative to the ion acoustic radius and the electron inertial length, the standard MHD Alfvn wave dispersion relation obtains. In the case in which the electron thermal velocity v_{te} is less than the Alfvén speed, $v_{te} = \sqrt{(2T_e/m_e)} < V_A$, or what is equivalent, that the electron beta is less than the electron to ion mass ratio, $\beta_e < m_e/m_i$, the parallel electric field is supported by electron inertia and the relevant scale length is the electron inertial length c/ω_{pe}. Small scale Alfvén waves in such plasma are sometimes referred to as Inertial Alfvén waves. In a plasma where the electron thermal temperature is greater than the Alfvén speed, $v_{te} > V_A$, and $m_e/m_i < \beta_e < 1$ the parallel electric field is supported by the parallel electron pressure gradient and the relevant scale length is the ion acoustic gyroradius. Small scale Alfvén waves in such plasma are often called Kinetic Alfvén waves. It should be noted that the relation between either the electron pressure or electron inertia and the parallel electric field are not causal explanations of the electric field generation, rather the parallel electric field comes about as a results of the displacement current in Ampere's law [Song and Lysak; 2006] associated with the parallel curl in B, which becomes important on these scales when there is insufficient electrons to support the physical current j. As mentioned the inertial or kinetic limit is determined by the plasma environment i.e. by the electron beta. In the magnetosphere, and in particular in the auroral zone, the inertial limit is most important below 3-4 R_E geocentric and the kinetic limit is most important above 4 R_E [Lysak and Carlson 1981; Stasiewicz et al 2000].

1.15 Concluding remarks

In this chapter we discussed some basic aspects of the structure and dynamics of the magnetosphere and some important properties of FACs and MHD waves, in particular their role in energy transport in the magnetosphere. In the next chapter we will look at previous works, both experimental and theoretical, that study the role of Alfvén waves in magnetospheric energy transport and in the powering of aurora. We will then in the third chapter discuss the satellites that provided data used in this thesis, their orbits, and instruments used. In the fourth chapter we will then turn to the main focus of this thesis which is the examination of the evolution, in latitude and intensity, of the high altitude wave Poynting flux and the low altitude downward electron kinetic energy flux on Earth's night side.

Chapter 2

Previous works on Alfvén waves and associated Poynting flux as an auroral energy source

2.1 Introduction

In the previous chapter we discussed some of the basic physics of the MHD processes that transport energy from the magnetosphere to the ionosphere. We also discussed basic properties of Alfvén waves and how in the small scale limit they can accelerate electrons along the magnetic field to energies capable of producing discrete aurora. In this chapter we examine previous works, both experimental and theoretical, that studied the role Alfvén waves play in accelerating electrons and powering aurora. We start by discussing experimental studies of high altitude Alfvén waves on the PSBL and the corresponding conjugate low altitude aurora. Next we review results from simulations Alfvén waves in and above the auroral zone and their ability to drive the acceleration of auroral electrons. Then we look at studies of the statistical, global (hemisphere > 60^{o}), energetic contribution and morphology of Alfvén waves and/or Alfvén accelerated electrons, done from either a high or low altitude standpoint. We then look at studies having to do with the generation in the geomagnetic tail of the night side Poynting flux. Penultimate, we review studies of the relation between Alfvén waves and substorms. In the presentation of these various studies, aspects of the method and techniques used therein are also discussed. This in part contextualizes their respective conclusions and defines the

limitations and advantaged of the various techniques used. Finally, the concluding part of this chapter will give justification for the research contained in this thesis.

2.2 Experimental studies of high altitude Poynting flux at the PSBL conjugate to low altitude auroral emissions/electron precipitation

Wygant et al [2000] is the first[14] experimental investigation into the role of high altitude (4-6 R_E) Alfvénic Poynting flux propagating earthward on the PSBL in powering auroral particle acceleration. In that study, intense Alfvénic electric and magnetic field fluctuations with associated Poynting flux sufficient to power magnetically conjugate auroral electrons, and the plasma environment thereof, were analyzed for the first time. Ultraviolet images of enhanced auroral luminosities at the magnetic foot point of the field lines on which the Poynting flux was observed simultaneously provided an estimate of the energy flux of the downgoing electrons at ionospheric altitudes. Concurrent with the Poynting flux were up flowing ion beams, further evidence of magnetic conjugation to the auoral acceleration region. This investigation was conducted with two events selected out of the most intense electric fields observed by Polar in the year 1997. They observed that the electric fields are routinely polarized perpendicular to the PSBL. Intense electric fields and associated large earthward Alfvénic Poynting flux are seen most frequently in the PSBL, but it is also seen deeper in the plasma sheet. The Polar spacecraft would typically spend 1-3 minutes at the PSBL compared to 30-50 minutes in

[14] An earlier observation of high altitude (>4R_E) Poynting flux associated with earthward directed Alfvén waves was made by Maynard et al [1996] with CRRES data. These Poynting flux were observed near the inner edge of the central plasma sheet during substorm onset. The Alfvén waves had an intensity of $\sim$0.8ergs/cm^{2}s in situ. That study was primarily concerned with investigating the relation of Poynting flux in energy feedback exchanges that establish the substorm current systems.

the plasma sheet, the relative amounts of time spent in each, combined with the higher likelihood of observation in the PSBL, suggest that the intense Alfvénic electric fields occur at the PSBL with a higher frequency [Wygant et al 2000; 2002].

To isolate the wave fields, the electric and magnetic fields data was detrended by subtracting a 180 second running average from the original data. The background magnetic field was found by averaging the full measured fields by 180 seconds. The electric and magnetic fields data was used to calculate the field aligned wave Poynting flux as $S_{\| \text{ in situ}} = \mathbf{S}\cdot\mathbf{B}_o/|\mathbf{B}_o|$, where $\mathbf{S} = \delta\mathbf{E}\text{x}\delta\mathbf{B}/\mu_o$. The in situ intensities where then mapped to the ionosphere: $S_{\|\text{iono}} = S_{\|\text{in situ}}*(B_{\text{iono}}/B_{\text{insitu}})$.

The waves in this frequency range (<180 seconds) were identified as Alfvénic by examining the ratio of electric to magnetic field perturbations, wave form, and phase relation. In addition, the magnitude of the transverse magnetic field perturbations were large compared to the variations in the total magnetic field magnitude, consistent with the Alfvén wave property of $\boldsymbol{B}_0 \cdot \delta\boldsymbol{B} = 0$ discussed in the last chapter.

The intense electric fields and associated Poynting flux were observed only at times when Polar was on field lines mapping down to regions of the most intense auroral emissions, as seen in UV images taken by Polar's UVI instrument. The Poynting flux was ~100 ergs/cm^{2}s and UVI measurements indicated that the electron kinetic energy flux estimated from auroral emissions was ~20 ergs/cm^{2}s, thus the Poynting flux had sufficient intensity to power the lower altitude acceleration processes that energize auroral electrons.

The field aligned wave Poynting flux of waves less than 180 second period was found to be significantly more intense than the Poynting flux associated with the large scale convective electric field and magnetic fields due to field aligned currents. The FAC/convection Poynting flux intensity was 1-5 ergs/cm^{2}s mapped to the ionosphere, whereas the Alfvénic was ~100 ergs/cm^{2}s.

Evidence was found that kinetic effects could be important. Wygant et al [2000] pointed out that if the smaller scale, ~1 second, electric field structures seen in these events are interpreted as purely spatial then their scales sizes are comparable to or smaller than those of the electron inertial length and ion gyroradius (~10-20 km). Thus for these waves the particle kinetics are likely important, and the general dispersion relation for these Alfvén waves will have to include finite ion gyroradius and electron inertia. Such small scale spikes, if they are kinetic Alfvén waves, will develop a parallel component in the electric field which can accelerate electrons. The environment where Landau damping is significant is controlled by the electron beta [Lysak and Lotko, 1996]. In the studied events, the electron beta $\beta_e \sim 0.001$, was comparable to the electron to ion mass ratio, $m_e/m_i = 0.0005$, which indicates that plasma conditions (i.e. $\beta > m_e/m_i$) were right for kinmetic Alfvén waves to undergo Landau damping.

These small-scale waves/spikes were further investigated in Wygant et al [2002]. That work provided the first evidence that the small scale spikes, ~1 seconds, embedded in the larger waves are kinetic Alfvén waves with small perpendicular wavelengths (~20 km), which can accelerate electrons. In these small scale spikes the electron thermal velocity

is comparable to the Alfvén speed, favorable to Landau resonant interaction between the waves and electrons.

Two Alfvénic temporal scales are discussed; larger scale Alfvén waves with significant power in the 20-60 second wave period range, and those of the shorter duration spikes, 0.25-1 seconds. The spike electric field perturbations where ~300mV/m with magnetic field perturbations ~0.5 to 5 nT. The E/B ratio for the spikes was 2 to 5 times that of the Alfvén speed, a property consistent with kinetic Alfvén waves. The Poynting flux carried by the spikes was about 25% that of the large-scale Alfvén waves. The in situ Poynting flux of the large scale Alfvén waves was ~ 1 erg/cm^{2}s and that of the spikes was 0.25 ergs/cm^{2}s, values intense enough to power visible aurora when mapped to the ionosphere.

Comparison of the values of the small scale E to B ratio, V_e^2/V_A^2, where V_e is the electron thermal speed, and the assumption that $T_i/T_e = 1$, to the theoretical dispersion relation from Lysak and Lotko [1996] and from Lysak [1998] indicated that the perpendicular wavelength of the electric field spikes are ~ 20 – 120 km.

For the observed electric field amplitudes ~100 mV/m and the shorter wavelengths from the dispersion relation, $\lambda_\perp$ ~ 20 - 80 km, the perpendicular potential should have been 2000-8000 V and parallel potential 100 – 4000 V, on the order for typical Alfvénic aurora electrons. Indicating that these waves have parallel potential drops that can accelerate electron beams, similar to those seen in aurora.

The two dimensional velocity space distributions showed that there were intense field aligned electrons (1 -2 keV), that coincided with the intense small scale kinetic Alfvén

spikes consistent with the predicted parallel potential, such beams are observed in situ with intensities ~0.7 ergs/cm^{2}s. In addition the up flowing ion beam also had energies of 1-2 keV.

Another important observation is that the intense large-scale Alfvénic fluctuations seen at and inside the PSBL, likely give rise to the smaller scale intense electric field spikes. The fact that there is more energy in the large scale Alfvénic fluctuations than the small kinetic fluctuations, and that the electric fields of both of these kinds of waves had similar amplitudes and polarity suggests that the large scale waves generate the small scale waves. The similar electric field amplitudes indicates that both the large-scale Alfvén waves and the small scale spikes correspond to similar velocity perturbations in the PBSL via $\delta\mathbf{v} = \delta\mathbf{E}\times\mathbf{B}_o/B_o^2$. Some possible mechanisms for this small scale wave generation could be wave mode coupling of the Alfvénic surface wave to the kinetic Alfvén wave via an interaction with the density gradient at the PSBL such as described by Hasegawa [1976]. An interaction of larger scale waves with smaller scale density gradients could also form small scale waves. Another possibility is that plasma flow shear could create surface waves through the Kelvin Helmholtz instability that may produce small perpendicular perturbations.

Further evidence, discussed below, that supports the generation of small scale waves from large scale Alfvén waves are given by Dombeck et al [2005] who study a conjunction between Polar and FAST and observed an increase between Polar and FAST altitudes of the higher frequency waves; and by Lysak and Song [2011] who presented theoretical support for the generation of small scale wave from larger wavelengths is via

phase mixing which occurs when Alfvén phase fronts cross gradients in the Alfvén speed, such as those the PSBL and in the Alfvén resonator. At lower altitudes in the auroral zone, it has been shown that turbulent cascades generate smaller scale waves [Stasiewicz et al 2000, Chaston et al 2008] and are capable of transporting sufficient power from large scale MHD waves to small scale dispersive waves to power the acceleration of auroral electrons [Chaston et al 2008].

The first statistical study that correlated auroral emissions with wave Poynting flux for a range of intensities in the plasma sheet and PSBL (4-7 R_E geocentric) was that of Keiling et al., [2002]. In that work, the high altitude Poynting flux was compared to the magnetically conjugate ionospheric electron energy flux determined from the Polar UVI measured auroral emissions at the magnetic foot points for 40 events.

They also provided two case studies of individual plasma sheet passes, one in which Polar is magnetically conjugate to intense aurora and one in which Polar is conjugate to weak aurora. In the first case the crossing of the plasma sheet was during a storm (AE ~ 500nT). The electric and magnetic field data was averaged 6 seconds, and a 3 minute running average was subtracted from the original data. The relation between the **E** and **B** wave fields suggests the waves were Alfvénic. There was intense field aligned Poynting flux of intensity ~ 1 erg/cm^{2}s in situ just inside the PSBL, and ~125 ergs/cm^{2}s mapped to the ionosphere. The Polar footpoint mapped to the poleward edge of the intense aurora

where the peak electron energy flux was ~25 ergs/cm^{2}s[15]. There was thus sufficient power in the Alfvénic Poynting flux to accelerate lower altitude auroral electrons for this event. The Poynting flux shows little reflected power, indicating that most of it was dissipated below Polar. That the auroral electrons only uses 25 ergs/cm^{2}s suggests that other processes could be involved using the balance of the energy; such as ion acceleration, joule heating, spatial broadening of Poynting flux, electron beams.

The event during the conjunction with the weak auroral emission was during a period of weak magnetic disturbance (AE = 30 nT, during the recovery of a substorm). The electric to magnetic wave field ratios for are Alfvénic, and the peak Poynting flux is ~0.02 ergs/cm^{2}s in situ or 2.5 ergs/cm^{2}s mapped (two orders of magnitude smaller than that in the intense event above). At the foot point, the weak auroral emissions are 2-4 ergs/cm^{2}s, i.e. on the order of the mapped Poynting flux.

The statistical part of the Keiling et al [2002] study used 40 plasma sheet crossings, incorporating a range from weaker to intense wave Poynting flux during which the geomagnetic activity ranges from quite to very active. The majority of the Poynting flux used was Alfvénic based on the wave fields E to B ratio and phase relation. The peak electron kinetic energy flux inferred from the UVI measured emissions within 1 degree latitude (the estimated accuracy of the mapping) and 0.5 hours MLT of the spacecraft footpoint near the time of the peak Poynting flux (the more intense UVI image of the two within the imaging cadence, 2-3 minutes) are compared to the Poynting flux intensity.

[15] However the UVI measurements could be underestimated because of the UVI intensity is averaged over a pixel, so the more intense individual arcs cannot be resolved.

Keiling et al find a direct correlation between Poynting flux intensity and electron kinetic energy flux intensity of the magnetically conjugate auroral emissions. For the 40 events studied the Poynting flux ranged from 0.002 to 2 ergs/cm^{2}s in situ or 0.2 to 200 ergs/cm^{2}s mapped to the ionosphere at 100 km. In many of the cases there is sufficient Poynting flux to power the acceleration of the electrons at low altitudes. When the Poynting flux is most intense ($S_{\|}$>~10 ergs/cm^{2}s) there is up to 10 times more than enough energy to accelerate the low altitude electrons. For the weakest events, the Poynting flux intensity are of similar or less intensities than what is needed for the accelerating the conjugate auroral electrons.

Further details in the wave energy transport along the PSBL to the ionosphere are provided by conjunctions between high and low altitude spacecraft, which allow for simultaneous, in situ examination of the energy balance, as well as look for features characteristic of Alfvén waves and Alfvénic acceleration.

Vaivads et al [2003] investigated a conjunction between the Cluster spacecraft array and DMSP 14 which took place[16] during a magnetically quiet time AE < 250 nT, on a auroral field lines in the southern hemisphere at about ~ 20 MLT. Cluster ion data indicate that the auroral arc was located on the outer edge of the plasma sheet population. The spacecraft foot points were found with both the Tsyganenko 96 and 01 models, both of which gave similar footpoints. The geomagnetic foot points of Cluster and DMSP were separated by about 40 -80 km longitude (1.5^o-3^o degrees). The direction and velocity of the current sheet associated with the aurora was estimated using minimum variance on

[16] April 28, 2001, 1915 -1918UT

Cluster and was found to be moving towards the pole at ~4 km/s along the spacecraft trajectory in the fixed reference frame. The velocity allowed for a more accurate integration of the energy flux over the trajectory.

Cluster was above the acceleration region at ~4.7 R_E and observed a bipolar converging electric field structure inside of which were beams of up going ~2 keV Oxygen ions. The integrated potential drop, ~3-4 kV, was consistent with the energy of ion beams at Cluster and the low altitude (~850 km) electron energy at DMSP. DMSP observed inverted-V type electron acceleration with maximum acceleration energy of ~3keV. These observations suggest that the inverted-V potential is a reasonable description at altitudes above the acceleration region.

The estimated downward electron kinetic flux at DMSP mapped to the ionosphere was ~20 ergs/cm^{2}s , the integrated value was 180W/m or 1.8x10^7 ergs/cm-s (the remaining unit of length being in the direction of constant geomagnetic latitude). Inside the arc at Cluster, the mapped electron kinetic energy flux was ~5 ergs/cm^{2}s integrated across the arc it was ~10 W/m. The mapped Poynting flux at Cluster was 19-60 ergs/cm^{2}s and 80-155 W/m integrated. The intensities and their integrated values are thus sufficient, or nearly sufficient, energetically, to power the low altitude electrons. The up-going ions accounted for a smaller part of the balance, ~0.005 ergs/cm^{2}s in situ, or ~0.5 ergs/cm^{2}s mapped.

The DMSP electron spectra was of the inverted-V, or mono-energetic type. As mentioned earlier, other aspects of the event were consistent with an inverted-V potential,

namely the consistency of the integrated potential with the ion and electron beam energies. The potential well depth, φ, and plasma parameters were also found to be consistent with Knight's relation $j = K\varphi$. They also note that while the DMSP electron spectra is an inverted V type, the E to B perturbation field ratio at Cluster is $\sim 10^4$ km/s which is in reasonable agreement with the Alfvén speed, suggesting the possibility that the structure was related to, or may have been part of an Alfvén wave. Such interpretation has a theoretical basis; Goertz [1984] noted that kinetic Alfvén waves can reasonably explain the observations of narrow inverted-V, or shock-like electron static fields. And Lysak [1998] has shown that Alfvén waves with small perpendicular wavelengths can appear as electrostatic shocks, especially at higher altitudes. Though on the other hand it should be mentioned that in Lysak [1998] this is expected for small scale structured that are a few km at the ionosphere, whereas the arc examined in Vaivades et al [2003] is on the order of 10 km. Also, the E to B ratio in this case was on the order of the Alfvén speed whereas kinetic Alfvén waves have a higher E to B ratio.

Dombeck et al [2005] presented the first simultaneous observation of Alfvén waves a high altitude, at the Polar spacecraft (located at $\sim 7R_E$), and at low altitude, at the FAST satellite (located at ~3500km), while these spacecraft were approximately magnetically conjugate, both were in the PSBL and at ~23 MLT, during the main phase of a major geomagnetic storm on October 22, 1999. The properties of the Poynting flux and electron kinetic energy flux at both spacecraft were investigated and compared.

In that event, eight overlapping frequency ranges (5-20 mHz, 10-40 mHz, 25-100 mHz, 50-200mHz, 100-400 mHz, 0.25-1Hz,0.5-2Hz, and 1-4 Hz) are examined. At the higher

frequency end of that range, the waves were 50% earthward, and the frequency was near the ion gyro frequencies (Ω_{O+} ~0.2 Hz and Ω_{H+} ~2.8 Hz). These wave periods were isolated by smoothing and detrending the fields. In the above frequency ranges, the peak, mean, and net earthward Poynting flux were calculated and mapped to the ionosphere. The median $\delta E/\delta B$ ratio, and the phase between δE and δB where examined to determine if the waves were traveling, standing, or a mix of both. It was found that the waves at Polar are generally a mix of Alfvénic and ionospherically coupled, except for in the three highest frequency ranges, where they are in between the Hydrogen and Oxygen Alfvén speeds. At FAST the waves in the three lowest frequency ranges are fully coupled to the ionosphere, and the waves at the higher frequencies are a mixture of Alfvénic and ionospherically coupled waves.

At Polar the Poynting flux were found to have larger intensities in the lower end of the frequency range than at the higher end. In addition, the intensity of the Poynting flux in the lower frequencies at Polar are larger than the Poynting flux at FAST in the same (low) frequency range, by about an order of magnitude.

The fraction of earthward Poynting flux at Polar decreases (somewhat monotonically) from ~90% to 50%, as frequency increases. At FAST the Poynting flux in the lowest three frequency bins is nearly 100% directed earthward, the percentage drops to ~30% in the third highest frequency bin (0.25 -1 Hz), which correspond to the frequencies of the ionosphere Alfvén resonator and then the percentage rises to 80% in the highest frequency bin. The waves with frequencies $\gtrsim$ 1 Hz have a the net wave power at FAST

that is higher than at Polar, indicating that waves of these frequencies are generated between Polar and FAST.

The peak Poynting flux at Polar (FAST) in the region studied is ~45 (~10) ergs/cm^{2}s, with a mean net value of ~3.8 (~1.7) ergs/cm^{2}s over the entire frequency range, 5 mHz – 4 Hz. This is an average decrease of ~2.1 ergs/cm^{2}s in the mean Poynting flux over the altitude range from Polar to FAST. The mean mapped value at Polar (FAST) of the earthward electron kinetic energy flux intensity is ~1 erg/cm^{2}s (~2.2 ergs/cm^{2}s). This indicates an increase in the electron kinetic energy flux of ~1.2 ergs/cm^{2}s between Polar and FAST. Comparing the 1.2 ergs/cm^{2}s increase in the electron kinetic energy flux to the mean Poynting flux dissipated between Polar and FAST of ~2.1 ergs/cm^{2}s indicates that the decrease in Poynting flux is by a sufficient intensity to power the increase in electron kinetic energy flux.

Further, the electron velocity space distributions and energy spectra at FAST were consistent with acceleration via Alfvén waves. The FAST data from intervals corresponding to traversal of the region of intense Alfvén waves show a warm field aligned population of electrons. In addition, the FAST electron spectra in the regions of Poynting flux are broadband. These observations are further empirical evidence that Alfvén waves accelerate electrons at the PSBL.

The above studies are those in which there is comparison between the high altitude Poynting flux and low altitude, magnetically conjugate, electron kinetic energy flux. These studies investigated important aspects of these events, such as the energy balance,

wave properties, plasma parameters, and show that the evidence strongly suggests the acceleration of electrons via the Alfvén waves. The basic conclusion from the conjunction events is that the high altitude Poynting flux is typically of sufficient intensity to power the magnetically conjugate aurora. The plasma environment (electron temperature, Alfvén speed, etc.) and wave properties (scale size) for such events suggest the conditions are present that allow for such acceleration to occur. The advantage of these studies is the stronger case for causally linking the physics and processes occurring at conjugate points simultaneously. Further the level of analysis available when examining a small number of short duration individual events is much greater than in a large statistical ensemble. But while there are strengths associated with studying data from a spatially and temporally limited regime, a limiting factor that emerges from this is that these studies are by their nature somewhat limited in their ability to investigate the evolution of the physics of these processes over larger spatial and temporal scales. Two spacecraft are typically only in conjunction for a relatively short amount to time. Using high altitude auroral images in place of a low altitude spacecraft does allow for a higher success rate of gathering conjugate data, but it sacrifices some of the detail that is obtainable in situ. Furthermore, for low latitudes using a UV imager is not ideal because the when the spacecraft is on field lines mapping to low latitude it is typically (at least in the case of Polar) are not at a high enough magnetic latitude image the auroral oval.

We will now look at theory and model results which also suggest that Alfvénic acceleration is an efficient mechanism for energizing auroral electrons.

2.3 Simulation and theoretical studies of the Alfvénic acceleration of Auroral electrons

Hasegawa [1976] was the first to theoretically suggest that small scale Alfvén waves generated at plasma boundaries could accelerate auroral electrons. That work examined the coupling, and consequences thereof, between macroscopic scales (MHD surface waves) and microscopic scales (those comparable to an ion gyroradius). The MHD surface wave dispersion relation for a plasma to vacuum interface was found by solving the Laplacian of the total pressure with boundary conditions requiring continuity of the total pressure and displacement vector across the boundary. The result was the standard Alfvén wave dispersion relation but multiplied by $\sqrt{2}$, with the plasma parameters being those in the unperturbed plasma. In reality the plasma density will not have a sudden sharp transition but some smooth variation in the transition boundary. Given the range of local Alfvén speeds, the corresponding wave frequencies will extend from infinity (since V_A becomes very large as the density approaches n=0), to $\omega=k_{\|}V_A$ where $n=n_o$. This range will always contain the surface mode frequency of $\omega=\sqrt{2}\, k_{\|}V_A$. In solving for the dispersion relation for the waves on the surface, the finite ion gyroradius was retained. If the gyroradius is assumed to be zero then separate groups of ions will remain frozen onto different field lines on either side of the boundary. Letting the gyroradius be finite leads to the ions near the boundary being able to move separate from the field lines, while the electrons are still frozen in. This gives rise to electrostatic perturbations, and the shear Alfvén waves are no longer isolated on separated field lines, can couple to neighboring field lines via this electric field.

As discussed in the last chapter, Kinetic Alfvén waves carry a component of their electric field aligned with the background magnetic field. In a collisionless environment, Landau damping occurs due to the interaction of the electrons with the parallel wave field. Hasegawa goes on to point out that energy released from the tail will likely excite surface waves. These waves will then excite kinetic Alfvén waves which can accelerate electrons through Landau damping to energies of a few keV. The Aurora produced in this way should have features consistent with discrete auroral arcs, i.e. narrow curtain shape, and wavy motions. Hasegawa suggests possible mechanisms that may allow for a more efficient acceleration. Such mechanisms are electron trapping by the wave along with nonlinear acceleration, or the condition in which the waves are in resonance with electron bounce motion between mirror points.

Shortly after Hasegawa [1976], Goertz and Boswell [1979] presented a simple model (neglecting gradients in the magnetic field and plasma) to investigate magnetosphere-ionosphere coupling in terms of the transient changes in the electric field mapping between them, in the finite time before which equilibrium, can be established. During this none steady state period, parallel electric fields can occur and are sufficient to accelerate electrons to a few keV. The electric field is assumed to reverse direction across the field lines as observed by satellites and rockets over auroral arcs.

In that study they found that when the plasma beta is greater than m_e/m_i the Alfvén wave couples to the ion acoustic mode, and when the beta is less than m_e/m_i the Alfvén wave couples to the plasma oscillations. In the investigation into how surface waves excite kinetic Alfvén waves on plasma gradients [Hasegawa 1976] addressed the regime of

warm (beta > m_e/m_i) plasma. Goertz and Boswell [1979] pointed out that the cold regime had not been explored, and for that regime developed a simple model to consider the temporal variations in the electric field mapping form the magnetosphere to the ionosphere. As the change in electric field propagates to the ionosphere it is accompanied by a parallel electric field at the leading edge of the propagating field. They argue that this parallel field can accelerate electron to a few keV and result in accelerated electrons capable of producing aurora.

While in these studies the warm (kinetic) and cold (inertial) limits are explored separately, Alfvén waves traveling from the magnetosphere to the ionosphere will encounter both regimes, the transition between the two occurring between 3 and 5 R_E geocentric [Lysak and Carlson, 1981]. The full kinetic dispersion relation for Alfvén waves taking into account full kinetic effects for both electrons and ions was developed by [Lysak and Lotko 1996]. In that work they found that Landau damping is as dependent on the perpendicular wavelength as it is to the ratio of thermal speed to the Alfvén speed. For cold plasma (beta << m_e/m_i) the Landau damping is small, but for beta > m_e/m_i it is dependent upon the perpendicular wavelength. Applying their dispersion relation to a model auroral field line they find that for wavelengths larger than 10 km at the ionosphere, Landau damping can be ignored.

A number of simulations have been also been used to investigate Kinetic and Inertial Alfvén waves and their ability to accelerate auroral electrons.

Kletzing [1994] presented a linear model of electron acceleration via kinetic Alfvén wave pulses propagating from the magnetosphere, at altitudes of 7000 km, to the ionosphere in a uniform, Maxwellian plasma and magnetic field. A driver electric field of 250 mV/m was used to launch the Alfvénic pulases. Parallel electric fields are generated in the wave fronts, and are intense enough to accelerate electrons to energies of ~1 keV. Kletzing notes that this acceleration mechanism is a Fermi-like resonant acceleration of a small population of the electrons up to velocities twice those of the Alfvén speed. One half second delays between the electron and wave arrival were observed. The results also indicated modest acceleration of the bulk background electrons. Later, Kletzing and Hu [2001] used an inertial Alfvén wave model in a simulation that included density and magnetic field variations for altitudes 4.5 to 1.1 R_E. Alfvén waves initiated with pulses of perpendicular electric fields of 40 mV/m, (380 mV/m mapped to the ionosphere) accelerated electrons to a similar energy range (300-1keV) and with similar temporal structures as those observed on rockets and satellites. The electron bursts arrive before the wave, and the dispersion in electron arrival times is generated due to the range of altitudes.

Thompson and Lysak [1996] presented a time-dependent, linear MHD model and test particle simulation for the propagation of inertial Alfvén waves (from 3.5 R_E geocentric) through a varying plasma density and magnetic field profile, including reflection off parts of rapid variation and the ionosphere, such as those forming the Alfvén resonator. This model incorporates the microscopic effects of electron inertia into the macroscopic featured of the plasma and field above the auroral oval. Alfvén waves are partially

trapped by the Alfvén resonator. Electrons are accelerated mainly either by falling through the parallel electric field quickly as if a quasi-static drop, or are Landau accelerated to keV energies. Electrons conics were also produced by the simulation.

Chaston et al [2002] used the Thompson and Lysak [1996] simulation for a case study of a transversal of the auroral region by FAST in which broadband electrons embedded in an inverted V structure are measured. They apply a time varying potential to the field lines 5 R_E above the auroral oval. More than 50% of the downward wave Poynting flux goes into the acceleration of downgoing electron kinetic energy flux. They are able to reproduce features seen in the FAST observation; i.e. similar wave forms, inverted V of~ 10keV, broadband electrons up to few 100 eV to few keV. However, there appear to be more upward electrons in the simulation result than in the FAST data however.

Pilipenko et al [2004] investigated the energy budget of Alfvénic interactions with the Auroral Acceleration Region (AAR), using an Alfvén burst spectrum following a k^{-p} power law. In that study, the AAR absorbed 30-50 % of the total wave power.

Swift [2007] presented a quasi-3D particle code that simulates the region from the ionosphere to an altitude of 4 R_E geocentric. Two types of electron acceleration are seen, one slow and one abrupt. The abrupt acceleration occurs at 3000-6000 km altitude at electric field spikes, and the slow occurs at higher altitudes. Swift finds that bipolar pulses in the electric field are more efficient accelerators than monoenergetic pulses. The strongest acceleration is upwards away from the ionosphere, and a larger population of

electrons ends up trapped than do precipitate. The results suggest a possibility that auroral electrons may be accelerated in the conjugate part of the opposite hemisphere.

Watt et al [2005] presented results from a 1D self-consistent kinetic simulation of large amplitude ($E_\perp \sim 50$ mV/m) shear Alfvén pulses on plasma electrons at altitudes 1-4.7 R_E. Velocity dispersed beams and suprathermal bursts were observed in the simulation results. The suprathermal electrons were caused by local heating needed to support the wave current, and are associated with a large perturbation in the distribution function that arises with the steepening of large amplitude pulses ($e\phi \gg k_B T_e$). The threshold for beam formation is a driver potential of $\phi_o = 50V$. The electrons in the bulk distribution function are energized through an interaction with the asymmetric parallel electric field. Watt et al also found that for wavelengths $k_\perp \delta_e \geq 2.7$ a beam is formed but when $k_\perp \delta_e \leq 2.1$ no significant beam is formed. When a beam is formed, the Alfvén pulse converts 15-20% of its initial Poynting flux into beam energy flux.

Watt and Rankin [2009] presented simulation results in which the interaction of an Alfvén wave with non-uniform plasma between 2.5 and 8 R_E geocentric is examined. The main conclusion is that in plasma where $V_{Te} > V_A$, nonlinear particle trapping of electrons occurs and prevents the Alfvén waves from being damped. In regions where the parallel electric field is weakened (plasma with larger V_{Te}/V_A) the accelerated and trapped electrons escape and form beams with distributions similar to those observed on the Polar satellite.

Watt and Rankin [2010] simulated the warm plasma in the PSBL at 4-7 R_E radial distance. The results indicate that shear Alfvén waves immediately lose 55-90% of their Poynting flux intensity as they enter the simulation domain (over a length of 0.1-0.15 R_E), so the energy transfer occurs over a very short distance. The Alfvén waves are introduced at 8 R_E. They conclude that shear Alfvén waves can be effective in the acceleration of electrons in the auroral zone > 4 R_E radial distance.

Lysak and Song [2003] presented calculations based on linear kinetic theory of Alfvén waves in the PSBL and Alfvén resonator to show that such waves are an efficient accelerator of auroral electrons. They examined both local and nonlocal kinetic theory; the latter is important where the gradients in the plasma parameters are on the order of the wavelength, such is the case in the Alfvén resonator. The local theory is applicable in the study of the higher altitude plasma of the PSBL. The conversion of energy through Landau dissipation occurs both in uniform plasma and in the Alfvén resonator region. The calculations indicated that such wave acceleration should occur at altitudes above, and down to, those at which inverted V potentials form. The local kinetic theory indicates that ~50% of the wave power is dissipated over a length of 10 R_E in the PSBL for waves with periods ~ 1 min, and V_A =1000 km/s, parameters comparable to the waves observed by Wygant et al [2000;2002]. For the Alfvén resonator, for various ratios of the electron thermal speed to the Alfvén speed, V_e/V_A =1,3,10, and 30 were used and they found the dissipation to be 0, 0.04,3 and 7.7 % of the input wave energy, respectively.

Lysak and Song [2011] presented results from a simulation model that included the kinetic effects of Landau damping and the full three dimensional geometry of auroral fields lines from the ionosphere to 4 R_E, including the gradient at the PSBL. The results of this simulation suggest that phase mixing is an important process that occurs even at weak plasma gradients, and is enhanced in stronger gradients such as the PSBL. Phase mixing quickly produces kinetic scale Alfvén waves that carry a parallel electric field capable of accelerating plasma electrons. The results of the study also indicate that electron acceleration occurs in the high altitude warm plasma at the PSBL density gradient where Landau damping is an important mechanism, and in the colder plasma at lower altitudes in the Alfvén resonator. In both cases the phase mixing produces small scale parallel electric field structures capable of accelerating electrons. In the PSBL these structures are ~a few 10s of km and in the Alfvén resonator such structures are ~ few km.

In this section, we presented brief summaries of some of the theoretical and simulation work done to model and investigate the physics of Alfvén waves in the acceleration of auroral electrons. The simulations differ in various aspects but agree that Alfvén waves can be effective in accelerating electrons along the magnetic field in the plasma above the auroral oval.

2.4 Studies into the global statistics of Alfvénic Aurora

In this section we look at the empirical work done to study the global morphology and energetic contribution of Alfvén waves to the aurora.

A global perspective of the relation between the high altitude wave Poynting flux and the aurora was first investigated by Keiling et al [2003] who studied the global morphology of the field aligned wave Poynting flux at 5 to 7 R_E geocentric using electric and magnetic field data collected by Polar over a period of 1 year (the year 1997). The wave Poynting flux is found for the period range 6 -180 seconds, and the field aligned Poynting flux mapped to the ionosphere. The mapped Poynting flux was binned according to magnetic latitude and local time in bins 2^oX0.75 hours, for the northern hemisphere, latitudes > 60^o. For each bin the average downward and upward Poynting flux values were calculated. The result shows that the distribution of down-going wave Poynting flux delineates the auroral oval. The general intensity distribution of the Poynting flux around the oval was found to be similar to the global auroral luminosity determined from the Polar UVI instrument. Both the oval delineated by the statistical Poynting flux and that by the average auroral intensity (from a statistical composite of auroral UVI images from 4 months, April through July, in 1997 from Liou et al, [1997]) show similar morphology including the brighter spots around 15 MLT and 21-01 MLT, as well as the same shift anti-sunward from the magnetic north pole of several degrees. In addition the fact that there was little reflected (upgoing) Poynting flux observed suggests that it is dissipated below the spacecraft altitude.

The intense Poynting flux,~ 0.9 ergs/cm^2s, as indicated by the colorscale saturation, extends to about 66-68^o latitude, on the night side around midnight.

It was also found that the wave Poynting flux can account for 30 to 35 % of the energy flux required to cause the global auroral luminosity. This fraction is based off the

comparison between the yearlong Poynting flux data with the four month composite UVI images. They point out that as auroral activity varies throughout the year, so there could be some distortion of the statistics, due to the fact that the data sets are of unequal length.

Keiling et al also mapped the distribution of individual Poynting flux events with mapped intensities of $S_{\parallel} > 5$ ergs/cm^{2}s. These individual events were of sufficient intensity to power visible aurora. It was found that these events are concentrated around the auroral oval, clustering around midnight and the afternoon sectors, again consistent with the statistical aurora.

The conclusion from this study is that the global distribution of auroral luminosity is closely related to the global distribution in high altitude Alfvénic Poynting flux, indicating that the ionosphere and the magnetosphere are coupled via Alfvén waves over the entire auroral region. The magnitude and morphology of the downward Poynting flux carried by the Alfvén waves suggests that Alfvén waves play an important role in powering the aurora globally.

In the same year Chaston et al [2003] showed that Alfvén waves delineate the morphology of the auroral oval at low altitudes (FAST) as well. In another low altitude investigation by Chaston et al [2007] the amount of particle acceleration that occurs in dispersive Alfvén waves (DAWs) (a term used to denote Alfvén waves in either the kinetic or inertial limit) relative to the total electron energy deposited in the ionosphere was investigated. In that study, a FAST data set collected over about 27 months was compiled to develop statistics on Alfvénic accelerated electrons and Alfvénic activity.

The region considered is the hemisphere at latitudes ILAT>60^{o} subdivided into bins 2 hours in MLT by 3 degrees in ILAT. The intervals in which Alfvénic acceleration was dominate were identified and separated on the basis of the ratio of electric to magnetic field perturbations measured transverse to the background field. The frequency range over which the Poynting flux is calculated was, at the low end, set by the width of the current filament, and on the high end by (the lower of) the resolution of the magnetic field or by the Oxygen ion gyro frequency.

In order to have counted as having been accelerated by a DAW, the electrons within the DAW wave field must have a differential energy flux spectra in which the field aligned population must be relatively monotonic or broadband in energy, so that there are no large peaks, unlike the spectra in the case of inverted V acceleration. The statistics only include electron with pitch angles that will allow them to reach the ionosphere without mirroring.

The particle flux and downward Poynting flux were integrated along the spacecraft trajectory, and separated into those found inside DAWs wave field and those that were not. A second integration was done over the longitudinal width of each bin at the spacecraft altitude, to get the resulting power in Watts. The power for each bin was totaled and divided by the number of FAST transversals through the respective bin.

The results of this statistical study show that DAWs occur throughout the low altitude auroral oval, with the occurrence of DAWs being the highest around noon and around midnight. The energy deposition from the integrated Poynting flux is highest around

midnight. The total wave energy directed towards the ionosphere observed by FAST is on average ~2GW, during active times is as large as ~10 GW.

As with the Poynting flux, the total average electron energy deposition is peaked on the night side, near midnight, and around noon. The total average power is higher ~18 GW, and may exceed 100GW during active times. Thus the electrons at FAST transport about 10 times the power as the Poynting flux, and the Alfvénic electrons are three times the intensity of the residual Poynting flux. The fraction of the deposited electron power which was coincident with, and has the characteristics of, being accelerated by DAW fields is ~50 % around noon and pre-midnight, and generally has a value of ~31% over the whole hemisphere (> 60^{o} ILAT). The nightside region where this significant fraction of Alfvénic aurora occurs extends down to latitudes of 69-72^{o}.

The fraction of total electron energy deposited attributable to DAWs per FAST orbit increased with auroral activity. The average over the whole hemisphere, above latitudes > 60^{o} ILAT, suggest that the fraction of the total electron energy flux incident on the hemisphere at FAST that is most likely driven by DAWs increases from 25% to 39% with increasing auroral activity (as determined from POES data). In the noon and pre-midnight sectors, on the poleward edge of the auroral oval during active times, they find that the electron fluxes in DAWs with energy spectra consistent with DAW acceleration, provide the dominant contribution to the electron energy deposition in the upper atmosphere.

Another low altitude study, with a longer dataset though without fields measurements was done by Newell et al. [2009] who used 11 year of DMSP electron and ion data for a low altitude (~ 850 km) statistical study to quantified the auroral energy budget as a function of solar wind driving.

The particle spectra were used to identify the type of acceleration. To identify an electron spectra as a mono-energetic event, the energy channel with the peak differential energy flux[17] value is identified and the drop in the differential energy flux in the two neighboring energy channels must be below 30% of the peak. A Maxwellian distribution measured by DMSP would have 80% of the peak value in the neighboring energy channel. The peak differential energy flux must also meet or exceed a threshold that diffuse aurora never reach.

Spectra that are not mono-energetic and have differential energy flux that exceed a given threshold value in three or more energy channels were considered broadband if it was not mono-energetic, and if the average energy per electron was greater than 80 eV. There also must have been at least one energy channel, above 140 eV, in which the differential energy flux met or exceeded a threshold. Any spectrum not mono-energetic and not broad band was counted as diffuse. An event was also excluded from being considered accelerated if the average energy was below 80 eV or the differential energy flux peaked in a channel below 100 eV.

[17]The differential energy flux, djE/dE, where jE is the energy flux per stradian, has units eV/(cm^2 s sr eV).

This study covered latitudes from 60 to 90 MLAT and sorts the data into bins 0.25 hr MLT by 0.25 MLAT. For each bin and for each of the four types of aurora (that is the three types of electron aurora plus diffuse ion aurora) a linear regression fit of auroral power to a function of form:

Auroral power (mlat_bin,mlt_bin,aurora_type) = a + bx $d\Phi_{MP}/dt$, where $d\Phi_{MP}/dt = v^{4/3}B_T^{2/3}\sin^{8/3}(\Theta/2)$ is the solar wind parameter used to represent driving, Θ is the clock angle, and B_T is the transverse field magnitude found from just By and Bz, first presented in [Newell 2007].

For each of the four types of aurora, the hemispheric power was determined by multiplying the surface area of each MLAT-MLT bin by the auroral power averaged over that bin, and summing the bins. This was done for the northern and southern hemispheres separately but then combined.

These statistics are divided into periods of high and low solar wind driving. Low solar wind driving is defined as $d\Phi_{MP}/dt = 0.25< d\Phi_{MP}/dt >$, and high solar wind driving is defined as $d\Phi_{MP}/dt = 1.5< d\Phi_{MP}/dt >$, where $< d\Phi_{MP}/dt >$ is the average over one solar cycle, $< d\Phi_{MP}/dt >=4421(km/s)^{4/3}(nT)^{2/3}$. The high driving condition threshold is itself only moderately active, and is within the range of normal activity. Between the low and high levels of solar wind driving the energy flux from mono-energetic events rises from 1.1 to 5.8 GW, an increase by a factor of 5.3, or as a percentage of total power, from 10% to 15% (most of the precipitation is in the pre midnight and dusk sectors) the intensity scale used saturated at 0.75 ergs/cm^{2}s, suggesting this represents an upper bound of the average intensity. The broadband precipitating energy flux increases from 0.6 GW to 4.8

GW, which is a factor of 8, and the highest of the four types. As a percentage of the total aurora, the contribution of broadband electrons increased from 6% to 13%. The broadband electrons are predominantly located between 21 and 0.5 MLT. (The energy scales used on the plot saturates at 0.5 ergs/cm^{2}s.) The diffuse electron energy precipitation increases by a factor of 3 from 6.8 GW to 20.2 GW, which in terms of the fraction of the total contribution is actually a decrease from 63% to 57%. The diffuse precipitation is located primarily in the post-midnight and dawn sectors (because electrons E×B drift eastward) , from about 21 to 9 MLT, (the scale saturates at 1.5 ergs/cm^{2}s.) The ion energy flux increases by a factor of 2.1 from 2.3 GW to 4.9 GW, 21% to 14% of the total. The diffuse ions predominantly located on the night side from 19 to 05 MLT.

The results by Newell et al [2009] suggest that the diffuse aurora is the dominant type in terms of total energetic contribution to the aurora. In terms of dynamic response to solar wind driving it is the broadband aurora that show the greatest increase. The contribution of broadband electrons (interpreted as Alfvénic) contribute 7.6% to 15.3% of the auroral power as a function of solar wind driving, relative to just the three types of electron spectra, i.e. excluding the diffuse ions. They also find that for times of high solar wind driving that the auroral oval of enhanced broadband electrons extends down to about 68^o ILAT near midnight. Another important result of Newell et al [2009] is that broadband aurora are not confined to areas near the poleward portion of the auroral oval, but occur at lower latitudes as well. In particular, the appearance of a narrow, non-contiguous, irregular ring of broadband electrons at ~65^o ILAT during high solar wind driving was

noted. This is interesting because much of the previous research identified the polarward edge of the oval and its high altitude extension, the PSBL, as the location where the most intense activity occurs. At high altitudes, the occurrence of Poynting flux in the plasma sheet had been noted earlier by Wygant et al [2002] and Keiling at al [2002].

The studies by Chaston et al [2003,2007] and Newell et al [2009] are both low altitude studies, where Keiling et al [2003] was a high altitude study. Another high altitude statistical study is that of Janhunen et al. [2006] who used five years of Polar data (gathered from the years 1996-2001) so that a full range of altitudes between 5,000 and 30,000km are covered, to build a statistical altitude profile of the down-going Poynting flux. Electric and magnetic field data were filtered such that the filter had a cutoff frequency that varied with altitude so as to give constant spatial cutoffs projected to the ionosphere of <20km, <50km, <100km, and <200km. They also tested a filter fixed in frequency (like that used in Keiling et al [2003]) and found the results to be qualitatively similar. The intensity of the down-going field aligned Poynting flux as a function of geocentric distance (from $\sim 1.5 - 6\ R_E$) in the nominal auroral zone (18-06 MLT, and 65^o-74^o ILAT) for three levels of magnetic activity, $Kp \leq 2$, $2 < Kp \leq 4$, and $Kp > 4$ was determined. A step-wise decrease in Poynting flux intensity with decreasing altitude is evident at 4-4.5 R_E, particularly for high Kp (for low Kp is it not so evident). The conclusion holds for all four of the above spatial filters.

They averaged the downward Poynting flux below 3.5 R_E and above 4.5 R_E separately, this division in altitude was determined by the location of sharp decrease in Poynting flux intensity mentioned above. The difference between the averaged Poynting flux

intensities is compared to the statistical intensity of total auroral electron precipitation as determined from the Hardy statistical model [Hardy et al., 1987]. For the three Kp ranges mentioned above they find that the decrease in Poynting flux is 10% of the total electrons for the low Kp range, 20% for the middle Kp range, and 40% for the high Kp range.

Janhunen et al point out that the region around the decrease in Poynting flux at 4-5 R_E is where the Alfvén speed and the electron thermal speed are comparable, suggesting that the waves could be in Landau resonance with the electrons, and so transfer a significant proportion of their energy to the electrons at this altitude.

The results of these statistical studies are summarized in Table 1.

Study	**Altitude and amount of data used**	**Region studied**	**% auroral (electron) power that is Alfvénic/broadband**	**Peak Average Intensity**	**Equatorward edge of contiguous intense part of aurora**
Keiling et al 2003	High altitude (Polar) 1 year of data.	ILAT>60^o	30-35% Wave $S_{\|\|}$, UVI used to observe auroral luminosity	~0.9 ergs/cm^{2}s	~66^o (extent of the intense high altitude Alfvén Poynting flux)
Chaston et al 2007	Low altitude (FAST) 2.25 years of data	ILAT > 60^o	25-39% Both wave fields and spectra used to ID auroral type.	Not presented	69^o-72^o
Janhunen et al 2006	High altitude (Polar) 5 years of data	Night side auroral zone only, ILAT 65-74^o. Fraction is a function of Kp	10%, 20%,40% for Kp <2, 2≤Kp<4, Kp>4 respectively. % change in wave $S_{\|\|}$ intensity at ~4R_E, relative to modeled electron precipitation.	Modeled electrons and Alfvénic intensity for high Kp: 2 ergs/cm^{2}s, 0.8 ergs/cm^{2}s	Not presented, statistics for 65^o-74^o combined.
Newell et al 2009	Low altitude (DMSP) 11 years of data	ILAT > 60^o	7.6 to 15.3% (fraction of broad band to total electron energy) For low and high solar wind driving. Spectral identification of acceleration type only.	Mono: 0.75 ergs/cm^{2}s Broadband: 0.5 ergs/cm^{2}s Diff: 1.5 ergs/cm^{2}s	Mono energetic : 72^o Broadband:70^o Diff:68^o (For high driving conditions) Irregular detached ring ~65^o

Table 2.1: A summary by study of the energetic contribution that Alfvén wave power, or electron spectra interpreted as Alfvén accelerated, makes statistically to the overall auroral electron precipitation power.

2.5 Generation of Poynting flux in the tail and its earthward propagation

Both empirical and theoretical evidence suggests that Alfvén waves propagating from the tail carry significant energy earthward capable of powering aurora. We now examine some studies that provide further evidence for this while also investigating the mechanisms producing these waves.

Angelopoulos et al [2002] investigated the relation between bursty bulk flows (BBF) in the tail and dissipation of energy via Poynting flux that propagates earthward with sufficient intensity to power aurora. The event studied occurred during a substorm during a Polar-Geotail meridional conjunction, the foot points where within 1.5 MLT on the night side (21 -03 MLT). Polar was on the magnetic equator around 22.3 MLT, ~5 R_E, and Geotail was in the tail ~-18R_E.

The main substorm activity in that event was of a global nature as indicated by ground based data from a meridian scanning photometer located between the spacecraft foot points and data from multiple magnetometers. Geotail observed two bursty bulk flows (BBF), the later accompanied by a dipolarization event.

The field aligned Poynting flux in the frequency range of 1 mHz to 0.1 Hz decreased by a factor of 10 (from 300 to 30 ergs/cm^{2}s, mapped) between Geotail and Polar. The field aligned Poynting flux decreased by a factor of three for higher frequencies, (from 640 ergs/cm^{2}s to 220 ergs/cm^{2}s for 0.1-20 second wave periods (10 -0.05 Hz). This suggests

significant dissipation of the Poynting flux occurred between Geotail and Polar. At Polar the Poynting flux is still sufficient to power the acceleration of auroral electrons to the larger intensities seen during intense precipitation events, ~140 ergs/cm^{2}s (a Figure quoted from Newell et al [2000] as being representative of the larger electron kinetic energy flux seen at low altitude). The earthward particle energy in the BBF at Geotail is ~2000 ergs/cm^{2}s (mapped to 100km) and is much larger than the Poynting flux at Geotail. Examination of the particle flow velocity and fields at Geotail indicated that the Poynting flux is most responsive to the y-GSM component of the flow, and the associated Ez electric field. The x component of the plasma flow, and the associated electric field Ey, are damped through coupling to the slow mode wave. They further estimate that the Poynting flux carried by Alfvén waves dissipates enough power to account for the breaking of the BBF.

It is interesting to note that the Ez component of the electric field being associated with the damping of BBF via the generation of Alfvénic Poytning flux in the tail is consistent with the fact that the intense Alfvén waves in the PSBL are polarized such that the electric field is perpendicular to the PSBL, i.e. mainly in the z direction [Wygant et al 2000; 2002]. This suggests that the intense Poynting flux observed in the PSBL may be generated by the damping of such flows further back the tail.

A simulation study of the relation between BBFs and the generation of Alfvén waves was done by Zhang et al [2012]. In particular, the generation and propagation of Alfvénic Poynting flux in and from the central plasma sheet to the ionosphere was examined using a global three dimensional simulation of the solar wind/magnetosphere/ionosphere

interaction, called the Lyon-Fedder-Mobarry (LFM) global simulation model. They found that the breaking of BBFs associated with time-variable reconnection generates both Alfvén mode and fast mode waves. The fast modes intensity diminishes as they propagate isotropic away from the source, and the Alfvén waves are focused by the converging field geometry and thus dominate at low altitudes. They find that projected onto the ionosphere, the morphology of the Alfvén waves reproduces that found empirically by Keiling et al [2003]. However, this model does not take into account the conversion of the fast mode waves into Alfvén waves via phase mixing, which is an important mode converting mechanism [Lysak and Song, 2011] and has been observed to be associated with the powering of aurora [Lessard et al 2006,2011]. Still, transverse Alfvén waves appear to be of predominant importance at high altitudes [Wygant et al, 2000;2002, Keiling et al 2002,2003 and Dombeck et al, 2005].

In addition transverse waves have been reported in the tail, in the ion jets from nearby reconnection region at X~-20R_E by Dai et al [2011]. These waves where plasma sheet confined surface waves (different from current sheet flapping) perpendicular to the background field and laying in the plasma sheet plane]. They observe evidence for velocity shear in the perpendicular velocity component of the jets as driving the waves via the Kelvin-Helmholtz instability. Intense Poynting flux in the 1-30 second period range mapped to the ionosphere had an intensity of ~100 ergs/cm^2s.

In this section we have been discussing work that examined the generation of Poyting flux in the tail. However it should be noted that the dayside aurora also is in part due to Alfvénic contribution. This is evident in the above described studies of Keiling et al

[2003], Chaston et al [2003,2007] and Newell et al [2009] who show that Poynting flux delineates the whole aroral oval, including the day side portion. Further, Cattell et al [2011] provided the first evidence for auroral electron emissions at the footpoint of dayside reconnection accelerated by reconnection Poyting flux. In that study, the auroral emission occurs in a localized spot that is approximately steady over the course of 1 hour during a substorm.

2.6 The relation between substorms and Alfvénic aurora

Substorms (described in the last chapter) are known in part for their accompanying auroral phenomenon. Given the impulsive release of energy during these events, it is not surprising that some of the energy ends up in the form of Alfvén waves. Some of the Alfvén waves likely contribute to powering the intensification in auroral activity.

Evidence that intense field aligned Alfvén Poynting flux occurs during the substorm expansion phase on the PSBL was presented by [Keiling et al 2000]. The events used in that study were chosen from a separate investigation by Keiling et al, published in [2001], in which 24 large amplitude electric field events (>100 mV/m) perpendicular to ambient magnetic field, on the night side in and around the PSBL and plasma sheet (of which ~85 % where in the PSBL), at 4 to 7 R_E geocentric altitude were examined. The five events chosen for the [2000] study were also magnetically conjugate to ground magnetometers during times of rapid decrease in the H (or northward) component of magnetometer data, an indicative signature of substorm expansion. The Poynting flux of Alfvén waves with periods 6 seconds to 1 to 3 minutes had mapped intensities between

100 and 315 ergs/cm^{2}s. These results indicate that Alfvénic Poynting flux is an important energy transport mechanism between the tail and the ionosphere, during the expansion phase of the substorm.

Further evidence for the substorm relation to Alfvénic aurora was provided by Mende et al [2003] who observed for the first time that the initial brightening of the early onset arc was Alfvénic in nature. The Alfvénic signatures in this study were observed by FAST and the occurrence of onset in terms of auroral brightening were observed by IMAGE's WIC instrument. FAST observations further indicated that equatorward of the onset surge the aurora tended to be the inverted V type.

Research by Lee et al [2010] prompted in part by the irregular ring of intense broadband electrons presented in Newell et al 2009 (discussed above), used night side DMSP electron data from 1916 substorm onsets (1800 of which were identified with Polar UVI) to identify broadband spectra at low latitudes($<68^o$ ILAT) . These low latitude broadband electrons were found to have a strong statistical association with the occurrence of substorms. The frequency of the occurrence in the broadband spectra peaks about 15 minutes after onset and extended to about an hour after onset. A more detailed investigation by Newell et al [2010] looked at statistical evolution of the various types of aurora in ILAT-MLT for ±120 minutes around substorm onset, and noted that consistent with Lee at al [2010] that broadband auroral become more prevalent at low latitudes during substorms.

Lessard et al [2006, 2011] studied an event, at substorm onset in which, fast mode waves in the Pi1B range (1-40 sec) at geosynchronous orbit, observed by GOES, propagated earthward and became Alfvénic by the time they arrive at FAST altitudes. At FAST, the Alfvénic Pi1B pulsations were observed concurrent with signatures of Alfvénic acceleration of electrons; FAST was conjugate to an auroral arc just after onset. This event was also located at low latitudes ~63^{o} ILAT. This presents a somewhat different picture than the higher altitude studies discussed above [e.g. Wygant 2000,2002 ; Keiling 2002; Dombeck et al., 2005] which investigated intense field aligned Alfvén waves at altitudes of 4-7 R_E and found them to be conjugate and sufficient to power intense aurora. It is possible that both processes occur, and it is important to understand the role each plays in energy transport. This consideration further underscores the importance of high altitude studies of the energetic contribution by Alfvén waves.

2.7 Reason for the study in this thesis

To date there have been no studies that look at the evolution in latitude of the wave Poynting flux at high altitudes over the course of major geomagnetic storms. Low altitude studies are not able to compare the high altitude Poynting flux to the low altitude precipitating electrons. Conjunction studies between high and low altitude spacecraft offer a detailed snapshot in time and localized in space. Statistical studies tend to average over the effects of individual storms, deemphasizing the larger storms. Further, reliably determining Alfvénic acceleration through low altitude electron spectra alone can be difficult, as other factors can give rise to spectra that appear broadband. This is particularly the case at low latitudes where the inverted-V potential drops tend to be less

than their higher latitude counterparts [Dombeck et al, 2013]. At higher latitudes, the inverted V potential can accelerate the plasma sheet electrons to energies above their Maxwellian temperature into a beam like distribution, but at lower latitudes the inverted V potential is sometimes less than that of the initial Maxwellian distribution temperature. In such cases the potential only significantly increases (as a fraction of initial energy) the energy of the electrons in the lower and middle range of the electron distribution, in total forming an electron population that appears broadband spectrally [Dombeck et al, 2013]. In addition, Alfvén waves may play a role in the acceleration of mono-energetic electrons as well [Vaivads et al, 2003]. In general energy continuity requires that the inverted-V system has some Poynting flux associated with the input of energy into it, and this may be associated with the Poynting flux carried by Alfvén waves [Song and Lysak 2001, 2006]. It has also been found that the quasi-static potential drop that accelerates inverted V electrons may be formed out of the Alfvénic acceleration systems of the PSBL [Hull et al, 2010; Newell et al, 2012]. All this suggests an intimate link between high altitude Poynting flux and the accelerated aurora electrons (both broadband and mono-energetic) at low altitudes. Low altitude studies also are limited in their ability to identify the properties of the high altitude waves, such as whether they are transverse modes waves [e.g. Wygant et al, 2000] or fast mode waves [Lessard et al, 2011]. Thus the observation of the waves themselves at high altitude is important for assessing their role in storm time auroral physics. The evolution over the duration of major storms of the energy transported by Alfvén waves at high altitudes between the source region in the tail, and the acceleration region at lower altitudes, has not been addressed. It is the aim of this

thesis to further the understanding of the role played by wave Poynting flux at these altitudes in conjunctions with the lower altitude auroral electrons during large storms.

Chapter 3

Spacecraft and Instrumentation

3.1 Introduction

The research presented in this thesis was conducted primarily with data provided by four spacecraft; Polar, FAST, and DMSP (F12 and F15). In addition, OMNI solar wind data provided by ACE, Wind and other satellites is used. Dst, and AE indices are generated from ground based magnetometer data.

3.2 Polar Spacecraft:

The Polar satellite [Figure 3.1] was launched on February 24, 1996 and was in commission until April of 2008. Polar was placed in an elliptical polar orbit [Figure 3.2] with an apogee of ~9 R_E, pedigree of ~2 R_E and an orbital period of ~18 hours. This orbit covered a range of invariant latitudes at altitudes between those of the generation of Alfvén waves in the tail and the auroral acceleration regions. Thus the orbit of Polar was well suited to the study of the earthward wave Poynting flux at high altitudes over the range of latitudes that aurora occur. The orbit allowed measurement of fields and particles over a wide range of latitudes, per hemisphere, on the night side, every 18 hours. Polar cartwheeled in its orbit, i.e. the spin plane of the spacecraft was in the orbital plane, and the spin period was 6 seconds.

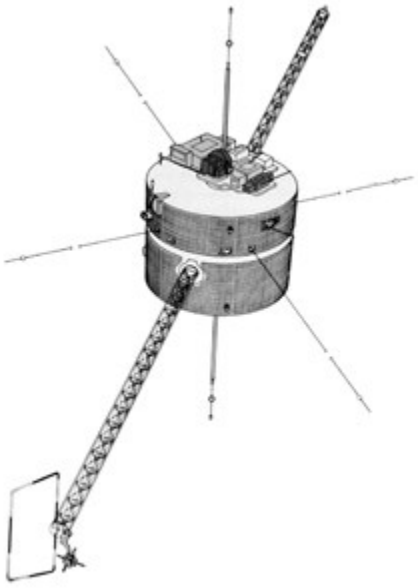

Figure 3.1: The Polar Spacecraft showing magnetometer boom and the two perpendicular pairs of electric field booms (shown truncated): Drawing of Polar courtesy NASA, Goddard Space Flight Center, found online at http://pwg.gsfc.nasa.gov/polar

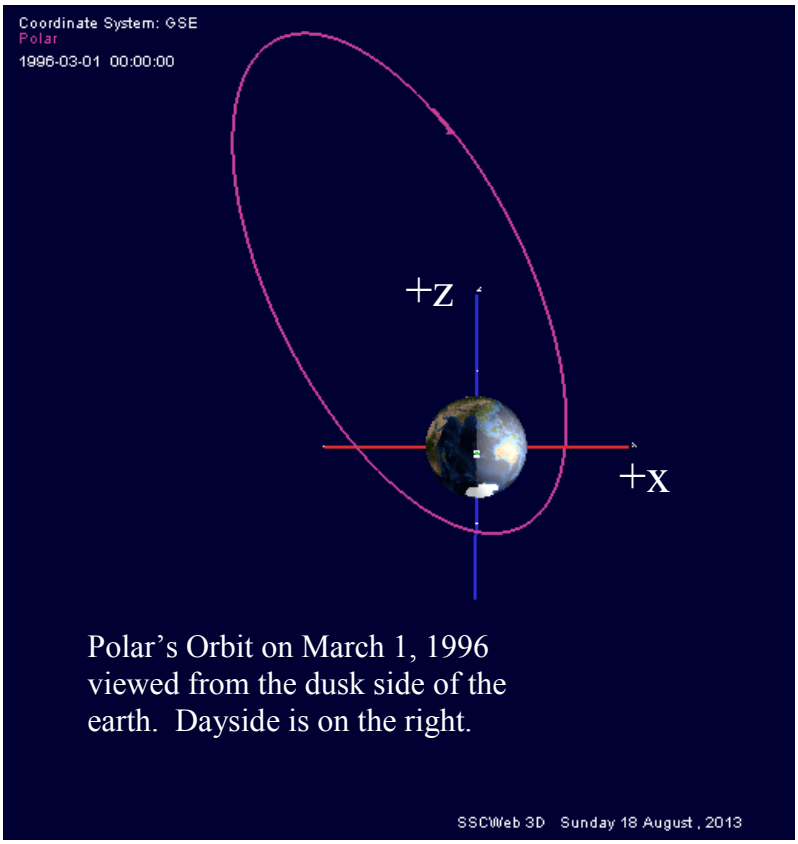

Figure 3.2: The orbit of Polar on March 1, 1996, shortly after launch. The sunward direction is to the right. Polar's is in an elliptical polar orbit. Figure generated with SSC web's 4D orbit viewer, supported by Goddard Space Flight Center.

The Polar Spacecraft carried several instruments used in this study: the Electric Field Instrument (EFI), the fluxgate magnetometer (FGM), the Hydra instrument, the Ultraviolet Imager (UVI) and the Visible Imaging System (VIS).

3.2.1 EFI (Electric Field Instrument)

The Electric Field Instrument (EFI) [Harvey et al 1995] had two pairs of current biased spherical double probes mounted on the ends of orthogonal wire booms centripetally

deployed in the spin plane with tip to tip separations of 130 meters (probe pair 1-2) and 100 meters (probe pair 3-4) and a shorter on-axis pair with tip to tip separation of 13.8 meters (probe pair 5-6). The electric field is determined from the potential difference between the probe pairs. Thus EFI was capable of making three dimensional electric field measurements, though in practice there are difficulties associated with using the data from the shorter spin axis probes which exhibit effects sensitive to due to plasma density and temperature. EFI made measurements from DC to 20 kHz, over a dynamic range of 0.02 to 1000 mV/m. In this study we use the spin period, 6 second, data for the long term survey of Poynting flux and higher resolution (0.02 sec cadence) for individual example events. The electric field data is used along with magnetic fields to calculate Poynting flux. Below we discuss the properties the probes and spacecraft should have to make accurate measurements of the electric field.

3.2.2 MFE (Magnetic Fields Experiment)

The magnetic fields instrument (MFE) consisted of two triads of orthogonal fluxgate magnetometers mounted on a 6 meter boom [Russell et al 1995]. MFE measured all three components of the magnetic field at ~9 Hz continuously (and snapshots of 100 Hz).

The sensors of the fluxgate magnetometer consisted of a magnetically permeable core brought into magnetic saturation with a field generated by a driver winding. In such a device, the ambient magnetic fields of the magnetosphere upset the magnetic hysteresis symmetry of the core and produces even harmonic signals with amplitudes proportional to the external field. These harmonic oscillations are picked up by a sensor coil.

In this study the magnetic field is used to calculate Poynting flux and to map in situ values of the Poynting flux to the ionosphere.

3.2.3 Hydra

The Hydra instrument [Scudder et al 1995] is a hot particle detector that consisted of two electrostatic analyzers and two parallel plate imaging analyzers that measured the three dimensional velocity space of electron and ions in the energy range of 12eV – 18 keV at 0.5 second cadence. Hydra data provides various moments including the density, velocity distributions, and kinetic energy flux, as well as the differential energy flux. In this study Hydra differential energy flux is used to identify the plasma sheet and plasma sheet boundary location.

3.2.4 UVI (UltraViolet Imager)

The UltraViolet Imager (UVI) [Torr et al 1995] took images of the aurora in the far ultraviolet part of the spectrum (1300-1900 Å). Such UV emissions result from the collisions of energetic particles, such as accelerated auroral electron beams, with the atmosphere. UVI was capable of imaging both the day and night side of the earth. It had a nominal frame rate of 37 seconds and a circular field of view of 8^{o}. The UVI images provide the intensity of the electron beams incident on the ionosphere. In the next chapter of this thesis we show a couple of example events with comparisons between the electron beam intensities at the Polar foot point inferred from the UVI images to the wave Poynting flux (mapped values) incident on that location. We also integrate the UVI

image intensity across the foot point track and compare it to the Poynting flux integrated along the Polar trajectory.

3.2.5 VIS (Visible Imaging System)

The VIS instrument [Frank et al,1995] consisted of a set of three cameras, two to image the nighttime aurora and a third to monitor the field of view of the first two with respect to the sunlit earth. The two auroral cameras operated in the visible spectrum (308 -732 nm) and had a spatial resolution at earth's surface from an altitude of 8 R_E of 10 and 20 km. The frame rate was 12 seconds. The VIS instrument images are used to show an example of the presence of large scale auroral intensifications across many hours MLT during storms.

3.3 FAST (Fast Auroral SnapshoT) Explorer

The FAST satellite [Figure 3.3] was launched on August 21, 1996 into an elliptical, low altitude (perigee of 350 km, and apogee of 4175 km), polar orbit [Figure 3.5] with a 133 minute period [Pfaff et al 2001]. FAST operations ended on May 1, 2009 [http://cse.ssl.berkeley.edu/fast_epo/]. FAST spun in cartwheel mode at a rate of 5 seconds. The orbit of FAST allowed it to make measurements over a wide range of latitudes per orbit in the auroral zones. Thus FAST was able to study the evolution of the

space plasma environment over a range of latitudes at altitudes in and below the auroral acceleration region, over the course of storms. FAST carried electron and ion electrostatic analyzers data from which are used in this study to determine electron kinetic energy flux incident on the ionosphere.

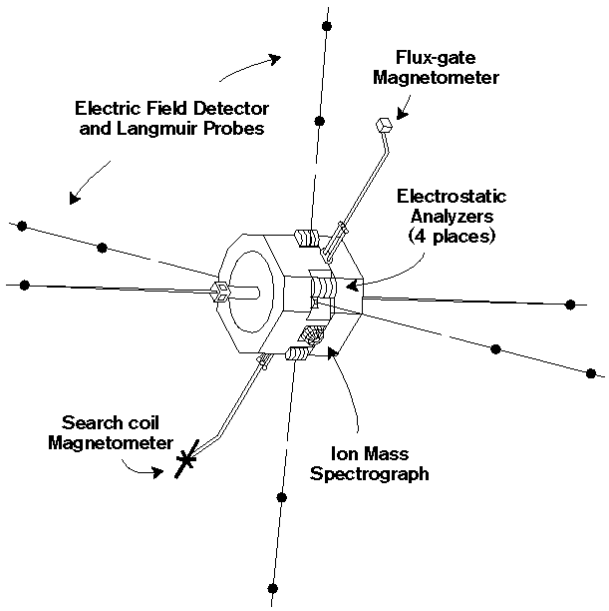

Figure 3.3: the FAST spacecraft showing electrostatic analyzers, electric and magnetic field instruments [courtesy SSL, online at http://sprg.ssl.berkeley.edu/fast/inst.html]

3.3.1 Electrostatic analyzer

The electron and ion electrostatic analyzers (EESA and IESA) each consisted of two stacks of four electrostatic analyzers mounted opposite each other on the spacecraft spin plane [Carlson et al 2001]. The analyzers each had a 180^{o} field of view, and the pairs

being mounted opposite each other on the spacecraft allowed for 360^{o} coverage. EESA measured electron spectra in the energy range of 4eV to 32 keV, and IESA measures ion spectra in the energy range of 3eV to 24 keV, over 48 energy channels, each at a sample rate of ~12.8 /s (64 sweeps in the 5 sec spin period).

The spin period resolution (5 sec) net earthward electron kinetic energy flux, is used in this thesis to study the downward electron kinetic energy flux during storms.

3.4 DMSP (Defense Meteorological Satellite Program)

The DMSP satellites [Figure 3.4] are in a polar, circular orbit [Figure 3.5] at an altitude of ~850 km and period of ~102 minutes. As with the case of Polar and FAST, this polar orbit allows for measurement over a wide range of latitudes every orbit. The low altitude of DMSP's orbit is ideal for measuring the post acceleration downward electron kinetic energy flux. The DMSP satellite program consists of multiple, similar, satellites over the years. For this study the specific spacecraft used were F12 (Launched August 29, 1994) [http://ghrc.nsstc.nasa.gov/uso/source_docs/] for the April/May 1998 event and F15 (launched December 12, 1999) for the October 2001 event.

Figure 3.4: A DMSP satellite [Image source https://heasarc.gsfc.nasa.gov/docs/heasarc/missions/dmsp.html]

3.4.1 SSJ/4 Precipitating Plasma Monitor

The DMSP satellites carry a SSJ/4 Precipitating Plasma Monitor [Hardy et al 1984] which consists of four electrostatic analyzers that measure the downward flux of precipitating electrons and ions at a cadence of 1 second in the energy range of 30 eV to 30keV in 20 fixed energy channels. The DMSP satellites do not measure up going particles as the detectors are oriented to observe only downward (earthward) particle fluxes. The electron fluxes are reported in units of $eV/cm^2s\text{-}sr$. Following Newell et al [2009] we find the kinetic energy flux by multiplying the kinetic energy flux per solid angle by pi. At DMSP altitudes, the loss cone half angle is ~56^o, which roughly corresponds to a solid angle of pi stradians. Thus we correct for the fact that some of the electrons will mirror before they reach the ionosphere.

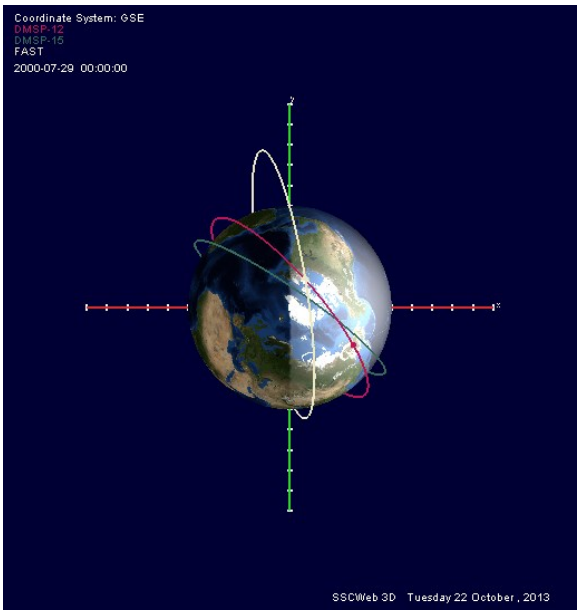

Figure 3.5: Low altitude polar orbits of FAST (white trace) DMSP F12 (red trace), and DMSP F15 (green trace) at the end of July 2000 (not one of the events examined herein) viewed in the northern hemisphere along the –z direction.

3.5 Dst and SYM-H index

The Disturbance storm time (Dst) index [http://wdc.kugi.kyoto-u.ac.jp/dstdir/dst2/onDstindex.html] is the disturbance magnetic field axially symmetric to earth's dipole axis, at earth's surface around the dipole equator. The horizontal field is measured by four magnetometers [Figure 3.6] dispersed in longitude and at very low latitudes. The Dst is normalized by subtracting an annual base line determined from averaging the five quietest days every month. The Dst index represents decreases in the magnetic field due to increases in ring current. These enhancements in ring current arise from the injection of plasma into the inner magnetosphere during storms, and thus Dst is an indicator of the occurrence and intensity of storms. Dst index is reported at a one hour

cadence and is provided by the World Data Center for Geomagnetism at Kyoto University.

Similar to the Dst is the Symmetric – Horizontal (Sym-H) index [Kyoto WDC http://wdc.kugi.kyoto-u.ac.jp/aeasy/asy.pdf]. This index is reported at a 1 minute cadence, and is measured with a different set of magnetometers than the Dst index is. The Sym –H index is determined by averaging the disturbance component over 1 minute from 6 of 11 magnetometers, some of which are at higher latitudes than those used to measure Dst. The difference in latitude is corrected by dividing the averaged magnetic disturbance by the six station average of the quantity $cos\theta_m$where θ_m is the dipole latitude of the station. The higher time resolution of the Sym-H index allows it to exhibit effects associated solar wind dynamic pressure variations.

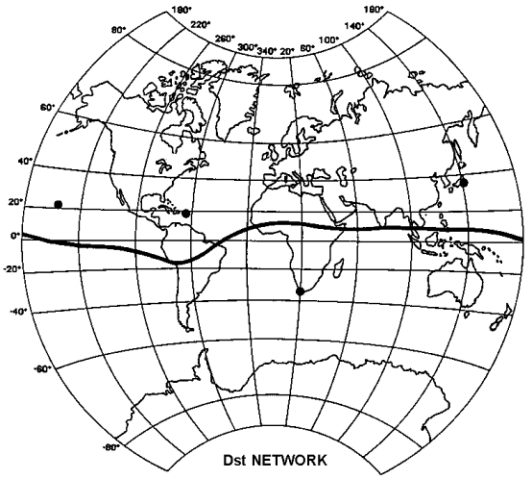

Figure 3.6: Network of the four Dst magnetometers, indicated by black dots. [courtesy Kyoto WDC]

3.6 AE index

The AE (Auroral Electrojet) index is derived from variations in the horizontal component of geomagnetic field measured at 10 to 13 ground stations in and around the northern hemisphere aurora zone. A base line average is established by averaging the five most quite days from each month. This baseline is subtracted from each month's worth of data. At any given time, the most positive disturbance at any of the stations is the AU index and the most negative at any of the stations is the AL index. The AE index is the difference between these two indices, AE = AU – AL. The AU index represents the strongest eastward electroject current intensity, and the AL index represents the strongest westward electrojet. The AE index is an indication of substorm activity.

3.7 OMNI data

Solar wind plasma and magnetic field data, in particular the density, speed (and thus ram pressure), and IMF, are provided in the OMNI data set at 1 and 5 minutes cadences. These data are measured by the ACE, Wind, IMP 8, and Geotail spacecraft, and shifted to nose of the bow shock. ACE is in orbit about the L1 point located ~230 R_E from the earth in the direction towards the sun. Wind is in a large elliptical orbit around the earth, between 90 R_E and ~250 R_E at apogee; IMP 8' s orbit around earth extends to about 25 R_E to 40R_E ; and Geotail's orbit locates it between 9 and 25 R_E, thus when it's apogee is not in the tail it's orbit carries it through the solarwind. The overall data set available from each spacecraft is: Geotail (1995-03-15 - 2006-12-31), IMP-8 (1973-11-04 - 2000-

06-09), ACE (1998-02-05 - 2013-05-12), Wind (1995-01-01 - 2013-07-31) [http://omniweb.gsfc.nasa.gov/html/HROdocum.html#1].

The OMNI solar wind data is used as an input parameter for the Tsyganenko model field (see below). As well as to describe the state of the solar wind during the events investigated herein.

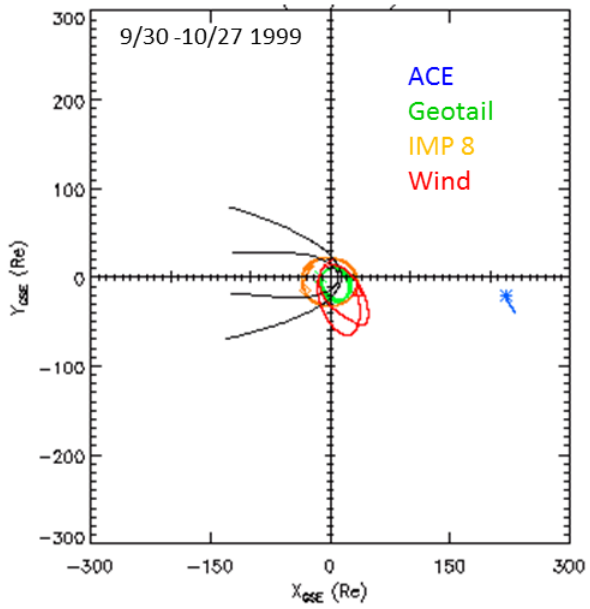

Figure 3.7 orbits of the four solar wind monitoring spacecraft; ACE, Wind, Geotail and IMP 8 in the fall of 1999. These orbits are shown in the X_Y GSE plane which extends to +/- 300 RE. The bow shock and magnetopause are drawn in and appear as the black parabolas. Figure made with plotting tools available at SSC web.

3.8 Tysganenko field models

The Tsyganenko model is mentioned here as data source as it supplies modeled data. The name derives from its author, Nikolai Tsyganenko. There are several commonly used

Tsyganenko models that sometimes go by different names: T89 (1989), T96 (1996), T01 (aka T02), T04s (aka T05), the number referring (approximately) to the year of publication.

These models are semi-empirical best fit representations for the geomagnetic field using parameterized data from both ground and space based sources. The models include the field contribution from the various magnetospheric current systems.

The T89 [Tsyganenko 1989] model parameterized the magnetic field based on the Kp index (a mid-latitude index of magnetic disturbance that tends to correlate with auroral activity.)

The T96 model [Tsyganenko 1995] uses Dst (or Sym-H) and OMNI solar wind density, speed, and, IMF and returns model values that assume the current state of the magnetosphere is immediately determined by the solarwind conditions, i.e. that the history of the parameters is not important. This model generally represents the inner magnetosphere as overstretched [Tsyganenko 2002], though suitable for representing the tail field.

The T01 model [Tsyganenko 2002] is specifically a model of the near magnetosphere $|X| \leq 15\ R_E$. To address the overstretching of the inner magnetosphere in the T96 model, this model includes an asymmetric ring current and field aligned closure currents that are adjusted in spatial location in response to the input parameters. This model also includes the previous hour of history of the solar wind parameters to take into account the finite response time of the magnetosphere to the solar wind drivers.

The T04s model [Tsyganenko and Sitnov; 2005] is specifically an inner magnetosphere storm (Dst ≤ -65 nT) model that parameterizes the response of the various magnetospheric current systems according to parameters calculated from the solar wind conditions and SYM-H from the start of the storm.

In this thesis the Tsyganenko 2001 field model is used to trace the magnetic field from the position of the Polar spacecraft to the ionosphere. This choice allows for a reasonable storm time mapping in the inner magnetosphere while maintaining comparability to quiet times and recovery phases.

3.9 The requisite spacecraft and probe properties for the electric field experiment

The electric field in space plasmas can be determined in two dimensions from the potential difference between pairs of current biased spherical probes deployed on the ends of wire booms [Figure 3.8]. Often two orthogonally pairs of such electric field booms are centripetally deployed in the spacecraft spin plan; held in place by the centripetal force. On some spacecraft, such as Polar, a third pair of probes is deployed along the spin axis, these are mounted on shorter, rigid booms. The following sections of this chapter will discuss important aspects needed with this measurement technique to

minimize spurious electric field measurements.

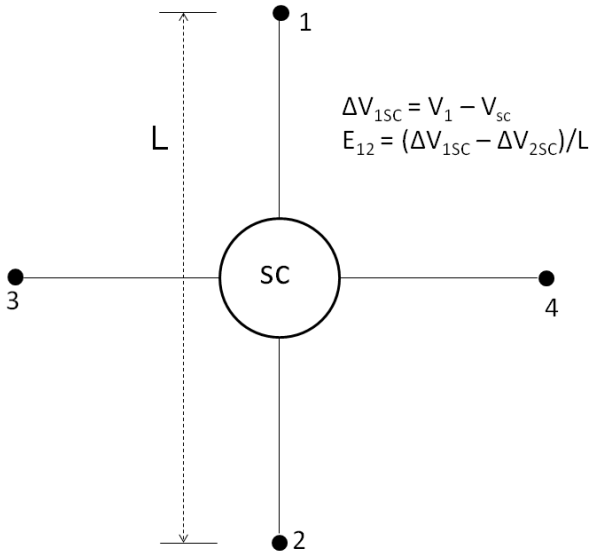

Figure 3.8 The Electric field is determined from the potential difference between pairs of spherical probes deployed at the ends of booms, with separations of distance L.

3.9.1 Shaded Object in Plasma

An object immersed in plasma with ion and electron temperatures of T_i and T_e, respectively, will be impacted upon by incident ions and electrons [Figure 3.9] moving with corresponding thermal speeds of $v_i = \sqrt{kT_i/M_i}$ and $v_e = \sqrt{kT_e/m_e}$ respectively,

where k is Boltzmann's constant, and $M_i(m_e)$ is the mass of an ion (electron).

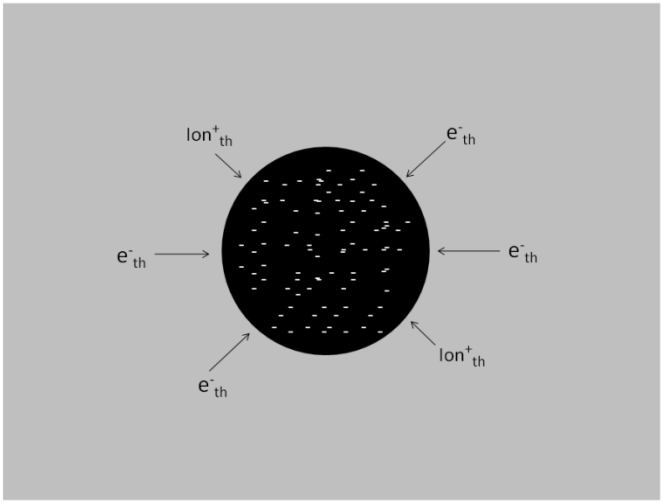

Figure 3.9: A Sphere in plasma with no solar illumination. The thermal electrons and ion from the plasma are incident upon it. Since the electrons are at least 42 times as fast as the ions, v= $(kT/m)^{1/2}$ the sphere charges up negative, and reaches equilibrium when the decreasing electron current is balanced by the approximately constant ion current.

Before it has accumulated a significant charge the initial electron and ion thermal current magnitudes to the object are given by $I_{i,th0} = Aenv_i$ and $I_{e,th0} = Aenv_e$, respectively, where A is the surface area of the object, e is the fundamental unit of charge, and $n = n_i = n_e$ is the number density of the ions and electrons. Assuming a hydrogen plasma in which electrons and ions have the same temperature, $T_i = T_e$, the initial magnitudes of the electron thermal current will be about 42 times that of the ions $I_{eth}/I_{ith} = v_e/v_i = \sqrt{M_i/m_e} = 42$. This results in an accumulation of negative charge on the object. The object will continue to charge negative until it reaches an equilibrium in which it has a sufficiently large negative charge so that only the higher energy

electrons (i.e. those in the Maxwellian tail) can overcome the potential and reach it. Under this condition the plasma electron thermal current is given by

$$I_{e,th} = Aen\sqrt{\frac{kT_e}{m_e}}\exp\left(\frac{V}{V_{e,th}}\right) = I_{e,th0}\exp\left(\frac{V}{V_{e,th}}\right) \quad (3.1)$$

where $V_{e,th} = kT_e/e$ and V is negative. As the potential decreases (becoming more negative), the electron current decreases to the point where it is balanced by the ion current. Because the ions do not have to overcome a repulsive potential, the ion current remains approximately constant as long as the Debye length is not large relative to the size of the object, and the potential of the probe is small compared to the ion temperature, i.e. $|V| \ll kT_i/e$. Under these approximations, the ion current from the plasma to probe of potential V is approximately constant and given by

$$I_{i,th} = Aenv_i = I_{i,th0} \quad (3.2).$$

The current equilibrium condition is $-I_{e,th} + I_{i,th} = 0$, with positive currents defined as currents to the object. The equilibrium expression written with (3.1) and (3.2) becomes

$$I_{i,th} - I_{e,th0}\exp\left(\frac{V}{V_{e,th}}\right) = 0 \qquad (3.3)$$

The equilibrium potential of the object, V, can be found to be:

$$V = V_{e,th}Ln\left(\sqrt{\frac{m_e}{M_i}}\right) \quad (3.4)$$

For a pure Hydrogen plasma, (3.4) becomes

$$V = V_{e,th} Ln\left(\frac{1}{42}\right) \approx -3.75 V_{e,th}$$

A shaded object in the magnetosphere can charge to a potential anywhere from -4 to -4000 volts, depending on the electron temperature, which can vary from 11,600K (~1 eV) in the ionosphere and plasmasphere to 1.16×10^7K (~ 1000 eV) in the plasma sheet.

3.9.2 Conducting Sunlit Probe in Tenuous Plasma

The above considerations were for the case of a shaded object in plasma. However, spacecraft are typically exposed to sunlight. Except when in a dense plasma, an isolated conductor in sunlight will charge positive, with the photoelectrons ejected from the conductor's surface dominating the negative electron thermal current to the conductor [Figure 3.10]

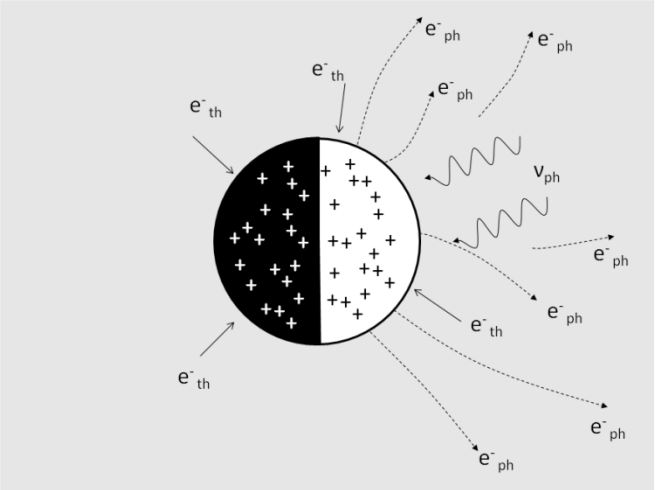

.

Figure 3.10: A conducting sphere in plasma illuminated by sunlight charges positive due to the photo electric emissions that (typically) dominate thermal electron currents.

The expression for the photoelectron current, I_{ph}, from a conductor in sunlit plasma is

$$I_{ph} = A_p I_0 \exp\left(-\frac{V}{V_0}\right) \quad (3.5)$$

where A_p is the projection of the surface area of the conductor on the plane perpendicular to the sun-spacecraft line, $I_0 = 1.5\text{x}10^{-9}$ Amp/cm^2 (at about 1 AU), and $V_0 = 1$ volt is the e-folding value. [Mozer, 1973]

The currents that are significant for an isolated conducting object in tenuous sunlit plasma are the photoelectric current and the plasma thermal electron current. If the conductor is not an isolated object, but a probe electrically coupled to a spacecraft, a current between the probe and spacecraft electronics, I_B, may be important as well. For a small bias current, the probe will charge positive since the photo current is larger than that of the electron thermal current. The ions are repelled by the positive potential and being much slower that the thermal electrons, contribute negligibly to the current. In this case the electron thermal current becomes $I_{eth} = Aen\sqrt{kT/m_e}$, again assuming that either the Debye length is small compared to the probe size, or that the probe potential is small compared to the electron temperature, i.e. $V_{eth} \gg V$. The current continuity equation for this condition is

$$A_p I_0 \exp\left(-\frac{V}{V_0}\right) - I_{eth} - I_B = 0 \quad (3.6)$$

From (3.6) we solve for the potential V. We obtain the expression:

$$V = -V_0 Ln\left[\frac{I_{eth}+I_B}{I_{ph0}}\right] \quad (3.7)$$

,where $I_{ph0} = A_p I_0$

Typical values for this potential in various of the plasma environments found in the magnetosphere, for a 4 inch diameter probe with bias current $I_B = 0$ range from +0.5 volts for the cold dense plasma of the plasmasphere to +8 volts for the warmer and more tenuous plasmas [Mozer et al. 1972] such as in the plasma sheet. Adjusting the bias

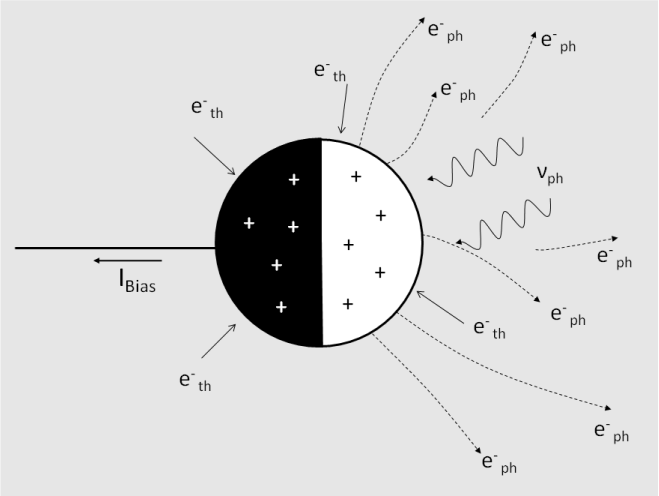

Figure 3.11: The probe in sunlight, thus with a photoelectric current, also with a bias current, and plasma electron current. The bias current can be adjusted to reduce the probe potential.

current allows the probe potential to be adjusted.

3.9.3 Sheath Impedance

The charged probe will polarize the plasma in its immediate vicinity forming a sheath around it. For an isolated probe ($I_B = 0$) in current equilibrium, net current through the sheath between the probe and neutral plasma will be zero. In the case of a current biased probe, a net current will flow through the sheath between the plasma and probe, and this

current, when the probe is in equilibrium, is equal in magnitude to that of the bias current flowing between the probe and spacecraft. Varying the bias current produces a change in the potential difference between probe and plasma, and can be seen by inspecting equation 3.7. The sheath around the probe thus has an effective impedance, $\partial V/\partial I$ that depends on the bias current.

The sheath impedance of the probe as a function of potential, V, is found by taking the derivative $\partial/\partial I_B$ of the current continuity equation (3.6), and solving for $\partial V/\partial I_B$ from which we obtain:

$$\frac{\partial V}{\partial I_B} = \frac{V_0}{I_{ph0}} \exp\left(\frac{V}{V_0}\right) \quad (3.8)$$

To express the sheath impedance in terms of currents, (3.7) is inserted into (3.8) and we obtain:

$$\frac{\partial V}{\partial I_B} = \frac{V_0}{I_{eth}+I_B} \quad (3.9)$$

The sheath impedance can be decreased by increasing the bias current form the probe.

Typical values for the sheath impedance for a 4 inch diameter probe in sunlight range from 10^7 ohms to 10^{10} Ohms [Mozer et al., 1972].

3.9.4 Importance of the Bias Current

The effect of current biasing on the probe is to reduce the sheath impedance $R_{sheath} = \partial V/\partial I_B$ and bring the probe to a potential closer to that of the nearby plasma. This is desirable because the sheath impedance and the input resistance, R_i, of the probe electronics together form a voltage divider [Figure 3.12]. In the case where $R_{sheath} > R_i$, a

significant drop in the potential occurs across the sheath whereas if $R_i >> R_{sheath}$, then the potential drop across R_i is close to that of the plasma potential.

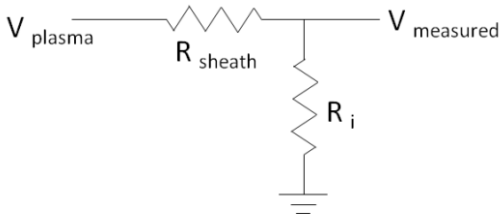

Figure 3.12: The sheath impedance around the probe, R sheath, and the internal resistance of the probe circuit function together to form a voltage divider, so that the measured voltage is $V_{measured} = V_{plasma}\left(\frac{R_{sheath}}{R_i} + 1\right)$ is close the plasma potential $V_{measured} \approx V_{plasma}$ when $R_{sheath} \ll R_i$.

To deliver the bias current, the probes contain a circuit the function of which is to act as a follower. In its simplest form, a follower is an operational amplifier with the output tied into the inverting input [Fig. 3.13]. An ideal follower has a gain of unity, and draws no current from the inputs. Thus in Figure 3.13 the output is the same potential as the probe. The bias resistor, R_B, connected across the probe and the negative potential referenced to the follower's output. The bias resistor thus has a lower potential on the side opposite that connected to the probe, and so the bias current $I_B = V_B/R_B$ flows from the probe,

making it less positive.

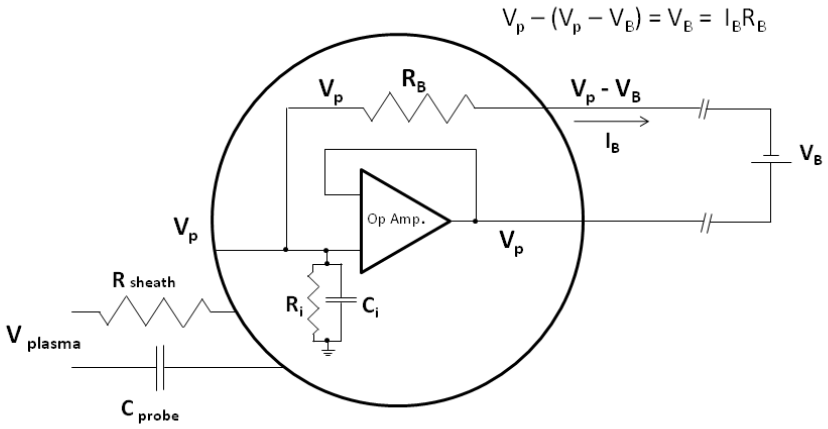

Figure 3.13: The probe (circle) with essentials of the internal circuitry represented; where V_p is the probe potential, R_i and C_i are the internal resistance and capacitance respectively, R_B, V_B, and I_B are the bias resistance, bias voltage, and bias current respectively. The sheath impedance R_{sheath}, and probe capacitance C_{probe}, are represented with electronic schematic symbols.

3.9.5 Importance of using Spherical Probes

In addition to being current biased, accurate measurement of the electric field in tenuous plasma also requires spherical (as opposed to cylindrical) probes. The spherical geometry benefits from being symmetric under any rotation, so that regardless of how the probe is rotated it has a constant projected surface area facing the sun, resulting in constant photocurrent to the probe. By contrast, a cylindrical probe will have an exposed

surface area that depends on the angle of the spacecraft rotation resulting in a variable photocurrent. The variation of the photocurrent with spacecraft rotation will cause the cylindrical probe's potential to vary. Even a small misalignment between two opposite cylindrical probes would cause them to have different areas exposed to sunlight, and thus to have different potentials, resulting in a spurious electric field [Mozer et al., 1972]. This spurious signal would vary with rotation, and it would be impossible to completely subtract off.

Using the current continuity expressions (3.6) for sunlit probes in tenuous plasmas, and the geometry shown in Figure 3.14, we can estimate the spurious electric field due to the misalignment.

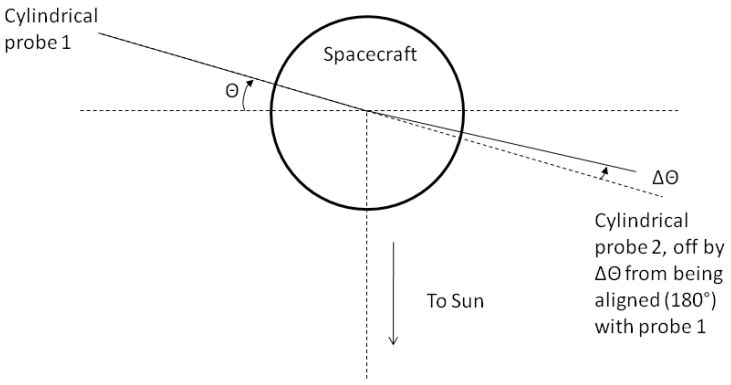

Figure 3.14: Spacecraft with cylindrical probes which are slightly misaligned from being 180 degrees from one another by an angle $\Delta\theta$

The current continuity expressions for probe 1 and 2, are respectively

$$A_{p1} I_0 \exp\left(-\frac{V_1}{V_0}\right) - A_1 e n_e \sqrt{\frac{kT_e}{m_e}} - I_{B1} = 0$$

$$A_{p2} I_0 \exp\left(-\frac{V_2}{V_0}\right) - A_2 e n_e \sqrt{\frac{kT_e}{m_e}} - I_{B2} = 0$$

Where $A_{p1,2}$ are the areas projected on the plane perpendicular to the sun spacecraft direction. Since the probes would be of the same construction, the total surface areas are equal $A_1 = A_2$, and have the same bias current, $I_{B1} = I_{B2}$, taking the difference of these two equations yields

$A_{p1} I_0 \exp\left(-\frac{V_1}{V_0}\right) - A_{p2} I_0 \exp\left(-\frac{V_2}{V_0}\right) = 0$ which can be expressed as

$$V_2 - V_1 = V_0 Ln\left[\frac{A_{p2}}{A_{p1}}\right] \quad (3.10)$$

From equation 3.10 it is apparent that if the sensors are spherical, then regardless of the orientation $A_{p1} = A_{p2}$, and so $V_2 - V_1 = 0$. But in the case of cylindrical probes, A_{p1} and A_{p2} do vary with the angle of the spacecraft rotation, θ. In this case, $A_{p1} = A\cos(\theta)$ and

$$A_{p2} = A\cos(\theta - \Delta\theta) = A[\cos(\theta)\cos(\Delta\theta) + \sin(\theta)\sin(\Delta\theta)]$$

where θ is the angle between probe 1 and the line perpendicular to the sun spacecraft line and Δθ is the amount by which probe 2 is displaced from being 180 degrees opposite

probe 1. A_{p2} is approximated as $A_{p2} \approx A[\cos(\theta) + \Delta\theta \sin(\theta)]$ where the approximation for small angles, $\sin(\Delta\theta) \approx \Delta\theta$, and $\cos(\Delta\theta) \approx 1$ are used. Where A in this case is the exposed area of probe 1 when $\theta = 0$. The ratio A_{p2}/A_{p1} then becomes $A_{p2}/A_{p1} \approx 1 + \Delta\theta \tan(\theta)$. Using this result in 3.10 the potential difference caused by cylindrical probes misaligned by a small angle $\Delta\theta$ is

$$V_2 - V_1 \approx V_0 Ln[1 + \Delta\theta \tan(\theta)] \quad (3.11)$$

Thus, the spurious potential difference can become large for angles near $\approx (n + 1/2)\pi$. At times in the rotation when $-1 < \Delta\theta \tan(\theta) \leq 1$ the approximation $Ln(1 + x) \approx x$ for -1 < x ≤ 1 can be used and (15) can be written as $V_2 - V_1 \approx V_0 \Delta\theta \tan(\theta)$, in agreement with Mozer et al [1972].

3.9.6 Probe Sensor should have Uniform Work Function

The probe surface and the top of the Fermi Sea of electrons inside the probe material differ in potential by the work function, typically a few eV for metals. Thus the probe material's work function, W, is among the potential differences that an electron crosses when passing between the plasma to the probe/spacecraft electronics. The potential drop due to the work function on one of the probe pair members is offset by that of the opposite probe if the work functions are equal. Unless the probes have the same work functions, a spurious electric field $E_{sp} \approx W_1 - W_2/L$, will be present. If both probes had uniform but different valued work functions, then this error would simply be a DC

offset which could be subtracted from the data. Non-uniform work functions pose the difficulty that the potential difference will vary depending what part of the probe is being illuminated by the sunlight, which changes as the spacecraft rotates. For this reason metals make poor probe materials as their lattice structure causes them to have anisotropic work functions [Pedersen and Lybekk, online reference]. Vitreous carbon, an amorphous carbon substance, is a material with the desired properties [Mozer 1972].

3.9.7 Conducting Spacecraft

As discussed above, an object immersed in tenuous plasma and illuminated by sunlight will charge positive on the illuminated surface due to the photoemission of electrons. If the object is a conductor, a uniform charge will be established with electrons from the shaded side of the object flowing to the illuminated side. If the object is an insulator, the electrons are inhibited from flowing to the sunlit side, and the shaded side of the body will charge to a negative potential because of the incident plasma electrons. Shaded surfaces tend to charge to large negative potentials on the order of ~-1000 V, in the magnetosphere, whereas the positive sunlit surfaces tend to charge to only a few volts positive. An insulating spacecraft will thus have a potential difference on the order of a thousand volts negative between the sunlit and shaded sides. Except for when the spin axis is along the spacecraft-sun line, a large electric field asymmetric with respect to the four spin plane booms will surround the spacecraft. This electric field is large in comparison to those present in the absence of the spacecraft. This large asymmetric electric field makes measurements of the electric field impossible since it dominates the actual electric field in space and saturates the probes pre amplifiers.

3.9.8 Probe booms must be long compared with spacecraft size

A spherical conductor placed in a uniform electric field, in vacuum, will develop a dipolar perturbation electric field aligned with the imposed electric field. As a result, the potential difference between two points, e.g. two probes, ΔV, along this direction separated by distance L, on opposites sides and equidistant from the sphere, will be

$$\Delta V = E_0 L(1 - (r/0.5L)^3) \quad (3.12)$$

where E_0 is the background electric field. When r<<L, the potential difference is $\Delta V = E_o L$ as it is in the absence of the spacecraft. In dense plasma with Debye length small compared to the spacecraft size, the screening of the plasma tends to reduce this spurious field more. The expression for finite Debye length is

$$\frac{\Delta V}{E_0 L} = 1 - \frac{(0.5L+\lambda_D)r^3}{(r+\lambda_D)(0.5L)^3} \exp\left(\left|\frac{r-0.5L}{\lambda_D}\right|\right) \quad (3.13) \quad \text{[Mozer et al. 1972]}$$

where λ_D is the Debye length.

The conducting booms of the spacecraft will partially short out the ambient electric field. This effect will be most pronounced in tenuous plasma. This effect was first investigated by Mozer et al. [1972] theoretically and empirically by Pedersen et al [1984] with data from the ISEE-1 spacecraft. Pedersen determined that the relation between the measured and actual electric field is $E_m/E = 0.65$ where E_m and E are the measured and actual electric field. Thus for ISEE-1 data, the electric field must be multiplied by 1.54 to get the correct value. For the Polar spacecraft, the measured electric field must be corrected by a factor of 1.3 [Wygant et al., 2002]

3.9.9 Spacecraft Relatively Symmetric with Respect to Booms

Large asymmetries in the spacecraft body can result in asymmetries in the electric potential of the charged spacecraft at the location of the probes. To estimate this, consider a spherical object of radius R_o mounted a distance x from the center of the spacecraft along the line of one of the boom pairs [Figure 3.15].

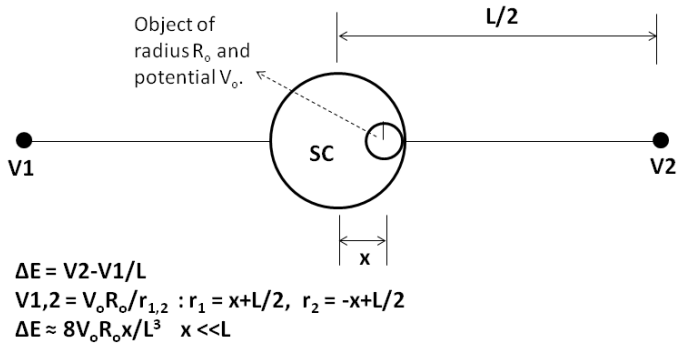

Figure 3.15: A spacecraft with an asymmetrical object of Radius R_o and potential V_o that is located a distance x from the center of the spacecraft. The spurious electric field ΔE determined from the potential difference between V1 and V2 due to asymmetrical object is calculated.

The spacecraft has electric field probe booms of length L/2 from the spacecraft center. For x<<L, the spurious electric field this will produce when the object is charged to a

potential V_o is $\Delta E \approx V_0 R_0 x/(0.5L)^3$. To ensure that $\Delta E < 0.1$mV/m, we consider the object charged up to a positive potential of $V_o = 10$ volts and located at the edge of the spacecraft, about x = 1.5 meters, then for a typical boom length of L/2 = 50 m we find that $R_o < 0.83$ meters. The object would have to be of a size on the order of the spacecraft to create significant spurious electric field measurements. Thus an approximately symmetric spacecraft should have a sufficiently symmetric field at the distance of the probes so as to not result in a significant spurious contribution to the measured electric field.

3.9.10 Summary of electric field instrument properties

In summary, the properties that the probes/spacecraft must have in order to be able to accurately measure the electric field in a tenuous space plasma are:

1.) The probes must be current biased

2.) The probes must be spherical,

3.) The probes must consist of a material with a uniform work function.

4.) The spacecraft and the boom system must be conducting

5.) The spacecraft must be approximately symmetric

6.) The boom length must be long relative the spacecraft body.

The above attributes are necessary to avoid spurious electric field signals.

Chapter 4

Observations of the Alfvénic Poynting flux at high altitudes; comparison to low altitude electron kinetic energy flux, auroral images, and evolution during geomagnetic storms

4.1 Introduction

This chapter consists of three different analyses. First, we present two comparisons, one from the May 2, 1998 storm and the other from the October 22, 2001 storm, between high altitude (Polar, ~2-9 R_E), earthward Alfvén wave (5.5-166 mHz, or 6 – 180 sec.) Poynting flux mapped to 100km, and low altitude (DMSP at ~850 km and FAST, between 1200-1800 km for both events) earthward, mapped, electron kinetic energy flux. We compare the intensities and integrated values of the Poynting flux to those of the electron kinetic energy flux, and to electron beam intensities inferred from Polar UVI auroral images. Second, we compare the integrated wave Poynting flux to the integrated electron kinetic energy flux for three different levels of geomagnetic activity during October 2001. Third, we investigate the evolution of the intensity of the night-side (18 – 6 MLT), high altitude (Polar) field-aligned Poynting flux being carried earthward by waves with a strong Alfvénic component on middle and low latitude field lines over the course of two major geomagnetic storms; one storm from May 1998, and the other from October 2001. The evolution of the Poynting flux intensity as a function of time and latitude is compared to the evolution of the night side, low altitude (FAST and DMSP)

earthward electron kinetic energy flux in the ~3 eV – ~30 keV range. Both the peak and averaged mapped intensities (per 0.5^o latitude) for the Poynting flux and electron kinetic energy flux are examined. This is the first study that simultaneously looks at the evolution of the high altitude Poynting flux and low altitude electron kinetic energy flux during major storms. Previous research, described in chapter 2, mainly focused either on short timescale (~minutes to tens of minutes) spacecraft conjunctions, or on much longer time scale (months to years) statistics. Further, the previous studies focused on higher latitude Poynting flux, typically at the PSBL. In this study we focus on the low latitude ($<65^o$ ILAT) regions. In addition, in contrast to earlier studies that inferred the possible role of Alfvénic Poynting flux from the observed electron spectra, we directly measure the Poynting flux at high altitudes. The role Alfvén waves play in the transport of energy into and within the inner magnetosphere, particularly when it is perturbed, is not yet understood. A detailed observational picture is important for understanding low latitude auroral physics, and inner magnetosphere processes.

4.2 Data Sets and Methodology

The electric and magnetic field data used in the calculation of Poynting flux are from the electric field instrument (EFI) and fluxgate magnetometer (MFE) on the Polar spacecraft described above (chapter 3). For the longer interval storm evolution study we use electric field data that has been spin fit from the longer pair of spin plane booms on Polar and has a cadence of 6 seconds. The electric field has also had the **V**x**B** field subtracted and has been antenna length adjusted. The calculation of the Poynting vector uses all three components of the magnetic field and only the two electric field components in the spin

plane. In this study, the exclusion of the third component of the electric field, along the spin axis, has minimal effect on the Poynting vector, as the electric fields associated with the waves of interest are mainly in the spacecraft spin plane [Wygant et al 2000; 2002]. This can also be seen by the fact that calculations using the spin plane and measured spin axis components yield nearly identical results to those using only the spin plane field. The magnetic field used in the calculation of the Poynting vector has had a model field subtracted. Note that the full magnetic field vector is used in determining the field aligned direction. The wave fields are calculated by subtracting a 180 second running averaged field from the original electric and model subtracted magnetic fields data to remove the slower variations, and then taking a 6 seconds running average of this difference to remove the faster variations; e.g. $\delta E = < E - < E >_{180\text{sec}} >_{6\text{sec}}$ where the < > brackets refer to running average of the enclosed quantity, over time interval indicated by the subscript. Inspection of a broader frequency range extending into higher frequencies indicates that the 6-180 second waves are the dominate energy carrier. The field aligned Poynting flux is then calculated as $\boldsymbol{S} = \delta \boldsymbol{E} \times \delta \boldsymbol{B}/\mu_o$ and $S_{\|} = \boldsymbol{S} \cdot \widehat{\boldsymbol{B}}$. The sign of the field aligned Poynting flux is determined such that positive values are always earthward. In the north hemisphere the positive earthward value come directly from the dot product of the Poynting vector **S** into the magnetic field **B**, since the field is earthward there. In the southern hemisphere, (ILAT and MLAT<0) the dot product of **S** into **B** yields a negative value for earthward Poynting flux since the field lines are pointed away from earth. As a result, when mapping to the southern hemisphere we multiply the field aligned Poynting flux by -1 so that in both hemispheres positive values of $S_{\|}$ refer to

downward or earthward. The resulting Poynting flux is rescaled to common reference altitude of 100 km at the ionospheric foot point. The magnetic foot point of Polar is determined from field line tracing of the Tsyganenko 2001model field from the location of Polar to the ionosphere. The magnetic field strength at the ionosphere is then estimated from a simple dipole model. The expression for determining the mapped Poynting flux magnitude is $S_{\parallel_{100km}} = S_{\parallel_{insitu}}(B_{100km}/B_{insitu})$; this relation comes about because of the conservation of magnetic flux along a converging flux tube, the fact that the field aligned Alfvénic Poynting flux follows the field line, and the conservation of energy.

The FAST electron kinetic energy flux presented herein is the net downward kinetic energy flux per spin period (~5 sec.) and has been mapped to an altitude of 100 km.

The DMSP electron kinetic energy flux is at 1 second cadence and only represents the downward electrons, as the SSJ/4 instrument cannot observe upward particles. The DMSP electron kinetic energy flux are converted from units of energy flux per stradian by multiplying by a solid angle pi, which corresponds to the typical loss cone of ~56^{o} at DMSP altitudes. Since DMSP does not have pitch angle resolution, this calculation assumes homogeneous distribution in pitch angle.

4.3 Comparison of the high altitude Poynting flux at Polar to low altitude electron kinetic energy flux at DMSP and FAST, and to UVI images, on May 2 1998 and October 22, 2001

In this section we present two examples of Polar, FAST, and DMSP data, the first from May 2, 1998 during a moderate storm, Dst ~ -60 nT, and the second during the major storm on October 22, 2001, Dst ~-130 nT. For each of these events we will be looking at the Polar wave electric and magnetic fields (5.5-166 mHz, or 6 – 180 sec.), the corresponding field-aligned wave Poynting flux (mapped to 100 km), the Poynting flux integrated along the mapped spacecraft trajectory, and the electron differential energy flux as an indicator of the space plasma environment (i.e. whether Polar is in the lobe or plasma sheet). Polar is at high altitudes; 3-6 R_E (geocentric) in the May 2, 1998 example and ~9 R_E (geocentric) for the October 22, 2001 example. For these two examples we also present the DMSP and FAST measured electron kinetic energy flux (mapped to 100 km), integrated electron kinetic energy flux, and the downward differential electron energy flux, during the passage through the auroral region that is closest in time to the respective Polar example. DMSP and FAST are at low altitudes; DMSP is at ~850 km, and FAST is at altitudes of ~1200km-1800km for both examples. We will compare the Poynting flux intensity and integrated value thereof to those of the DMSP and FAST electron kinetic energy flux. We also present the UVI auroral image closest in time to the observation of the intense Poynting flux observed at Polar for each event. The UV intensity of the auroral images is a proxy for the electron energy deposited in the ionosphere and the portion of the image along Polar's foot point will be compared energetically to the mapped Poynting flux.

4.3.1 Comparison of the Poynting flux at Polar to the electron kinetic energy flux at DMSP and FAST, and a UVI image, on May 2, 1998 for a single night side pass

In this section we compare the Polar Poynting flux to DMSP and FAST electron kinetic energy flux on May 2, 1998 for a single night side pass. DMSP and FAST spacecraft are each separated from Polar by about 2 to 4 hours in magnetic local time. Figure 4.1 shows the relative locations of the Polar (red trace), DMSP F12 (green trace), and FAST (blue trace) mapped foot point trajectories for this event.

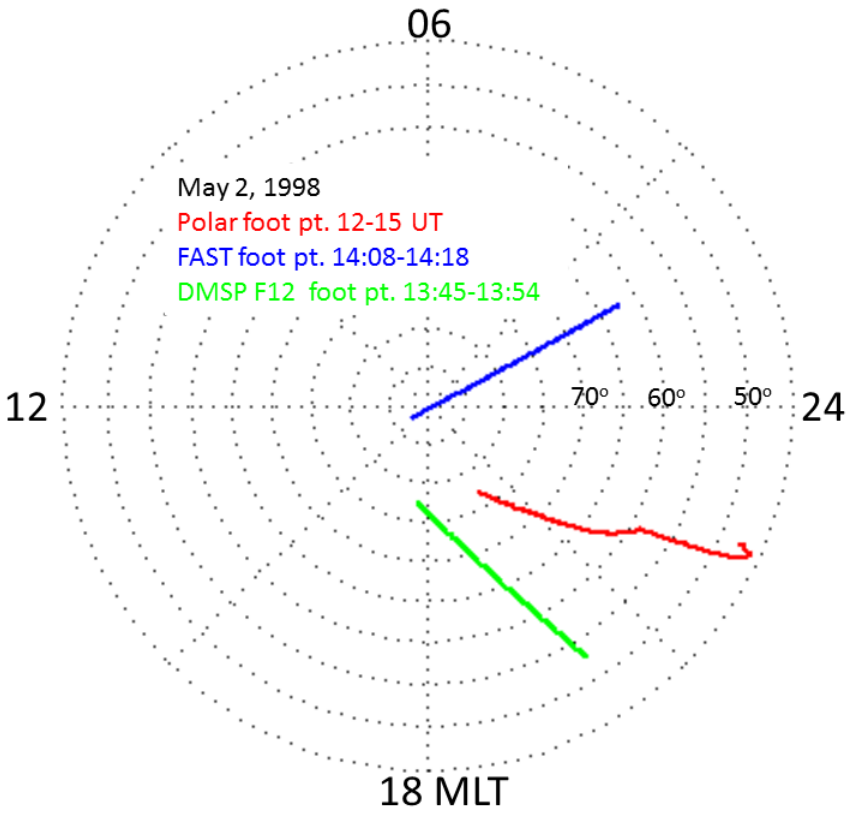

Figure 4.1 The mapped foot points of Polar (red, 12:00 to 15:00 UT), DMSP F12 (greed, 13:45-13:54 UT), and FAST (blue, 1408 to 14:18 UT) on May 2, 1998 in MLT and ILAT. The spacecraft are separated by a few hours in MLT. Polar observes intense Poynting flux at ~13:26 UT and DMSP F12 passes through the same latitude ~ 30 minutes later, and observes intense electron kinetic energy flux. FAST passes through

the same latitude where the intense Poynting flux occur about 45 minutes after Polar and 20 minutes after DMSP, and observed intense electron kinetic energy flux.

Figure 4.2 shows ~2 hours of Polar wave electric and magnetic fields, field aligned Poynting flux, Poynting flux integrated along the spacecraft trajectory and electron differential energy flux on May 2, 1998 during moderate storm activity, Dst ~-60 nT (and decreasing), on the night side. The wave electric field in Figure 4.2(a) is the perpendicular component in the spin plane, with positive values corresponding to ~-**z** gsm direction, detrended to retain fluctuation in the 6-180 second range. The wave magnetic field shown in Figure 4.2(b) is along the spin axis (~ **y** gsm) and is perpendicular to the electric field, and approximately perpendicular to the background magnetic field. The magnetic field is also detrended to retain fluctuations in the 6-180 second range. Note that while this is the dominant component of the wave magnetic field, for the calculation of the Poynting flux in Figure 4.2(c) all three components of the magnetic field are used. The field aligned wave (5.5-166 mHz, 6-180 sec.) Poynting flux in Figure 4.2(c) has been calculated and mapped to 100 km as described in section 4.2. In Figure 4.2(d) is the field aligned mapped Poynting flux integrated along the mapped spacecraft trajectory using the assumption that the spacecraft velocity is the relevant velocity between the spacecraft and the plasma structure through which the waves propagate. In Figure 4.2(e) is the electron differential energy flux. The electron differential energy flux indicates the plasma environment; from 12:30-13:20 UT Polar is on open field lines in the lobe as indicated by the polar rain electrons with energies $\lesssim$ 500

eV. Then at ~13:25 Polar enters the PSBL, indicated by the sudden (~few minutes) enhancement in the electric differential energy flux by two to three orders of magnitude above energies of ~1keV. There is a period of intense Poynting flux at the PSBL as is commonly observed [Wygant et al 2000, 2002] and another deeper in the plasma sheet at ~13:55 UT, where there is a further enhancement of the electron differential energy flux. This intensification in the electron energy around ~13:55 UT is broadband and suggests that there may be heating and acceleration of electron at altitudes above Polar. In both regions, the Poynting flux is large enough to power visible aurora $S_{\parallel} > 1$ erg/cm^{2}s (mapped). The Poynting flux at the PSBL has a peak intensity of ~40 ergs/cm^{2}s (mapped) and a reflected component which is significantly less than the incident, whereas the Poynting flux deeper in the plasma sheet (14:00 UT /± 10 min), has a peak earthward intensity of ~5 ergs/cm^{2}s, and has distinct periods of both upwards and downwards Poynting flux of similar intensity. This is further supported by the fact that the second interval of Poynting flux, when integrated, Figure 4.2(d), carries only a small net energy whereas the first interval clearly carries net downward energy that must be absorbed or dissipated at lower altitude.

The ratio of electric to magnetic field perturbations, δE/δB, is consistent with Alfvénic fluctuations, that is, they are similar to the Alfvén speed. The δE to δB ratio near 13:25 UT and 14:00 UT is approximately ~ 1500 - 2000 km/s. For Alfvén waves in magnetospheric plasmas the δE to δB ratio is typically between the Alfvén speed for pure hydrogen and pure oxygen plasma due to the presence of both ions. In the present case, based on the field strength and plasma density, the Alfvén speeds for pure hydrogen and

oxygen plasmas are V_{AH+} ~ 6000 km/s and V_{AO+} ~ 1500 km/s respectively. Here the δE to δB ratio suggests oxygen rich plasma. This is also suggested by the TIMAS ion composition data (not shown), which indicates enhancements of O+ ions in the plasma sheet. In addition, there could be some coupling via field aligned currents to the ionosphere, for which the δE to δB ratio is smaller, $\delta E/\delta B \approx 1/\mu_o\Sigma_p$, [Paschmann, et al., 2002]; typically this yields E to B ratios between 80km/s and 800 km/s depending on the ionosphere conductivity.

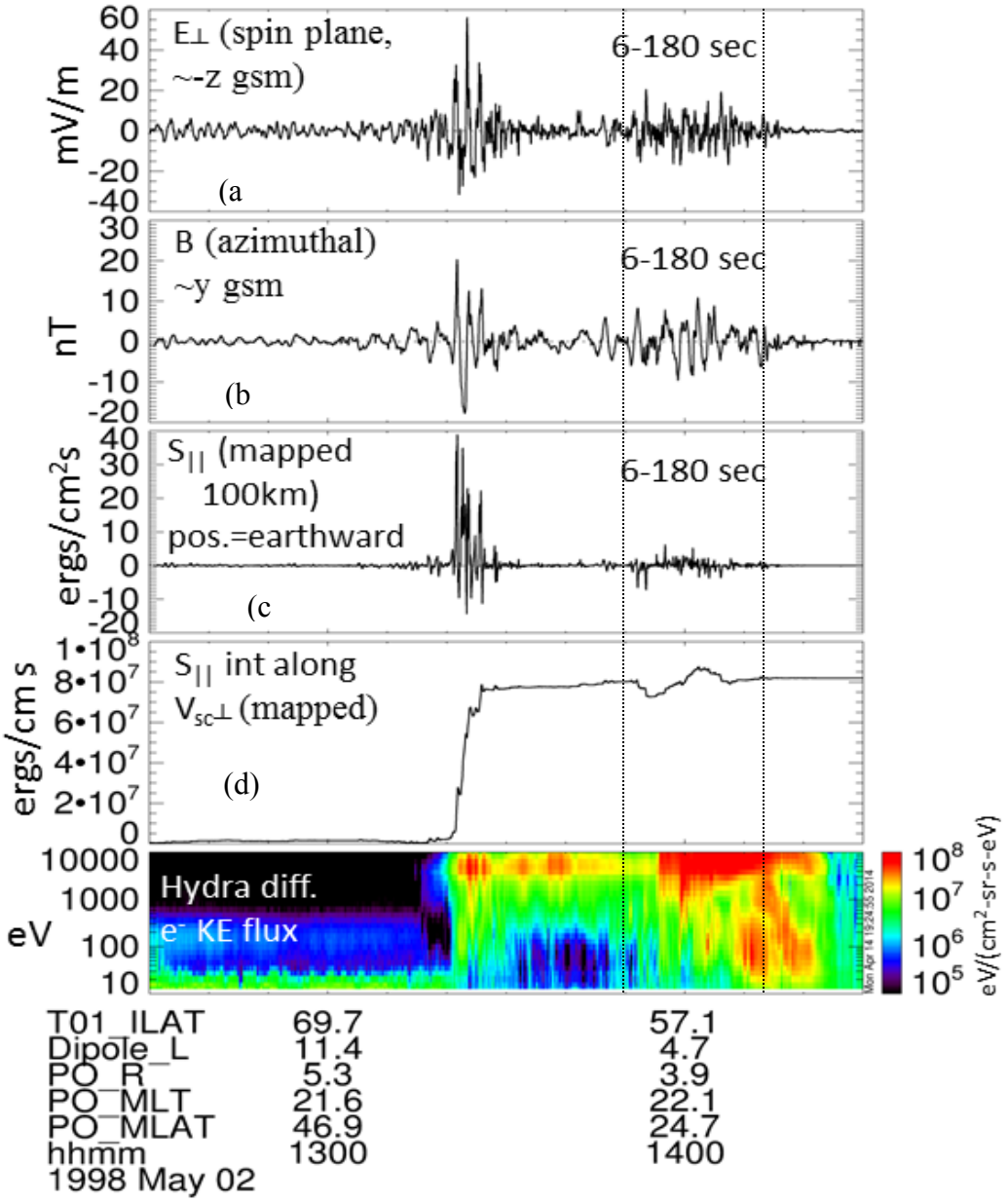

Figure 4.2: Example of a Polar spacecraft pass from the tail lobe, through the plasma sheet boundary layer (PSBL) and plasma sheet to low latitudes during an active period (Dst ~-60 nT, AE ~1000nT) on May 2, 1998. Panel (a) shown the perpendicular electric field in the spin plane for the period range of 6-180 seconds, positive values corrpond to an E field roughly in the negative z gsm direction. In panel (b) is the azimuthal (~y gsm) magnetic wave field, also in the 6-180 second period range. In panel (c) is the corresponding field-aligned Poynting flux, mapped to an altitude of 100 km. The integrated values of the mapped Poynting flux along the mapped spacecraft foot point trajectory are in (d). And in (e) is the electron differential energy flux, indicating the PSBL by a sudden two order of magnitude increase in ≳ 1keV electrons, seen around 13:25 UT. Prior to the encounter of the PSBL the lower fluxes of electrons with energies

≤ 500 eV, the polar rain, indicates that Polar was on open field lines. The two vertical dotted lines indicate times of DMSP F12 (13:50 UT) (left) and FAST (14:12 UT) (right) passes, the electron data from which will be compared to the Polar observation.

Figure 4.3 shows nine minutes of DMSP F12 electron data, during its pass through the auroral region occurring closest in time to the observation of intense Poynting flux at Polar shown in Figure 4.2 as the vertical dashed line (left). Figure 4.3(a) shows the earthward electron kinetic energy flux mapped to 100 km. The electron kinetic energy integrated along the mapped spacecraft trajectory is in Figure 4.3(b), and in Figure 4.3(c) is the electron differential energy flux spectrum. Spectra are consistent with both inverted-V acceleration and wave acceleration can be seen, and the total electron kinetic energy flux contains contributions from each. Note the broad band of lower energy electrons seen around ~13:47:45 UT, may correspond the broad band population of electrons seen at Polar around ~14:10 -14:20 UT in Figure 4.2(d). The intensity of the mapped electron kinetic energy flux in Figure 4.3(b) is ~28 ergs/cm^{2}s, somewhat less than the wave Poynting flux in Figure 4.2(c), however this DMSP pass occurs ~30 minutes after the intense Poynting flux observed on Polar at the PSBL. It is uncertain whether the Poynting flux in Figure 4.2(c) is only present during Polar's observation or is part of a moving structure that passes over Polar and persists long enough for DMSP to traverses the same latitude. We must further consider that the peak electron kinetic energy flux in Figure 4.3(a) is well inside the auroral region at PBSL. The electron kinetic energy flux in the latter region is ~10 ergs/cm^{2}s. The total integrated value of the electron kinetic energy flux in Figure 4.3(b) is 4x10^8 ergs/cm-s. If we assume that the

Poynting flux at Polar persists only at the location where it is observed, and that Polar traverses that whole region with the relative velocity to plasma structure being the spacecraft velocity, then the Poynting flux carries energy at a rate indicated in Figure 4.2(d) of $8x10^7$ ergs/cm-s. This interpretation suggests that the Poynting flux carries about 20% of the energy needed to power the low altitude electron kinetic energy flux at DMSP. Note however that the spacecraft velocity is not necessarily the full velocity between Polar and the plasma structure through which the Poynting flux passes. Because Polar is at high altitudes, the field lines may be expanding over the spacecraft, especially during active storms times. At this altitude, 4-6 Re, Polar has a speed of ~ 4 km/s, while the estimated typical plasma sheet expansion speed is ~ 10-20 km/s [Wygant et al 2000 and references therein]. We can estimate the speed of the plasma sheet by inferring the motion of poleward edge of the aurora in UVI images, and mapping this up to the altitude of Polar. For this event, the poleward edge of the aurora moved poleward 0.5^o ILAT in 19 seconds, corresponding to a velocity of ~2.9 km/s. Mapping this speed to Polar gives an expansion speed of ~27 km/s. So the integral $\int S_{||} V_{sc} dt$ could be ~27/4 times larger or ~6.7 times larger, yielding and integrated Poynting flux ~$5.36x10^8$ ergs/cm-s, or 130% of the low altitude electron kinetic energy flux.

Another possibility is that the Poynting flux exists over a larger spatial region than just at the PSBL. As has been pointed out, even though the most intense Poynting flux typically occurs at the PSBL, it can occur deeper in the plasma sheet as well. It is possible that the wave Poynting flux is simultaneously present throughout a large portion of the near earth tail and plasma sheet during substorm or other active periods, so that the relative motion

between Polar and the plasma structure may not carry the total region of intense Poynting flux past the position of Polar before the wave intensity decreases to quieter levels. In this case the total amount of energy carried by the Poynting flux will be even larger. Such an analysis is discussed in more detail in the next section (4.4).

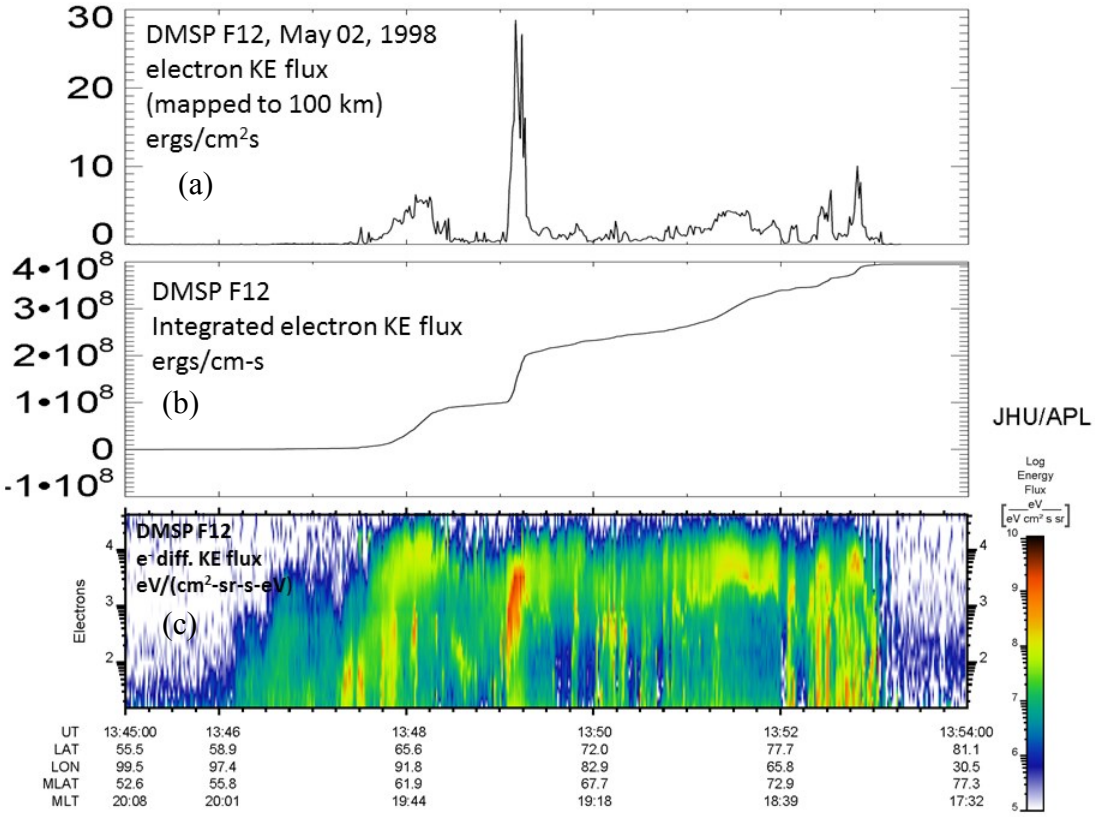

Figure 4.3: DMSP F12 electron data from 13:40 to 14:00 UT on May 2, 1998. From top to bottom is shown the (a) downward electron kinetic energy flux mapped. In (b) is the electron kinetic energy flux integrated along the spacecraft foot point trajectory. In (c) is the differential electron energy flux. Intense electron differential energy flux of the auroral zone is evident between 13:46-13:53 UT, between the latitudes of ~ 56^{o} and 75^{o}. Both broadband and mono-energetic electrons are present (particularly near 13:53 UT, and perhaps 13:49 UT) and contribute to the total overall kinetic energy flux examined here. DMSP measured only the downward electron kinetic energy flux. These data are on a one second cadence.

Figure 4.4 shows ~10 minutes of FAST electron data during a night side pass through the auroral region, that occurred closest in time to the observation of intense Poynting flux at Polar. Figure 4.4(a) shows the electron kinetic energy flux mapped to 100km, Figure 4.4(b) shows the integrated electron kinetic energy flux, mapped, and electron differential energy flux spectrum of the downward electrons is shown in Figure 4.4(c). Both broadband and mono-energetic electrons are present (particularly near 13:53 UT, and perhaps 13:49 UT) and contribute to the total overall kinetic energy flux examined here. Note that DMSP measures only the downward electron kinetic energy flux, and it has been shown by Dombeck et al [2013] that with only the downward measurement, broad band spectra are not definitive evidence of wave acceleration.

The electrons in Figure 4.4 observed at FAST occur ~40 minutes after the Poynting flux observed at Polar and are also separated by about 4 hours in local time. The electron kinetic energy flux, Figure 4.4(a), peaks at an intensity of 6 ergs/cm^{2}s at the low altitude extension of the PSBL (observed just after 14:13 UT). This intensity is about a factor of 6 smaller than the intensity of the Poynting flux observed at the PSBL by Polar 40 minutes earlier. If the Poynting flux at the PSBL does persist for periods longer than the Polar observations, it is quite possible that the intensity will vary over timescales of 40 minutes and so may have weakened. Alternatively, the Poynting flux may have spread out somewhat across field lines; though shear Alfvén waves cannot not do this, kinetic Alfvén waves could. The integrated electron kinetic energy flux in Figure 4.4(b) has a value of 1.2x10^8 ergs/cm-s. This value is smaller than the integrated electron kinetic energy flux at DMSP, Figure 4.3(b) of 4x10^8 ergs/cm-s. The energy carried by the FAST

electron kinetic energy flux, $1.2x10^8$ ergs/cm-s, is similar to that Polar Poynting flux, $8x10^7$ ergs/cm-s; this suggests that the high altitude Poynting flux can account for 67% of the energy carried by the low altitude electrons at FAST.

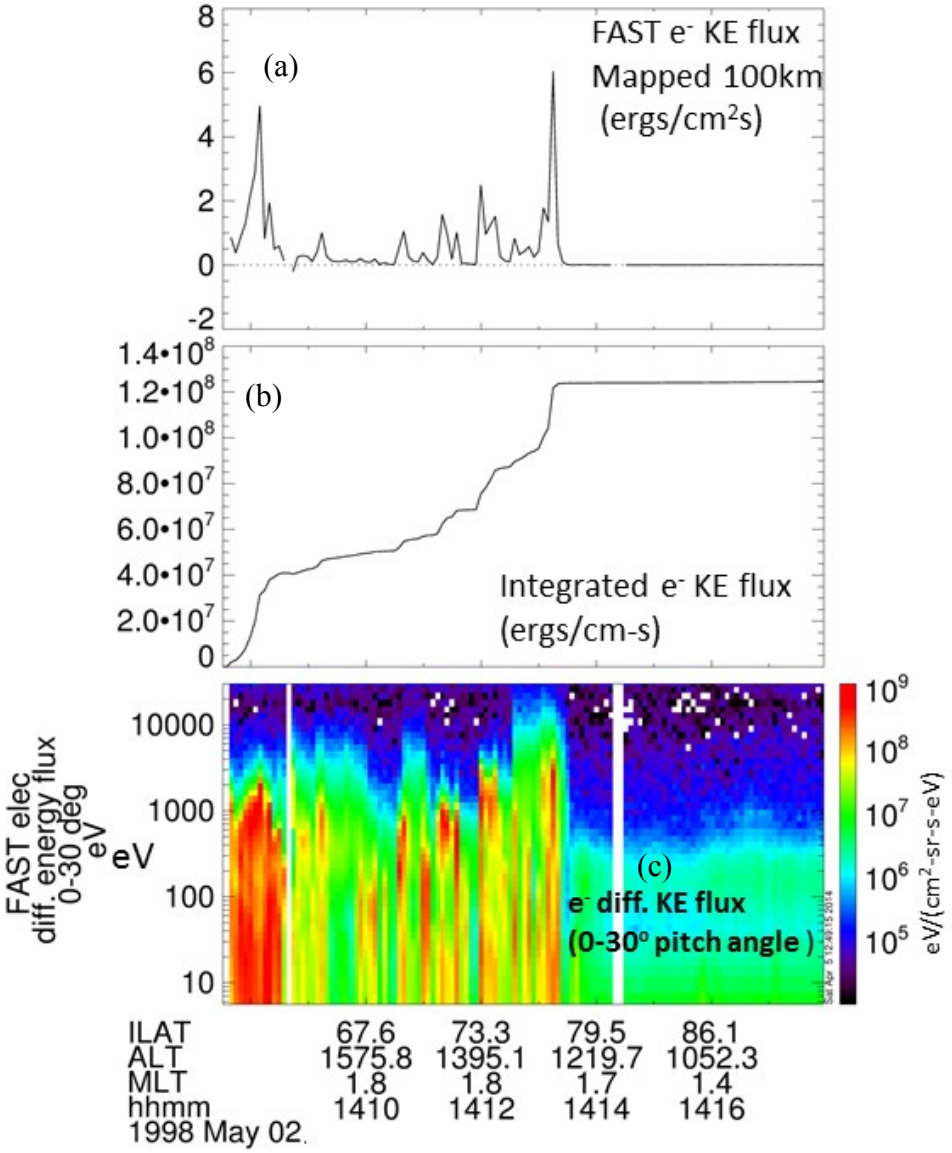

Figure 4.4: Electron data from a 10 minute long pass of the FAST satellite through the night side, post-midnight auroral zone during the May 2, 1998 storm. From top to bottom; (a) is the net earthward electron kinetic energy flux mapped to 100km; at 5

second (spin period resolution), with the energy flux determined by averaging the upward and downward over each spin. (b) the mapped electron energy flux integrated along the spacecraft foot point, and (c) the differential electron kinetic energy flux of the earthward electrons (in 0-30 degree pitch angle). Distributions consistent with both wave and inverted-V acceleration are present and contribute to the overall electron kinetic energy flux. This FAST pass is the one occurring closest in time to the Polar observed intense Poynting flux in Figure 4.2, and is indicated in Figure 4.2 by the vertical dashed line at ~ 14:12 UT.

Figure 4.5 shows the Polar UVI auroral image taken at the time of the in situ observation of intense Poynting flux at Polar. The approximate foot point of Polar's trajectory is shown as the black dashed line. Around the location of Polar's foot point the peak intensity on the scale provided is ~ 70 photons/cm^{2}s, which corresponds to 19 ergs/cm^{2}s. This conversion into erg/cm^{2}s is done by dividing the photon intensity by a factor of 3.7 [Liou et al 1997 and Keiling et al 2003]. The peak intensity suggested by the UVI image is thus about half that of the Poynting flux observed simultaneously at Polar. Integrating the UVI image by multiplying the intensity by the distance across the region of intense UV emissions (dividing this process up into separate intervals for regions of different intensities) yields an integrated energy rate of ~8.1x10^8 ergs/cm-s. The integrated Poynting flux at Polar is 8 x10^7 ergs/cm-s, Figure 4.2(d), using the spacecraft velocity, or 5.36x10^8 ergs/cm-s after this value is adjusted with the estimated plasma sheet expansion speed. Assuming that Polar observed the entire region of Poynting flux, and the relative velocity is the expansion speed, the Poynting flux carries ~66% of the energy in the simultaneously observed aurora. If we assume that the relevant velocity between the plasma structure and Polar is the spacecraft velocity, then the actual fraction of the energy supplied by the Poynting flux is ~10%.

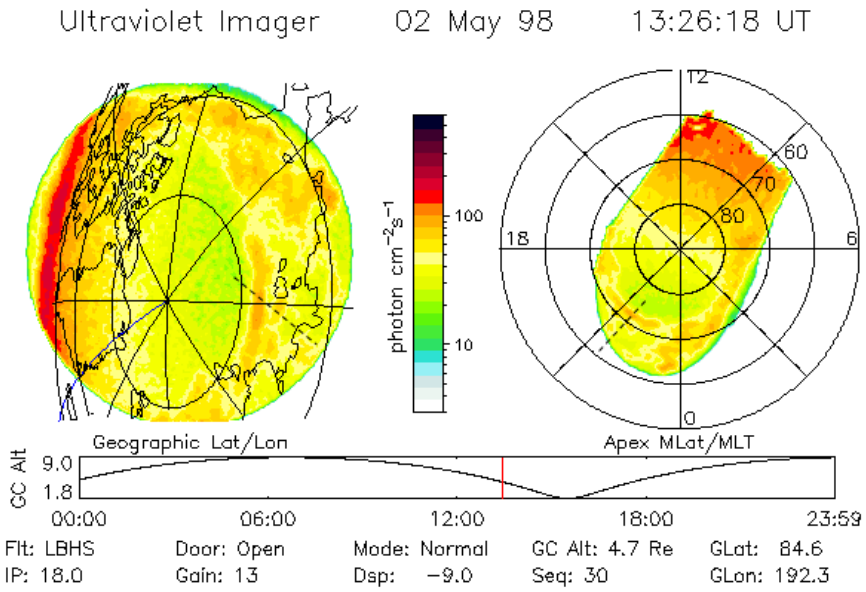

Figurer 4.5: Polar UVI image showing the UV emissions from the ionosphere in both geographic coordinates (left) and MLT-ILAT (right). The photon intensity shown in the color scale can be converted into ergs/cm^{2}s by dividing by 3.7. The black dashed line represents the approximate path of Polar's foot point.

Table 4.1 summarizes the peak values of the Poynting flux and electron kinetic energy flux and the integrated values thereof from this event.

May 2, 1998	Peak intensity	Integrated (mapped)	Time of peak	MLT of S/C
Polar $S_{\|\|}$ (100km)	40 ergs/cm^{2}s	$8x10^7$ ergs/cm-s for V= V_{sc} $5.4x10^8$ ergs/cm-s for V~ V_{PS}	13:22 UT	~22 MLT
DMSP e- KE flux (100 km)	28 ergs/cm^{2}s	$4x10^8$ ergs/cm-s	13:49 UT	~19.3 MLT
FAST e KE flux (100 km)	6 ergs/cm^{2}s	$1.2x10^8$ ergs/cm-s	14:13 UT	1.8 MLT
Polar UVI	~19 ergs/cm^{2}s	~$8.1x10^8$ ergs/cm-s	13:26 UT	~22 MLT

Table 4.1 Summary of the peak intensities of the Polar Poynting flux and DMSP F12 and FAST electron kinetic energy flux, UVI data and their integrated values for the May 2, 1998 example.

4.3.2 Comparison of the Poynting flux at Polar to the electron kinetic energy flux at DMSP and FAST, and a UVI image, on October 22, 2001 for a single night side pass

In this section we compare the Polar Poynting flux to electron kinetic energy flux at DMSP and FAST on October 22, 2001 for a single night side pass. Figure 4.6 shows the relative location of the foot point trajectories for Polar (red trace, 10-12 UT), DMSP F15 (green trace, 10:50 -11:15 UT) and FAST (blue trace, 10:50 – 11:15 UT) for October 22, 2001. Polar is about 1 hour of MLT separated from DMSP and FAST.

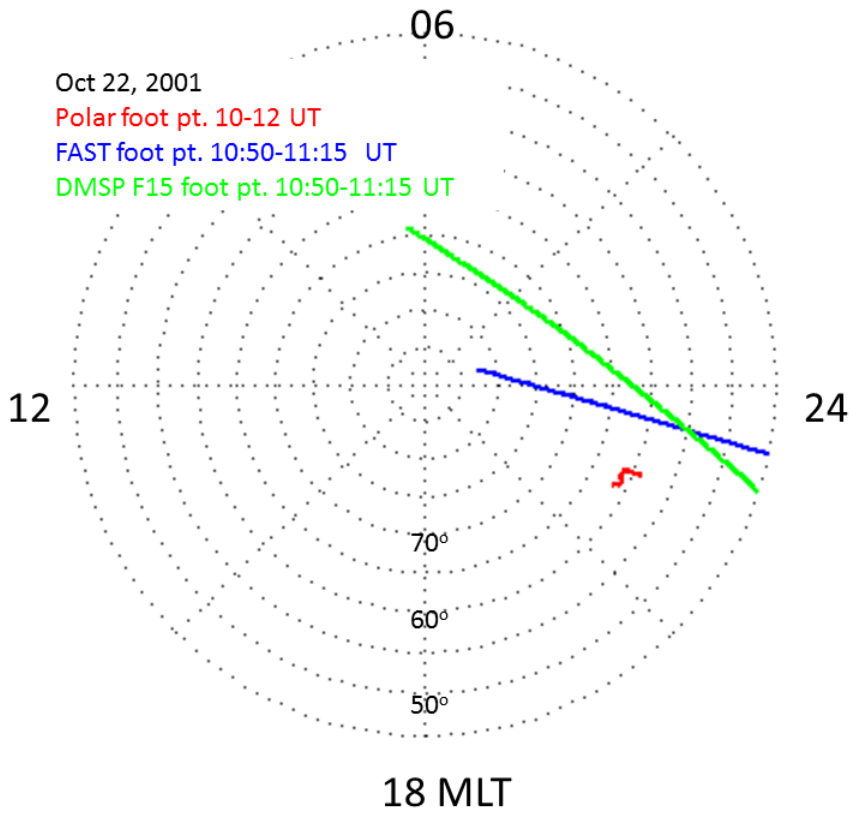

Figure 4.6 Mapped foot points of Polar (red), from 10:00 to 12:00 UT, DMSP F15 (Green) and FAST (blue) from 10:50 to 11:15 UT on October 22, 2001. At this time, the three spacecraft are close in MLT, within 1 hour, and pass through the same latitude within 15 minutes of one another. Polar observed intense Poynting flux at 11:15 UT and DMSP F15 and FAST passed through the same latitude ~ 15 minutes earlier (~11:00 UT), within a few minutes of one another.

Figure 4.7 shows 2 hours of Polar wave electric and magnetic fields, field aligned mapped Poynting flux, mapped Poynting flux integrated along the spacecraft foot point trajectory and electron differential energy flux on October 22, 2001 during major storm, Dst ~-130 nT, on the night side. The wave electric field in Figure 4.7(a) is the

perpendicular component in the spin plane, with positive values corresponding to ~**z** gsm direction, detrended and smoothed to retain fluctuation in the 6-180 second range. The wave magnetic field shown in Figure 4.7(b) is along the spin axis (~ **y** gsm) and is perpendicular to the electric field, and approximately perpendicular to the background magnetic field. The magnetic field is also detrended and smoothed to retain fluctuations in the 6-180 second range (5.5-166 mHz). Note that while this is the dominant component of the wave magnetic field, for the calculation of the Poynting flux in Figure 4.7(c) the all three components of the magnetic field are used. The field aligned wave (5.5-166 mHz, 6-180 sec.) Poynting flux in Figure 4.7(c) has been calculated and mapped to 100 km as described in section 4.2. In Figure 4.7(d) is the field aligned Poynting flux integrated along the spacecraft trajectory using the assumption that the spacecraft velocity is the relevant velocity between the spacecraft and plasma structure through which the waves propagate. In Figure 4.7(e) is the electron differential energy flux. Polar is in the plasma sheet during this the whole interval. During this event there are three intervals with intense mapped Poynting flux, occurring at 10:25 UT, 10:40 UT, and 11:15 UT, with peak intensities of 75 ergs/cm^{2}s, 25 ergs/cm^{2}s, and 150 ergs/cm^{2}s respectively. Each of these bursts of Poynting flux carries net earthward energy, as is indicated by the Poynting flux being mainly earthward and by the integrated Poynting flux having a net positive value.

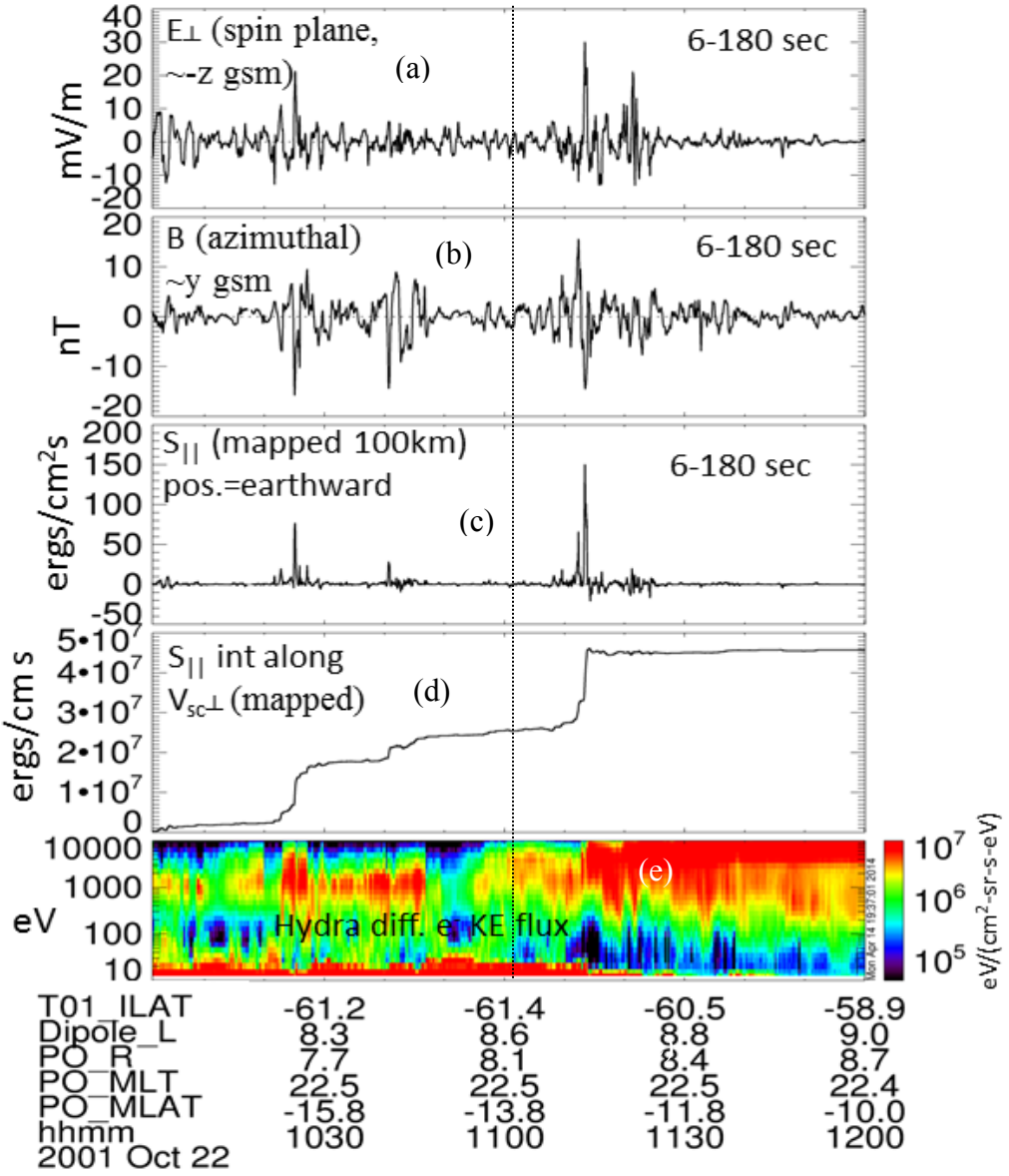

Figure 4.7: Two hours of Polar data from a night side, south hemisphere, pass during an active period (Dst ~-130 nT, AE ~300nT-1400nT) on October 22, 2001. The perpendicular electric field (spin plane, ~z gsm) and magnetic field (azimuthal, ~y GSM) in the wave period range of 6 to 180 seconds are shown in (a) and (b) respectively. The corresponding field-aligned Poynting flux, mapped to an altitude of 100 km, is shown in (d). The electron differential energy flux in (e) indicates the PSBL by increases in the ≳ 1keV electrons, seen intermittently. The vertical dotted line indicates the time of the DMSP F15 and FAST passes through the same latitude as that at which the intense Poynting flux is observed at Polar.

The ratio of electric to magnetic field perturbations, δE/δB, is consistent with Alfvénic fluctuations. The δE to δB ratio near the intense Poynting flux around 10:30 and 11:15 is ~1000-3000 km/s. For this event the Alfvén speed should be between 1000 -10000 km/s depending on the ion composition of the local plasma. The waves are thus in the range we would expect for Alfvén waves in an oxygen rich plasma. In addition, there could be some coupling via field aligned currents to the ionosphere, for which the δE to δB ratio is smaller, as described above.

Figure 4.8 shows three and a half minutes of DMSP F15 electron data during its pass through the auroral region occurring closest in time to the observation of intense Poynting flux at Polar. Figure 4.8(a) shows the earthward electron kinetic energy flux mapped to 100 km. The electron kinetic energy integrated along the mapped spacecraft trajectory is in Figure 4.8(b), and in Figure 4.8(c) is the electron differential energy flux spectrum. Inverted V and wave spectra are both visible in the spectra, and the total electron kinetic energy flux contains contributions from each. The intensity of the mapped electron kinetic energy flux is ~80 ergs/cm^{2}s, less than the peak value of the wave Poynting flux, ~150 ergs/cm^{2}s, at 11:15 UT in Figure 4.7(c), however this DMSP pass occurs ~15 minutes before the intense Poynting flux observed on Polar. It is uncertain whether the Poynting flux in Figure 4.7(c) is only present during Polar's observation or is part of a moving structure that passes over Polar, and was present elsewhere 15 minutes earlier when DMSP traverses the same latitude. The time of the DMSP event is indicated in Figure 4.7 as the dotted vertical line. The total integrated value of the electron kinetic energy flux in Figure 4.8(b) is 6.5x10^8 ergs/cm-s. If we

assume that the Poynting flux at Polar persists only at the location where it is observed, and that Polar traverses that whole region with the relative velocity being that of the spacecraft, then the intense burst of Poynting flux near 11:15UT carries energy of $2x10^7$ ergs/cm-s, indicated in Figure 4.7(d). This interpretation suggests that the Poynting flux carries about 3% of the energy needed to power the low altitude electron kinetic energy flux at DMSP. If we include the Poynting flux observed for the whole two hour interval, then the Poynting flux contribution to the electron flux is ~7%. The energy carried by the Poynting flux may be higher if we assume that the plasma structure containing the Poynting flux expands over Polar with a velocity larger than the spacecraft velocity. At the altitude, of this event 8-9 R_E, Polar has a speed of ~ 2 km/s. We can also estimate the plasma sheet expansion speed in the same manner as we did in the previous section. Between 11:08:32 and 11:14:03 UT the poleward edge of the aurora moved poleward by three degrees, or 1 km/s. Mapping this velocity to Polar yields an estimated speed of the 21 km/s, consistent with the estimated typical plasma sheet expansion speeds of ~ 20-40 km/s [estimated from Wygant et al 2000 and references therein], so the integral $\int S_{\parallel} V_{sc} dt$ should be ~10 times larger, yielding and integrated Poynting flux of ~$2x10^8$ ergs/cm-s (for just the interval around 11:15 UT) or 30% of the low altitude electron kinetic energy flux.

As stated above, if the Poynting flux exists over a larger region, so that the relative motion between Polar and the plasma sheet does not carry this whole region over Polar before the Poynting flux de-intensifies, then the total amount of energy carried by the Poynting flux will be even larger than what is observed.

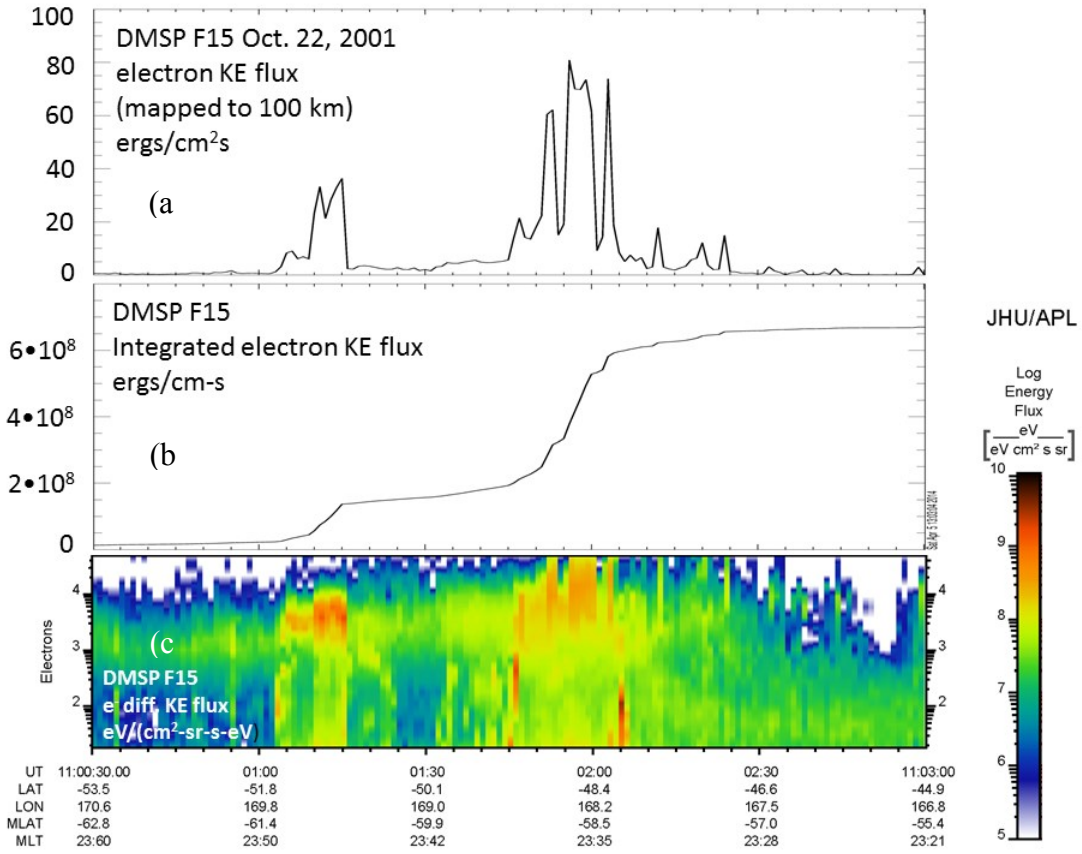

Figure 4.8: Two and a half minutes DMSP F15 electron data from 11:00:30 to 11:03:00 UT on October 22, 2001. In (a) is the downward electron kinetic energy flux mapped to an altitude of 100km, in (b) is the electron kinetic energy flux integrated along the mapped spacecraft trajectory, and in (c) is the electron differential energy flux. A mix of inverted V and broadband electrons are present and both contribute to the total downward electron kinetic energy flux. The peak intensity of the electron kinetic energy flux is 80 ergs/cm^{2}s. The integrated electron kinetic energy flux is 6.5x10^8 ergs/cm-s.

Figure 4.9 shows ~8 minutes of FAST electron data, from 10:55 UT to 11:03 UT during the night side pass through the auroral region that occurred closest in time to the observation of intense Poynting flux at Polar at 11:15 UT. Figure 4.9(a) shows kinetic

energy flux mapped to 100km, Figure 4.9(b) shows the integrated mapped electron kinetic energy flux, and the corresponding differential energy flux spectra of the downward electrons are shown in Figure 4.9(c). The electrons in Figure 4.9 observed at FAST occur ~15 minutes before the intense Poynting flux observed at Polar. The electron kinetic energy flux at FAST, Figure 4.9(a), peaks at an intensity of 9 ergs/cm^{2}s. This intensity is about a factor of 9 times smaller than the peak electron kinetic energy flux observed nearly simultaneously at DMSP F15 and ~15 times smaller than the intensity of the Poynting flux observed at Polar 15 minutes later. If the Poynting flux at does persist for periods longer than the Polar observations, it is possible that the intensity could vary over timescales of 10s of minutes and so may have been weaker 15 minutes earlier. Alternatively, the Poynting flux may have spread out somewhat across field lines.

The integrated electron kinetic energy flux at FAST, Figure 4.9(b), has a value of 2.1x10^8 ergs/cm-s. This is an order of magnitude larger than what is carries by the Polar Poynting flux, 2x10^7 ergs/cm-s. This suggests that the high altitude Poynting flux can account for ~8% of the energy carried by the low altitude electrons at FAST. If the plasma sheet is expanding with velocities between 20 and 40 km/s, then the Poynting flux may account for 80%-160% of the energy carried by the electron kinetic energy flux for this event.

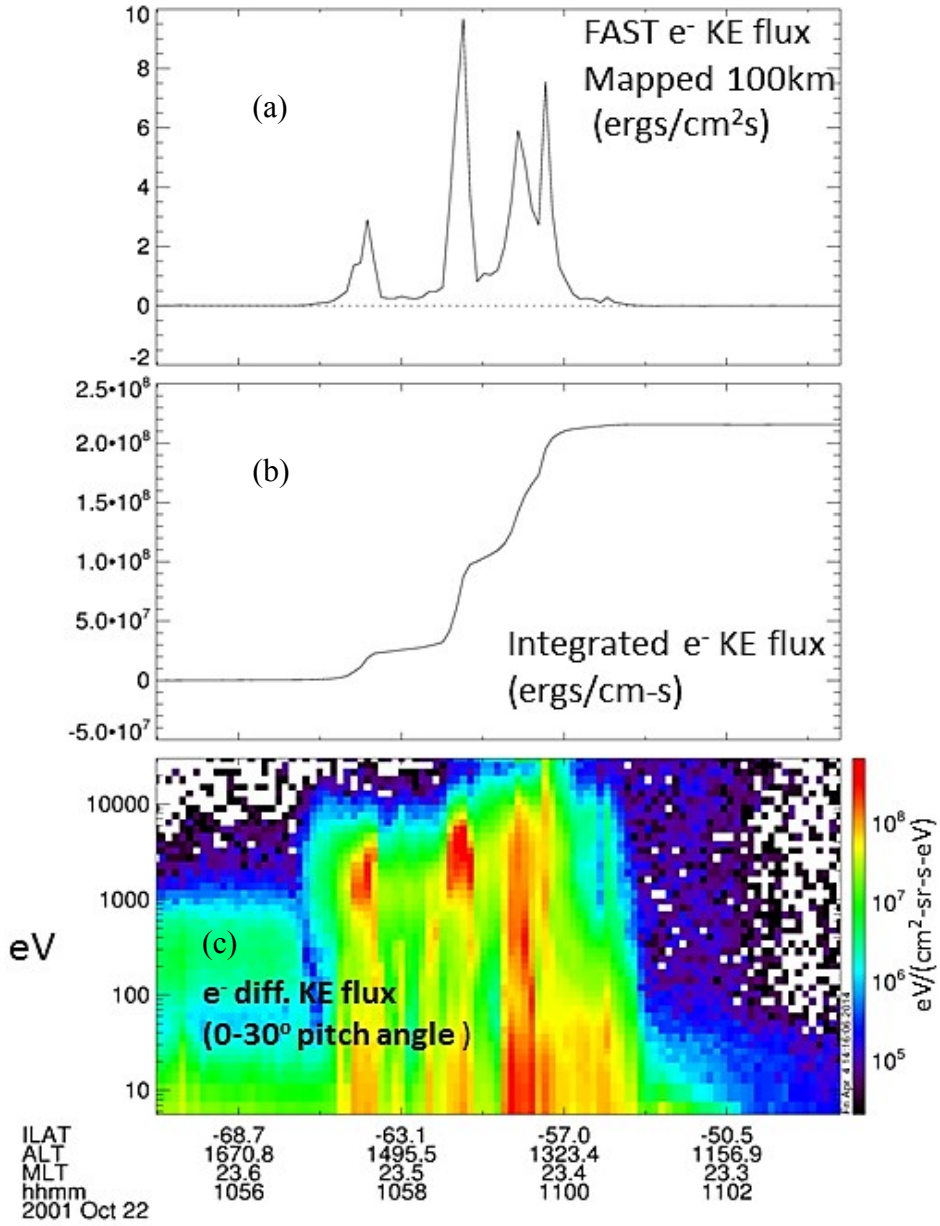

Figure 4.9: Eight minutes of FAST electron data from 10:55 to 11:03:00 UT on October 22, 2001. From top to bottom is shown the (a) downward electron kinetic energy flux mapped to an altitude of 100km, the (b) electron kinetic energy flux integrated along the spacecraft foot point trajectory. In (c) is the differential electron energy flux. A mix of inverted V and wave electron are present and both contribute to the total downward electron kinetic energy flux. The peak intensity of the electron kinetic energy flux is 9 ergs/cm^{2}s. The integrated electron kinetic energy flux is 2.1x10^8 ergs/cm-s.

Figure 4.10 shows a Polar UVI auroral image taken at 11:14 UT, nearly simultaneously with the observation of intense Poynting flux at Polar. The approximate foot point of Polar's trajectory is shown as the black dashed line. Around the location of Polar's foot point the peak intensity on the scale provided is ~ 70 photons/cm^{2}s, which corresponds to ~19 ergs/cm^{2}s. The peak intensity suggested by the UVI image is thus only about a sixth of that of the peak Poynting flux intensity observed simultaneously at Polar. Integrating the UVI image by multiplying the intensity by the distance across the region of intense UV emissions (dividing this process into separate intervals for regions of different intensities) yields an energy rate of ~8.1x10^8 ergs/cm-s. Again, the integrated Poynting flux at Polar is 2x10^7 ergs/cm-s (Figure 4.7(d)). Assuming that Polar observed the entire region of Poynting flux, and that the relative velocity is the spacecraft velocity, comparison of the wave Poynting flux to the integrated auroral images suggests that the Poynting flux carries ~2.5% of the energy in the simultaneously observed aurora. This percentage becomes ~5.5% if we use the entire two hours of Poynting flux in comparison to the UV image. If we assume that the relevant velocity between the plasma structure and the Polar spacecraft is due to plasma sheet expansion, this suggests that the actual fraction of the energy is supplied by the Poynting flux is ~10 times larger, or 25% (and 55% for the whole 2 hours of Poynting flux in Figure 4.7) of the total electron energy suggested by the UVI auroral image.

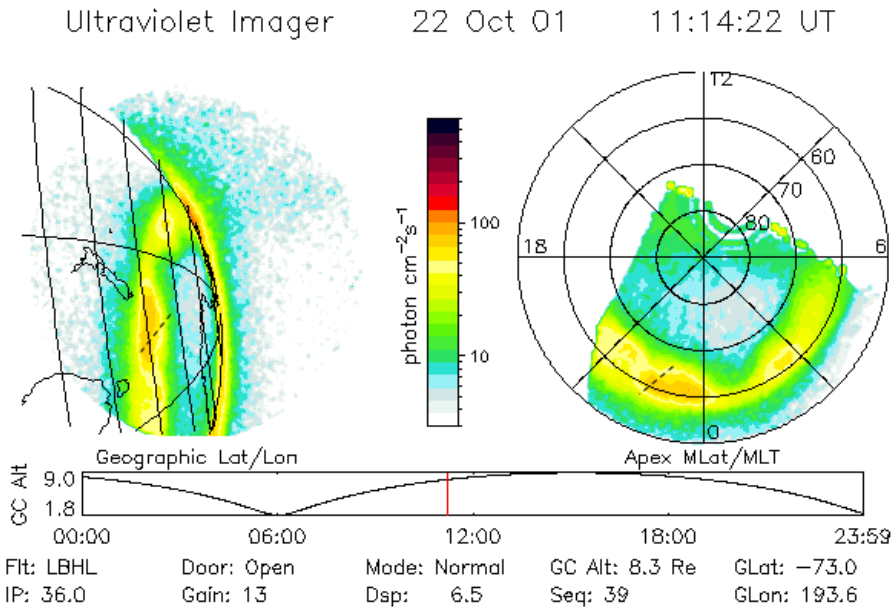

Figure 4.10 Polar UVI auroral image taken simultaneous with the observation of intense Poynting flux at Polar. The black dashed line shows the approximate foot point trajectory through the intense auroral region around this time.

Table 4.2 summarizes the peak values of the Poynting flux and electron kinetic energy fluxes, and integrated values thereof for the October 22, 2001 event.

Oct. 22 ,2001	Peak intensity	Integrated (mapped)	Time of peak	MLT of S/C
Polar $S_{\|\|}$ (100km)	150 ergs/cm^{2}s	2x10^7 ergs/cm-s for V=V_{sc} or 2x10^8 ergs/cm-s for V~V_{ps}	11:14 UT	~22.5 MLT
DMSP e- KE flux (100 km)	80 ergs/cm^{2}s	6.5x10^8 ergs/cm-s	11:02 UT	~23.5 MLT
FAST e KE flux (100 km)	9 ergs/cm^{2}s	2.1x10^8 ergs/cm-s	10:59 UT	~23.5 MLT
Polar UVI	~19 ergs/cm^{2}s	~8.1x10^8 ergs/cm-s	11:14 UT	~22.5 MLT

Table 4.2: Summary of the peak intensities of the Polar Poynting flux and DMSP F15 and FAST electron kinetic energy flux, and integrated values thereof , for the October 22, 2001 example.

These two examples (May 2, 1998 and October 22, 2001) show a correspondence between the high altitude wave Poynting flux and auroral activity in the ionosphere consistent with earlier studies. The observations here agree with the conclusions of Wygant et al [2000] and Keiling et al [2002] (discussed in chapter 2) in that the peak intensity of the Poynting flux is typically greater than the UV imager inferred electron kinetic energy flux incident on the conjugate foot point ionosphere. Given that the majority of the auroral power is thought to come from diffuse and inverted V electrons, the fact that the integrated values of the Poynting flux are ~3%-50% of the integrated low

altitude electron kinetic energy flux are not surprising. This result is consistent with the observations of Keiling et al [2003], Chaston et al [2007], Janhunen et al [2006] and Newell et al [2009] in that those studies have variously put the contribution of the Alfvén accelerated electrons between a few and 50% of the aurora, depending on location and activity.

4.4 Comparing integrated Poynting flux and electron kinetic energy flux for October 2001 storm, during moderate activity, major storm activity and the recovery phase.

In this section we investigate the fraction of energy that the high altitude wave Poynting flux is capable of supplying to the acceleration processes resulting in the downward electron kinetic energy flux observed at low altitudes for three different intervals with different levels of geomagnetic activity during October 2001.

This investigation required integration of the Poynting flux which has various uncertainties associated with it. Because we are using only one spacecraft at high altitudes, we cannot use spacecraft timing to estimate the relative velocity between Polar and the plasma structures through which the Poynting flux propagate. Therefor there is an uncertainty in converting between time and spatial domains. There are two possible velocities that one can use, the spacecraft velocity, which is known, and the velocity of the plasma sheet expanding over the spacecraft, which we do not know. In addition, because we only have one high altitude spacecraft we do not know the spatial extent over

which the intense Poynting flux is present. It is possible that the whole plasma structure carrying intense Poynting flux passes over Polar, but it is also possible that the Poynting flux is present throughout a much larger portion of the night side near earth tail, and lasts only for the duration of Polar's observation, and that Polar thus only sees the portion of the Poynting flux that maps down to the ionosphere. For this reason, we estimate the integral of the Poynting flux in three different ways. The first way is to integrate the mapped Poynting flux along the foot point trajectory of the spacecraft. The second way is by assuming that the plasma sheet expands over Polar at speeds of 10-20 km/s. This number is estimated by extrapolating the estimated typical plasma sheet expansion speed in Wygant et al [2000] and references therein, given for altitudes of $6R_E$, to 9 R_E. Both of these integration techniques were used in the previous section. The third way is to assume that the Poynting flux is present through a large part of the night side tail through which Polar passes, and to do the spatial integration by multiplying the average in situ Poynting flux during each "burst" of enhanced Poynting flux by the scale size of the region Polar traverses on the night side. This value is then adjusted by scaling the remaining unit of distance to the ionosphere using the local and ionospheric field strength.

Figure 4.11 shows a representation of the scenario in which Polar traverses a localized area of intense Poynting flux. The ellipse is a Polar orbit on October 22, 2001. The red portion of the orbit is a ten hour period during which the intense Poynting fluxes are observed on the night side. The scale size of the night side orbit shown is ~ 8 R_E, so if the region of intense Poynting flux mapping down to either hemisphere occupies half of

this, or 4 R_E, then the Poynting flux integrated over 4 R_E is the best estimate of the energy.

Figure 4.12 shows a representation of the third scenario in which intense Poynting flux simultaneously occurs throughout the night side region covered by Polar's orbit for the durations typical (~10-15 min) of the periods characterized by intense spikes of Poynting flux. As in Figure 4.11, the ellipse is the Polar orbit during the October, 2001 storm. The red segment is a ten hour portion of the orbit, on the night side, typical of the range in which intense Poynting flux are observed. In the third integration approach described above, we will use a scale of 4 R_E, since half of the Poynting flux over the 8 R_E region will go to either the north or south hemisphere.

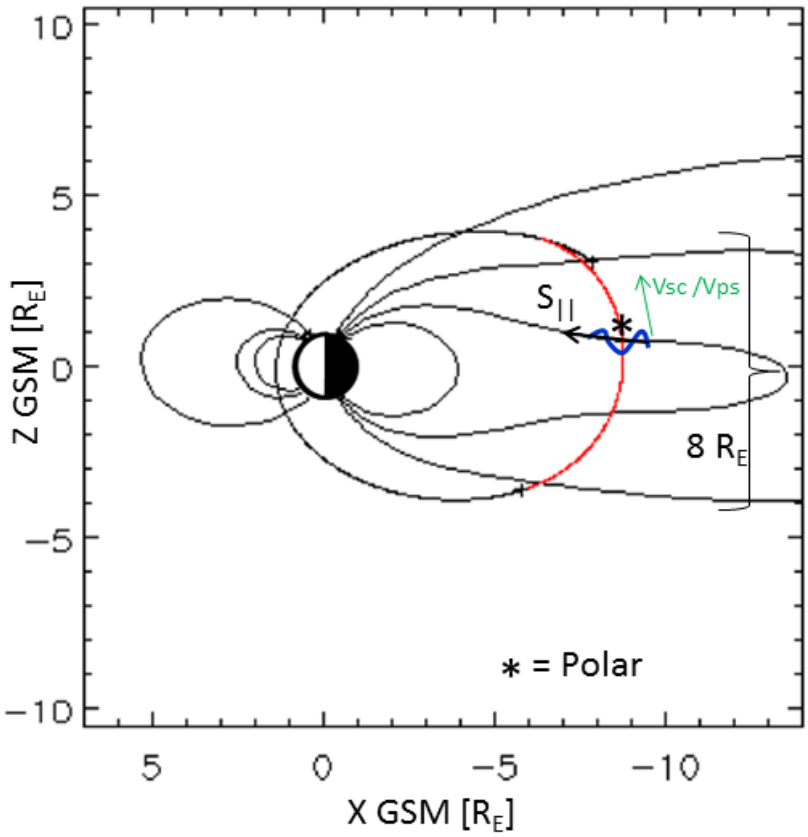

Figure 4.11 representation of the scenario in which Polar traverses a localized area of intense Poynting flux (represented by the blue wave and black arrow). The ellipse is the Polar orbit during the October, 2001 storm. The red segment is a ~ ten hour portion of the orbit, on the night side, typical of the range in which intense Poynting flux are observed.

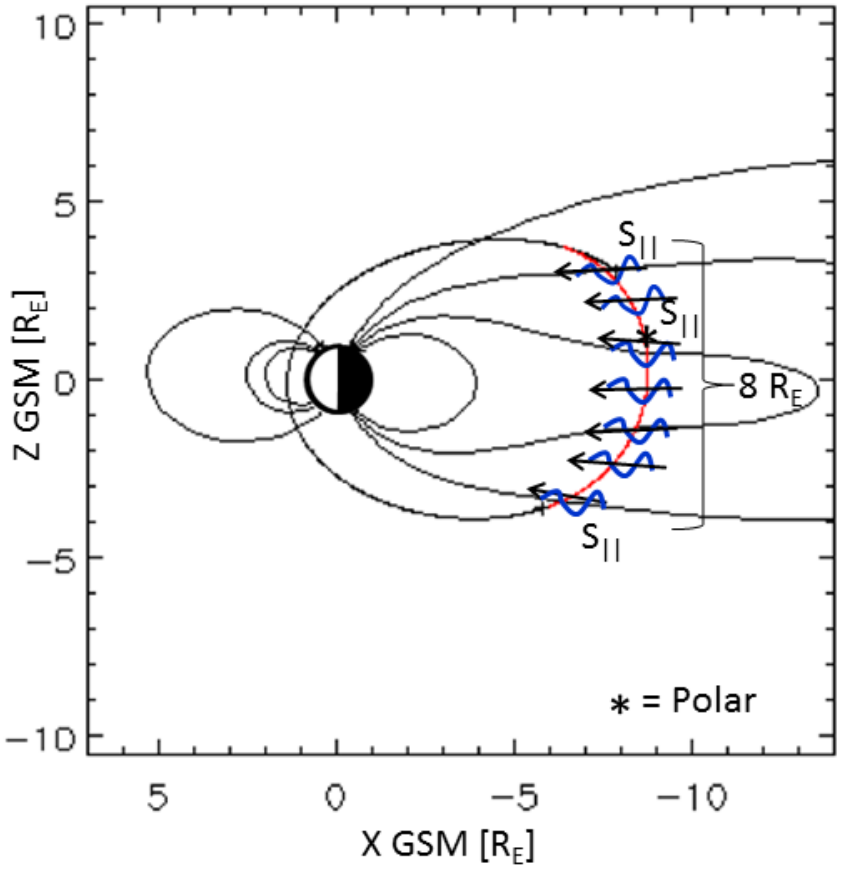

Figure 4.12: A representation of the scenario in which intense Poynting flux (blue waves and back arrows) simultaneously occurs throughout the night side region covered by Polar's orbit for the duration typical of the bursts of intense Poynting flux (~10-15 min). The ellipse is the Polar orbit during the October, 2001 storm. The red segment is a ~ten hour portion of the orbit, on the night side, typical of the range in which intense Poynting flux are observed.

Figure 4.13 shows the mapped wave Poynting flux at Polar (a) and mapped electron kinetic energy flux measured by FAST (c) and the spatial integration of each along their respective mapped foot point trajectories in (b) and (d), respectively, for an eight hour interval (14:00-22:00 UT) on October 18, 2001. This interval is characterized by

moderate substorm activity, AE ~ 150 nT. During this interval Polar is around apogee on the night side, while FAST makes multiple orbits, about 3. The Polar Poynting flux in Figure 4.14(a) and integrated Poynting flux in 4.14(c) occur in discreet bursts, or intervals, typically 10-15 minutes in duration.

Figure 4.13 presents an eight hour interval of Polar field aligned wave Poynting flux (mapped) and FAST electron kinetic energy flux (mapped) on October 18, 2001, from 14:00 to 22:00 UT, an interval characterized by major storm and substorm activity, Dst ~-4 nT and AE ~150 nT. The mapped wave Poynting flux in Figure 4.13(a) occurs in (typically) brief intervals of 10-60 minutes duration. Six such intervals of intense Poynting flux are apparent over the course of the eight hours. The peaks of these intervals are in the range of 10-110 ergs/cm^{2}s. In Figure 4.13 (b) is the mapped Poynting flux integrated using the spacecraft velocity along the mapped spacecraft trajectory. The integral over the whole eight hours is 3.3x10^7 ergs/cm-s and the average integral over each interval of intense Poynting flux is 5.5x10^6 ergs/cm-s. If we assume the relevant velocity is not the spacecraft velocity, but that of the estimated plasma sheet expansion velocity, ~20 km/s, then the integrated value per intense Poynting flux burst will be ~10 times larger or 5.5x10^7 ergs/cm-s, and the integrated value of the full interval is 3.3x10^8 ergs/cm-s. According to the third method of integrating, we average the in situ Poynting flux per burst over the average duration per burst (or intense Poynting flux interval), multiplying this by 4 R_E and scaling the result value to 100 km using the square root of the ratio of ionospheric to in situ magnetic field value. This scaling scales the remaining, azimuthal, length scale in the integrated value. This process yields an integrated

Poynting flux of 1.4×10^8 ergs/cm-s. In Figure 4.13(c) is the FAST electron kinetic energy flux, mapped to 100 km, for all four of the night side, southern hemisphere, auroral zone passes during the 14:00 -22:00 UT interval. The peak intensities are between 2 and 5 ergs/cm^{2}s. The integrated values of the electron kinetic energy flux for the four passes are shown in Figure 4.13(d). The average integrated FAST electron kinetic energy flux per auroral zone pass is 2.6×10^7 ergs/cm-s. Comparing this value to the above integrated values of the Poynting flux, we find that if the Polar spacecraft passes the Poynting flux burst with the spacecraft velocity, then on average the Poynting flux will be able to supply 21% the energy. If the relative speed between the Polar spacecraft and plasma sheet is the plasma sheet expansion speed, then these fractions will be 10 times larger, or 210% of the integrated electron kinetic energy flux. The third integration technique, which assumes the Poynting flux fills the night side magnetosphere along Polar's orbit, suggests that the Poynting flux is capable of supplying ~450% of the energy needed for the electron kinetic energy flux. These results are summarized in Table 4.3.

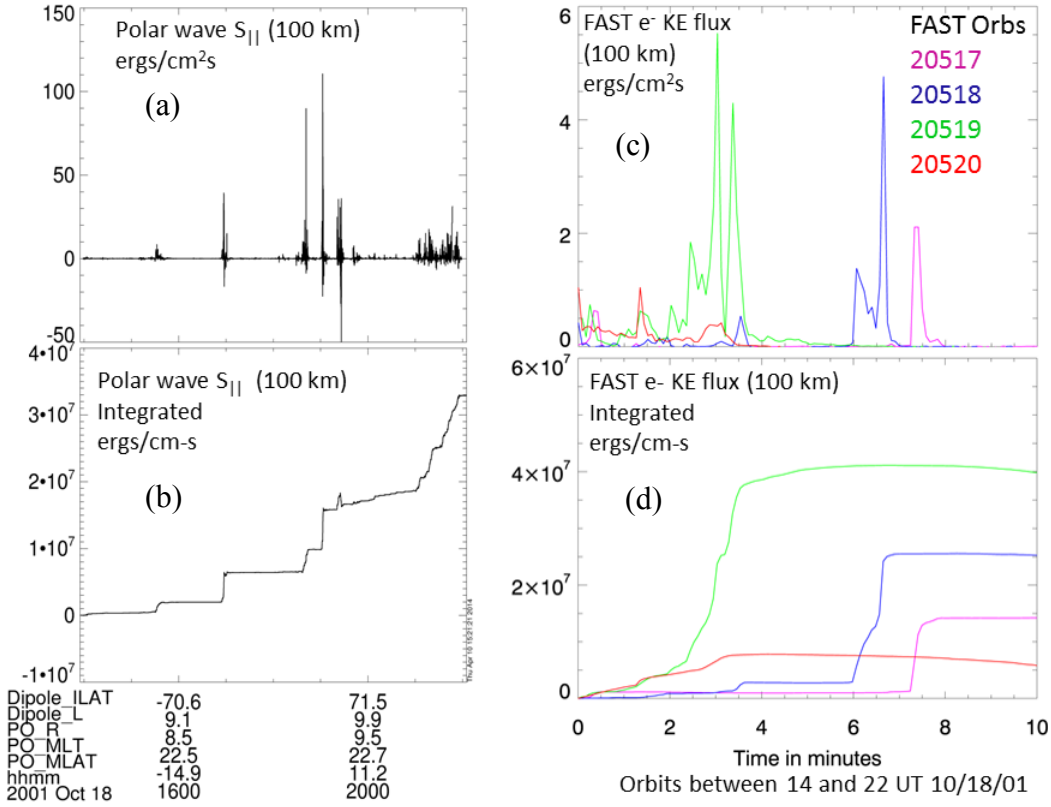

Figure 4.13: Eight hours (14:00 to 22:00 UT) of night side Polar and FAST data on October 18, 2001, an interval characterized by moderate substorm activity, AE ~150 nT. In (a) is the wave Poynting flux at Polar, mapped to 100 km, and the integrated value thereof, using the spacecraft velocity, is shown in (b). This integration is along the mapped spacecraft trajectory. In (c) is the FAST electron kinetic energy flux mapped to 100 km from all four night side, southern hemisphere auroral zone passes. In (d) is the spatially integrated FAST electron kinetic energy flux. The integrations being taken along the foot point of the spacecraft and the remaining spatial unit along the earth azimuthally.

Figure 4.14 presents a ten hour interval of Polar field aligned wave Poynting flux (mapped) and FAST electron kinetic energy flux (mapped) on October 22, 2001, from 10:00 to 20:00 UT an interval characterized by major storm and substorm activity, Dst ~-130 nT and AE ~2000 nT. The mapped wave Poynting flux in (a) occurs in (typically)

brief intervals or burst of 15-60 minutes duration. At least five such intervals are apparent over the course of the ten hours. The peaks of these intervals are in the range of 75-270 ergs/cm^{2}s. In Figure 4.14 (b) is the mapped Poynting flux integrated, using the spacecraft velocity, along the mapped spacecraft trajectory. The average integral over each interval of intense Poynting flux is 4.2×10^7 ergs/cm-s. If we assume the relevant velocity is not the spacecraft velocity, but that of the estimated plasma sheet expansion velocity, ~20 km/s, then the integrated value per intense Poynting flux burst will be 10 times larger, or 4.2×10^8 ergs/cm-s. According to the third method of integrating, we average the in situ Poynting flux per burst over the average duration per burst (or intense Poynting flux interval), multiplying this by 4 R_E and scaling the result value to 100 km using the square root of the ratio of ionospheric to in situ magnetic field value. This scaling scales the remaining, azimuthal, length scale in the integrated value. This process yields an integrated Poynting flux of 8.6×10^8 ergs/cm-s. In Figure 4.14(c) is the FAST electron kinetic energy flux mapped to 100 km, for the five night side, southern hemisphere, auroral zone passes during the ten hour interval. The peak intensities are between 6 and 11 ergs/cm^{2}s. The integrated value of the electron kinetic energy flux is shown in 4.4(d). The average integrated FAST electron kinetic energy flux per auroral zone pass is 2.8×10^8 ergs/cm-s. Comparing this value to the above integration for the Poynting flux, we find that if the Polar spacecraft passes the Poynting flux burst with the spacecraft velocity, then on average the Poynting flux will be able to supply 15% the energy. If the relative speed between the spacecraft and plasma is the plasma sheet expansion speed, then the fraction will be 10 times larger, or 150% of the integrated

electron kinetic energy flux. The third integration technique suggests that the Poynting flux is capable of supplying ~300% of the energy needed for the electron kinetic energy flux. These results are summarized in Table 4.3.

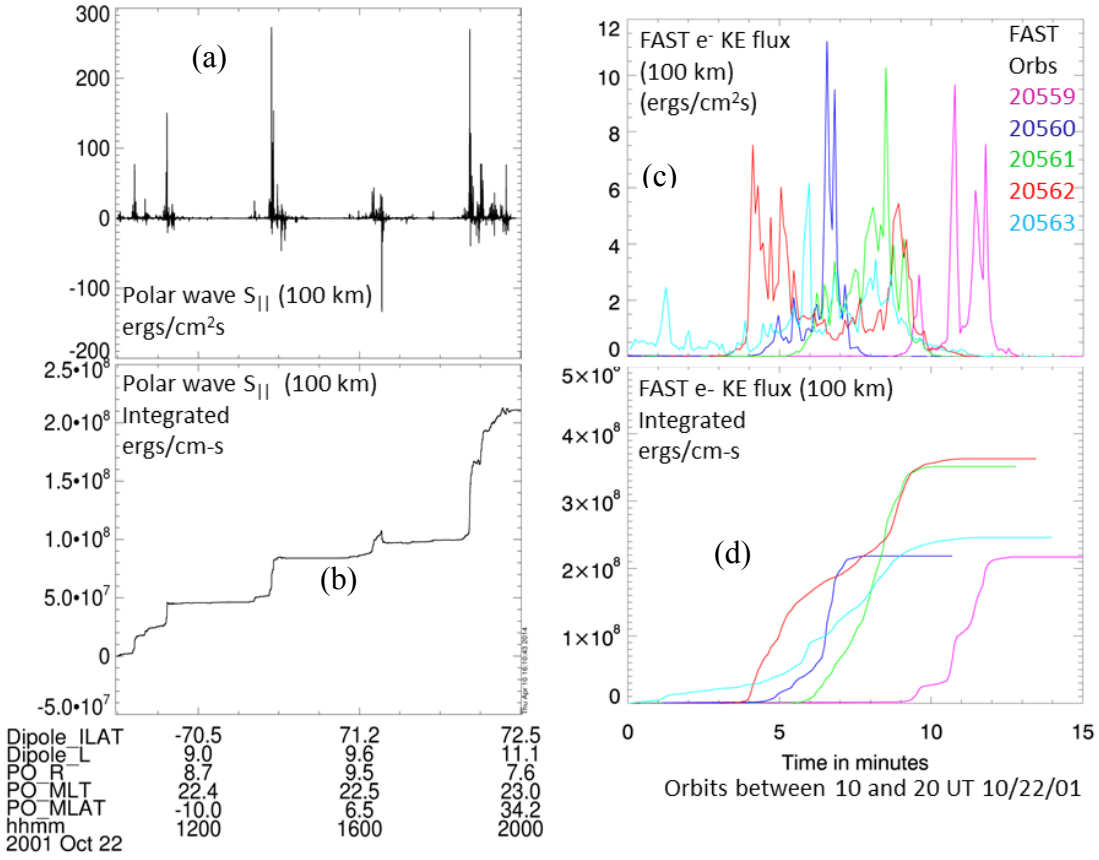

Figure 4.14 Ten hours (10:00 to 20:00 UT) of night side Polar and FAST data on October 22, 2001, an interval characterized by major storm and substorm activity, Dst ~-130 nT and AE ~2000 nT. In (a) is the wave Poynting flux at Polar, mapped to 100 km, and the integrated value thereof along the mapped spacecraft trajectory is shown in (b). This integration is done with the velocity of Polar. In (c) is the FAST electron kinetic energy flux mapped to 100 km for the five night side, southern hemisphere, auroral zone passes during this interval. The integrated value of the electron kinetic energy flux is shown in (d).

Figure 4.15 presents a ten hour interval of Polar field aligned wave Poynting flux (mapped) and FAST electron kinetic energy flux (mapped) on October 24, 2001, from 00:00 to 10:00 UT an interval characterized by the recovery phase and minimal substorm activity, Dst ~-70 nT, and increasing, and AE ~60 nT. The mapped wave Poynting flux in Figure 4.15(a) occurs in longer intervals that what is typical during the more active conditions. There are two intervals of enhanced Poynting flux of 2 to 3 hours duration. The peaks of these intervals are in the range of 0.5-2 ergs/cm^{2}s. In Figure 4.15 (b) is the mapped Poynting flux integrated using the spacecraft velocity along the mapped spacecraft trajectory. The average integral over each interval of intense Poynting flux is $9x10^5$ ergs/cm-s. If we assume the relevant velocity is not the spacecraft velocity, but that of the estimated plasma sheet expansion velocity, ~20 km/s, then the integrated value per intense Poynting flux burst will be 10 times larger, or $9x10^6$ ergs/cm-s. We do not have adequate UVI images to resolve the auroral speed at this time, but as this is a quiet period it is likely not moving as fast at the storm time plasma sheet expansions. Using the third method of integrating the Poynting flux, i.e. assuming the Poynting flux pervades a 4 R_E area per hemisphere on the night side around Polar's orbit, yields an integrated Poynting flux of $1.8x10^6$ ergs/cm-s. In Figure 4.15(c) is the FAST electron kinetic energy flux mapped to 100 km, for the four night side, southern hemisphere, auroral zone passes. The peak intensities between 0.5 and 7.5 ergs/cm^{2}s. The integrated value of the electron kinetic energy flux is shown in 4.15(d). The average integrated FAST electron kinetic energy flux per auroral zone pass is $1.9x10^7$ ergs/cm-s. Comparing this value to the above integrations of the Poynting flux, we find that if the Polar spacecraft passes the

Poynting flux bursts with the spacecraft velocity then on average the Poynting flux will be able to supply 4.7% the energy. If the relative speed between the spacecraft and plasma is the ~20 km/s plasma sheet expansion speed, then the fraction will be 10 times larger, or 47%, of the integrated electron kinetic energy flux. The third integration technique suggests that the Poynting flux is capable of supplying ~9.5% of the energy carried by the electrons. In this case the duration of the most intense Poynting flux for this interval are long, and the Polar spacecraft can move significantly during that time, ~2.5 R_E. The higher values, assuming the plasma sheet expansion velocities are unlikely for this event due to the fact that this interval is during a geomagnetically quiet period. These results are summarized in Table 4.3.

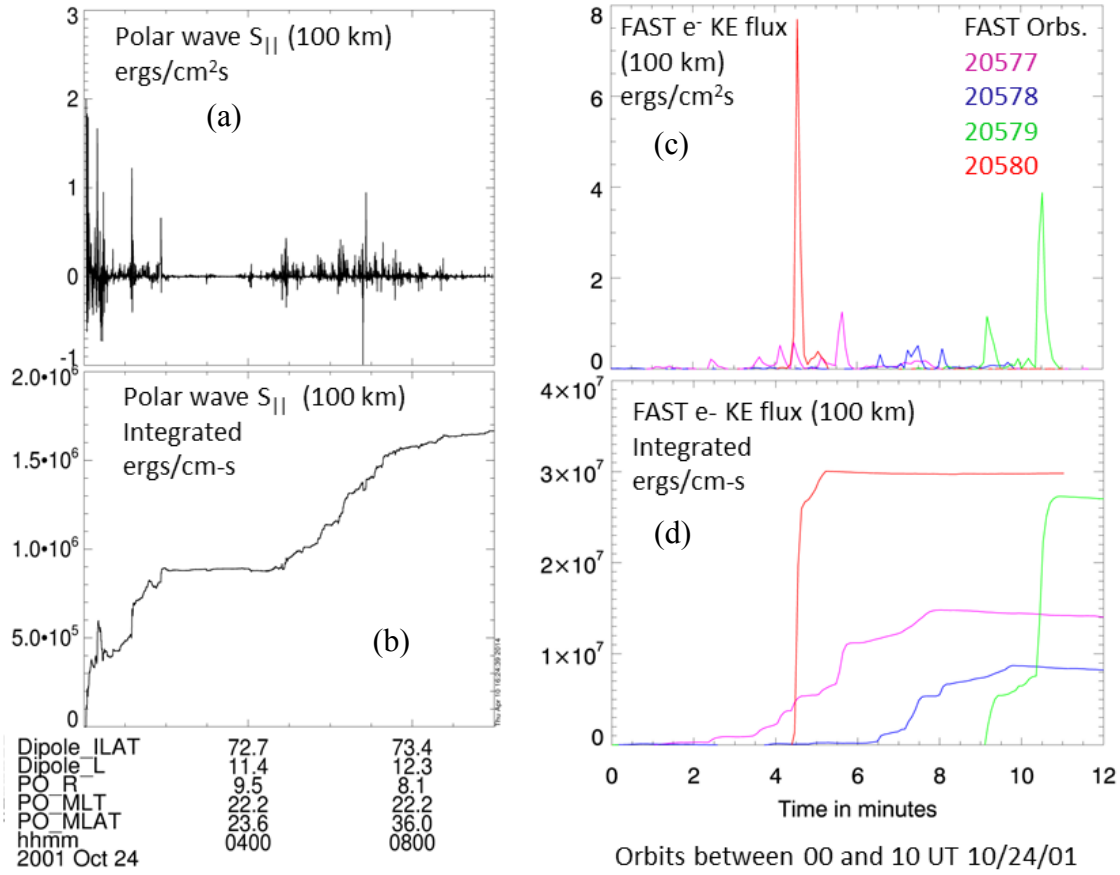

Figure 4.15: Ten hours (00:00 to 10:00 UT) of night side Polar and FAST data on October 24, 2001, an interval during the recovery phase of the major storm Dst ~-70 nT and increasing, and quiet substorm activity, AE ~60 nT. In (a) is the wave Poynting flux at Polar, mapped to 100 km, and the integrated value thereof is shown in (b). This integration is along the mapped foot point trajectory of Polar. In (c) is the FAST electron kinetic energy flux mapped to 100 km for the four night side, southern hemisphere, auroral zone passes that occur during this interval. In (d) is the integrated value of the electron kinetic energy flux.

October 2001	Oct 18 (pre storm, Dst ~-4, moderate substorms AE ~150 nT)	Oct 22 major storm (Dst ~-130 nt, AE ~2000 nT	Oct 24 quiet recovery DST ~-70, increasing, AE ~60 nT
Polar $S_{\|\|}$ peak, mapped	10-110 ergs/cm^{2}s	75-750 ergs/cm^{2}s	0.5-2 ergs/cm^{2}s
Polar $S_{\|\|}$ int along S/C traj. V=Vsc, per burst (a)	5.5x10^6 ergs/cm-s	4.2x10^7 ergs/cm-s	9x10^5 ergs/cm-s
Polar $S_{\|\|}$ int along traj, V~Vps, per burst (b)	5.5x10^7 ergs/cm-s	4.2x10^8 ergs/cm-s	9x10^6 ergs/cm-s
Polar $S_{\|\|}$ ave S burst int. across whole trajectory (c)	1.4x10^8 ergs/cm-s	8.6x10^8 ergs/cm-s	1.8x10^6 ergs/cm-s
FAST e KE flux mapped peaks	2-5 ergs/cm^{2}s	6-11 ergs/cm^{2}s	0.5-8 ergs/cm^{2}s
FAST e KE flux ave. integration per pass	2.6x10^7 ergs/cm-s	2.8x10^8 ergs/cm-s	1.9x10^7 ergs/cm-s
Fraction of Poynting flux energy (a,b,c) to e- KE energy	a.) 21% b.)210% c.) 450%	a.) 15% b.) 150% c.) 300%	a.) 4.7% b.) 47% c.) 9.5%

Table 4.3 Summary of the typical peak Poynting and electron kinetic energy flux intensities and integrated fluxes.

Depending on the assumptions used in the integration of the Poynting flux, the results can vary by an order of magnitude. The assumption that the Polar spacecraft moves through or across a localized area of Poynting flux, and that the spacecraft velocity is the relevant velocity to use, suggests the Poynting flux is capable of contributing ~5-20% of the power for the acceleration of the electrons. These values are consistent with the results of prior statistical studies [e.g. Janhunen et al 2006, Chaston et al 2007], whereas the larger values typically given by the other two integration techniques are not. However, as we are investigating the Poynting flux with a method not used by the previous studies, and

the uncertainties with the Poynting flux integration will not be completely resolved without multiple spacecraft. The possibility that the Poynting flux contributes a much greater fraction to the low altitude electron energy budget than previously thought is an important result.

4.5 Latitudinal evolution of the high altitude Poynting flux and low altitude downward electron kinetic energy flux during major storms

In this section we investigate the latitudinal evolution of the high altitude (Polar) wave Poynting flux mapped intensities, on the night side (18-6 MLT), over the course of two intervals (~10s of days) during each of which a pre-storm, main phase and recovery phase of a major geomagnetic storm occur. These two intervals are April 21-May17 1998, and October 17-28, 2001. For these two intervals we also investigate the latitudinal evolution of the low altitude (FAST and DMSP) electron kinetic energy flux mapped intensities, on the night side (18-6 MLT). The investigation will also compare the latitudinal evolutions of high altitude wave Poynting flux to that of the low altitude electron kinetic energy flux.

4.5.1 Event 1: April 21 to May 18, 1998

In this section we investigate the latitudinal intensity evolution for the Polar Poynting flux and of the FAST and DMSP electron kinetic energy flux for April 21 – May 18 , 1998. Figure 4.16 shows a view of the Polar, FAST and DMPS f12 orbits looking southward from a vantage point north and duskward above the earth on May 2, 1998, the

characteristic relative configuration of the orbits for this event. The spacecraft orbits are not all in the same plane, and their foot points are separated by few hours MLT.

Figure 4.17 presents a Polar VIS image showing visible auroral activity and approximate foot point locations of Polar, FAST and DMSP F12 for an active time on May 02, 1998. During such times the auroral activity can be longitudinally extensive, though not necessarily homogeneous. Thus even though the spacecraft foot points are separated 2-4 hours in MLT, the azimuthally extensive aurora provide a more suitable circumstance for comparing energetic flux at the different spacecraft, in that, on similar field lines at similar, though longitudinally separate, latitudes, the energetics are more likely to be similar. In addition, though such measurements at similar latitudes may be made at different times, the extensive aurora can persist for hours making it likely that multiple spacecraft can make comparable measurements, especially during active times. The observations of a coherent pattern, i.e. obtaining similar values at similar ILATs over multiple orbits, suggest that those values are typical of that latitude and geomagnetic activity level. This coherence for a given geomagnetic activity levels is significant because it allows us to examine the evolution in the Poynting or electron kinetic energy flux over the course of storms. We thus gain a new aspect of the total picture of auroral energy transport and dynamics that is different than that available through short duration conjunction studies and that through long term statistical studies.

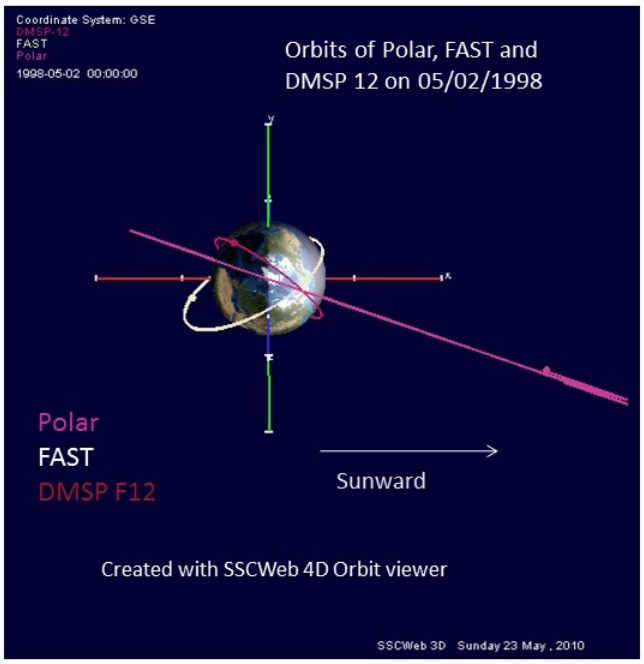

Figure 4.16: View of the Earth and spaceacraft (Polar, FAST, and DMSP F12) orbits looking southward from a vantage point north and duskward above the earth. Note that the spacecraft orbits are not all in the same plane, and their foot points will be separated by few hours MLT.

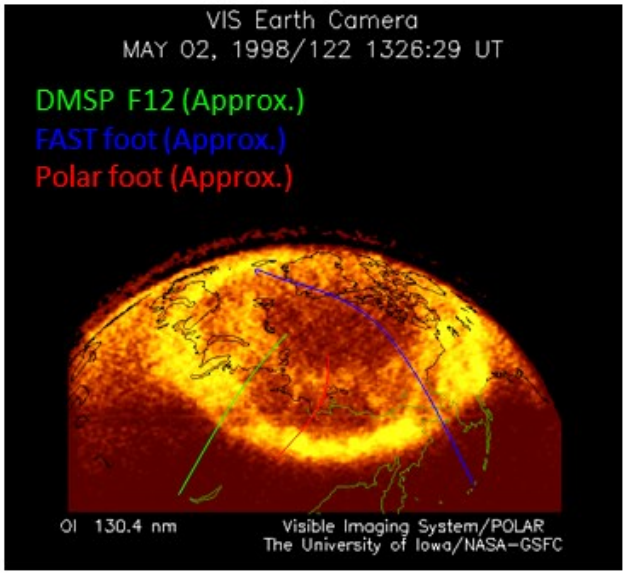

Figure 4.17: A Polar VIS image showing visible auroral activity and approximate foot point locations of the Polar, FAST and DMSP satellites for an active time on May 02, 1998. Note that the auroral activity can be longitudinally extensive, though not necessarily homogeneous, during active time. These conditions provide more suitable circumstances (i.e. similar field lines at similar, though longitudinally separate, latitudes) for comparing energetic flux at different spacecraft.

In Figure 4.18 is presented the peak mapped intensity per 0.5^{o} ILAT for the night side Polar wave Poynting flux plotted as a function of ILAT and time in (a), the peak mapped intensities per 0.5^{o} ILAT for the night side FAST and DMSP F12 electron kinetic energy flux plotted as a function of ILAT and time in (b) and (c) respectively, and the Dst index for a 26 day interval from April 21, 1998 to May17, 1998. This plot of intensity versus ILAT – time shows the latitudinal evolution of the high altitude night side wave Poynting flux and low altitude kinetic energy flux over the course of the storm.

For this interval, the geomagnetic activity according to Dst index is as follows; and is shown in Figure 4.18(d). The magnetic disturbance is small from April 21 to the end of the 23^{rd} at which point a moderate storm occurs with Dst decreasing to about -70 nT. The recovery phase lasts until April 30, in part being prolonged by a small storm on the 26^{th} of Dst = -60 nT. On May 2^{nd} a moderate storm occurs and Dst decreases to about -80 nT. The Dst starts to recover and then the major storm main phase occurs on May 4, with the Dst decreasing to -200 nT. The Dst recovers until May 8 when a moderate storm halts or prolongs the recovery until the 15^{th}. The Dst is quiet ($|Dst|<30$ nT) between the 15^{th} and 17^{th}.

The Poynting flux intensities (peak intensity per 0.5 degrees ILAT) in Figure 4.18(a) at low latitudes ($\leq 65^o$ ILAT) are typically on the order of ~ 0.01 ergs/cm^{2}s or less (~ few 0.001 ergs/cm^{2}s) during geomagnetically quiet times (Dst $\gtrsim$ -30 nT). At latitudes between about 65^o and 75^o ILAT, during quiet times, the Poynting flux intensity is typically a few 0.1 ergs/cm^{2}s to 1 ergs/cm^{2}s. In this range there are intervals in latitude, 0.5 to 1 degree, in which the peak Poynting flux is larger, ~10 ergs/cm^{2}s. At latitudes above about 75^o, during quiet times, the Poynting flux is typically on the order of a few 0.01 to 0.1 ergs/cm^{2}s. The coverage between around 82^o ILAT to 90^o is intermittent, varying on a three day period, corresponding to the beat frequency between the rotation of earth's dipole and Polar's orbit. During times of enhanced geomagnetic disturbance, Dst < -30 nT, the Poynting flux intensifies at lower latitudes ($< 65^o$) from their quiet time values on the order of 0.001 to 0.01 ergs/cm^{2}s to intensities on the order of a few ergs/cm^{2}s to 10s or ergs/cm^{2}s. These enhancements extend down to around 60^o to the upper 50^os ILAT for the moderate disturbances, such as on the 24th and 26th of April, May 8th and 12th and down to 55 degrees during the storm on May 2nd. The Poynting flux slightly enhances at higher latitudes, just above 75 degrees, during the times of enhanced geomagnetic activity from about a few 0.01 ergs/cm^{2}s to around 0.1 ergs/cm^{2}s, with intensities up to 10s ergs/cm^{2}s in some limited, localized places. Above about 78 degrees enhancements are typically small and are not well correlated with Dst. (the two areas of high latitude enhancement ~85^o on May 4 and May 16 are likely in the sheath).

The overall region of the more intense Poynting flux (0.1 to 1 ergs/cm^{2}s up to 10s) in time-latitude may be described as an envelope that widens in a range from about 65^o to

low 70^{o}s ILAT during quiet times to one ranging from 55^o-60^o to the upper 70^{o}s ILAT during major storms. In this envelope is the speckling of 0.5-5 degree intervals in latitude with the most intense peak Poynting flux, up into the tens of ergs/cm^{2}s. Not all locations of the intense Poynting flux are at the upper ILAT limit of this envelope, where the PSBL is expected to be. The high latitude storm time enhancements are not as distinct as the low latitude ones.

During the period of high geomagnetic disturbance, from May 2 to May 5, the two to three orders of magnitude enhancement in Poynting flux extends to low latitudes (<65^o ILAT) for five consecutive Polar spacecraft orbits. The lowest latitude at which large enhancements in Poynting flux occur during this event is 55^o ILAT on May 2, even though this is not the most magnetically active period. Polar is not on field lines mapping to the night side northern hemisphere during the most active period.

Other low latitude excursions of the Poynting flux enhancements occur on April 23-24, 26,May 8,12. These extend down to roughly 60^o ILAT.

In Figure 4.18(b) is the FAST satellite mapped electron kinetic energy flux as a function if ILAT and time for the same 26 day interval. FAST has coverage down to about 61^o ILAT for the April-May 1998 event. During the active times, at low latitude (≤ 65^o ILAT) the electron kinetic energy flux intensifies up to a few ergs/cm^{2}s to 10s of ergs/cm^{2}s. This region of enhanced intensity extends down to at least where the coverage cut off occurs. The low latitude quiet time values range from < 0.01 to a few ergs/cm^{2}s. The larger intensities seen at low latitude during relatively quiet times (Dst > -30) are

associated with small dips in Dst, indicating association with some level of storm activity. These periods are brief enough that Polar may miss the Poynting flux generated by the small storm (i.e. be in the wrong location to observe them). Above 70^{o} ILAT there is noticeable enhancements in the intensity of electron kinetic energy flux.

Figure 4.18 (c) shows the DMSP F12earthward electron kinetic energy flux mapped to 100km. These intensities tend to be between a few 0.01 ergs/cm^{2}s to around a few 0.1 ergs/cm^{2}s during magnetically quiet times at low latitudes, below about 65^{o} ILAT. Typically the earthward kinetic energy flux with sufficient intensity to cause visible aurora, i.e. intensities at or above 1 erg/cm^{2}s occur above 65^{o} and typically no lower than 68^{o} during the quiet intervals. During geomagnetically active periods the earthward electron kinetic energy flux intensifies at latitudes below 65^{o}; on May 2nd and the 3rd the kinetic energy flux intensity enhancements occur down to about 60^{o}; on May 4th down to about 57^{o}; and on April 24 the kinetic energy flux also enhances down to about 60^{o}. Such enhancements are typically on the order of a few to 10's or ergs/cm^{2}s and can be up to the orders 100 ergs/cm^{2}s in some locations. The DMSP high latitude coverage is sporadic, but the data present in the May 1998 event indicate that during magnetically active times the earthward electron kinetic energy flux intensities at latitude above 80 does not enhance significantly.

The region in time-latitude in which the intense ($\geq$ 1 erg/cm^{2}s) kinetic energy flux extends down to between 68^{o} to 65^{o} in latitude during quiet times and down to ~ 60^{o} to 57^{o} ILAT during active times. The intense kinetic energy flux extends to latitudes up to 75^{o} to the upper 70^{o}s degrees ILAT during active times. There are intervals during quiet

times when the extent in latitude of the more intense ($\geq$ 1 ergs/cm^{2}s) kinetic energy flux is only a narrow interval of a degree or two around 70 degrees ILAT.

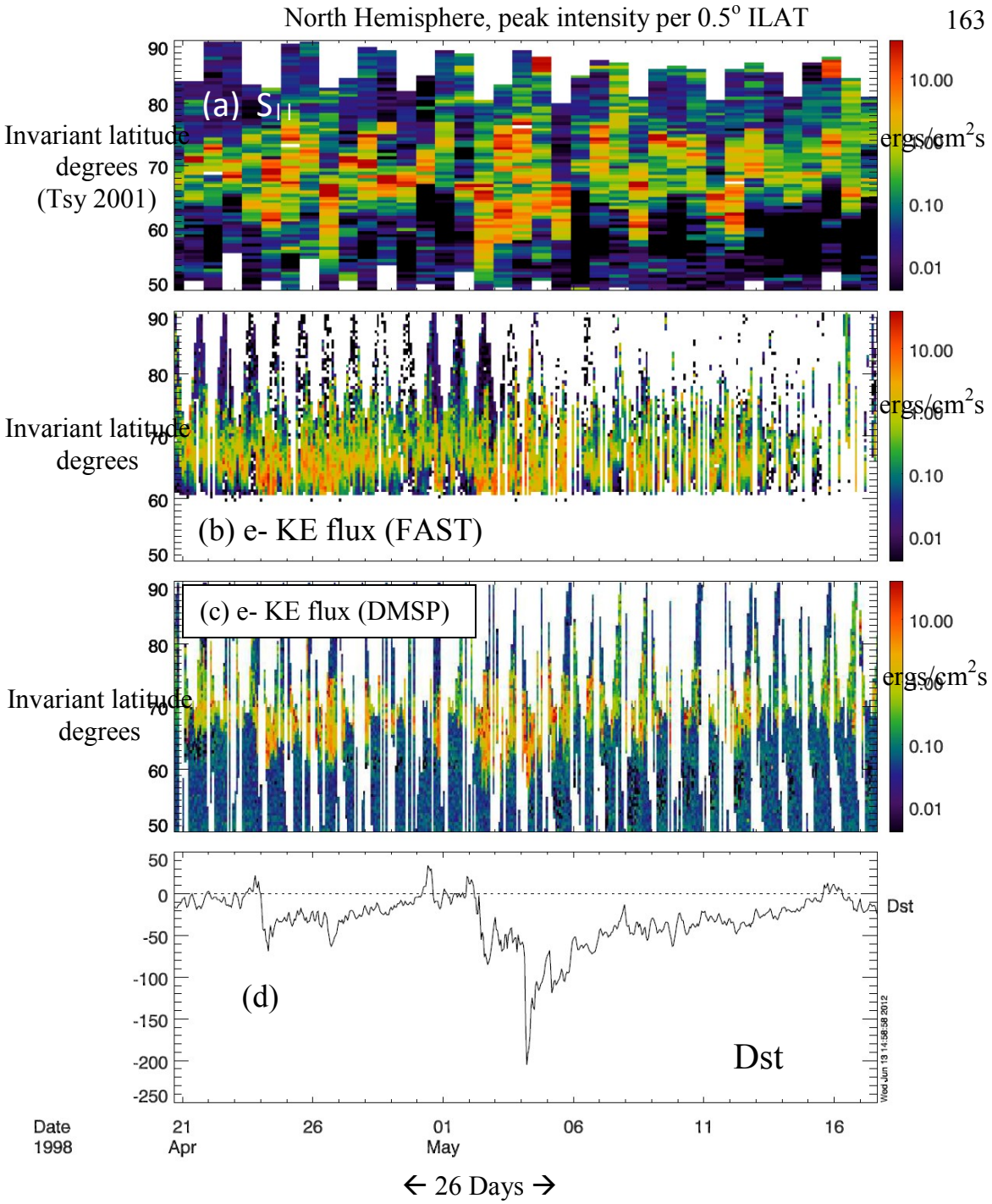

Figure 4.18: Twenty six days of Polar, FAST, and DMSP F12 data, and Dst index, from April 21 to May 17, 1998. In the top panel (a) is high-altitude (Polar), earthward, field-aligned wave (6 – 180 sec) Poynting flux (mapped to 100km) as a function of invariant latitude (ILAT) and time the night side (18 – 6 MLT). The ILAT-sorted peak Poynting flux intensity per 0.5 degree ILAT are coded according to the color bar to the right, and shown over a range of ILAT from 50° to 90° for the 26 days on an orbit-by-orbit basis. The bins are 18 hours (one Polar orbit) wide. In the second panel from the top (b) is the

night side, downward, electron kinetic energy flux at low altitude (FAST satellite) (mapped to 100 km) plotted as a function of ILAT and time, peak intensity per 0.5^o ILAT. Electron kinetic energy flux from FAST below about 61 degrees is unavailable for this event, hence the absence of data below that latitude on the plot in (b). In panel (c) is the night side, downward electron kinetic energy flux (mapped to 100 km) at low altitude (DMSP F12), plotted as a function of ILAT and time. These data are all in reference to the northern hemisphere. In (d) is the Dst index.

In Figure 4.19 is presented the average mapped intensity per 0.5^o ILAT for the night side Polar wave Poynting flux, plotted as a function of ILAT and time (a), the average mapped intensities per 0.5^o ILAT for the night side FAST and DMSP F12 electron kinetic energy flux plotted as a function of ILAT and time in (b) and (c) respectively, and the Dst index for a 26 day interval from April 21, 1998 to May17, 1998. The distribution in time and latitude of the most intense regions of the averaged Poynting flux, Figure 4.19 (a), is similar to that of the peak intensity per bin discussed above. The average Poynting flux at low latitudes during quiet times is on the order of 10^{-4} ergs/cm^{2}s to up to 10^{-2} ergs/cm^{2}s, though typically around 10^{-3} ergs/cm^{2}s. During active times the intensity enhances to 10^{-1} to 1 ergs/cm^{2}s down to ILATs as low as the middle to upper 50^os. There are numerous intervals in latitude in which the average Poynting flux is negative, that is, upwards from the ionosphere. Most of these upward Poynting flux are small, 0.001-0.001 ergs/cm^{2}s (averaged and mapped) with a smaller number of regions where the upward intensity is 0.5 ergs/cm^{2}s. One such region of these more intense upwards Poynting flux are show in Figure 4.2(c). However, the majority of the bin values are positive, i.e. have average earthward Poynting flux.

Figure 4.19(b) shows the average intensity per 0.5^o ILAT of FAST electron kinetic energy flux (mapped). This averaged latitudinal evolution is similar to that displaying the peak per 0.5^o ILAT, but roughly lower by a factor of 2 or 3. Figure 2.19(c) shows the average intensity per 0.5^o ILAT of DMSP F12 electron kinetic energy flux. As was the case with FAST, the DMSP averaged latitudinal evolution of electron kinetic energy flux is similar to that for the peak intensities per 0.5^o ILAT, but roughly lower by a factor of 2 or 3.

The latitudinal evolution for the night side, high altitude Poynting flux and low altitude electron kinetic energy flux peak intensity enhancements are similar; in both cases the region of intense ($\gtrsim$ 1 ergs/cm^{2}s) Poynting and electron kinetic energy flux extend to low latitudes of 55^o to 60^o ILAT, and these low latitude enhancements have values of $\sim$1-10s ergs/cm^{2}s. These low latitude enhancements represent increase over their quiet time values by two to three orders of magnitude. The similarity in the latitudinal evolution of intensities suggests that the high altitude Poynting flux is important for the low altitude electron acceleration processes. The overall decrease the averaging introduces to the mapped Poynting flux intensities in Figure 4.19 (a) is compared to the averaging of the electron kinetic energy flux is a reflection of the fact that the observed Poynting flux tends to carry less energy than the electron kinetic energy flux.

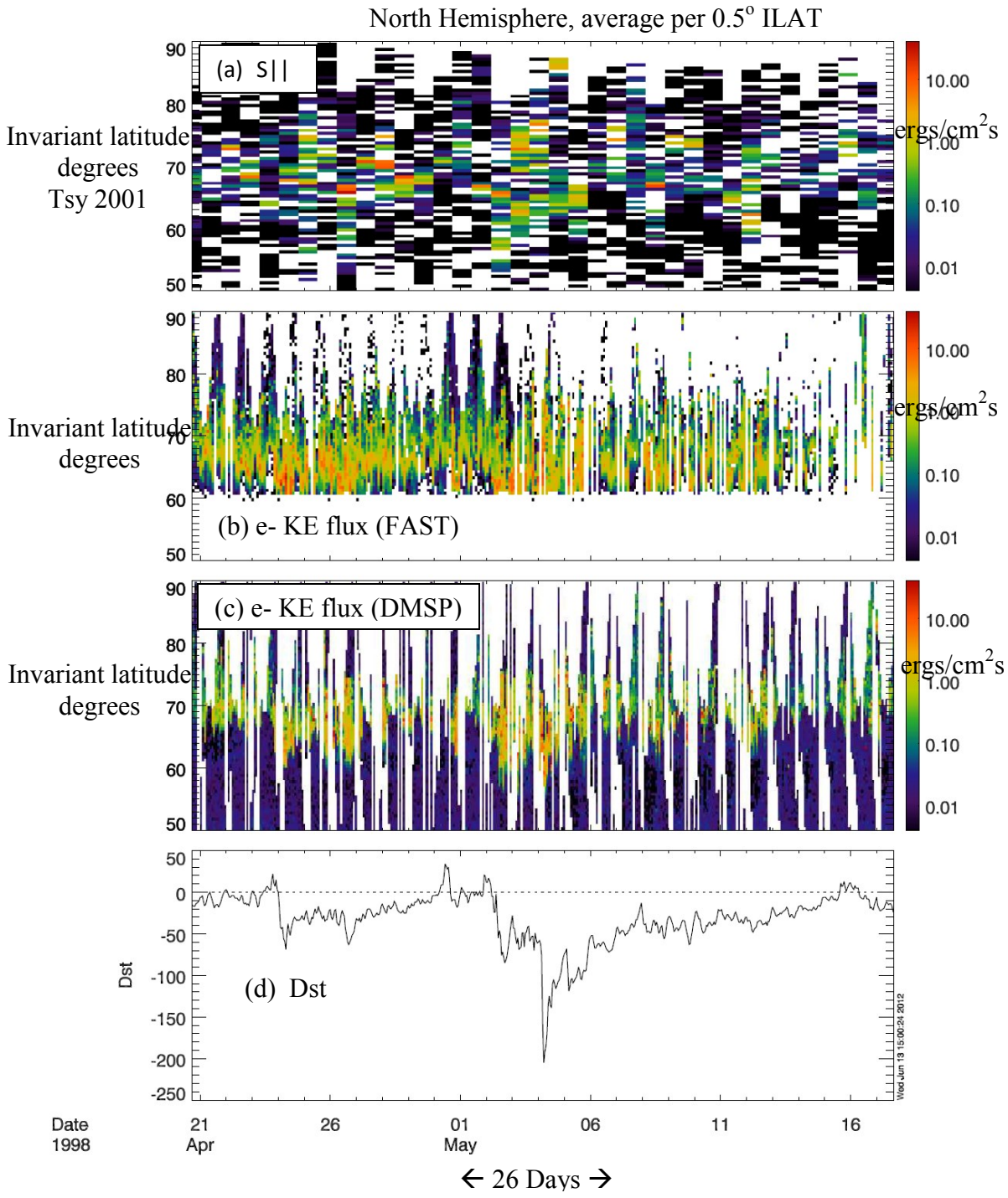

Figure 4.19: Twenty six days of Polar, FAST and DMSP data and Dst index, for April 21-May 17, 1998. The average mapped Poynting flux intensity as a function of ILAT and time is shown in (a) The FAST and DMSP F12 electron kinetic energy flux, mapped,

averaged per 0.5^{o} ILAT, are in panels (b) and (c) respectively. The Dst index in in panel (d).

4.5.2 Event 2: October 17-28 2001

In this section we investigate the latitudinal intensity evolution for the Polar Poynting flux and of the FAST and DMSP electron kinetic energy flux for October 17-28, 2001. Figure 4.20 shows a view of the Polar, FAST and DMPS F15 orbits looking southward from a vantage point north and duskward above the earth on October 22, 2001, the characteristic relative configuration of the orbits for this event. The spacecraft orbits are close to being in the same plane, and their foot points are separated by ~1 hour MLT.

Figure 4.21 presents a Polar VIS image showing visible auroral activity and approximate foot point locations of Polar, FAST and DMSP F15 for an active time on October 22, 2001. During the storm all spacecraft pass through regions of intense aurora. The longitudinally extensive aurora, though not necessarily homogeneous, provide a more suitable circumstance for comparing energetic flux at the different spacecraft, in that, the energetics on field at similar latitudes are likely to be similar .

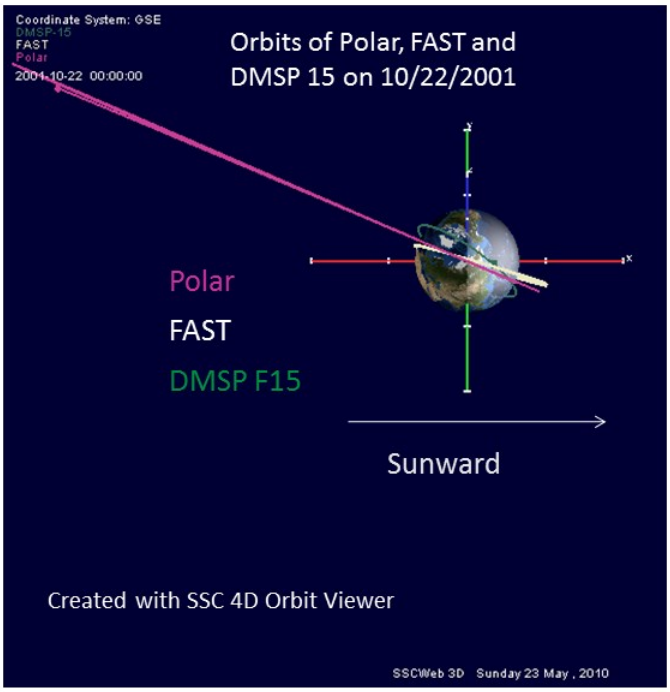

Figure 4.20 The orbits of Polar, FAST and DMSP F15 during the October 2001 event. the orbital planes of the spacecraft are close to one another such that they will sample field lines closely spaced in MLT.

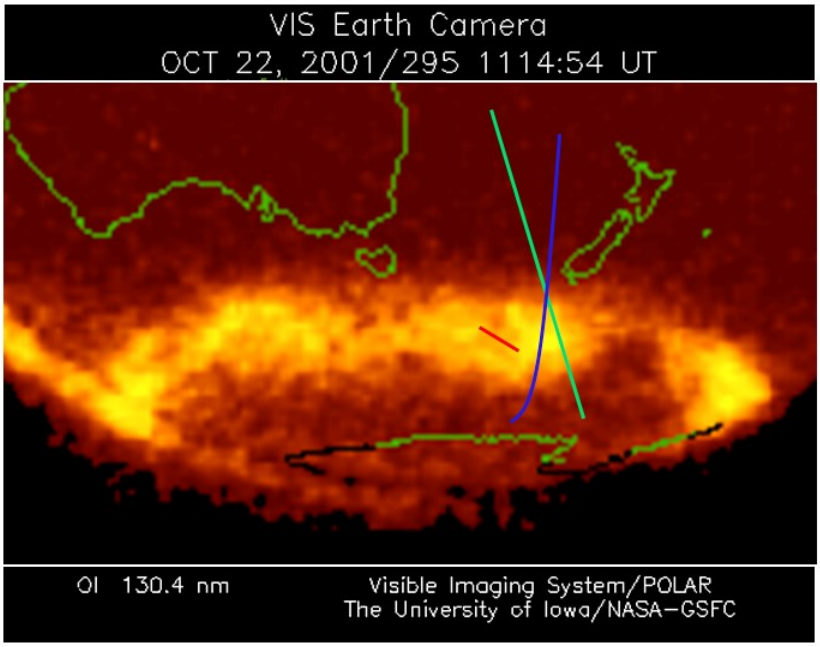

Figure 4.21: A detail of a Polar VIS image showing extensive auroral activity continuous across many hours MLT on the night side during the October 2001 storm. The red green and blue traces are the approximate mapped foot points of Polar, DMSP F15, and FAST respectively.

The interval for the October 2001 event studied herein extends from October 18 to October 26 and encompasses pre-storm activity, main phase, and recover phase of the major geomagnetic storm on October 22. In Figure 4.22(d) is the Dst index showing that the activity is small until about half way through October 19 when the Dst index starts to decrease, reaching -55 nT just before the end of October 19. The recovery of the Dst is interrupted by smaller intermediate storms until 16 UT on October 21when a major storm

occurs with a decrease in Dst to -185 nT. The recovery of the Dst index to zero lasts until October 25. The storm is a double dip, as another storm occurs midway through October 22 in which the Dst dips down from ~-140 nT to -165 nT.

In Figure 4.22(a) is the peak intensity (per 0.5^o ILAT) of the night side, Polar (~8-9 R_E), wave Poynting flux mapped to 100km, as a function of time and ILAT latitude for the Southern hemisphere. During the geomagnetically quiet intervals there are localized (± a few degrees of 70^o ILAT) of intense (~few ergs/cm^{2}s) Poynting flux. At higher latitudes intense (1-10s ergs/cm^{2}s) Poynting flux is present, though typically not above about 77 degrees. During storms the Poynting flux intensifies at low latitudes (< 65^o ILAT) from the quiet times values to intensities ~1 to 10s or ergs/cm^{2}s, and up to intensities on the order of 100 ergs/cm^{2}s in some places. During the major storm on October 22 the intense Poynting flux occurs as low as 52 degrees ILAT. Intense Poynting flux is observed at higher latitudes 65^o-76^o during storms as well. Intense Poynting flux between 55^o and 75^o ILAT is extensively present in the three orbits during the major storm from October 21 through October 23. During the Polar orbits on October 19 and 20 the, during the period of moderate activity in Dst, (~-40,-50 nT) intense Poynting flux present between about 62^o and 70^o degrees.

Note that during quiet intervals Polar's coverage of Poynting flux only extends down to latitudes of ~ 65^o ILAT, but that during the storm observations of lower latitude field lines are possible. Figure 4.23 shows the Polar orbit and stretched (T01 generated) magnetic field lines for the orbit on October 22, 2001. During this event, Polar's apogee is on the night side and can only sample field lines mapping to the lower latitudes (below

~ 65^{o}) during geomagnetically active periods when these low latitude field lines become stretched tail-ward, and extend out to Polar's orbit.

In Figure 4.22(b) is the FAST electron kinetic energy flux data from the Southern hemisphere for the October 2001 event. During the magnetically quiet intervals, the low latitude (≤65^{o} ILAT) peak kinetic energy flux of precipitating electrons is typically less than 0.01 ergs/cm^{2}s. During storms, electron kinetic energy flux enhancements to intensities on the order of 1 to 10 ergs/cm^{2}s extend down to low latitude to ~55^{o} ILAT. This is a two to three order of magnitude storm time enhancement in the kinetic energy flux intensity at low latitudes during the major storm from October 21, 18:30 UT to almost the end of the day October 22. The low latitude extent of the enhanced electron kinetic energy flux recovers poleward to above low latitudes by around 12UT October 23. The upper latitude limit of intense (>1 erg/cm^{2}s) electron kinetic energy flux typically is around 68^{o} to 74^{o} ILAT, with brief intervals occurring at high latitudes, up to 80^{o} ILAT.

In Figure 4.22 (c) is the DMSP F15 peak electron kinetic energy flux for the southern hemispheres as a function of time and ILAT. During the magnetically quiet intervals, the low latitude kinetic energy flux of earthward electrons is typically on the order of ~0.1 ergs/cm^{2}s. During storms at low latitudes, these electron kinetic energy flux typically enhance to intensities on the order of ~1 to 10 ergs/cm^{2}s; and up to an order of 100 ergs/cm^{2}s in a few localized areas. These two to three order of magnitude intensity

enhancements in the kinetic energy flux extents down to as far as about 54^{o} during the major storm from October 21 18:30 UT to near the end of the day October 22. The low latitude extent of the enhanced electron kinetic energy flux recovers poleward of low latitudes around 16 UT on October 23. The upper latitude limit of the extensive, intense (>1 erg/cm^{2}s), electron kinetic energy flux is typically is around 70^{o} ILAT, with brief intervals occurring at high latitudes. The occurrence of intense electron kinetic energy flux does not appear to be strongly dependent on geomagnetic activity. There is some evidence in both the FAST and DMSP electron data that the upper limit to the extent in ILAT characterized by intense electron kinetic energy flux decreases to about 68-70 degrees during the major storm.

The FAST and DMSP south hemisphere electron kinetic energy flux intensity latitudinal evolutions are remarkably similar to one another. The orbital plains for both spacecraft are close, with in a couple hours MLT (21 DMSP and 19-22 for FAST). While the distribution in time and latitude of the intense electron kinetic energy flux for DMSP and FAST are similar, the FAST electron kinetic energy flux is not as intense as the DMSP electron kinetic energy flux. One possible reason for this is because the FAST electron data used is the spin average data, which is the net average electron kinetic energy flux over one ~5 seconds spin period. The DMSP data are at a one second cadence, and only use the downward electrons.

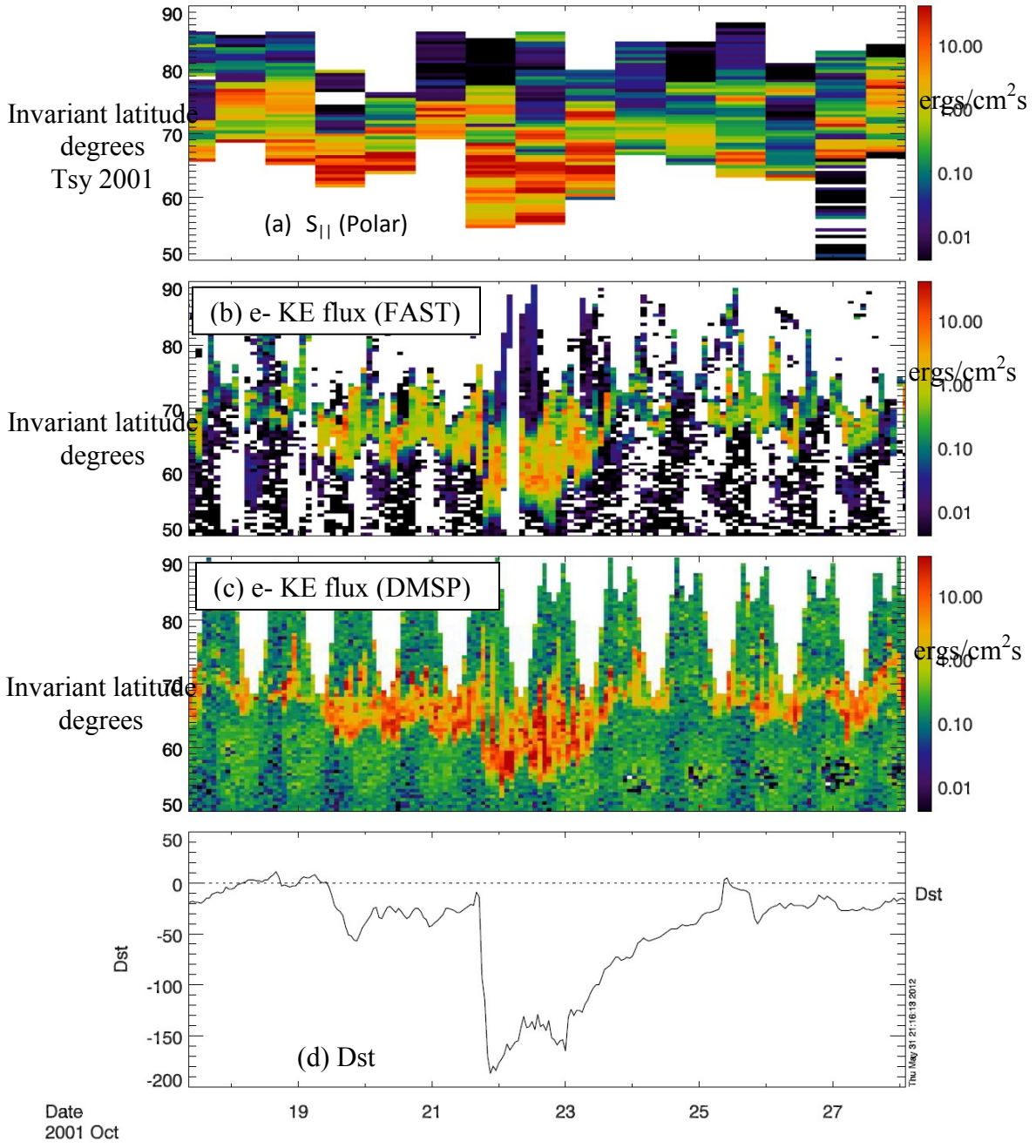

Figure 4.22: Ten and a half days of Polar, FAST, and DMSP F15 data and Dst index, from October 17 to October 28, 2001. The spacecraft data are from the southern hemisphere, on the night side of the earth. In the top panel (a) is high-altitude (Polar SC), earthward, field-aligned wave (6 – 180 sec) Poynting flux (mapped to 100km) as a function of invariant latitude (ILAT) and time. The ILAT-sorted peak mapped Poynting flux intensity per 0.5° ILAT are coded according to the color bar to the right, and shown over a range of ILATs on an orbit-by-orbit basis. The bins are 18 hours (one Polar orbit)

wide. In the second panel from the top (b) is the downward electron kinetic energy flux at low altitude (FAST satellite) (mapped to 100 km) plotted as a function of ILAT and time, peak intensity per 0.5° ILAT, with the bines being one FAST orbit wide, ~2.2 hours. In panel (c) is the night side, peak down-going electron kinetic energy flux (mapped to 100 km) at low altitude (DMSP F12), likewise plotted as a function of ILAT and time. In (d) is the Dst index.

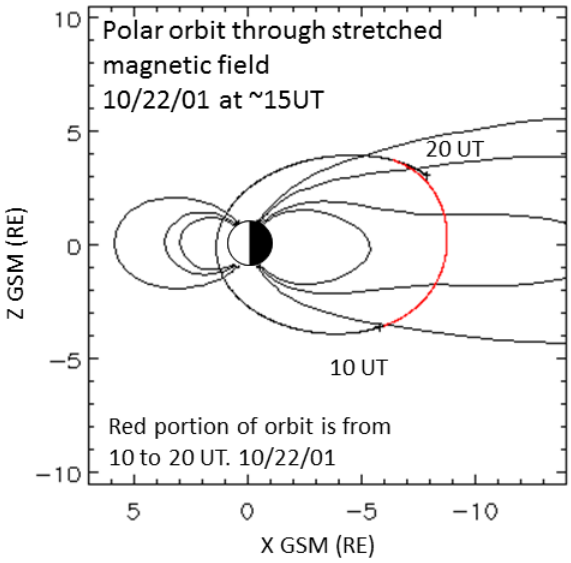

Figure 4.23: The Polar orbit and stretched magnetic field lines on October 22, 2001. For this event Polar's apogee is on the night side and can only sample field lines mapping to lower latitudes ($\lesssim 65^{o}$ ILAT) during geomagnetically active periods when these low latitude field lines become stretched tail-ward, and extend out to Polar's orbit. The red segment of Polar's orbit takes ten hours to traverse, and corresponds to the region where intense night side Poynting flux are observed.

In Figure 4.24 the average mapped intensities of the Polar Poynting flux, FAST and DMSP F15 electron kinetic energy, per 0.5° ILAT, for the Southern Hemisphere are presented. Figure 4.24 (a) is the average mapped wave Poynting flux intensity. These

Poynting flux are often significantly reduced, typically by an order of magnitude or two, compared to the corresponding peak intensities shown in Figure 4.22(a). Typical values of the averaged Poynting flux are 0.01-0.5 ergs/cm^{2}s. There are locations, including low latitude locations, in which the averaged Poynting flux is intense, over 1 erg/cm^2, during the storm (October 21 and 22) and on October 19.

In some intermittent locations, over widths of 0.5^o -2^o ILAT, the average Poynting flux is upwards. These upward values are negative by the convention used, and so on the log scale used the area of net upward Poynting flux appear white rectangles, since the negative values cannot be plotted on the log scale. Inspection of these data indicate that the upward intensities tend to be smaller than the downward flux. Typically these averages upward intensities are of the order ~0.001-0.1 ergs/cm^{2}s.

In Figure 4.19(b) and Figure 4.19(c) is the averaged intensity of the FAST and DMSP F15 downward electron kinetic energy fluxes per 0.5^o ILAT. The latitudinal evolution of these intensities is similar to the cases in which the peak per 0.5^o ILAT is used. The averaging appears to reduce the intensities by a factor between 2 and 4.

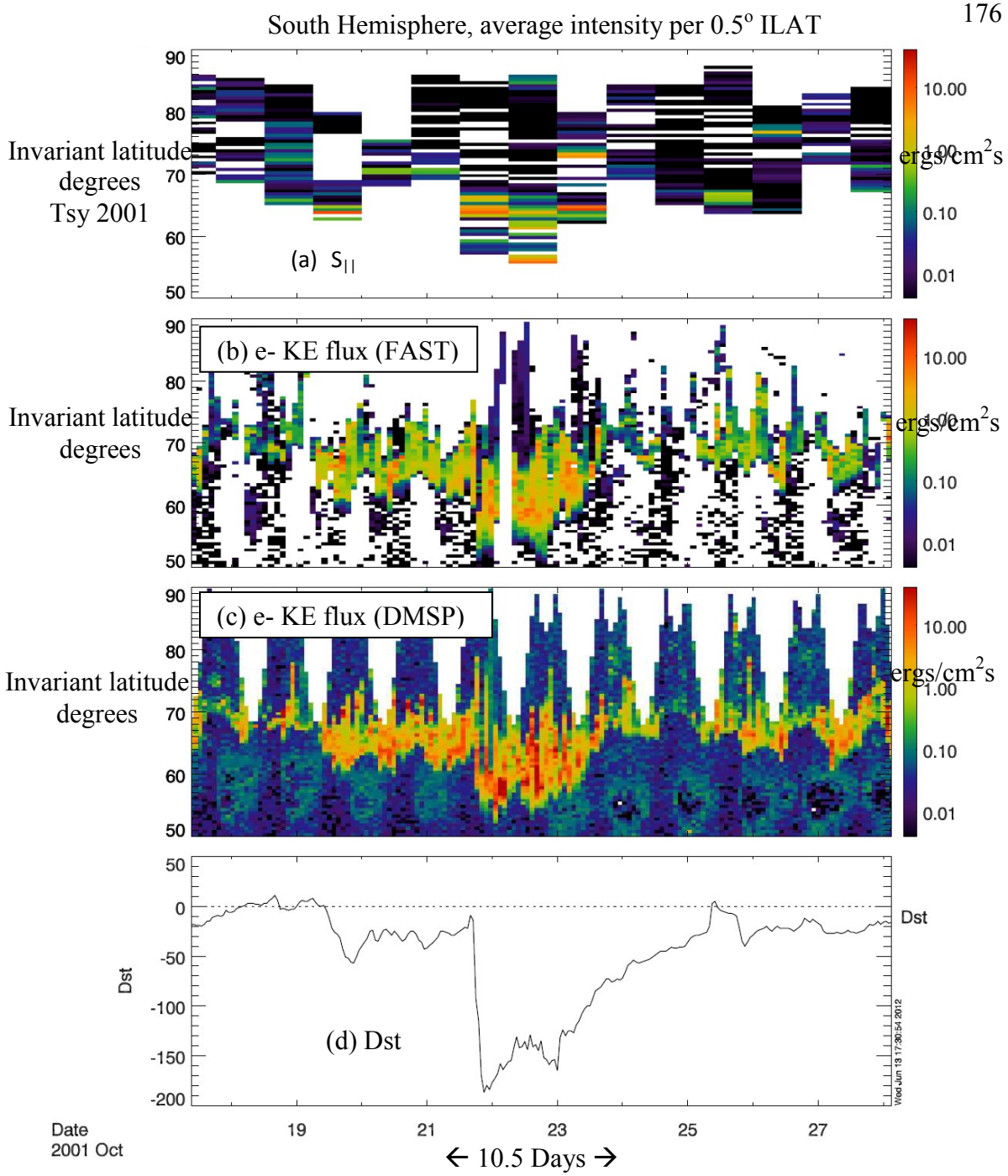

Figure 4.24: Ten and a half days of southern hemisphere, night side, Polar, FAST, and DMSP F15 data and Dst index for October 17-October 18, 2001. The average intensity per 0.5° ILAT of the mapped field aligned wave Poynting flux is shown in (a) and the average intensities per 0.5° ILAT of the mapped FAST and DMSP F15 downward electron kinetic energy flux are shown in (b) and (c) respectively. The Dst index is shown in (d).

Polar and DMSP F15 both also have north hemisphere night side data for the October 2001 event, but FAST does not. In Figure 4.25 are the northern hemisphere, night side, Polar spacecraft wave Poynting flux and DMSP F15 electron kinetic energy flux, peak intensities per 0.5^{o} ILAT. The latitudinal evolution of the peak intensity of the high altitude Poynting flux, Figure 4.25(a), and of the low altitude DMSP electron kinetic energy flux, Figure 4.25(b) are similar to their southern hemisphere counterparts, shown in Figure 4.22(a) and Figure 4.22(c) respectively. As was the case in the southern hemisphere, in the northern hemisphere the latitudinal evolutions of the peak intensities of high altitude Poynting flux and of the low altitude DMSP electron kinetic energy flux are similar, and intense wave Poynting and electron kinetic energy flux both reach low latitudes during the major storm. Figure 4.24 shows the average intensities of the Polar wave Poynting flux and DMSP electron kinetic energy flux per 0.5^{o} ILAT, for the night side, northern hemisphere. The relation is similar to that shown in Figure 4.24.

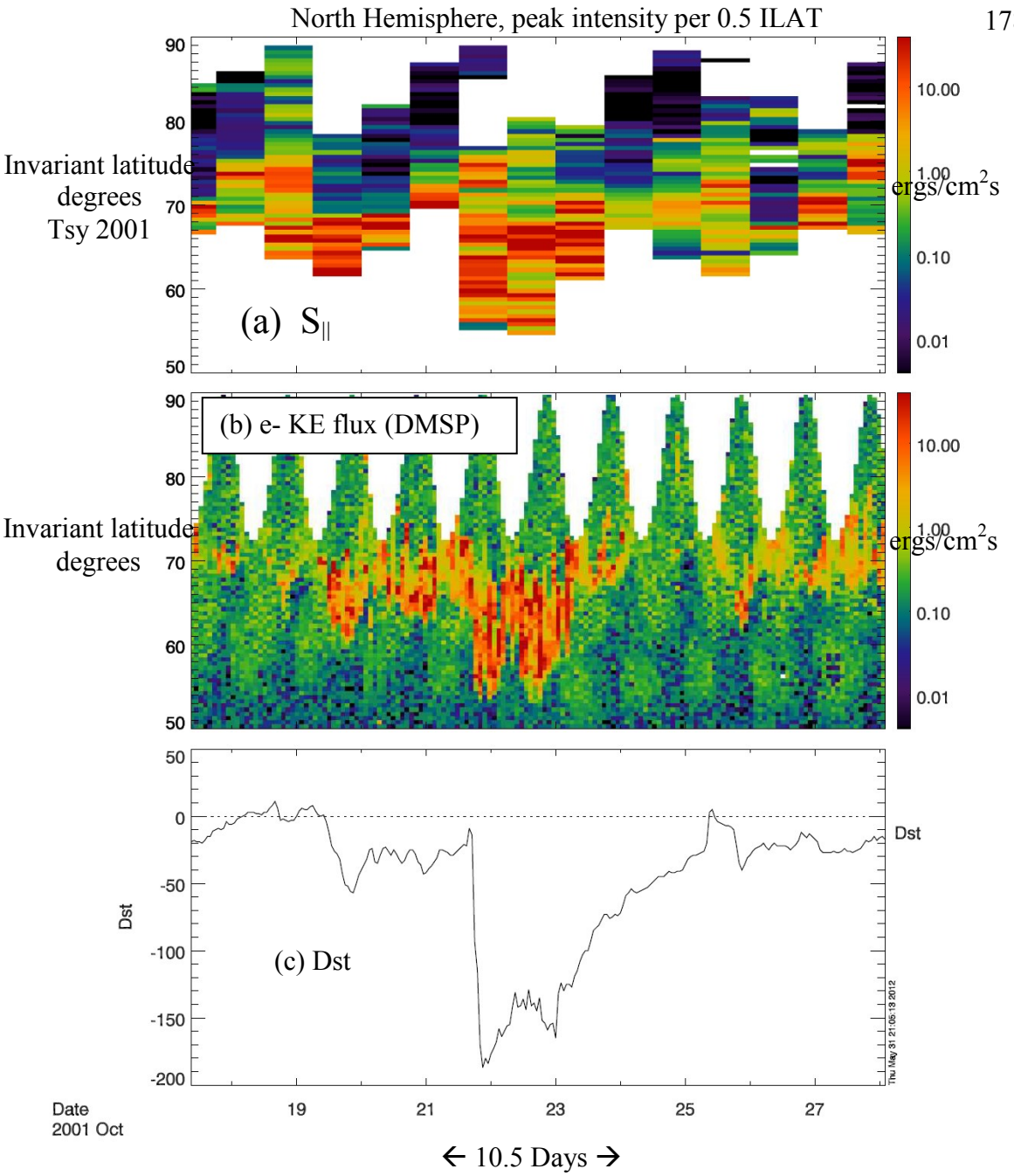

Figure 4.25: Ten and a half days of Polar and DMSP F15 from the night side, northern hemisphere, and Dst index. In (a) is the field-aligned, earthward, high altitude (Polar) wave Poynting flux (mapped), and in (b) is the downward, mapped, low altitude (DMSP F15) electron kinetic energy flux (both peak intensity per 0.5^{o}) as a function of ILAT and time. In (c) is the Dst index.

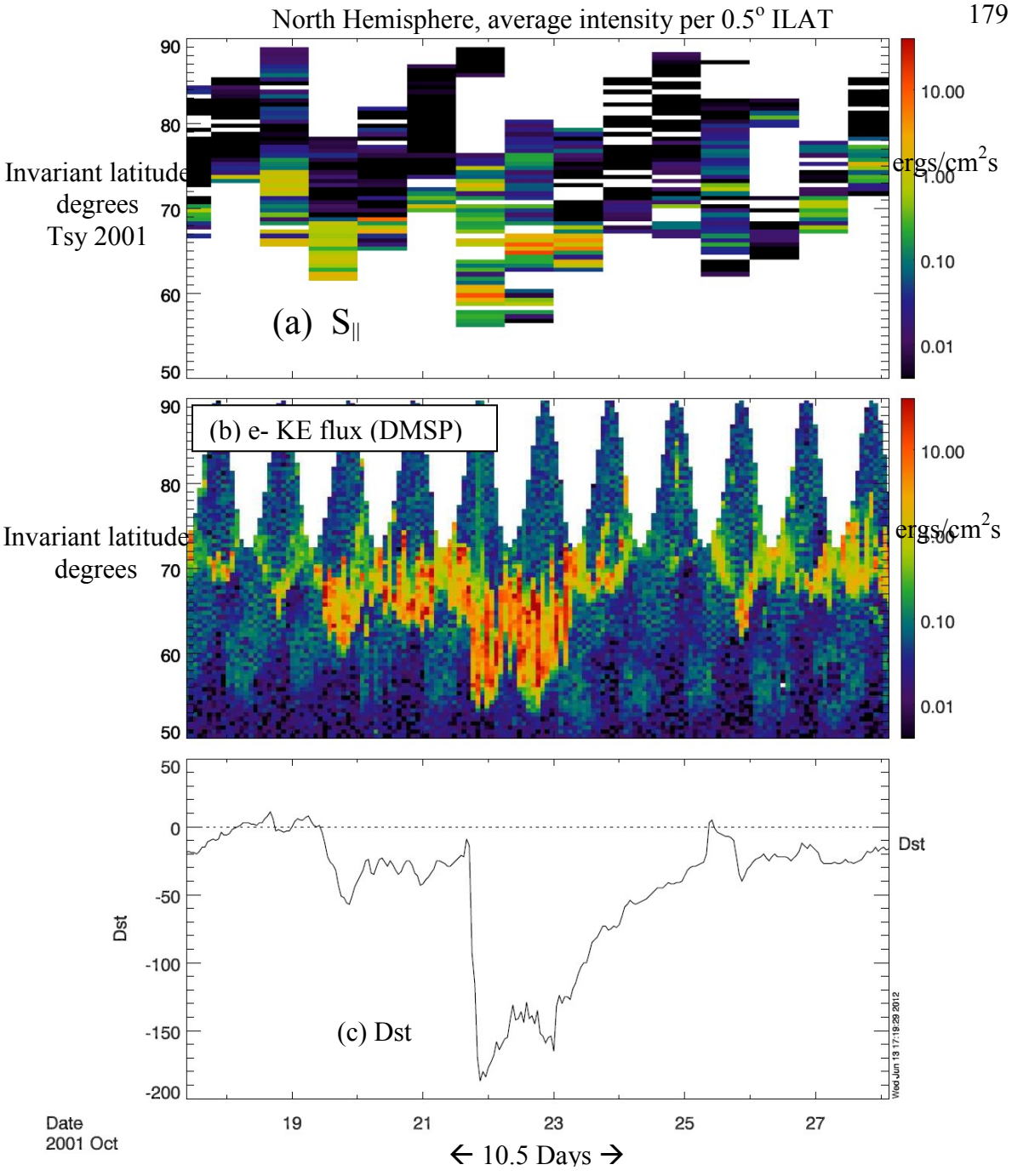

Figure 4.26: Ten and a half days of northern hemisphere, night side, Polar and DMSP F15 data and Dst index for October 17 - October 18, 2001. The average intensity per 0.5° ILAT of the mapped field aligned wave Poynting flux is shown in (a) and the average intensity per 0.5° ILAT of the mapped DMSP F15 downward electron kinetic energy flux are shown in (b). The Dst index is shown in (c).

The latitudinal evolution of the mapped intensity (peak per 0.5^{o} ILAT) of both the high altitude field-aligned earthward wave Poynting flux and low altitude earthward electron kinetic energy flux are similar in terms of intensity and over all distribution in time and ILAT for both the April-May 1998 and October 2001 events. In particular, the low latitude intensifications in the Poynting and electron kinetic energy flux are well correlated with one another. The fact that energy to power auroral process comes from high altitudes suggests that the relation between the Poynting flux and electrons may be a causal one, with the Poynting flux providing, at least some, of the energy for the auroral electron acceleration processes described in chapters 1 and 2. However it is also observed the averaged intensities of the Poynting flux are often significantly smaller than the averaged intensities in electron kinetic energy flux, suggesting that only a portion of the total energy needed for the acceleration of the electrons can be provided by the wave Poynting flux. Examination of the integrated fluxes of individual also suggests this, but under the assumption that the plasma structures carrying the intense Poynting flux are localized and that Polar traverse them with a relative velocity equal to its orbital velocity. Typically the wave Poynting flux can only account for roughly ~5-20% of the energy needed to power the acceleration of downward electrons. The fact that the regions of intense Poynting flux and electron kinetic energy flux are approximately coextensive over the course of major storm (including at low latitudes) suggests that they are tied to similar energetic or generative mechanisms; that the downward, low altitude electrons, even if not directly accelerated by the Poynting flux are likely powered by energy from tail processes which also are involved with the generation of the Poynting flux. Possible

relations may include: 1.) direct acceleration by Alfvén wave Poynting flux via acceleration mechanisms at low altitude, 2.) Alfvén wave generation of waves that scatter already accelerated electrons into the loss cone 3.) the simultaneous generation of both Poynting flux and accelerated electrons further back in the tail. Investigation of the electron kinetic energy flux at Polar is left for future work.

4.6 Conclusions

The main observations and conclusion from the above are:

1.) The latitudinal evolution of intensity of the night side (18 – 6 MLT), high-altitude (Polar S/C), earthward field-aligned, wave (5.5 – 166 mHz or 6-180 sec) Poynting flux (mapped to 100 km), and of the night side, low-altitude (FAST and DMSP), downward electron kinetic energy flux (mapped to 100km) on an orbit-by-orbit basis over intervals of ~10-20 days containing the pre-storm, main phase, and recovery phase, of major geomagnetic storms, are similar when expressed as the peak intensity per 0.5^{o} ILAT. The fact that the high and low altitude latitudinal evolutions of these intensities correspond with each other suggests that there is a generative relation between them that exists over the course of the storm; either some of the electrons are accelerated by the waves or the electrons and waves are both produced by some third mechanism.

2.) The comparison between the average intensities (per 0.5^{o} ILAT) of the mapped Poynting and electron kinetic energy flux, as a function of ILAT and time,

suggest that there is more energy carried by the electrons than the Poynting flux. Comparisons of the mapped wave Poynting flux to auroral images and to integrated electron kinetic energy flux, suggests the Poynting flux carries anywhere from ~10% to 500% of the energy needed to drive the low altitude electron acceleration processes.

3.) During magnetically quiet times (Dst > -30nT) the night-side, earthward, field-aligned wave Poynting flux peak intensities (mapped to 100km) at low latitudes (<65^{o} ILAT) are typically on the order of 10^{-3} to 10^{-2} ergs/cm^{2}s. During major storms (Dst ≤ -150 nT) the Poynting flux typically intensify about three orders of magnitude to 1 to 10 ergs/cm^{2}s, with such enhancements extending down to latitudes of at least 55^{o} ILAT. The low latitude (≤ 65^{o} ILAT), low altitude electron kinetic energy flux (peak intensities) are typically on the order of 0.1 ergs/cm^{2}s pre storm, and intensifies to the order of 1 to 10s ergs/cm^{2}s during storms.

4.) The existence of intense Poynting flux (≳1 erg/cm^{2}s) at low latitudes (in both peak and average values), at latitudes similar to those at which intense downward electrons are observed, suggest that Alfvén waves are important for, or at least closely related to, low latitude auroral acceleration processes.

5.) The similarity between the peak Poynting flux and electron kinetic energy flux distributions in time and latitude, suggests that Alfvénic auroral may occur

throughout the region of enhanced auroral activity over the duration of major storms, as well as during less active times.

Chapter 5

Comparisons between the large scale and small scale (wave) Poynting flux.

5.1 Introduction

The large scale convection cycle of magnetic field lines from the day side to the night side and then sunward again drives plasma convection in the ionosphere (as discussed in chapter 1) and the associated field aligned currents closing through the ionosphere. As a result, energy dissipation in the ionosphere via Ohmic heating occurs in association with the closing Pedersen currents. The electromagnetic energy transfer from the magnetosphere to the ionosphere corresponds to a Poynting vector that can be determined through the electric field associated with the field line motion and the magnetic field perturbations associated with the field aligned current and field line motion. This is in contrast to the Poynting vector that one would obtain by crossing the electric field into the total magnetic field, which represents the electromagnetic energy transfer of the magnetic energy contained in the convecting flux tubes themselves. The large scale electric fields, magnetic perturbations and corresponding Poynting flux are associated with the stress transferred from the magnetosphere to the ionosphere. Here we refer to this as the "large scale" Poynting flux, and use a field perturbation range of 600-7200 seconds, or 10 minutes to 2 hours, to determine the perturbation fields associated with this process. In this wave period range, the E to B ratio is typically 100-300 km/s, which

is well in the range expected of ionosphically couple Poynting flux, typically 80-800 km/s. In some places the E to B ratio approaches that for the Alfvén speed, ~1000km/s. The wave period range in between that of the small scale (Alfvénic) waves in the range of 6-180 seconds, and the large scale Poynting flux, 600-7200 sec., is a mixture of Alfvénic and ionospherically coupled waves, with E to B ratio of 500-1000 km/s.

In this chapter, we compare the large scale Poynting flux to the "small scale" or wave Poynting flux in the 6 to 180 second period range investigated in chapter 4. The large scale Poynting flux are calculated in the same manner as the wave Poynting flux, described earlier (chapter 4), the only difference being that a different field perturbation range is used.

The comparison between the large and small scale Poynting flux is done in two ways. The first way is by comparing the small and large scale Poynting flux as a function of time for three intervals during individual night side passes, characterized by moderate substorm, a major storm, and recovery phase, respectively. We also compare the integrated Poynting flux values. The second kind of comparison consists in the examination of the latitudinal evolution of the Poynting flux intensities over the course of two major storms.

Both the wave and large scale Poynting fluxes play an important role in driving ion outflows [Zheng et al, 2005]. One causal pathway from the Poynting flux to ion outflow, as presented by [Strangeway et al., 2005], is as follows: Poynting flux → Joule Dissipation → Ion Scale Height Increase → Ion Upwelling → ELF/VLF waves (possibly

also powered by Poynting flux, heats ions) → Ion Outflows. Ion outflows are an important process; they supply oxygen ions to the magnetospheric plasma. The presence of oxygen in the magnetosphere lowers the Alfvén speed (as was discussed in chapter 4). The oxygen ions also can be further energized and become part of the population of ring current ions. Thus the large scale Poynting flux plays a role in determining these aspects of magnetosphere dynamics.

5.2 Comparison between wave and large scale Poynting flux during individual Polar orbit passes on the night side

In this section we compare the wave (6 – 180 sec.), or small scale, Poynting flux to the large scale (600 – 7200 sec.) Poynting flux associated with field line convection and field aligned currents, and integrated values thereof, during three different intervals from October 2001, characterized by three different levels of geomagnetic activity. These three levels of geomagnectic activity are; 1- moderate substorms, but small Dst; 2- major storm, and 3- recovery phase with low substorm activity. The three intervals used are the same three used in chapter 4 section 4.4. This comparison allows us to assess the relative contributions of these two forms of electromagnetic energy flux incident on the ionosphere, i.e. how much of the energy is in the form of Alfvén waves and how much is transferred by field aligned current, and convecting field lines.

Figure 5.1 shows the mapped wave and large scale Poynting fluxes, observed at Polar, during an eight hour (14:00 – 22:00 UT) night side pass on October 18, 2001. As is shown in Figure 5.1(e,f) this period is characterized by quiet Dst and moderate substorm

activity as indicated by AE; the Dst varies between -4 and 10 nT, the AE index is between 50 and 150 nT. The peak AE is associated with a substorm starting around 17:00 UT during which there are local peaks in the both the small-scale/wave and large scale Poynting flux. The substorm activity peaks around 18:00 UT then there are smaller substorms near 19:00 UT and 19:40 UT, and moderate activity in the AE index after. In Figure 5.1(a) shows the field aligned wave Poynting flux, mapped, and Figure 5.1(c) shows the field aligned large scale Poynting flux, mapped. The large local peak values in the wave and large scale Poynting flux are of intensities of 40 – 110 ergs/cm^{2}s and 4-15 ergs/cm^{2}s respectively. These intensity peaks tend to occur around the same time, and often, but not always, during, or at the commencement of activity in the AE index. Figure 5.1(b) and Figure 5.1(d) show the mapped integrated values of the wave and large scale Poynting flux along the Polar foot point. For the whole eight hour interval the integrated wave and large scale Poynting flux are 3.3x10^{7}ergs/cm-s and 6.1x10^7 ergs/cm-s respectively. Thus while the local peak intensity is about an order of magnitude larger for the waves, the large scale Poynting flux carries almost twice the energy.

This integration is done assuming the relative motion between Polar and the plasma structures to be that of the spacecraft. And that both kinds of Poynting flux are primarily present in localized regions which Polar passes through. Since both quantities are at Polar, the relative velocity should be the same for both, and so, for a relative comparison, knowing the velocity is not as important. However the relative extent to which each kind of Poynting flux fills the night side magnetosphere, i.e. whether each or either exists in

localized structures seen by Polar, or exists over a much broader expanse is not known.

The integration is done in the same manner for the following two events in this section.

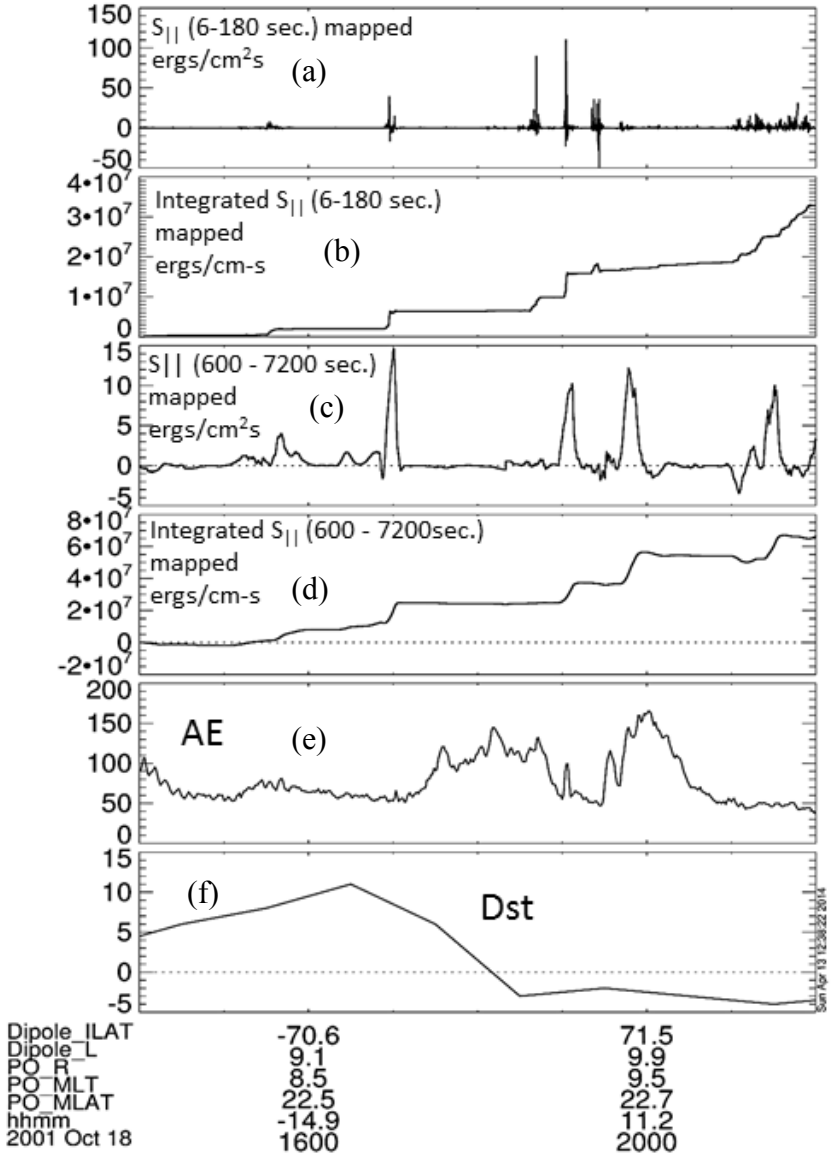

Figure 5.1: Eight hours of Polar data, Dst, and AE indices, from14:00-22:00 UT on October 18, 2001. (a) The earthward, field aligned wave (6-180 sec) Poynting flux at Polar, on the night side, mapped to 100km. (b) The integrated wave Poynting flux from

(a) along the mapped spacecraft trajectory. (c) The earthward, field aligned, large scale (600- 7200 sec.) Poynting flux at Polar, mapped to 100 km. (d) The large scale Poynting flux in (c) integrated along the mapped spacecraft foot point trajectory. (e) The Dst index, and (f) the AE index.

Figure 5.2 shows ten hour of wave and large scale Poynting flux (mapped intensities) observed at Polar during the major storm on October 22, 2001. During this interval, the Dst is ~-140 nT, and the AE is ~500 -2000 nT, as can be seen in Figure 5.2(e) and Figure 5.2(f) respectively. Figure 5.2(a) is the mapped wave Poynting flux, which exhibits intense local peaks ranging from ~40 ergs/cm^{2}s to ~270 ergs/cm^{2}s. The localized bursts of intense Poynting flux tend to occur around increases in the AE index, shown in Figure 5.2 (e), suggesting that the energy being carried by these waves may have been released during a substorm. Figure 5.2(c) shows the mapped field aligned large scale Poynting flux for this interval. The localized peaks in the large scale Poynting flux are in the range from 9 ergs/cm^{2}s to 30 ergs/cm^{2}s. These peaks tend to occur around the same time as the peaks in wave Poynting flux intensity.

Figure 5.2(b) shows the integrated wave Poynting flux, and in Figure 5.2(d) is the integrated large scale Poynting flux. Over the ten hour interval the integrated values for the wave and large scale Poynting flux are, 2.1x10^8 ergs/cm-s and 3.0x10^8 ergs/cm-s respectively. Thus the wave Poynting flux carries about 2/3 the energy of the large scale Poynting flux.

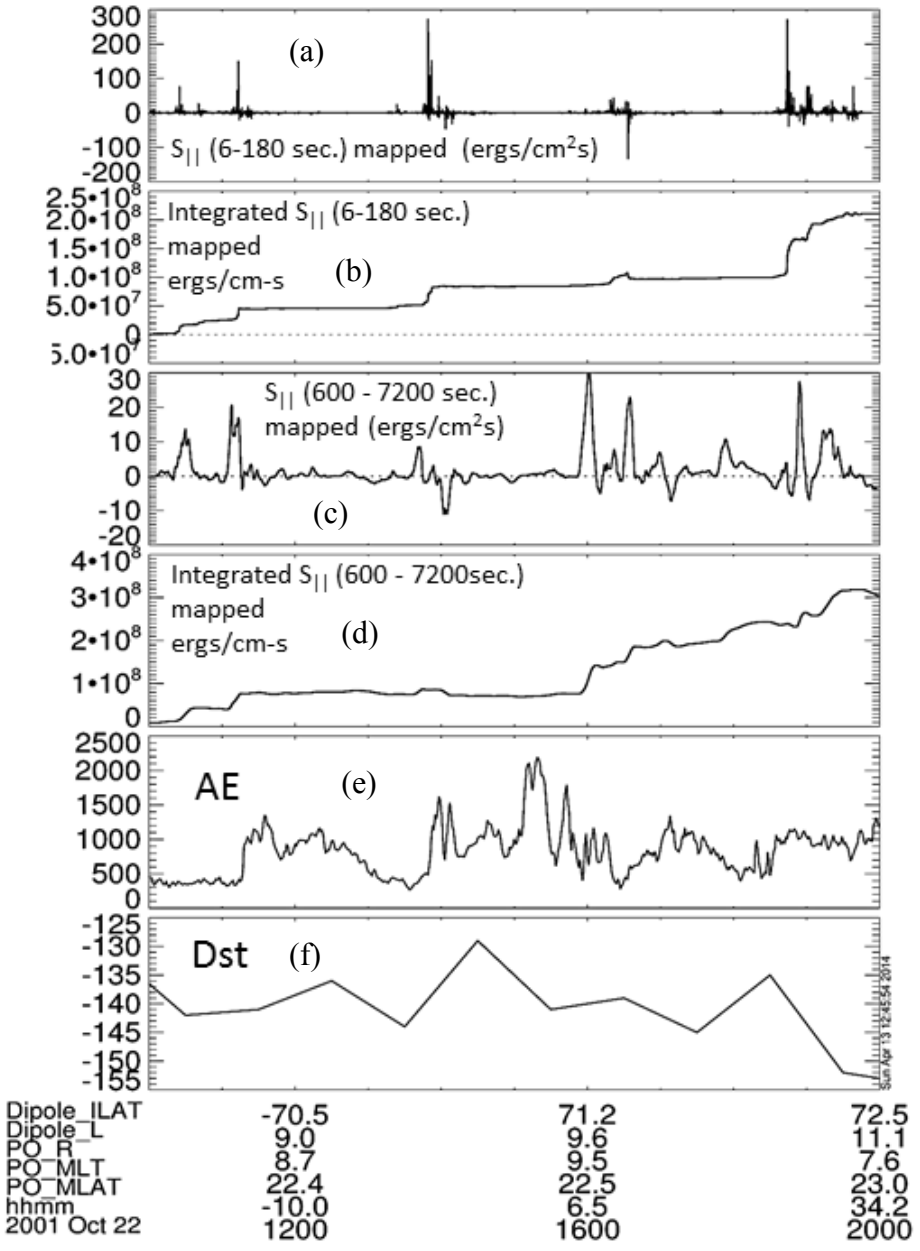

Figure 5.2: Ten hours of Polar data, Dst, and AE indices, from10:00-20:00 UT on October 22, 2001. (a) The earthward, field aligned wave (6-180 sec) Poynting flux at Polar, on the night side, mapped to 100km. (b) The integrated wave Poynting flux from (a) along the mapped spacecraft trajectory. (c) The earthward, field aligned, large scale (600- 7200 sec.) Poynting flux at Polar, mapped to 100 km. (d) The large scale Poynting flux in (c) integrated along the mapped spacecraft foot point trajectory. (e) The Dst index, and (f) the AE index.

Figure 5.3 shows ten hours of wave and large scale Poynting flux (mapped intensities) observed at Polar during the recovery phase on October 24, 2001, following the major storm. During this interval, the Dst is ~-70 nT, and increasing, and the AE is ~20 - ~60 nT, as can be seen in Figure 5.3(e) and Figure 5.3(f) respectively. Figure 5.3(a) is the mapped wave Poynting flux, which exhibits local peaks ranging from ~0.5 ergs/cm^{2}s to ~2 ergs/cm^{2}s. These values are two orders of magnitude smaller than those during the moderate substorm, and major storm intervals discussed above. Figure 5.2(c) shows the mapped field aligned large scale Poynting flux for this interval. The localized peaks in the large scale Poynting flux are in the range from 0.5 ergs/cm^{2}s to 1.5 ergs/cm^{2}s, similar to the peak wave Poynting flux intensities.

Figure 5.3(b) shows the integrated wave Poynting flux, and in Figure 5.3(d) is the integrated large scale Poynting flux. Over the ten hour interval the integrated values for the wave and large scale Poynting flux are, 1.7x10^6 ergs/cm-s and 1.7x10^7 ergs/cm-s respectively. Thus for the quiet interval the wave Poynting flux carries only about 1/10 of the energy of the large scale Poynting flux.

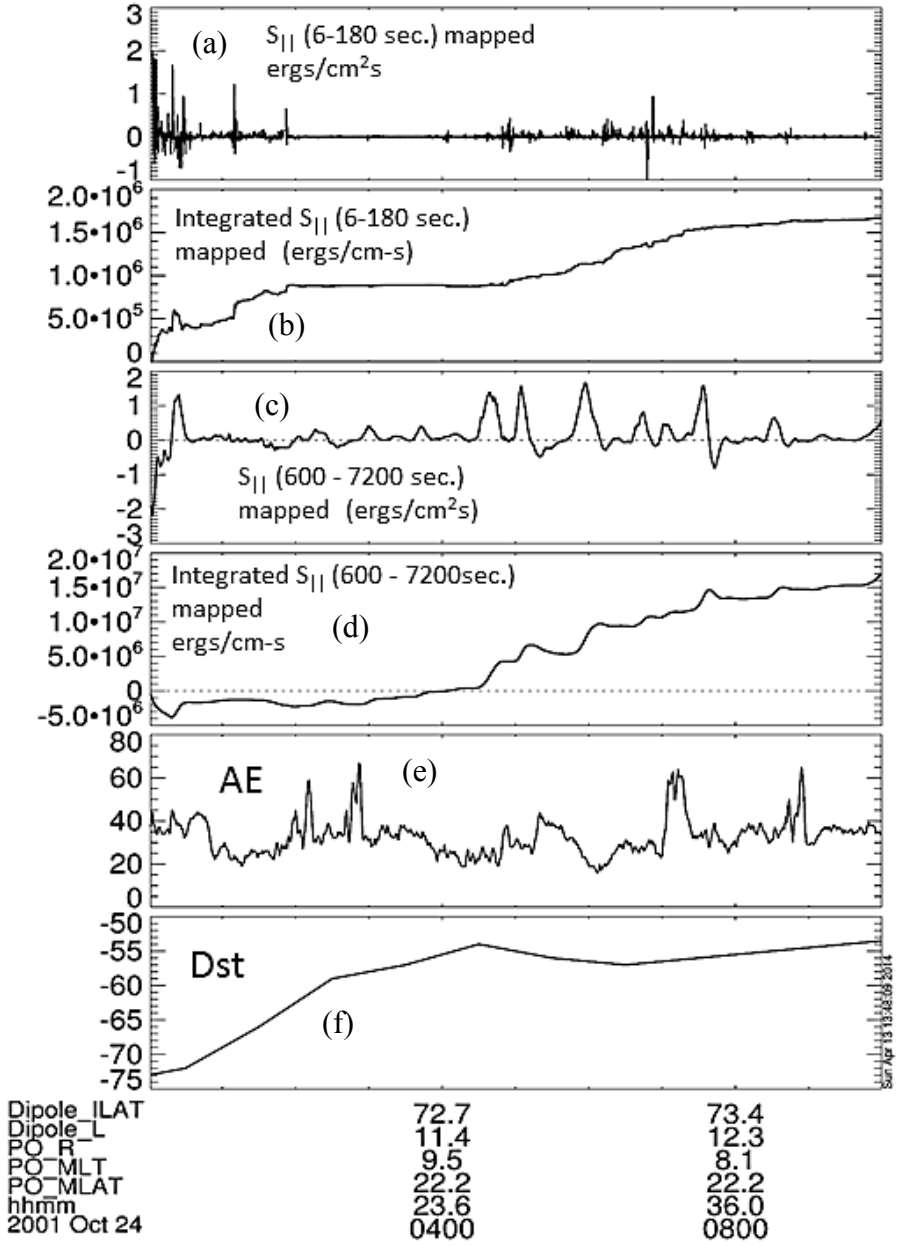

Figure 5.3: Ten hours of Polar data, Dst, and AE indices, from 00:00-10:00 UT on October 24, 2001. (a) The earthward, field aligned wave (6-180 sec) Poynting flux at Polar, on the night side, mapped to 100km. (b) The integrated wave Poynting flux from (a) along the mapped spacecraft trajectory. (c) The earthward, field aligned, large scale (600- 7200 sec.) Poynting flux at Polar, mapped to 100 km. (d) The large scale Poynting flux in (c) integrated along the mapped spacecraft foot point trajectory. (e) The Dst index, and (f) the AE index.

Table 5.1 summarized the peak intensities and integrated values for the three intervals described above. In addition to the wave and large scale Poynting flux shown in Figures 5.1,5.2, and 5.3, we also include the peak intensities and integrated values for the intermediate range (180 – 600 sec.) Poynting flux.

Oct., 2001	Oct 18 (pre storm, Dst ~-4, moderate substorms AE ~150 nT)	Oct 22 (major storm) Dst ~-130, AE ~2000	Oct 24 (recovery phase) Dst ~-70 (increasing) AE ~20-60
$S_{\|\|}$ (6-180 sec.) mapped, peaks	40-110 ergs/cm^{2}s	40-270 ergs/cm^{2}s	0.5-2 ergs/cm^{2}s
Int. $S_{\|\|}$ (6-180 sec.)	3.3x10^7 ergs/cm-s	2.1x10^8 ergs/cm-s	1.7x10^6 ergs/cm-s
$S_{\|\|}$ (180-600 sec.) mapped, peaks	2-15 ergs/cm-s	25-50 ergs/cm^{2}s	0.3-0.7 ergs/cm-s
Int. $S_{\|\|}$ (180-600 sec.)	1.7x10^7 ergs/cm-s	1.6x10^8 ergs/cm-s	2.2x10^6 ergs/cm-s
$S_{\|\|}$ (600-7200 sec.) mapped, peaks	4-15 ergs/cm^{2}s	9-30 ergs/cm^{2}s	0.5-1.5 ergs/cm^{2}s
Int. $S_{\|\|}$ (600-7200 sec.)	6.5x10^7 ergs/cm-s	3.0x10^8 ergs/cm-s	1.7x10^7 ergs/cm-s
Relative fraction Int. wave/total Int. med./total Int. large scale/total	 28.7% 14.8% 56.5%	 31.3% 23.9% 44.8%	 8.1% 10.5% 81.3%

Table 5.1: The localized peak intensities (mapped) and integrated values of the wave (6-180 sec., small scale), intermediate scale (180-600 sec.) and large scale (600 – 7200 sec.) Poynting flux for the separate intervals of different levels of geomagnetic activity.

As indicated in Table 5.1, both the peak intensities and integrated values of all three period ranges increase with increasing geomagnetic activity, most significantly with geomagnetic activity indicated by AE. The Dst can still have storm like values during the recovery phase, after substorms and injection of ion has ceased, but before it has time to decay. While the Dst may be disturbed during these times, the impulsive releases of energy from the tail, and convection has subsided, leading to decreased in the Poynting flux intensities of the various scale MHD perturbations. The relative fraction of wave Poynting flux increases with increasing geomagnetic activity, at the same time the relative fraction of energy carries by the large scale Poynting flux decreases with increasing geomagnetic activity.

The level of Poynting flux activity depends on the AE index; this index corresponds to the auroral electrojet, that is, to the enhancement of ionospheric currents corresponding the occurrence of substorms, associated with which are enhanced field line convection (large scale Poynting flux) and plasma flows. If the commencement of field line convection earthward from the tail is initiated by, or happens approximately at the same time as magnetic reconnection in the near earth tail, then the reconnection jets, or plasma flows, should be concurrent with the field line convection. Such plasma flows give rise to wave Poynting flux via the Kelvin-Helmholtz instability [Dai et al 2011].

One possible explanation for the relative increase in wave energy to large scale convection energy during storms may be the following. In order for there to be energy released from the night side, magnetospheric convection of field lines from the day to night side must first take place to store the energy in the tail. For periods of low activity

the convection may be closer to being steady state, without rapid, impulsive field line reconfigurations and fast turbulent flows that occur during active times, and which can give rise to Alfvén waves. If this is the case then large scale Poynting flux should dominate the energy transport at quieter times. During active times, the large scale Poynting flux will be enhanced, but there will also be the turbulent flows and impulsive field line reconfigurations that generate Alfvén waves. Thus during active times, a greater fraction of the energy will end up in waves then it does during quieter times.

5.3 Latitudinal evolution in small scale (wave) and large scale Poynting flux

In this section we compare the latitudinal evolutions of the mapped wave and large scale Poynting flux over the course of two ~10s of days intervals, each containing a major storm. The first interval is April 21 to May 17, 1998, and the second interval is October 17- October 27, 2001. These intervals encompass the pre-storm activity, main phase and recovery phase of the storms. These are the same two intervals examined in chapter 4 section 4.5 with respect to high altitude wave Poynting flux and low altitude electron kinetic energy flux.

Figure 5.4 shows 28 days, April 21-May17 1998, of the mapped wave (6-180 sec.) and large scale (600 – 7200 sec.) Poynting fluxes at Polar, peak intensity per 0.5^{o} ILAT, as a function of time and latitude. The latitudinal evolution of the mapped wave Poynting flux intensity is shown in Figure 5.4(a) and has been described in chapter 4. Figure 5.4(b) shows the latitudinal evolution of the mapped large scale Poynting flux intensity.

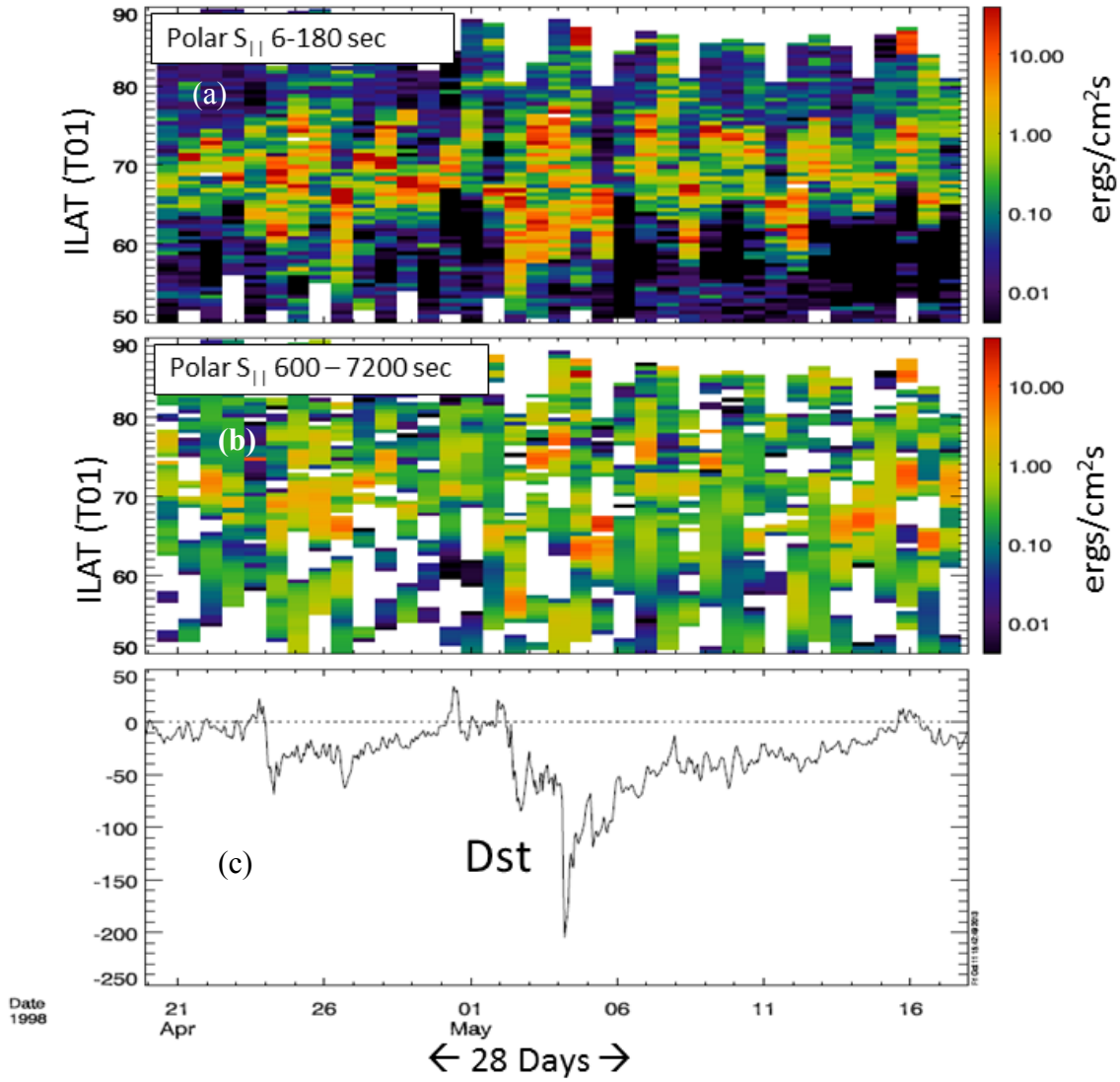

Figure 5.4: Twenty eight days of Polar Poynting flux and Dst index from April 21 through May 17 1998. (a) The field aligned wave (6-180 sec.) Poynting flux mapped to 100 km from Polar, as a function of time and latitude. (b) The field aligned large scale (600-7200 sec.) Poynting flux mapped to 100 km, as a function of time and latitude. These plots show the peak intensity per 0.5^{o} ILAT. (c) The Dst index.

For this event, the latitudinal evolution of the wave and large scale Poynting flux intensifications have some similarities; namely the regions of the most intense Poynting

flux of each type generally coincide. The large scale Poynting flux tends to be less intense (by about a factor of ~2-10) than that of the waves in those regions in which the wave activity is at its most intense. However, the large scale Poynting flux tends to be more intense than the wave Poynting flux in those locations in which the wave Poynting flux is small, for example at low latitude during quiet times. At low latitudes during quiet times the large scale Poynting flux is about an order or magnitude larger than the wave Poynting flux (~0.2 ergs/cm^{2}s relative to ~0.02 ergs/cm^{2}s).

It is also evident in Figure 5.4 (b) that there are numerous periods in which the large scale Poynting flux is directed upwards, and thus have negative values by the standard used herein (i.e. that positive Poynting flux is downward, or earthward), and so cannot appear on the logarithmic scale. As a result these areas of upward Poynting flux appear as white (absence of data), but correspond to times and latitudes for which small scale Poynting flux are present (i.e., the small scale Poynting flux is referenced as a proxy to indicating that there are data for such intervals, and that the lack of appearance of the large scale Poynting flux is due to it being upwards).

Figure 5.5 shows the average intensity per 0.5^o ILAT of the mapped large scale Poynting flux on both a logarithmic and a linear scale of intensity. Both scales are used because the averaging reduces the number of intervals with downward Poynting flux. Figure 5.5(a) shows the averaged mapped large scale Poynting flux per 0.5^o ILAT, on the linear intensity scale. Both downward and upward regions of Poynting flux in time and ILAT are evident. There are intense (~3-5 ergs/cm^{2}s) averaged mapped downward large scale

Poynting flux at low latitudes during the storm, such can be seen in Figure 5.5(a) and Figure 5.5(b) on May 2nd ,4th and 5th, 1998.

Inspection of Figure 5.5(a) suggests there are locations where the average upwards large scale Poynting flux is ~ 1 to 2 ergs/cm^{2}s. Such intervals occur between ~60^o and 78^o ILAT. The low latitude intervals of the upward large scale Poynting flux tend to occur during geomagnetically active times.

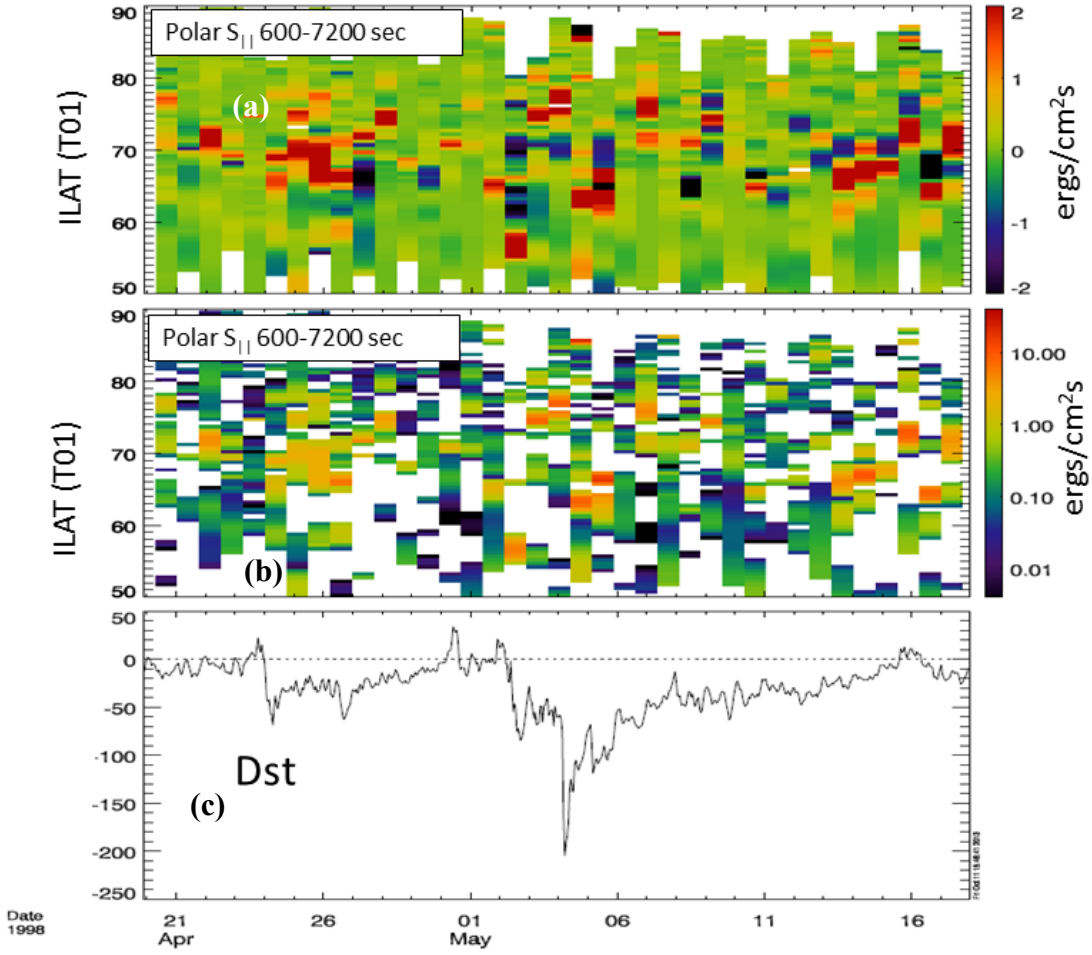

Figure 5.5: Twenty eight days of Polar large scale Poynting flux and Dst index from April 21 through May 17 1998. (a) The field aligned large scale (600-7200 sec.) Poynting flux mapped to 100 km from Polar, as a function of time and latitude, on a linear intensity

scale. (b) The field aligned large scale (600-7200 sec.) Poynting flux mapped to 100 km, as a function of time and latitude, on a logarithmic intensity scale. These plots show the average intensity per 0.5^{o} ILAT. (c) The Dst index.

We now examine the latitudinal evolution of the wave and large scale Poynting flux from the October 2001 storm. For this event, Polar has equal coverage of both north and south hemispheres. Since the Poynting flux intensity distributions in time and ILAT for the north and south hemispheres are similar, here we will only present the southern hemisphere Poynting flux. Figure 5.6 shows the mapped peak intensities of the wave and large scale Poynting flux as a function of time and ILAT from October 17 to October 26, 2001. A comparison between the wave Poynting flux in Figure 5.6(a) and the large scale Poynting flux in Figure 5.6 (b) indicates that the distribution in time and latitude of the intense ($\geq$ 1 erg/cm^{2}s) Poynting fluxes are similar. The intense large scale Poynting flux are typically an order of magnitude smaller than the intense wave Poynting flux at the same time and ILAT. Both of these observations are consistent with the observations in section 5.2 of this chapter. During the main phase of the storm the large scale Poynting flux intensifies down to low latitudes. Intensities ~5 erg/cm^{2}s make it down to latitudes at least as equatorward as ~56^{o} ILAT.

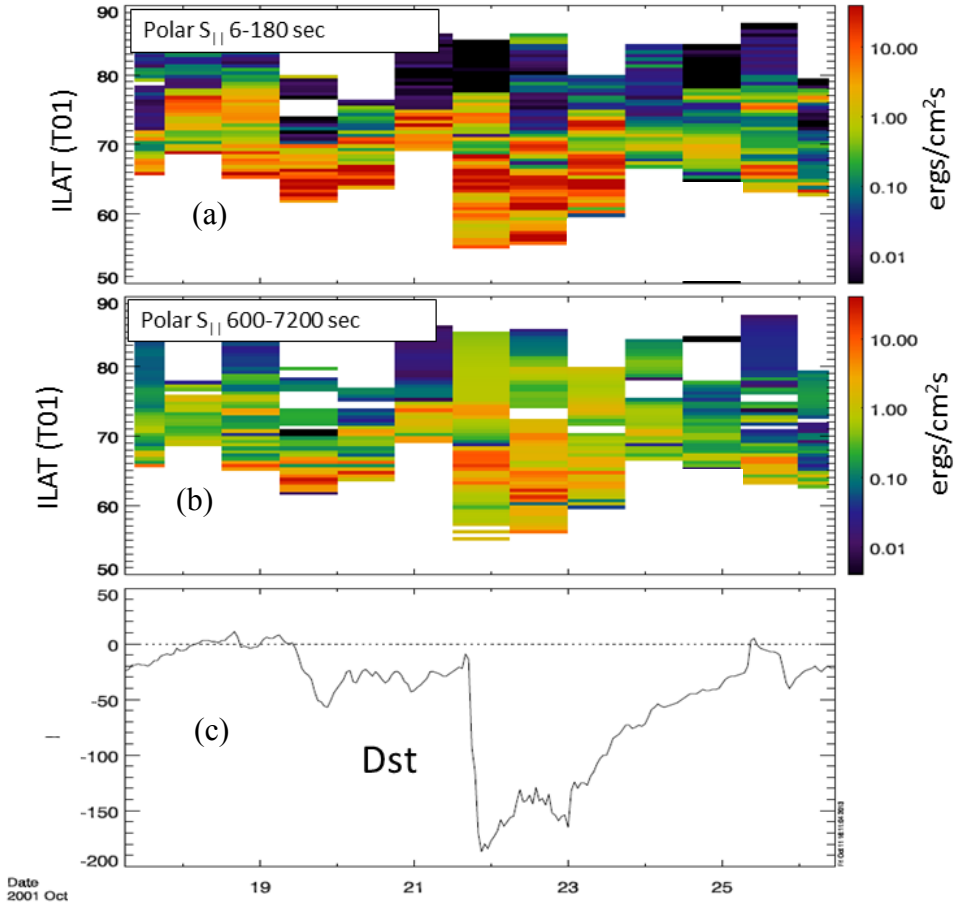

Figure 5.6: Nine days of Polar wave and large scale Poynting flux and Dst index for October 17 – October 26, 2001. (a) The field aligned wave (6-180 sec.) Poynting flux mapped to 100km, as a function of time and latitude. Peak intensity per 0.5^{o} ILAT for the southern hemisphere. (b) The field aligned large scale (600-7200 sec.) Poynting flux mapped to 100km, as a function of time and latitude. Peak intensity per 0.5^{o} ILAT for the southern hemisphere. (c) Dst index.

In Figure 5.7 we present the average intensity per 0.5^{o} ILAT of the mapped large scale Poynting flux on both linear and logarithmic intensity scales. The averaged values of the mapped large scale Poynting flux reach intensities up to a few ergs/cm^{2}s at low latitudes during the storm on October 22, as well as at localized intervals, over ~1^{o} ILAT, on

October 19 and 21. On other days it is not uncommon for there to be such localized intense large-scale Poynting flux at higher latitudes, typically 67°-75° ILAT. There are also location at which there is average upward Poynting flux of ~ 2 ergs/cm^{2}s at low latitude during the storm.

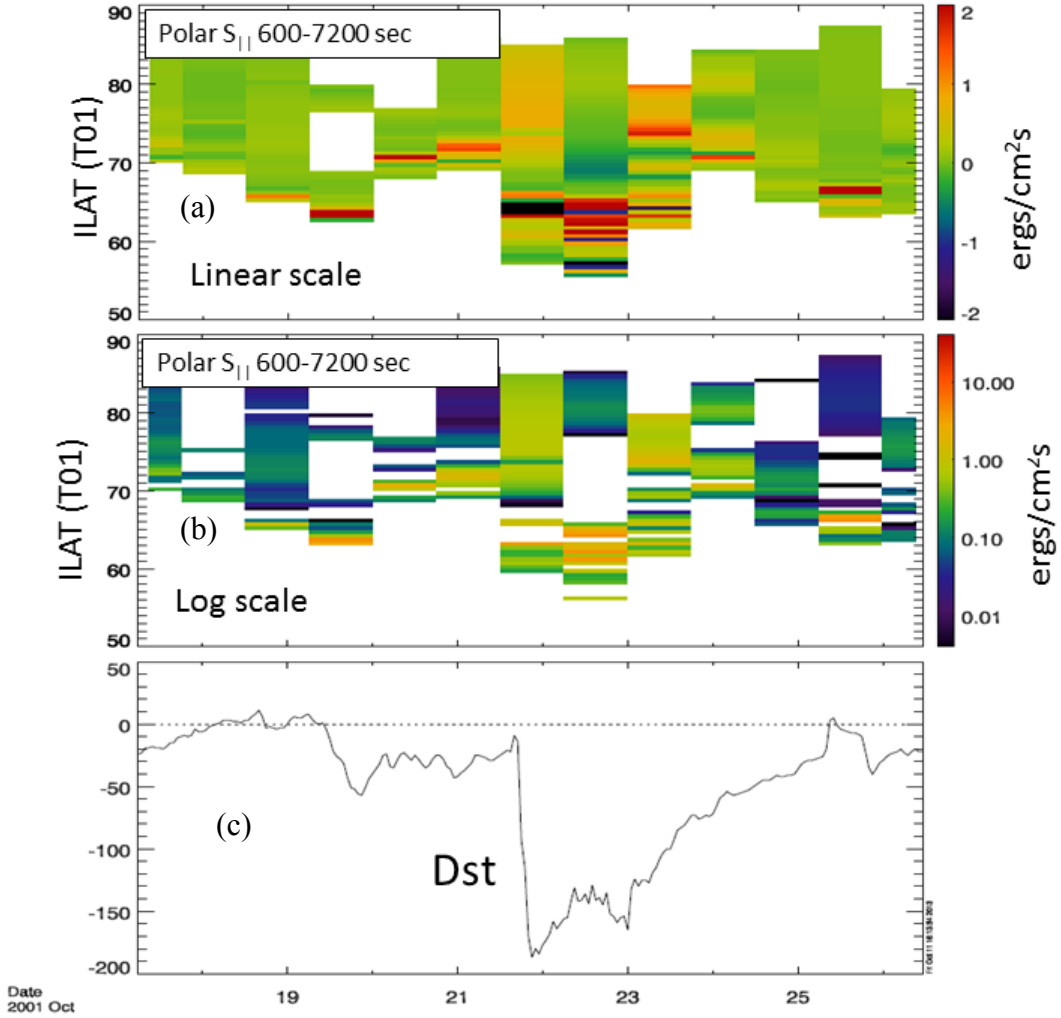

Figure 5.7: Nine days of Polar large scale Poynting flux and Dst index; from October 17 to October 26, 2001. (a) The field aligned large scale (600-7200 sec.) Poynting flux mapped to 100km, average intensity per 0.5° ILAT as a function of time and latitude, for the southern hemisphere, shown on a linear intensity scale. (b) The field aligned large scale Poynting flux, mapped to 100km, average intensity per 0.5° ILAT, as a function of time and latitude, shown on a logarithmic intensity scale. (c) Dst index.

5.4 Summary and Discussion

In this chapter we examined the large scale (600 -7200 sec.) Poynting flux in relation to the wave (6-180 sec.) Poynting flux. The general trend in the latitudinal evolution of the Poynting flux intensities is that the intense large scale Poynting flux tends to occur on the same field lines, or on field lines near those, as those on which the wave Poynting flux is located, especially during more geomagnetically active times. This suggests that both wave and the large scale Poynting flux may have a common origin or a related generative mechanism. Previous studies suggest that the Alfvén waves are produced by busty bulk flows of plasma [Angelopoulos et al 2002] and that the Kelvin Helmholtz instability in reconnection jets can gives rise to Alfvénic surface waves on the plasma sheet boundary [Dai et al 2011]. Such plasma flows originate from magnetic reconnection, and the reconnected field lines then undergo earthward/sunward convection. Thus the convecting field lines that carry large scale Poynting flux are also likely to be in the environment of the turbulent plasma flows, which should result in both wave and large scale Poynting flux occurring on the same field lines.

The large scale Poynting flux is typically not as intense as the wave Poynting flux. Typical large scale Poynting flux intensities are ~ 1 ergs/cm^{2}s for quiet intervals and 10s of ergs/cm^{2}s for active intervals. However the large scale Poynting flux tends to carry more energy, ranging from 1.5 times as much during the major storm to 10 times as much during the recovery phase. The fact that there is more energy carried by the large scale

Poynting flux suggests that, overall, the field aligned currents and flux tube convection processes transmit more energy to the ionosphere than do the waves. Though for localized places, and short intervals, the wave power often dominates by an order of magnitude. One possible reason for the variable partition of energy could be that during less active times field line convection is not as intense and likely more steady, with fewer impulsive releases of energy and fast turbulent flows of plasma, both of which tend to generate Alfvén waves. As a result, during such quieter intervals, when conditions for wave generation are less favorable, the fraction of the total energy that is placed into the large scale Poynting flux is larger than it is during active times when wave generation is favorable. During active times the sudden impulsive releases of large amounts of energy may place a larger fraction of the energy that will make up the total Poynting flux into wave generating processes.

Chapter 6

Summary and Conclusions

In this thesis we have investigated the latitudinal evolution of both high altitude wave and large scale Poynting flux and of the low altitude electron kinetic energy flux over the course of two major geomagnetic storms, including the pre-storm and recovery phase, on the night side, on an orbit by orbit basis. Previous research has focused on either localized conjunctions or on much larger timescale statistics. The current study is the first to look at the evolution in latitude of wave Poynting flux from a high altitude standpoint, and to compare that the evolution in the low altitude downward electron kinetic energy flux. Previous studies also focused on higher latitude Poynting flux, at the PSBL. In this study we are particularly interested in the low latitude ($\leq 65^{o}$ ILAT). Low latitude field lines map to the inner magnetosphere, and the energy transport processes into and through the inner magnetosphere are not yet fully understood. The role of the wave and large scale Poynting flux on low latitude field lines helps constrain and direct our understanding of these processes.

In comparing the high altitude wave Poynting flux to the low altitude electron kinetic energy flux intensities, on the night side, as a function of time and ILAT on an orbit by orbit basis, we find that the latitudinal evolution of the peak intensity per 0.5^{o} ILAT of the wave Poynting flux (mapped) and of the electron kinetic energy flux (mapped) are similar. During magnetically quiet times (Dst > -30nT) the wave Poynting flux peak intensities (mapped to 100km) at low latitudes are typically on the order of 10^{-3} to 10^{-2}

ergs/cm^{2}s. During storms the low latitude wave Poynting flux typically intensifies by about two or three orders of magnitude to 1 to 10 ergs/cm^{2}s; such enhancements extend down to latitudes of at least 55^o ILAT during major storms. The low latitude, low altitude electron kinetic energy flux (peak intensities) are typically on the order of 0.1 ergs/cm^{2}s pre storm, and intensifies to the order of 1 to 10s ergs/cm^{2}s during storms.

Even though their peak intensities are similar, the comparison of the average intensities (per 0.5^o ILAT) of the wave Poynting flux to the electron kinetic energy flux (as a function of ILAT and time) indicates that the average Poynting flux is typically significantly less than by the electron kinetic energy flux, indicating that there is more energy carried by the electrons than the Poynting flux. However there are still times and places, including low latitudes, where the average Poynting flux is still intense, $\gtrsim$ 1 erg/cm^{2}s. The existence of intense Poynting flux ($\gtrsim$ 1 erg/cm^{2}s) at low latitudes (in both peak and average values), at latitudes similar to those at which intense downward electrons are observed suggest that Alfvén waves are important for low latitude auroral acceleration processes.

The similarity between the latitudinal evolution in the peak Poynting flux and electron kinetic energy flux intensities suggests that Alfvénic auroral may occur throughout the region of enhanced auroral activity [consistent with the earlier works of Keiling et al [2003] and Chaston et al [2003]. In addition this similarity also suggests possible relation between the waves and electrons; such possible relations may be a.) that the high altitude wave Poynting flux power the acceleration of the lower altitude electrons, b.) that both

are produced together at higher altitudes, or that c.) the Poynting flux through some mechanism supplies energy to other waves that do not directly accelerate electrons, but scatter their pitch angle into the loss cone allowing them to precipitate into the ionosphere.

Comparisons of the wave Poynting flux to the UVI images and to integrated electron kinetic energy flux suggests that the Poynting flux carries between ~5-500% of the electron energy depending on the integration technique used. The lower values are similar to those suggested by previous studies [Keiling et al, 2003, Chaston et al 2007, Newell et al 2009. Janhunen et al 2006]. The possibility that the wave Poynting flux may play much larger role energetically in auroral dynamics is interesting, and will be the subject of future work.

The large scale Poynting flux, is less intense than the wave Poynting flux by about an order of magnitude during active times, and roughly the same intensity during quiet times. However, while the waves can deliver a greater power in localized times and places, overall the large scale Poynting flux carries more energy to the ionosphere over longer periods, from about 10 times more during quiet intervals too little over 1.3 times during major storms. The relative increase in the total amount of energy carried by the waves relative to the large scale Poynting flux with increasing activity may be due to a situation in which magnetic field line convection becomes more intense with activity, but also an increase in more sudden, impulsive, releases of energy that can launch Alfvén waves and turbulent flows that may generate intense waves Poynting flux, occurs, thus

putting an increased fraction of the total energy released into waves relative to the large scale convective processes.

One of the difficulties in determining the total amount of energy carried by the Poynting flux is the uncertainty in the relative velocity between the Polar spacecraft and the plasma sheet. In this thesis we attempted to estimate this speed by examining auroral images for the speed at which the poleward edge of the aurora expands, and mapping this speed up to the altitude of Polar. In addition there is another difficulty in that we do not know if and in what other parts of the near earth tail intense Poynting flux is present, we only observe that present at Polar's location. Two or more spacecraft at Polar altitudes, in polar orbits, would mitigate these problems. We would have measurements from two positions simultaneously and thus be able to see if there where concurrent intense Poynting flux, and if the structures seen at spacecraft one where later seen at spacecraft two, etc. This later observation would enable a much better velocity estimate.

Another aspect critical to understanding the total energy transport into and through the inner magnetosphere is the high altitude electron kinetic energy flux. The main focus of this thesis was the relation between the high altitude Poynting flux and low altitude electron kinetic energy flux. It is possible that some of the electrons constituting the low latitude electron kinetic energy flux are accelerated at altitudes above Polar. Determining the high altitude electron kinetic energy flux will require identifying intervals during which Polar's Hydra instrument resolves the field aligned distributions well, and adjusting the loss cone to take into account only those electrons that are field aligned enough at Polar so that they can precipitate without further field aligned acceleration.

However the integration difficulties mentioned above will still introduce uncertainties in the integration of the mapped electron kinetic energy flux.

Bibliography

Akasofu, S.I. (1964), The development of the auroral substorm, *Planetary and Space Science*, Vol. 12.

Akasofu, S.-I. (2004), Several 'controversial' issues on substorms, *Space Sci. Rev*., 113, 1–40, doi:10.1023/B:SPAC.0000042938.57710.fb

Angelopoulos, V., W. Baumjohann, C. F. Kennel, F. V. Coroniti, M. G. Kivelson, R. Pellat, R. J. Walker, H. Lühr, and G. Paschmann (1992), Bursty bulk flows in the inner central plasma sheet, *J. Geophys. Res*., 97(A4), 4027–4039, doi:10.1029/91JA02701.

Angelopoulos, V., J. A. Chapman, F. S. Mozer, J. D. Scudder, C. T. Russell, K. Tsuruda, T. Mukai, T. J. Hughes, and K. Yumoto (2002), Plasma sheet electromagnetic power generation and its dissipation along auroral field lines, *J. Geophys. Res*., 107(A8), 1181, doi:10.1029/2001JA900136.

Apatenkov, S. V., V. A. Sergeev, M. V. Kubyshkina, R. Nakamura, W. Baumjohann, A. Runov, I. Alexeev, A. Fazakerley, H. Frey, S. Muhlbachler, P. W. Daly, J.-A. Sauvaud, N. Ganushkina, T. Pulkkinen, G. D. Reeves, and Y. Khotyaintsev (2007), Multi-spacecraft observation of plasma dipolarization/injection in the inner magnetosphere, *Ann. Geophys*., 25, 801–814, doi:10.5194/angeo-25-801-2007.

Arnoldy, R. L., T. E. Moore (1983), Longitudinal structure of substorm injections at synchronous orbit, *J. Geophys. Res. Vol. 88* doi:10.1029/JA088iA08p06213.

Arnoldy, R. L., J. L. Posch, M. J. Engebretson, H. Fukunishi, H. J. Singer (1998), Pi1 magnetic pulsations in space and at high latitudes on the ground, *J. Geophys. Res.,* Volume 103, Issue A10.

Baumjohann, W., G. Paschmann, H. Lühr (1990a) Characteristics of high-speed ion flows in the plasma sheet, *J. Geophys. Res., 95*, 3801–3809.

Baumjohann W. and G. Paschmann (1990b), Geometry of the near-Earth plasma sheet, *J. Geophys Res*. Volume 95, Issue A7, pages 10707–10710.

Bortnik, J., R. M. Thorne, U. S. Inan, (2008) Nonlinear interaction of energetic electrons with large amplitude chorus*, Geophys. Res. Lett.,* Volume 35, Issue 21, DOI: 10.1029/2008GL035500.

Carpenter, D. L., and R. R. Anderson (1992), An ISEE/Whistler model of equatorial electron density in the magnetosphere, *J. Geophys. Res*., 97(A2), 1097–1108.

Carlson, C. W., R. F. Pfaff, J. G. Watzin, Fast Auroral Snapshot (FAST) mission, Geophys. Res. Lett., 25, 2013, 1998.

Carlson, C.W., J.P. McFadden, P. Turin, D.W. Curtis, A. Magoncelli (2001) The Electron and ion Plasma Experiment for Fast, Space Science Reviews, Volume 98, Issue 1-2, pp 33-66

Cattell, C., J. Dombeck, J. Wygant, J.F. Drake, M. Swisdak, M.L. Goldstein, W. Keith, A. Fazakerley, M. André, E. Lucek, A. Balogh (2005), Cluster observations of electron holes in association with magnetotail reconnection and comparison to simulations*, J. Geophys. Res*., Volume 110, Issue A1, 10.1029/2004JA010519

Cattell, C., J.R. Wygant, K. Goetz, K. Kersten, P.J. Kellogg, T. von Rosenvinge, S.D. Bale, I. Roth, M. Temerin, M.K. Hudson, R.A. Mewaldt, M. Wiedenbeck, M. Maksimovic, R. Ergun, M. Acuna, C.T. Russell (2008), Discovery of very large amplitude whistler-mode waves in Earth's radiation belts. *Geophys. Res. Lett. 35,* 01105 doi:10.1029/2007GL032009.

Cattell, C.A., A. Breneman, K. Goetz, P. J. Kellogg, K. Kersten, J. R. Wygant, L. B. Wilson III, M. D. Looper, J. B. Blake, and I. Roth (2012), Large-Amplitude Whistler Waves and Electron Acceleration in the Earth's Radiation Belts: A Review of STEREO and Wind Observations *GEOPHYSICAL MONOGRAPH SERIES, VOL. 199*, PP. 41-51.

Cattell, C., Dombeck, J. Preiwisch, A. Thaller, S. Vo, P. Wilson, L. B., III, Wygant, J. Mende, S. B., Frey, H. U., Ilie, R.; Lu, G. (2011), Observations of a high-latitude stable electron auroral emission at ~16 MLT during a large 25 substorm, J. Geophys. Res., 116, A07215, doi:10.1029/2010JA016132.

Chaston, C.C., J.W. Bonnell, L.M. Peticolas, C.W. Carlson, R.E. Ergun, J.P. McFadden, (2002), Driven Alfvén waves and electron acceleration: A FAST case study. Geophys. Res. Lett. doi:10.1029/2001GL013842

Chaston, C.C., J.W. Bonnell, C.W. Carlson, J.P. McFadden, R.E. Ergun, R.J. Strangeway, (2003), Properties of small-scale Alfvén waves and accelerated electrons from FAST. J. Geophys. Res. 108(A4), 8003. doi:10.1029/2002JA009420

Chaston, C. C., C. W. Carlson, J. P. McFadden, R. E. Ergun, and R. J. Strangeway (2007), How important are dispersive Alfvén waves for auroral particle acceleration? Geophys. Res. Lett., 34, L07101, doi:10.1029/2006GL029144.

Chaston, C. C., C. Salem, J. W. Bonnell, C. W. Carlson, R. E. Ergun, R. J. Strangeway, and J. P. McFadden (2008), The turbulent Alfvénic aurora, Phys. Rev. Lett., 100, 175003, doi:10.1103/PhysRevLett.100.175003.

Cowley S.W.H. (1991),The acceleration of charged particles in magnetic current sheets, *Adv. Space Res*. 11.

Cowley, S.W.H. (2000), Magnetosphere-Ionosphere Interactions: A tutorial Review *AGU monograph* 118.

Daglis, I. A., R. M. Thorne, W. Baumjohann, and S. Orsini (1999), The terrestrial ring current: Origin, formation, and decay, *Rev. Geophys*., 37*(4),* 407–438*, doi:*10.1029/1999RG900009.

Dai, L., J. R. Wygant, C. Cattell, J. Dombeck, S. Thaller, C. Mouikis, A. Balogh, and H. Rème (2011), Cluster observations of surface waves in the ion jets from magnetotail reconnection *J. Geophys. Res. 116*, A12227, doi:10.1029/2011JA017004.

Dombeck, J., C. Cattell, J.R. Wygant, A. Keiling, J. Scudder, Alfvén waves and Poynting flux observed simultaneously by Polar and FAST in the plasma sheet boundary layer. J. Geophys. Res. 110, A12S90 (2005). doi:10.1029/2005JA011269

Dombeck, J., C. Cattell, J. Wygant, J. McFadden, R.J. Stangeway, FAST Satellite Evidence for Nightside Low-Latitude Low potential Drop Inverted-V and Alfvénic Accelerated Electron Precipitation During Large Geomagnetic Storms, In press (2013)

Dungey, J.W. (1961), Interplanetary magnetic field and the auroral zones, *Phys. Rev. Lett. 6*,2.

Fairfield, D. H., T. Mukai, M. Brittnacher, G.D. Reeves, S. Kokubun, G.K. Parks, T. Nagai, H. Matsumoto, K. Hashimoto, D.A. Gurnett, T. Yamamoto (1999), Earthward flow bursts in the inner magnetotail and their relation to auroral brightenings, AKR intensifications, geosynchronous particle injections and magnetic activity *J Geophys Res*., Vol. 104, A1.

Fahleson, U., (1967), Theory of Electric Field Measurements Conducted in the Magnetosphere with electric Probes. Space Sciences Reviews 7 238-262.

Frank, L. A., and J. B. Sigwarth (2003), Simultaneous images of the northern and southern auroras from the Polar spacecraft: An auroral substorm, J. Geophys. Res., 108(A4), 8015, doi:10.1029/2002JA009356.

Goertz, C.K., R.W. Boswell, Magnetosphere-ionosphere coupling. J. Geophys. Res. 84, 7239–7246 (1979)

Goldstein, J. (2006), Plasmasphere response: tutorial and review of recent imaging results, *Space Sci. Rev*.

Gonzalez, W. D., J. A. Joselyn, Y. Kamide, H. W. Kroehl, G. Rostoker, B. T. Tsurutani, *and* V. Vasyliunas (1994), What is a geomagnetic storm. *J. Geophys. Res.*, *99,* 5771–5792.

Gurnett, Donald A., and Amitava Bhattacharjee (2005), Introduction to Plasma Physics; With Space and Laboratory Application*s*, Cambridge.

Hardy, D. A.; Schmitt, L. K.; Gussenhoven, M. S.; Marshall, F. J.; Yeh, H. C. (1984), Precipitating electron and ion detectors (SSJ/4) for the block 5D/Flights 6-10 DMSP (Defense Meteorological Satellite Program) satellites: Calibration and data presentation , Environmental Research Papers No. 902

Hardy, D. A., M. S. Gussenhoven, R. Raistrick, and W. J. McNeil (1987), Statistical and functional representations of the pattern of auroral energy flux, number flux, and conductivity, J. Geophys. Res., 92(A11), 12275–12294, doi:10.1029/JA092iA11p12275.

Harvey, P., Mozer, F. S.; Pankow, D.; Wygant, J.; Maynard, N. C.; Singer, H.; Sullivan, W.; Anderson, P. B.; Pfaff, R.; Aggson, T.; Pedersen, A.; Fälthammar, C.-G.; Tanskannen, P., (1995), The Electric Field Instrument on the Polar satellite, The Global Geospace MissionC. T. Russell, 583, Kluwer Acad., Norwell, Mass.

Hasegawa, A., (1976) Particle acceleration by MHD surface wave and formation of aurora. J. Geophys. Res. 811, 5083–5090.

Hashimoto, K. K., T. Kikuchi, and Y. Ebihara (2002), Response of the magnetospheric convection to sudden interplanetary magnetic field changes as deduced from the evolution of partial ring currents, *J. Geophys. Res*., 107(A11), 1337, doi:10.1029/2001JA009228.

Hones, E. W., Jr. (1976), Observations in the Earth's magnetotail relating to magnetic merging, *Sol. Phys., 47*, 101–113, doi:10.1007/BF00152248.

Hones, E. W., Jr., T. Pytte, and H. I. West Jr. (1984), Associations of geomagnetic activity with plasma sheet thinning and expansion: A statistical study, *J. Geophys. Res*., 89, 5471–5478, doi:10.1029/JA089iA07p05471.

Horne, Richard B., Richard M. Thorne, Yuri Y. Shprits, Nigel P. Meredith, Sarah A. Glauert, Andy J. Smith, Shrikanth G. Kanekal, Daniel N. Baker, Mark J. Engebretson, Jennifer L. Posch, Maria Spasojevic, Umran S. Inan, Jolene S. Pickett and Pierrette M. E. Decreau (2005), Wave acceleration of electrons in the Van Allen radiation belts, *Nature*, 437. doi: 10.1038/nature03939

Hull, A. J., M. Wilber, C. C. Chaston, J. W. Bonnell, J. P. McFadden, F. S. Mozer, M. Fillingim, and M. L. Goldstein (2010), Time development of field-aligned currents, potential drops, and plasma associated with an auroral poleward boundary intensification, J. Geophys. Res., 115, A06211, doi:10.1029/2009JA014651.

Janhunen, P., A. Olsson, C. T. Russell, and H. Laakso (2006), Alfvénic electron acceleration in aurora occurs in global Alfvén resonosphere region, Space Sci. Rev., 122(1–4), 89–95, doi:10.1007/s11214-006-7017-5.

Keiling, A., J.R. Wygant, C. Cattell, M. Temerin, F.S. Mozer, C.A. Kletzing, J. Scudder, C.T. Russell, W. Lotko, A.V. Streltsov, Large Alfvén wave power in the plasma sheet boundary layer during the expansion phase of substorms. Geophys. Res. Lett. 27, 3169 (2000)

Keiling, A., J. R. Wygant, C. Cattell, M. Johnson, M. Temerin, F. S. Mozer, C. A. Kletzing, J. Scudder, and C. T. Russell (2001), Properties of large electric fields in the plasma sheet at 4–7 RE measured with Polar, *J. Geophys. Res.*, 106(A4), 5779–5798, doi:10.1029/2000JA900130.

Keiling, A., J. R. Wygant, C. Cattell, W. Peria, G. Parks, M. Temerin, F. S. Mozer, C. T. Russell, and C. A. Kletzing (2002), Correlation of Alfvén wave Poynting flux in the plasma sheet at 4–7 RE with ionospheric electron energy flux, *J. Geophys. Res., 107*(A7), 1132, doi:10.1029/2001JA900140.

Keiling, A., Kim, K.-H., Wygant, J. R., Cattell, C., Russell, C. T., Kletzing, C. A., (2003), Global morphology of wave Poynting flux: Powering the aurora. Science 299, 383. doi:10.1126/science.1080073

Kivelson, M. and C.T. Russell (Eds.) (1995), *Introduction to Space Physics*, Cambridge University Press.

Kletzing, C. A. (1994), Electron acceleration by kinetic Alfvén waves, J. Geophys. Res., 99, 11,095–11,103, doi:10.1029/94JA00345.

Kletzing, C.A., S. Hu, Alfvén wave generated electron time dispersion. Geophys. Res. Lett. 28, 693–696 (2001)

Knight, S. (1973), Parallel electric fields, *Planet. Space Sci., 21*(5), 741–750, doi:10.1016/0032-0633(73)90093-7.

Lee, A. R., P. T. Newell, J. Gjerloev, and K. Liou (2010), Relatively low-latitude wave aurora and substorms, Geophys. Res. Lett., 37, L06101, doi:10.1029/2009GL041680.

Lessard, M.R., E.J. Lund, S.L. Jones, R.L. Arnoldy, J.L. Posch, M.J. Engebretson, K. Hayashi, Nature of Pi1B pulsations as inferred from ground and satellite observations. Geophys. Res. Lett. 33, L14108 (2006). doi:10.1029/2006GL026411

Lessard, M. R., E. J. Lund, H. M. Kim, M. J. Engebretson, and K. Hayashi (2011), Pi1B pulsations as a possible driver of Alfvénic aurora at substorm onset, J. Geophys. Res., 116, A06203, doi:10.1029/2010JA015776.

Liou, K.; Newell, P. T.; Meng, C.-I.; Brittnacher, M.; Parks, G., (1997) Synoptic auroral distribution: A survey using Polar ultraviolet imagery, Journal of Geophysical Research, Volume 102, Issue A12, p. 27197-27206

Liu Chen and Akira Hasegawa (1974), Plasma heating by spatial resonance of Alfvén wave, Phys. Fluids 17, 1399 (1974)

Lyons, L.R. (1980), Generalization of Large-Scale Regions of Auroral Currents, Electric Potentials, and Precipitation by the Divergence of Convection electric fields, *J. Geophys Res*. 85.

Lysak, R. L., and C. W. Carlson (1981), The effect of microscopic turbulence on magnetosphere-ionosphere coupling, *Geophys. Res. Lett*., 8(3), 269–272, doi:10.1029/GL008i003p00269.

Lysak, R. L. and W. Lotko (1996), On the Kinetic Dispersion Relation for Shear Alfvén Waves, *J. Geophys. Res*. 101, 5085.

Lysak, R. L., Relationship between electrostatic shocks and kinetic Alfvén waves, Geophys. Res. Lett., 25, 2089, 1998

Lysak, R. L., and Y. Song (2003), Kinetic theory of the Alfvén wave acceleration of auroral electrons, J. Geophys. Res., 108(A4), 8005, doi:10.1029/2002JA009406.

Lysak, R. L., and Y. Song (2011), Development of parallel electric fields at the plasma sheet boundary layer, J. Geophys. Res., 116, A00K14, doi:10.1029/2010JA016424

Maynard, N. C., W. J. Burke, E. M. Basinska, G. M. Erickson, W. J. H. ughes, H. J. Singer, A. J. Yahnin, D. A. Hardy, F. S. Mozer, Dynamics of the inner magnetosphere near times of substorm onset, J. Geophys. Res., 101, 7705, 1996.

McPherron, R. L. (1970), Growth phase of magnetospheric substorms, *J. Geophys. Res.*, 75(28), 5592–5599, doi:10.1029/JA075i028p05592.

McPherron, R. L. (1972), Substorm related changes in the geomegnetotail: The growth phase, *Planet. Space Sci*., 20(9), 1521–1539, doi:10.1016/0032-0633(72)90054-2.

McPherron, R. L., C. T. Russell, and M. P. Aubry (1973), Phenomenological model for substorms, *J. Geophys. Res*., 78, 3131.

Mende, S. B., C. W. Carlson, H. U. Frey, L. M. Peticolas, and N. Østgaard (2003), FAST and IMAGE-FUV observations of substorm onset, J. Geophys. Res., 108(A9), 1344, doi:10.1029/2002JA009787.

Meredith, N.P., R.B. Horne, R.R. Anderson (2001), Substorm dependence of chorus amplitudes: implications for the acceleration of electrons to relativistic energies. *J. Geophys. Res. 106*, 13165 doi:10.1029/2000JA900156b.

Millan, R.M., and R.M. Thorne, (2007) Review of radiation belt relativistic electron losses, *J. Atmos. and Solar terr. phys., 69*.

Mizera, P. F., D. J. Gorney, and J. F. Fennell (1982), Experimental verification of an S-shaped potential structure, *J. Geophys. Res*., 87(A3), 1535–1539, doi 10.1029/JA087iA03p01535.

Mozer, F.S., U.V. Fahleson, C.G.Fälthammer, M.C. Kelley, K. Knott, A. Pedersen., (1972), A Proposal to Measure Quasi-Static Electric fields on the Mother Daughter Satellites. University of California at Berkeley, Space Sciences Laboratory Report, vol. UCBSSL No. 454, published 1 September 1972.

Mozer, F.S., Analysis of Techniques for Measuring DC and AC Electric Fields in the Magnetosphere Space Sciences Reviews 14 (1973) 272-313

Mozer, F. S., C. W. Carlson, M. K. Hudson, R. B. Torbert, B. Parady, J. Yatteau, M. C. Kelley (1977), Observations of paired electrostatic shocks in the polar magnetosphere, *Phys. Rev. Lett*., 38, 292.

Mozer, F. S., T.D. Phan, S.D. Bale (2003), The complex structure of the reconnecting magnetopause , *Physics of Plasmas*, Volume 10, Issue 6, pp. 2480-2485.

Mozer F.S. (2006), Collisionless magnetic field reconnection from first principles: What it can and cannot do, arXiv:physics/0606047v1.

Newell, P. T. (2000), Reconsidering the inverted-V particle signature: Relative frequency of large-scale electron acceleration events, J. Geophys. Res., 105(A7), 15779–15794, doi:10.1029/1999JA000051.

Newell, P. T., T. Sotirelis, K. Liou, C.-I. Meng, and F. J. Rich (2007), A nearly universal solar wind-magnetosphere coupling function inferred from 10 magnetospheric state variables, J. Geophys. Res., 112, A01206, doi:10.1029/2006JA012015.

Newell, P. T., T. Sotirelis, and S. Wing (2009), Diffuse, monoenergetic, and broadband aurora: The global precipitation budget, J. Geophys. Res., 114, A09207, doi:10.1029/2009JA014326.

Newell, P. T., A. R. Lee, K. Liou, S.-I. Ohtani, T. Sotirelis, and S. Wing (2010), Substorm cycle dependence of various types of aurora, J. Geophys. Res., 115, A09226, doi:10.1029/2010JA015331.

Newell, P. T., T. Sotirelis, and E. J. Mitchell (2012), Evolution of auroral acceleration types inferred from two-satellite coincidences, J. Geophys. Res., 117, A12216, doi:10.1029/2012JA018287.

Parker, E. N. (1957), Sweet's mechanism for merging magnetic fields in conducting fluids, *J. Geophys. Res*., 62, 509.

Paschmann, G., Stein Haaland and Rudolf Treumann (Eds.) (2002), *Auroral Plasma Physics*, *Space Sciences Reviews 103*: Kluwer.

Pedersen, A., F. Mozer, G. Gustafsson. Electric Field Measurements in a Tenuous Plasma with Spherical Double Probes. Fields Geophysical Monograph 103. , American Geophysical Union, 1998.

Pedersen, A. and B. Lybekk, From Langmuir Probes to Electric Field Double Probes. Found at www.fys.uio.no/plasma/star/pdf/IntroEfield.pdf

Pedersen, A., Cattell, C. A., Mozer, F., Falthammar, C.-G., Lindqvist, P.-A., Formisano, V., Torbert, R. (1984), Quasistatic electric field measurements with spherical double probes on the GEOS and ISEE satellites. Space Sciences Review 37 269-312

Petschek, H. E. (1964), Magnetic field annihilation, in AAS/NASA Symposium on the Physics of Solar Flares, edited by W. N. Ness, p. 425, NASA, Washington, D. C.

Pfaff, R., C. Carlson, J. Watzin, D. Everett, and T. Gruner (2001), An overview of the Fast Auroral Snapshot (FAST) satellite, Space Sci. Rev., 98, 1.

Pilipenko, V.A., E. Fedorov, M.J. Engebretson, K. Yumoto, Energy budget of Alfvén wave interactions with the auroral acceleration region. J. Geophys. Res. 109, A10204 (2004). doi:10.1029/2004JA010440

Reeves, G. D., K. L. McAdams, R. H. W. Friedel, and T. P. O'Brien (2003), Acceleration and loss of relativistic electrons during geomagnetic storms, *Geophys. Res. Lett.,* 30(10), *1529, doi:*10.1029/2002GL016513.

Russell, C. T., R.L. McPherron (1973), The Magnetotail and Substorms, *Space Science Reviews*, Volume 15, Issue 2-3.

Russell, C. T., R. C. Snare, J. D. Means, D. Pierce, D. Dearborn, M. Larson, G. Barr, G. LE, The GGS/Polar Magnetic Fields Investigation, The Global Geospace MissionC. T. Russell, 563, Kluwer Acad., Norwell, Mass., 1995.

Schulz, M. and L. Lanzerotti (1974), *Particle diffusion in the radiation belts,* Physics and Chemistry in Space, Berlin: Springer.

Scudder, J., Hunsacker, F., Miller, G., Lobell, J., Zawistowski, T., Ogilvie, K., Keller, J., Chornay, D., Herrero, F., Fitzenreiter, R., Fairfield, D., Needell, J., Bodet, D., Googins, J., Kletzing, C., Torbert, R., Vandiver, J., Bentley, R., Fillius, W., McIlwain, C., Whipple, E., Korth, A. (1995), A 3-dimensional electron and ion hot plasma instrument for the Polar spacecraft of the GGS mission, The Global Geospace MissionC. T. Russell, 495, Kluwer Acad., Norwell, Mass.

Sergeev, V. A., D.G. Mitchell, C.T. Russell, D.J. Williams (1993), Structure of the tail plasma/current sheet at ~11 RE and its changes in the course of a substorm *J. Geophys. Res.*, Volume 98, Issue A10, p. 17345-17366.

Song, Yan, and Robert L. Lysak (2001), Towards a new paradigm: from a quasi-steady description to a dynamical description of the magnetosphere *Space Science Reviews, v. 95*, Issue 1/2, p. 273-292.

Song, Y., and R. L. Lysak (2006), The displacement current and the generation of parallel electric fields, *Phys. Rev. Lett*., 96, 145002.

Stasiewicz, K. , P. Bellan, C. Chaston, C. Kletzing, R. Lysak, J. Maggs, O. Pokhotelov, C. Seyler, P. Shukla, L. Stenflo, A. Streltsov, J.-E. Wahlund (2000), Small Scale Alfvénic Structures in the Aurora, *Space Sciences Reviews* 92.

Stasiewicz, K.; Khotyaintsev, Y.; Berthomier, M.; Wahlund, J.-E., Identification of widespread turbulence of dispersive Alfvén waves , Geophysical Research Letters, Volume 27, Issue 2, p. 173-176 (2000)

Strangeway, R.J., R.E. Ergun, Y.-J. Su, C.W. Carlson, and R.C. Elphic (2005), Factors controlling ionospheric outflows as observed at intermediate altitudes, *J. Geophys. Res*., VOl 110, A03221, doi:10.1029/2004JA010829.

Sweet, P. A. (1958), The neutral point theory of solar flares, in Electromagnetic Phenomena in Cosmical Physics, edited by B. Lehnert, p. 123, Cambridge Univ. Press, New York.

Swift, D. W. (2007), Simulation of auroral electron acceleration by inertial Alfvén waves, J. Geophys. Res., 112, A12207, doi:10.1029/2007JA012423.

Thompson, B. J., and R. L. Lysak (1996), Electron acceleration by inertial Alfvén waves, J. Geophys. Res., 101, 5359–5369, doi:10.1029/95JA03622.

Thorne, R.M., B. Ni, X. Tao, R.B. Horne, N.P. Meredith (2010), Scattering by chorus waves as the dominant cause of diffuse auroral precipitation *Nature 467*, 943–946.

Torr, M. R., Torr, D. G., Zukic, M., Johnson, R. B., Ajello, J., Banks, P., Clark, K., Cole, K., Keffer, C., Parks, G., Tsurutani, B., Spann, J. (1995), A Far Ultraviolet Imager for the International Solar Terrestrial Physics Mission, The Global Geospace MissionC. T. Russell, 329, Kluwer Acad., Norwell., Mass.

Tsyganenko, N. A., A magnetospheric magnetic field model with a warped tail current sheet, Planet. Space Sci., 37, 5, 1989.

Tsyganenko, N. A. (1995), Modeling the Earth's magnetospheric magnetic field confined within a realistic magnetopause, J. Geophys. Res., 100(A4), 5599–5612, doi:10.1029/94JA03193.

Tsyganenko, N. A. (2002a), A model of the near magnetosphere with a dawn-dusk asymmetry: 1. Mathematical structure, J. Geophys. Res., 107(A8), 1179, doi:10.1029/2001JA000219.

Tsyganenko, N. A. (2002b), A model of the near magnetosphere with a dawn-dusk asymmetry: 2. Parameterization and fitting to observations, J. Geophys. Res., 107(A8), 1176, doi:10.1029/2001JA000220.

Tsyganenko, N. A., and M. I. Sitnov (2005), Modeling the dynamics of the inner magnetosphere during strong geomagnetic storms, J. Geophys. Res., 110, A03208, doi:10.1029/2004JA010798.

Vaivads, A., André, M., Buchert, S., Eriksson, A. I., Olsson, A., Wahlund, J.-E., Janhunen, P., Marklund, G., Kistler, L. M., Mouikis, C., Winningham, D., Fazakerley, A., Newell, P. (2003),What high altitude observations tell us about the auroral acceleration: A Cluster/DMSP conjunction, Geophys. Res. Lett. 30, 1106. doi:10.1029/2002GL016006

Watt, C. E. J., R. Rankin, I. J. Rae, and D. M. Wright (2005), Self-consistent electron acceleration due to inertial Alfvén wave pulses, J. Geophys. Res., 110, A10S07, doi:10.1029/2004JA010877.

Watt, C. E. J., and R. Rankin (2009), Electron trapping in shear Alfvén waves that power the aurora, Phys. Rev. Lett., 102(4), 045002, doi:10.1103/PhysRevLett.102.045002.

Watt, C. E. J., and R. Rankin (2010), Do magnetospheric shear Alfvén waves generate sufficient electron energy flux to power the aurora? J. Geophys. Res., 115, A07224, doi:10.1029/2009JA015185.

Wygant, J., D. Rowland, H.J. Singer, M. Temerin, F. Mozer, M.K. Hudson (1998), Experimental evidence on the role of the large spatial scale electric field in creating the ring current, *J. Geophys Res, Vol 103*, Issue A12.

Wygant, J. R., A. Keiling, C. A. Cattell, M. Johnson, R. L. Lysak, M. Temerin, F. S. Mozer, C. A. Kletzing, J. D. Scudder, W. Peterson, C. T. Russell, G. Parks, M. Brittnacher, G. Germany, J. Spann (2000), Polar spacecraft based comparisons of intense electric fields and Poynting flux near and within the plasma sheet-tail lobe boundary to UVI images: An energy source for the aurora, *J. Geophys. Res*., 105(A8), 18675–18692, doi:10.1029/1999JA900500.

Wygant, J. R., C.A. Cattell, R. Lysak, Y. Song, J. Dombeck, J. McFadden, F.S. Mozer, C.W. Carlson, G. Parks, E.A. Lucek, A. Balogh, M. Andre, H. Reme, M. Hesse, C. Mouikis (2005), Cluster observations of an intense normal component of the electric field at a thin reconnecting current sheet in the tail and its role in the shock-like acceleration of the ion fluid into the separatrix region , *J. Geophys Res*, Volume 110, Issue A9, CiteID A09206.

Zhang, B., W. Lotko, O. Brambles, P. Damiano, M. Wiltberger, and J. Lyon (2012), Magnetotail origins of auroral Alfvénic power, J. Geophys. Res., 117, A09205, doi:10.1029/2012JA017680.

Zheng, Yihua, Thomas E. Moore, Forrest S. Mozer, Christopher T. Russell, and Robert Strangeway, (2005), Polar study of ionospheric ion outflow versus energy input. J. Geophys. Res., Vol 110, A07210, doi:10.1029/2004JA010995.